THE UNIVERSITY *of* EDINBURGH

Standardisation of Preclinical PET/CT Protocols Across Multiple Research Centres

Wendy Anne McDougald

Doctor of Philosophy

Centre for Cardiovascular Science
Edinburgh Medical School Deanery of Clinical Sciences
College of Medicine and Veterinary Medicine

Abstract

Preclinical Positron Emission Tomography/Computed Tomography (PET/CT) is a well-established non-invasive imaging tool for studying disease development/progression, the development of novel radiotracers and pharmaceuticals for clinical applications. Over the last five years more than 8,200 preclinical studies using PET/CT were conducted. Despite this pivotal role, standardisation of preclinical PET/CT protocols, including CT absorbed dose guidelines, is essentially non-existent. Therefore, the first and second aims of this project were: (1) to quantitatively assess the variability of current preclinical PET and CT acquisition and reconstruction protocols in routine use across multiple centres and scanners; and (2) to propose optimized standardised acquisition and reconstruction PET/CT protocols for routine scanning procedures across all sites in a preclinical PET/CT laboratory. By assessing quantitative accuracy (known versus measured) and precision (reduced variability) of currently used routine protocols between five different sites/scanners (Bruker Albira, Mediso nanoPET/CT, Sedecal Super Argus, Siemens Inveon and Trifoil LabPET/CT), standard protocols were determined. Thereby, irrespective of scanner characteristics the least biased empirical quantitative and qualitative protocol results defined the standard protocol. In essence, neutralizing the manufacturers' difference, replacing scanner variability for scanner similarity to establish global standard protocols.

The analysis of sites' routine protocol results revealed significant quantitative differences between all five sites/scanners. Whereas the standard protocols put forth improved accuracy and precision across all sites. Additionally, the large disparity and measured amounts of CT absorbed ionising radiation amongst sites brought to light the lack of preclinical radiation guidelines and dose regulations. Unregulated CT radiation dose is of great concern. CT ionising radiation is known to have biological adverse effects. Thus, overexposure of radiation will potentially cause unnecessary animal suffering and confound research outcomes. Overall, the proposed standard CT protocol reduced radiation doses. The implementation of preclinical PET/CT standardised protocols, developed and tested in this project, will provide more robust, reliable and reproducible translational data sets for clinical applications. In accordance with the National Centre for the Replacement, Refinement and Reduction of Animals in Research (NC3Rs) objectives, the refinement of PET/CT protocols and reduction of CT absorbed dose impacts animal

welfare positively and potentially reduces the number of animals used. Reducing study variability in site and across sites through standardisation of protocols improves statistically significant results using less animals.

For study specific imaging parameters in preclinical PET/CT rodents are commonly used to design the protocol. The third aim of this project strives to develop a tissue equivalent material (TEM) anthropomorphic rodent phantom for the replacement of animals when designing and optimizing varying *in vivo* rodent imaging protocols. Using a TEM phantom reduces potential biological experimental variability caused by the animals and increases reproducibility of findings. To address this aim, twenty-four commercially available 3D printing materials were X-rayed for the evaluation Hounsfield units (HU). A comparison of calculated 3D material attenuation coefficients and accepted tissue attenuation coefficient was also done. CT images were acquired using four CT protocols and the developed standard CT protocol. Based on measured material HUs compared to accepted tissue/organ HU values, four materials were chosen for testing and further evaluation in a 3D printed phantom prototype was undertaken. In order to obtain the anatomical features of the rodent a CT acquisition of a scheduled 1 rodent was acquired. The CT images were used for the 3D printing design. A 3D printed (TEM) anthropomorphic rodent phantoms was printed and tested. Measured HU analysis of the phantom TEM materials shows promise as a replacement strategy. This imaging protocol optimisation approach is also in line with the NC3Rs objective of replacing and/or avoiding the use animals.

Lay summary

Images acquired by X-rays (CT) are used in assisting doctors to diagnose health problems. Another medical imaging technique used by doctors is positron emission tomography (PET). Combined with CT imaging this is called PET/CT. In scientific research PET/CT is a key tool for disease identification and tracking as well as for assessing treatment response and the development of new medicines. The information gained from using PET/CT in animal studies can be directly related to humans. Therefore, it is imperative that researchers using PET/CT in the laboratory have standard procedures/protocols that are followed. Currently, in animal (preclinical) research studies using PET/CT no set of standard protocols exist. For that reason, this doctoral research project focuses on determining standard routine PET/CT protocols for use in research institutes using small laboratory animals. The established standard protocol will allow for consistency, reproducibility and continuity across research sites and imaging data sets. An additional benefit to establishing preclinical protocols is the improvement of animal welfare along with the reduction in the use of animals in research. Initiating standard protocols eliminates unnecessary repeated studies and thus reduces the number of animals used. This will also remove the need for each institute to develop an onsite routine PET/CT protocol. Another important factor for establishing standard protocols is to reduce the X-ray doses being absorbed by the laboratory animals. Therefore, reducing potential cumulative severity and animal suffering from absorbed X-ray dose. The PET/CT protocols determined will be for routine use in preclinical research. However, occasionally a study specific PET/CT imaging protocol is required. In order to avoid using animals for protocol design, this project also focuses on developing a 3D printed plastic model of a rodent. The 3D printed rodent model will replace the use of animals in study specific imaging protocol parameters. The plastic rodent model will be tested to match rodent tissue densities in order to ensure X-rays will pass through the plastic the same way they pass through tissue.

This project collected and analysed PET/CT imaging data and CT dose measurements at five different institution. Results clearly showed vast variability when using each institution's own protocols. When using the developed global standard protocol data analysis showed significant improvements in accuracy and precision across all sites. Adhering to standard PET/CT protocols will immediately improve data comparisons across sites, creating more robust, precise and accurate

data sets; establishing a gold standard. This project applies all three of the National Centre for the Replacement, Refinement and Reduction of Animals in Research (NC3Rs) objectives; refines imaging protocols for reducing the number of animals used and replacing animals for protocol optimisation, while improving animal welfare.

Declaration

I declare that the thesis has been completely written by myself and it is a record of work performed by me. This work has not been submitted for any other degree or professional qualification. I have written and submitted certain components of this thesis for publication.

In Chapter 4, the initial measured attenuation coefficient data set of twenty 3D-printing materials was from a previous study carried out and obtained from Dr Nick Weir, Department of Medical Physics, NHS Lothian.

Whatever disasters befall, do not flinch.
Go all the bolder to face them, follow your fate to the limit.

Aeneid Book VI, Publius Vergilius Maro (29-19BC)

With honour, pride, respect and deep-seated love I dedicate all I've become to Sterling, Victoria, Radcliffe, Prudence, Wells, and wee Caroline – you are the reasons I did not, could not flinch.

Acknowledgements

Dr Adriana Alexandre dos Santos Tavares let me start by saying: Since 1865 Stetson Company has been making top of the line hats. They are the founders and pioneers of the original American western hat - from cowboy to cavalry! Today Stetson is still considered the best of the best, most prestigious American West hat maker. Owning one is not to be taking lightly - it is to be treated with respect and pride. There is an analogy in this somewhere. Adriana, your dedication, resolve and taking up the cudgels on my behalf ensured this work didn't end up collecting dust in UoE's archives - whilst spurious comparison ran amok. I earnestly thank you, am so very grateful you took this adventure with me and I am incredibly proud to have had you as my supervisor. You're a Stetson. Muito obrigada pelo seu apoio.

Molls you're the best sister - Kili 2021!
Dziękuję za wsparcie i zachętę.

Aye - Hollywood I think that John J Bowman said it all, but I'll acknowledge you for your constant support and Mendeley help; willingness to listen then telling me I was wrong (glad you're a friend).

Anne, I've seriously appreciated your advice and our coffee breaks - of which I thank you. However, most importantly - I have thoroughly enjoyed meeting and spending time with you and your family (looking forward to more).

I once said after presenting these results that I did not walk this path alone. It is true. I have been incredibly fortunate to have brilliant collaborators. Aberdeen, Ghent, Leeds, Seattle: thank you so very much, erg bedankt for being part of my PhD, for kindly allowing me to walk through your doors and for giving me your support.

Hmmm, PET is Wonderful - agree, but maybe it's really the people in PiW that are wonderful! From day 1 - talk 1 to day 1095 - talk 10,456 - thank you for always listening and being there for me.

How do I say thank you to the people I've shared a cramped office space with day in and out? Fraser, Joe, Anjie, Agne - think you guys have seen the best of me and gracefully endured the worst of me; joyous, exuberant, eager, fatigued, pissed, frustrated, miserable... joyous. No accolades or tokens of appreciation do the trick. Sorry, I guess a simple and honest thank you, you guys are great will have to do. I wish all the best for each of you as you continue your adventures. Agne - FYI - do not underestimate the time needed to format.

To my wonderful Seattle friends: Jeannie, Dinglebrants and Pam - I do want to sincerely thank you for your unwavering belief in me, your encouragement. Adair and Pam - I'm overwhelmed by your enthusiastic kind willingness to actually suffer through reading my thesis - true friends indeed!

A very special thank you Steve for all the times you opened the doors when I locked myself out - very much appreciated.

Ahhhh - Terry! You've definitely put a huge smile on my face. I'm so honoured. Looking forward to many more physics and PET discussions.

Yes, a "shout out" to the SB crew - you guys are fantastic, many thanks.

Yuri - though we will never meet again - I now carry the strength you convinced me I already had, Спасибо for not letting me even think of stumbling - perfect timing. I hope you wear my crampons until they grip no more. Very best wishes.

Dearest sweet Baxter Buddie and Stinky Winkie the journey became deeply sorrowful without you. From the bottom of my heart I am so grateful to have been part of your life's, to have received your love. You will always remain with me. I truly couldn't have started along this path and gotten this far without you two.
Miss you terribly.

Table of contents

List of figures

individual sinograms which also shows difference in size and location of each source detected. University of Washington, *Introduction to PET Physics* by Ramsey Badawi.

Figure 1.13: Flow diagram represents the mathematical iterative process for OSEM. These steps are repeated until the requested iterations over all projection data is completed.

Figure 2.1: Flow chart representing the approach/process of image data analysis: acquisitions with the IQ phantom and the PET rod spatial resolution phantom; multiple reconstruction methods for quantitative analysis; default and standard reconstruction methods for visual analysis.

Figure 2.2: Screen shot of the Mediso's MATLAB software tool for the PET IQ analysis displaying the regions of the IQ phantom (uniformity, RC and SOR) as well as the placements of the regions. Panel (A) top down shows the placement of the ROIs (each hot rod) for RC, panel (B) top down show the placement of the uniformity ROI and panel (C) shows the placement of the ROIs for the spill-out ratio, white air chamber, blue water chamber.

Figure 2.3: PMOD screen shot showing the VOI placement on the PET IQ uniformity region for SUV measurements. Panels (A), (B) and (C) display the VOI placement from axial, sagittal and coronal views respectively.

Figure 2.4: Recovery coefficients (RCs) for hot rods of 1, 2, 3, 4 and 5 mm of the PET IQ phantom extracted for each scanner. Panel (A): default reconstruction iterative methods. Panel (B): displays RCs with standardisation of iterative methods of reconstruction. Panel (C): RCs for each site using FBP reconstruction with the exception of scanner 4 (reconstruction option not available yet).

Figure 2.5: Image slice through the uniformity section of the PET IQ phantom for each scanner shows variability in scanner uniformity as well as SUV measurements when using the scanner default and varying reconstruction protocols. Panel (A) shows the default, panel (B) the standard and panel (C) displays the FBP reconstruction method.

Figure 2.6: Image slice and horizontal profile through the PET rod phantom. Panel (A): Scanners 2, 3 and 5 resolved 2.0, 1.5 and 1.2 mm rods using default reconstruction protocols. Panel (B): Standardised reconstruction methods improved the spatial resolution of scanner 4 (2.0 and 1.5 mm rods are seen) and essentially did not change the spatial resolution of scanner 5. Panel (C) shows the QRM hot rod phantom configuration and size.

Figure 3.1: Flow chart representing the approach/process of image data analysis: acquisitions with the air/water and TEM phantom for quantitative HU analysis; CT bar phantom default and standard acquisitions for visual analysis. Absorbed dose measurements on all protocols.

Figure 3.2: PMOD screen shot showing the VOI placement on the CT water and air region for HU measurements. Panel (A) provide an axial view point and panel (B) displays a coronal view showing the water (left) and air (right) chambers.

Figure 3.3: PMOD screen shot showing the VOI placement on the CT TEM phantom rods for HU measurements. Panel (A) (axial view) and (B) (coronal) show the different size rods.

Figure 3.4: Schematic representation of panel (A) in Figure 3.3 showing the location and identification of the rods, along the manufactures reported densities. Rods 1- 4 are 4 mm, rods 5-8 are 2 mm, rods 9 and 11 are 4 mm and rod 10 is 5 mm.

Figure 3.5: Clearly seen in the water section of the CT air/water phantom are ring artefacts. Scanners 1, 3 and 4 all have a centre of rotation error. This error can be corrected for by running the scanner calibrations. Scanner 5, however, has a detector error, which will require replacement.

Figure 3.6A: CT TEM, air and water HU results. For each material, each data point represents a measurement from a scanner (n=3) from four different sites. Densities 1.08 to 1.57 g/mL include rod sizes 2 mm and 4 mm as reported by the manufacturer. The x-axis clearly shows the spread of HU values per density (A) and displays the significant variations measured using the default protocols ($p<0.0001$, one-way ANOVA, n=3 per group).

Figure 3.6B: CT TEM, air and water HU results. For each material, each data point represents a measurement from a scanner (n=3) from four different sites. Densities 1.08 to 1.57 g/mL include rod sizes 2 mm and 4 mm as reported by the manufacturer. Panel (B) clearly shows improved precision across scanners and densities when using the standardised protocol.

Figure 3.7: Plotted scanner's outputted grey scale values for CT TEM phantom. Grey scale results shows linearity.

Figure 3.8: CT bar phantom images displaying QRM pattern for spatial resolution using the default (A) and post standardisation (B) of CT protocols.

Figure 4.1:(A) schematic representing the principles of generating Compton scattering. (B) schematic representing the principles the Photoelectric effect.

Figure 4.2: Drawing represents the ranges of accepted clinical HU values.

Figure 4.3: Drawing represents the experimental design measuring each material's attenuation coefficient varying tube voltage and material thickness. The thickness of each material was varied by changing the material position, i.e. different thickness are shown in (A) and (B).

Figure 4.4: Photographs of selected 3D-printing materials used in this study. (A) Vero Blue (B) Perspex, (C) Vero Clear, (D) Vero White and (E) Tango Black. From

A to E there is a change in material density. Panel (F) is a representative image (axial and coronal planes in display) showing VOI placement on the CT acquisition for each material for HU measurements (F).

Figure 4.5: Flow chart representing the approach/process of image data analysis: CT acquisitions, surface rendering of DICOM files, conversion to SLT, export to CAD. for 3D printing preparation.

Figure 4.6: Images showing rodent CT acquisition, surface rendered whole body and skeleton to image of whole body and skeleton in CAD software prior to any repairs.

Figure 4.7: Shows the STL files as seen in the CAD software. Panel (A) displays the mesh file voids/holes, overlapping surfaces and artefacts. Panel (B) represents the beginning process of removing artefacts and repairing. Panel (C) shows the outlined version of the cleaned file.

Figure 4.8: The skeleton after being removed from the whole body is shown at its final stage for printing. The 3D printing of the skeleton file is done in the whole body and separately.

Figure 4.9: Similar to Figure 4.7, Panel (A) represents the beginning process of removing artefacts, repairing and rebuilding for the brain. Panel (B) shows the same for the heart.

Figure 4.10: Shows the STL files as seen in the CAD software and the fully repaired version. Both panel (A) and (B) are zoomed in views. Panel (A) is the close up of the head showing the striking difference before and after file repairs. The same is true for the abdomen in panel (B).

Figure 4.11: Image from the CAD software showing the mesh file repaired, rebuilt, cleaned and all vertexes aligned for printing. The phantom whole body with internal organs and skeleton can clearly be seen in panel (A). Panel (B) shows the split which allows for the removable of scaffolding material in the lungs.

Figure 4.12: PMOD screen shot showing the VOI placement on the CT acquisition on the Tango and Vero Clear 3D printing phantom. Panel (A) is the placement on the brain, panel (B) displays the placement for the lung (green), heart (dark blue) and CaHA capsule (light blue) and panel (C) shows the liver (pink) and both kidneys (orange and red).

Figure 4.13: Calculated attenuation coefficient curves for all nine 3D-printing materials. Though values were calculated from 5 keV to 135 keV displayed is 30 keV to 120 keV for visual distinction between materials.

Figure 4.14: Material Endur calculated X-ray fluence spectrum. Data presented as the distribution of the number of photons as a function of their energies.

Figure A3.1: CT TEM, air and water HU results for tested protocol with 170 projections. For each material, each data point represents a measurement from a scanner (n=3) from four different sites. Densities 1.08 to 1.57 g/mL include rod sizes 2 mm and 4 mm as reported by the manufacturer. The x-axis clearly shows the spread of HU values per density.

Figure A3.2: CT TEM, air and water HU results for tested protocol with 480 projections. For each material, each data point represents a measurement from a scanner (n=3) from four different sites. Densities 1.08 to 1.57 g/mL include rod sizes 2 mm and 4 mm as reported by the manufacturer. The x-axis clearly shows the spread of HU values per density - though not as bad as the 170 data.

Figure A3.3: CT TEM, air and water HU results for tested protocol with 720 projections. For each material, each data point represents a measurement from a scanner (n=3) from four different sites. Densities 1.08 to 1.57 g/mL include rod sizes 2 mm and 4 mm as reported by the manufacturer. The x-axis clearly shows the spread of HU values per density, similar to the 480 projections.

Figure A5.1: Spectrums of the material Perspex showing X-ray tube voltages of 102, 81, 70 and 60 kVp for the 5 different thicknesses in which a measurement was obtained.

Figure A5.2: Spectrums of the materials Med 160 showing X-ray tube voltages of 102, 81, 70 and 60 kVp for the 5 different thicknesses in which a measurement was obtained.

Figure A5.3: Spectrums of the materials High Temp showing X-ray tube voltages of 102, 81, 70 and 60 kVp for the 5 different thicknesses in which a measurement was obtained.

Figure A5.4: Spectrums of the materials Vero Clear showing X-ray tube voltages of 102, 81, 70 and 60 kVp for the 5 different thicknesses in which a measurement was obtained.

Figure A5.5: Spectrums of the materials Vero White showing X-ray tube voltages of 102, 81, 70 and 60 kVp for the 5 different thicknesses in which a measurement was obtained.

Figure A5.6: Spectrums of the materials Vero White Plus showing X-ray tube voltages of 102, 81, 70 and 60 kVp for the 5 different thicknesses in which a measurement was obtained.

Figure A5.7: Spectrums of the materials Tango Black showing X-ray tube voltages of 102, 81, 70 and 60 kVp for the 5 different thicknesses in which a measurement was obtained.

Figure A5.8: Spectrums of the materials Tango Black Plus showing X-ray tube voltages of 102, 81, 70 and 60 kVp for the 5 different thicknesses in which a measurement was obtained.

Figure A6.1: Comparison of calculated 3D material Tango Black at the X-ray tube voltage of 125,102, 81, 70 and 60 kVp to each measured output at the defined thicknesses (0.5, 0.7, 2.9, 5.8 and 15 cm).

Figure A6.2: Comparison of calculated 3D material Tango Black Plus at the X-ray tube voltage of 125,102, 81, 70 and 60 kVp to each measured output at the defined thicknesses (0.5, 0.7, 2.9, 5.8 and 15 cm).

Figure 6.3: Comparison of calculated 3D material High Temp at the X-ray tube voltage of 125,102, 81, 70 and 60 kVp to each measured output at the defined thicknesses (0.5, 0.7, 2.9, 5.8 and 15 cm).

Figure A6.4: Comparison of calculated 3D material Med 160 at the X-ray tube voltage of 125,102, 81, 70 and 60 kVp to each measured output at the defined thicknesses (0.5, 0.7, 2.9, 5.8 and 15 cm).

Figure A6.5: Comparison of calculated 3D material Vero Clear at the X-ray tube voltage of 125,102, 81, 70 and 60 kVp to each measured output at the defined thicknesses (0.5, 0.7, 2.9, 5.8 and 15 cm).

Figure A6.6: Comparison of calculated 3D material Vero White at the X-ray tube voltage of 125,102, 81, 70 and 60 kVp to each measured output at the defined thicknesses (0.5, 0.7, 2.9, 5.8 and 15 cm).

Figure A6.7: Comparison of calculated 3D material Vero White Plus at the X-ray tube voltage of 125,102, 81, 70 and 60 kVp to each measured output at the defined thicknesses (0.5, 0.7, 2.9, 5.8 and 15 cm).

Figure A6.8: Comparison of calculated 3D material Perspex at the X-ray tube voltage of 125,102, 81, 70 and 60 kVp to each measured output at the defined thicknesses (0.5, 0.7, 2.9, 5.8 and 15 cm).

List of tables

Table A2.1: Hounsfield Units (HU) measured using the CT air/water phantom and default or 170 projections acquisition protocol. Results presented as the mean±standard error of the mean HUs for each scanner (n=3).

Table A2.2: Hounsfield Units (HU) measured using the CT air/water phantom and default or 480 projections acquisition protocol. Results presented as the mean±standard error of the mean HUs for each scanner (n=3).

Table A2.3: Hounsfield Units (HU) measured using the CT air/water phantom and default or 720 projections acquisition protocol. Results presented as the mean±standard error of the mean HUs for each scanner (n=3).

Table A4.1 CT absorbed doses measured using default protocols and CT protocol 170 projections for mice and rats. Results expressed as mean±standard deviation, n=3.

Table A4.2: CT absorbed doses measured using default protocols and CT protocol 480 projections for mice and rats. Results expressed as mean±standard deviation, n=3.

Table A4.3: CT absorbed doses measured using default protocols and CT protocol 720 projections for mice and rats. Results expressed as mean±standard deviation, n=3.

Table A7.1: Measured and calculated attenuation coefficients values along with the calculated percent difference from calculated to measured are shown for High Temp, Med 160, Tango Black and Vero White.

Table A8.1: Evaluation of HU values for the 3D printing materials, acquired using 3 different CT protocols.

Table A8.2: Evaluation of HU values for the 4 newly acquired 3D printing materials, acquired using the standard CT protocol.

List of abbreviations

^{18}F-NAF	Sodium fluoride-18
AC	Attenuation coefficient
ACRIN	American college of radiology imaging network
APD	Avalanche photodiode
BaF2	Barium fluoride
BGO	Bismuth germanate
CAD	Computer aided design
CaHA	Calcium hydroxyapatite
CHN	Carbon, Hydrogen, Nitrogen
CIRS	Computerized imaging reference systems, Inc
CT	Computer tomography (x-rays)
CTDI	CT dose index
DICOM	Digital imaging and communications in medicine
DMLS	Direct metal laser sintering
DPL	Digital light processing
EM	Expectation maximization
EPI	Edinburgh preclinical imaging
ESMI	European Society for Molecular Imaging
FBP	Filtered back projection
FDM	Fused deposition modelling
FFT	Fast Fourier transformation
FORE	Fourier rebinning
FOV	Field of view
GSO	Gadolinium orthosilicate
HU	Hounsfield units
IQ	Image quality
LaBr3	Lanthanum bromide
LFS	Lutetium fine silicate
LOR	Line of response
LSO:Ce	Lutetium oxyorthosilicate
LuAP:Ce	Lutetium aluminium perovskite
LuI3:Ce	Lutetium iodide
LYSO:Ce	Lutetium yttrium orthosilicate
MAXFOV	Maximum field of view
MICROPET/CT	Preclinical positron emission tomography/computer tomography
MIP	Maximum intensity projection
MLEM	Maximum likelihood expectation maximization
NaI:Tl	Sodium iodide thallium
NANODOTS	Dosimeter for multiple use single point radiation detectors
NC3RS	National centre for the replacement, refinement and reduction
NEMA	National electrical manufactures association

NEC	Noise equivalent counts
NHS	National health service
NIST	National institute of standards and technology
OSEM	Ordered subset expectation maximization
OSIRIX	Imaging analysis software
PET	Positron emission tomography
PMOD	Imaging analysis software
PMT	Photo multiplier tubes
QC	Quality control
RC	Recovery coefficient
SiPM	Silicon photomultipliers
SNMMI	Science of Nuclear Medicine and Molecular Imaging
SLT	Standard tessellation language
SOR	Spill-out ratios
SSRB	Single-slice rebinning
SUV	Standard uptake value
TE	Tissue engineer
TEM	Tissue equivalent material
TLD	Thermoluminescent dosimeter
UV	Ultra violet
VOI	Volume of interest
XPS	X-ray Phosphorescence Spectroscopy

List of publications, presentations, patents and awards

Publications:

1. McDougald W, Christian Vanhove C, Lehnert A, Lewellen B, Wright J, Mingarelli M, Corral C, Schneider JE, Plein S, Newby D, Welch A, Miyaoka R, Vandenberghe S, Tavares A. Standardisation of preclinical PET/CT imaging to improve quantitative accuracy, precision and reproducibility: a multi- center study. *Journal of Nuclear Medicine*, 2019, 27/09. doi:10.2967/jnumed.119.231308.

2. McDougald W, Vanhove C, Lehnert A, *et al.* Multi-centre standardisation of preclinical PET/CT imaging: a necessary step towards achieving translational imaging datasets. *Mol Imaging Biol*. 2018;20(1):84. doi:10.1007/s11307-018-01305-2.

3. McDougald W, Collins R, Green M, Tavares AAS. High Dose MicroCT Does Not Contribute Toward Improved MicroPET/CT Image Quantitative Accuracy and Can Limit Longitudinal Scanning of Small Animals. *Front Phys*. 2017;5 (October):1-11. doi:10.3389/fphy.2017.00050.

4. McDougald W, Collins R, Green M, Tavares AAS. Evaluation of the effects of different microCT parameters on microPET/CT imaging. *Eur J Nucl Med Mol Imaging*. 2016;43:S523-S524.

Presentations:

Scottish Imaging Network: A Platform for Scientific Excellence (SINAPSE) conferences (2017-2019):

1. McDougald, W., Collins, R., Weir, N., Inglis, S., Tavares, A., Development of a new rodent anthropomorphic 3D printed phantom for preclinical PET/CT imaging. SINAPSE Annual Conference, June 21st 2019, Dundee. Poster

2. McDougald W, Vanhove C, Lewellen B, Lehnert A, Wright J, Mingarelli M, Corral C, Schneider JE, Plein S, Welch A, Miyaoka R, Vandenberghe S, Tavares AT, Multi-centre standardisation of preclinical PET/CT Imaging. Scottish Molecular Imaging Conference, September 19th 2018, Beatson Institute for Cancer Research, Glasgow. Poster

3. McDougald W, Vanhove C, Lewellen B, Lehnert A, Wright J, Mingarelli M, Corral C, Schneider JE, Plein S, Welch A, Miyaoka R, Vandenberghe S, Tavares AT, Standardisation of Preclinical PET/CT Imaging Protocols and Absorbed CT dose Across Multiple Research Centres. SINAPSE Annual Conference, June 25th 2018, Royal College of Surgeons of Edinburgh, Edinburgh. Oral: Plenary

4. McDougald W, Tavares AT, Postdoctoral and early career researcher exchanges (PECRE): Standardisation of preclinical PET/CT protocols across multi-centres. SINASPE: Welcome Student Symposium, February 23rd 2018, Dundee. Oral

5. McDougald W, Vanhove C, Lewellen B, Lehnert A, Wright J, Mingarelli M, Corral C, Schneider JE, Plein S, Welch A, Miyaoka R, Vandenberghe S, Tavares AT, Standardisation of Preclinical PET/CT Imaging Protocols and Absorbed CT dose Across Multiple Research Centres. SINAPSE: Molecular Imaging Radiochemistry and Tracer Development, February 5th 2018, Glasgow. Oral

6. McDougald, W., Weir, N., Wilson, A., Inglis, S., Tavares, A., Evaluation of three different 3D-printed materials for development of preclinical PET/CT phantoms, SINAPSE Annual Scientific Conference, June 16th 2017, QEUH Glasgow. Poster

7. Watson, S., Collins, R., McDougald, W., Tavares, A., Impact of different microCT reconstruction protocols on measured Hounsfield Units (HU) and image resolution, SINAPSE Annual Scientific Conference, June 16th 2017, QEUH Glasgow. Poster

National and International Conferences/Symposiums 2018 - 2019:

1. McDougald W, Vanhove C, Lehnert A*, et al.* Multi-centre standardisation of preclinical PET/CT imaging: a necessary step towards achieving translational imaging datasets European Molecular Imaging Meeting (EMIM), March 19 - 22nd, 2019, Glasgow. Oral

2. McDougald W, Vanhove C, Lewellen B, Lehnert A, Wright J, Mingarelli M, Corral C, Schneider JE, Plein S, Welch A, Miyaoka R, Vandenberghe S, Tavares AT, Standardisation of Preclinical PET/CT Imaging Protocols and Absorbed CT dose Across Multiple Research Centres. Laboratory Animal Science Association (LASA) Annual Conference, November 27 - 29th, 2018, Birmingham. Oral

3. McDougald W, Vanhove C, Lehnert A, *et al.* Multi-centre standardisation of preclinical PET/CT imaging: a necessary step towards achieving translational imaging datasets. Edinburgh Imaging Expo, October 18th 2018, Edinburgh. Poster

4. McDougald W, Vanhove C, Lehnert A*, et al.* Multi-centre standardisation of preclinical PET/CT imaging: a necessary step towards achieving translational imaging datasets, World Molecular Imaging Congress (WMIC), September 12-15th 2018, Seattle, WA, USA. Poster

5. McDougald W, Vanhove C, Lewellen B, Lehnert A, Wright J, Mingarelli M, Corral C, Schneider JE, Plein S, Welch A, Miyaoka R, Vandenberghe S, Tavares AT, Standardisation of Preclinical PET/CT Imaging: a necessary step toward achieving translational imaging datasets. Scanner Industry Mediso Meeting, May 16th, 2018, Glasgow. Oral

6. McDougald W, Vanhove C, Lewellen B*, et al.,* Standardisation of Preclinical PET/CT Imaging: a necessary step toward achieving translational imaging datasets, PiW International Symposium, February 19th 2018, Edinburgh. Oral

National and International Conferences/Symposiums 2017:

1. Nick Weir, Scott Inglis, Wendy McDougald, Ashley Wilson, Elli-Noora Salo, Adriana Alexandre S Tavares, X-ray properties of 3D printed materials, NHS Lothian Research & Development Conference, March 10th 2017, Edinburgh. Poster

2. McDougald, W., Inglis, S., Weir, N., Tavares, A., Evaluation of X-ray properties of 3D printing materials for preclinical Positron Emission Tomography/Computed Tomography (PET/CT) for anthropomorphic phantom development. Edinburgh Preclinical Imaging: PhD Expo, October 18th 2017, Edinburgh. Poster

3. McDougald, W., Inglis, S., Weir, N., Tavares, A., Evaluation of X-ray properties of 3D printing materials for preclinical Positron Emission Tomography/Computed Tomography (PET/CT) phantom development. 3R World Congress Alternatives and Animal Use in the Life Sciences, August 20-24th 2017, Seattle, WA, USA. Poster

4. McDougald, W., Inglis, S., Weir, N., Tavares, A., Evaluation of X-ray properties of 3D printing materials for preclinical Positron Emission Tomography/Computed Tomography (PET/CT) for anthropomorphic phantom development. 3R Symposium, May 1st 2017, Edinburgh. Poster

Patent:

1. Novel 3D printed tissue equivalent material anthropomorphic rodent phantom for preclinical scanner calibration and testing study specific imaging protocols. Inventor: McDougald, Wendy; Contributors: Tavares, Adriana; Collins, Richard. Application under review.

Awards:

Grants:

1. Pool Engagement in European Research (PEER) award. Research collaboration in Belgium, Ghent University, on preclinical PET/CT standardisation. Scottish Imaging Network: A Platform for Scientific Excellence (SINAPSE).

2. Postdoctoral & Early Career Researcher (PECRE) award. Research collaboration in Seattle, WA, USA, University of Washington, on preclinical PET/CT standardisation. SINAPSE.

Conferences:

1. Speaker Travel Award, Laboratory Animal Science Association (LASA) Annual Conference (November 27 - 29th, 2018), Birmingham. Talk covering multi-centre preclinical PET/CT standardisation results and PET/CT 3D printed calibration/protocol development tool.

2. Highly Commended poster, Edinburgh Imaging Expo (October 18th 2018). Poster presentation of preclinical PET/CT standardisation.

3. Nominated for Women in Molecular Imaging Network Scholar Award, World Molecular Imaging Congress (WMIC), (Sept 12-15th 2018) Seattle, WA, USA.

4. Travel Award World Molecular Imaging Congress (WMIC) (Sept 12-15th 2018) Seattle, WA, USA. Poster presentation of multi-centre preclinical PET/CT standardisation results.

5. Plenary Talk Award, SINAPSE Annual Scientific Meeting (June 25th 2018) Edinburgh. Plenary talk on multi-centre preclinical PET/CT standardisation results.

6. Travel award, 3R World Congress (20-24th August 2017) Seattle, WA, USA. Poster presentation on preclinical PET/CT 3D printed calibration tools.

Chapter One: Introduction

1. Role of preclinical Positron Emission Tomography/Computed Tomography (PET/CT) in biomedical research

Preclinical PET/CT is a key non-invasive imaging tool in biomedical research. It allows for reduction of the number of animals used, while simultaneously improving statistical power by using each animal as its own control in longitudinal studies, with consequential scientific benefit. Diagnostic and therapeutic agents can be developed and tested on identical platforms to human, thus accelerating the translational process [2–5]. The continued increased usage of preclinical PET/CT imaging in research has stimulated efforts to develop optimised standard acquisition and reconstruction protocols. Optimisation of preclinical acquisition and reconstruction protocols will have a widespread impact across several biomedical research fields using PET/CT, including: biomarker research [6–8], research in neurodegenerative diseases, cardiovascular diseases [9–13], metabolic diseases, musculoskeletal disorders and oncology [14–17].

Despite this pivotal role, global standardisation of acquisition and reconstruction preclinical PET/CT imaging protocols is still lacking. This is completely the opposite from clinical PET/CT in which standardisation of imaging protocols and system calibration are the norm with established guidelines from the National Electrical Manufactures Association (NEMA) and the American College Radiology Imaging Network (ACRIN). To date the majority of studies looking into preclinical PET/CT optimisation of acquisition and reconstruction protocols have been performed primarily using the manufacturers default protocol or slight variations thereof [18,19]. Therefore, the impact of varying PET/CT parameters on preclinical data and preclinical research results is poorly defined and not fully understood. Furthermore, the significance of different CT parameters on radiation exposure to small laboratory animals is scarcely described in the literature [20,21], in particular cumulative severity for longitudinal studies. Given that cumulative radiation doses can become increasingly toxic [22], accurate CT absorbed dose measurements are essential when undertaking longitudinal preclinical research. This is most relevant and obvious when working with rodent tumour models in order to assure a clear distinction between diagnostic radiation imaging and radiotherapy [20,22–25]. Systematically and comprehensively this doctoral research addresses such lack of global standardised preclinical PET/CT imaging protocols by evaluating biases

across centres using default scanner protocols, followed by developing standardised protocols for optimisation of PET/CT imaging at multiple centres. Empirically known quantitative image acquisition results from the various scanner protocols provides the opportunity to establish global standard protocols, replacing variability for similarity.

The fundamental principles and mechanisms of standardisation are intertwined with the development and evolution of the PET/CT scanner. Chapter 1 provides a brief, chronological narrative of PET, CT and the fusion of the two pointing out the beginnings of standardisation. Unfortunately, to date this standardisation only applies to clinical PET/CT.

2. Brief chronological development and principles of PET and CT

2.1. PET

The roots of positron emission tomography can be traced back to the early days of radioisotope research and span several decades of physics, chemistry, mathematics, engineering, material and computer science research [26,27]. Each field was required in order for PET to become a mainstay as a clinical and preclinical nuclear imaging tool.

The primary success of PET is due to the fact that Nobel Laureate physicist Paul Dirac theoretically postulated the existence of an electron with a positive charge (e^+). In his 1928 paper, Dirac stated: “The true relativity wave equation should thus be such that its solutions split up into two non-combining sets, referring respectively to the charge e^- and the charge e^+” [28]. Dirac also noted that experimentally, the electron, when transitioning would appear as suddenly changing its charge from e^- to e^+ [28]. This provided the opportunity and eventually led to Nobel Laureate physicist Carl Anderson experientially proving the existence of an electron with a positive charge: the realization of the positron [29]. Expanding on Dirac’s theory, many years later Nobel Laureate physicist Richard Feynman computationally claimed that positrons were actually virtual electrons scattered backwards in time to annihilate an electron [30]. This electron positron annihilation is key to PET. For when an electron and positron annihilate two gamma rays with energy of 511 keV are emitted at 180 ± 0.6 degrees (opposite directions) due to the conservation of momentum [31,32]. Regardless of the direction or nature of the positron, it is the two nearly colinear gamma rays emitted that are essential for and detected in PET. The

dependability on the detection of the two gamma rays, from the annihilation, means positrons are needed. Hence, the production of positron emitting radioisotopes is required for imaging.

Physicist Dr Ernest Lawrence's resolve to research the nucleus lead to the successful production of artificial radioactive elements (radioisotope); winning the 1939 Nobel Prize in physics "for the invention and development of the cyclotron and for results obtained with it, especially with regard to artificial radioactive elements". Simply described in his 1932 paper:

> Semi-circular hollow plates, not unlike duants of an electrometer, are mounted with their diametral edges adjacent, in a vacuum and in a uniform magnetic applied to the plate electrodes producing an oscillating electric field over the diametral region between them [33,34].

In his Nobel Prize lecture, Lawrence not only gracefully acknowledged the work done by Nobel Laureates Frédéric and Irène Joloit-Curie, in which their paper announced the production of artificial radioactive elements, but also put forward questions and designs for further research in radioactive elements [35]. Lawrence's continued development and successful work with the cyclotron eventually yielded the production of positron emitting radioisotopes for PET such as carbon-11 (^{11}C), nitrogen-13 (^{13}N), oxygen-15 (^{15}O) and fluorine-18 (^{18}F) [34].

After the design, the capability to actually detect the 511 keV gamma rays was required. The concept of using, detecting and measuring radioisotopes (nuclear medicine) fundamentally started in the 1940 with the use of Geiger-Muller counters [36]. Then in 1951 with the use of improved developed scintillation counters Wrenn *et al.* (1951) published the design and results of their novel PET system [37]. This new approach took advantage of the resulting gamma rays from the positron electron annihilation. Wrenn clearly stated their design was founded on the two gamma rays which "emerge simultaneously and oppositely directed, with a precision of 1/137 radian…to count these 2–γ rays in coincidence, the source of activity must then lie somewhere on a straight line joining the 2 counters" [37]. Independently, the same year physicist Dr Gordon Brownell's research using coincidence PET detecting was also tested and published by Sweet *et al.* (1951) [38,39]. Though both Brownell and Wrenn focused on brain tumour detection, Wrenn tested zinc-65 (^{65}Zn) and copper-64 (^{64}Cu) whereas Brownell's design included

testing sodium-22 (^{22}Na). Regardless, the designs and results provided great promise for future coincidence counting.

Brownell's group at the Physics Research Laboratory at Massachusetts General Hospital (MGH) went on to develop the first recognized PET systems for clinical and preclinical usage as well as continuing with the development and enhancement of future PET systems. For example, one of the first improvements to PET came in the form of a mathematical reconstruction method instead of hardware. Expanding on the conventional back projection method for reconstruction group member Dr David Chesler developed the algorithm filtered back projection (FBP), applying a filter in order to reduce blurring. Implementing this algorithm to PET and CT substantially improved image quality. Dr Chesler's conceptual drawing is shown in Figure 1.1 [40–43].

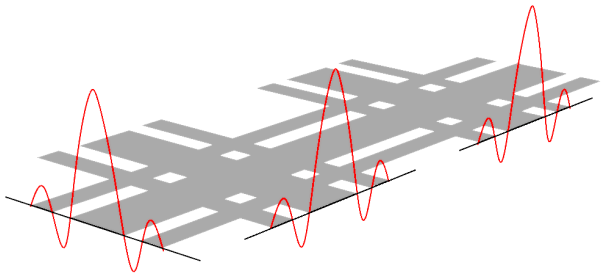

Figure 1.1: Representative of Chesler's FBP mathematical concept. Modified from Chesler's drawings [42,43].

As reconstruction algorithms improved - next so did the PET system designs. By 1973 Dr J.S. Robertson working at Brookhaven National Laboratory designed and constructed a system with 32 detectors in a ring formation as opposed to Brownell's parallel detector systems. Unfortunately, and as Robertson noted, "In its present form the system does not give as good spatial resolution as do others… but there is a potential for improvement" [44]. However, the relevance and impact this design had on the advancement of PET becomes obvious when simply viewing 21st century PET scanners, PET ring design in Figure 1.2.

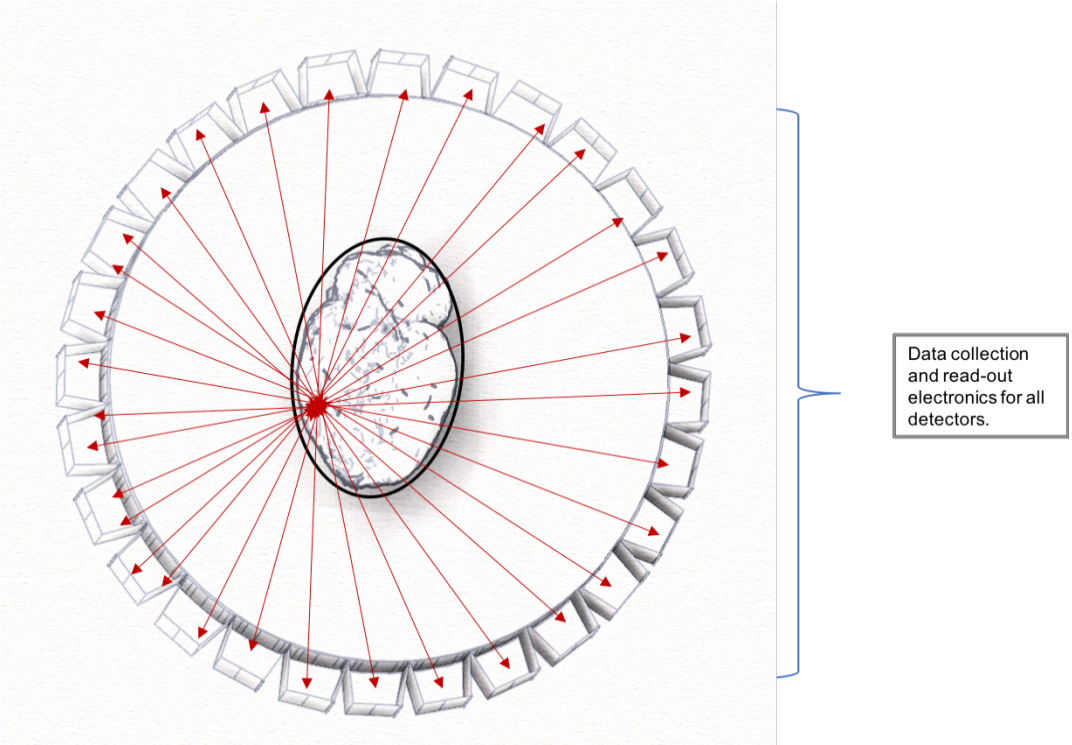

Figure 1.2: A representation of Robertson's design consisted of a ring containing of thirty-two 3.2 cm scintillation crystals with electronic cabling for detecting every crystal pairing in coincidence, represented by the arrows. Modified from Robertson's drawing [44].

Shortly thereafter, in 1974 biophysicist Dr Michael Phelps, nuclear chemist Dr Edward Hoffman from Washington University in St. Louis, Missouri and with physicist Dr Michael Ter-Pogossian, in collaboration with the company EG&G ORTEC (Oakridge, Tennessee, USA) built what is consider the first fully functional PET scanner, officially coining the acronym PET. This newly designed hexagonal PET scanner (PET III) consisting of 48 scintillation crystals successfully produced improved quality images [40,45]. The PET III also included its own computer for controlling a 60-degree rotation of the gantry, the motion of the detectors, the bed, a display and performing image reconstruction [27,38,42,46,47]. Based off the PET III design EG&G ORTEC built the first commercial PET scanner installed in 1976 at the University of California, Los Angeles. It now might appear as if PET, proven worthy, would take off as an integral component, imaging tool for the clinics/hospitals while continuing to be at the forefront of nuclear medicine research [38].

This unfortunately was not to be – yet. Though the results, images acquired using PET from brain tumour and blood flow studies proved coincidence positron emission detection was successful several concerns remained; image quality,

scatter corrections, system sensitivity and attenuation corrections. At this point, it should be noted one aspect of the research done by Phelps and Hoffman set the foundation for testing the intrinsic and extrinsic characteristics of PET, essentially establishing future calibration testing and clinical standardisation. Their work in 1974 addressed and analysed the spatial resolution and contrast, depth independent resolution and sensitivity, pulse height analysis, accuracy of attenuation correction methods and the efficiency of the detectors. They also included testing what is now called spill out ratios (SOR) and recovery coefficients (RC) using hot and cold spots as well as small rods (1 cm – 3.5 cm) within a phantom. Such testing became fundamental in establishing the performance of a scanner. SOR measured the ratio between regions of no activity concentration (cold) to the mean activity (hot) in the background, indicating the scatter correction performance of the scanner. The RC measurement reflects the scanner's inherent limited spatial resolution [42].

Advancement of PET lay in the improvement of scintillation detectors and the development of radiopharmaceuticals (radiotracers). First, in order to detect, collect, and count coincidence gamma rays an efficient detector system is paramount. The basic set up for the detection of the gamma rays (photons within the accepted energy range/threshold) includes scintillator crystals, a light guide and photomultiplier tubes (PMT). The concept is straightforward; photons reach the crystals, the crystal converts the photons to light, next PMTs capture (by a photocathode) the light converting it into photoelectrons then moving (by an electric field) them through a set of plates (dynodes) multiplying the number of photoelectrons via a potential difference across the dynodes to be read out as the signal.

Initially PET detectors used thallium doped sodium iodide NaI:Tl scintillating crystals, as they possess qualities required for photon detection. For acceptable detection scintillation crystals need to have at least three main features: good stopping power (ability to stop the incoming photons, dense and high Z number), fast light pulse rise and decay times (fast increase in light intensity and fast exponential decrease of maximum intensity) and high optical light transmission (high light output). For the most part NaI:Tl crystals met such requirements with the exception of not having great stopping power. They were and still are commonly used due to their high light output [48–50]. In the late 1970s bismuth-germanate (BGO) crystals became popular due to their high Z number and ease of

manufacturing. Currently, BGO has been deemed the primary crystals for PET detectors even though its light output is substantially lower then NaI:Tl crystals. Improvements continue. For example, lutetium (yttrium) oxyorthosilicate crystals of various doping (LYSO:Ce and LSO:Ce) have moved into the forefront of research for PET usage given their high light output, density and Z number, though they remain costly. Table 1.1 displays basic characteristics of the common crystals [48,49].

Table 1.1: Properties for some of the more commonly used scintillators crystals in PET. The scintillation crystals used are mainly bismuth, lutetium and gadolinium with various doping [[51]].

Property	NaI:Tl	BaF2	BGO	LSO:Ce	GSO	LYSO:Ce	LaBr3	LFS	LuAP:Ce	LuI3:Ce
Effective atomic number (Z)	51	54	74	66	59	60	47	63	65	60
Linear attenuation coefficient (cm−1)	0.34	0.44	0.92	0.87	0.62	0.86	0.47	0.82	0.9	0.56
Density (gm cm−3)	3.67	4.89	7.13	7.4	6.7	7.1	5.3	7.3	8.34	5.6
Index of refraction	1.85		2.15	1.82	1.85	1.81	1.88	1.78	1.95	
Light yield (% NaI:Tl)	100	5	15	75	30	80	160	77	16	190
Peak wavelength (nm)	410	220	480	420	430	420	370	430	365	470
Decay constant (ns)	230	0.8	300	40	65	41	25	35	18	30
Hydroscopic	Yes	Slight	No	No	No	No	No	No	No	Yes

NaI:Tl	sodium iodide thallium	LYSO:Ce	lutetium yttrium orthosilicate
BaF2	barium fluoride	LaBr3	lanthanum bromide
BGO	bismuth germanate	LFS	lutetium fine silicate
LSO:Ce	lutetium oxyorthosilicate	LuAP:Ce	lutetium aluminium perovskite
GSO	gadolinium orthosilicate	LuI3:Ce	lutetium iodide

Second, the successful development of PET radiotracers plays a significant role. In Missouri at Washington University blood flow studies with PET imaging using ^{11}C-labelled glucose proved successful. However, it was Sokoloff *et al.* (1977) with the use of ^{14}C-labelled deoxyglucose for measuring glucose utilization in the brain that lead the way for the synthesis of ^{18}F-deoxyglucose, [^{18}F]FDG at the Brookhaven National Laboratory [52,53]. In collaboration with the University of Pennsylvania and the National Institutes of Health the Brookhaven group using their novel synthesized [^{18}F]FDG set out to determine its metabolic properties. Gallagher *et al.* (1978) concluded this metabolic trapping could be a principle radiotracer for probing function or tumour location in PET; "The tissue content of ^{18}F radioactivity that can be measured *in vivo* by tomographic techniques might provide a measure of the ability of the brain and heart to transport, phosphorylate, and thus utilize glucose *in vivo*" [54]. This led to the expansion of PET research, extensively covering studies in multiple organs, no longer just in the brain, heart and lungs or blood flow. Numerous studies were being done covering biochemical and metabolic characterization of diseases, including the diagnosis, progression or regression of tumours. Today, even though PET is still facing challenges due to limits in spatial resolution and scatter correction, over the last five years alone, more than 32,000 research papers reported the use of PET imaging (preclinical and clinical, ISI Web of Science, search conducted on the 21st October 2017 with key words "positron emission").

Clearly, PET has become an integral component in medical imaging. Again, it should be stated that along PET's arduous path of development the standards for clinical scanner calibrations were established; acceptable intrinsic and extrinsic "gold standards" for quality and quantification assurance. Clinical standards that include scanner patient protocols were also designed and implemented, NEMA and ACRIN [55,56]. Unfortunately, until 2019 such standards were essentially non-existent in the preclinical imaging platform. This void in preclinical standardisation is the rationale behind this study.

2.2. CT

CT did not have nearly as arduous a path towards successful acceptance as did PET. CT is a tomographic methodology devised by engineer Sir Godfrey Hounsfield that was immediately met with approval and implemented, (winning the Noble Prize for Physiology in 1979 with physicist Dr Allan Cormack) [57,58]. Prior to CT, conventional X-ray

(radiograms/radiography) was accomplished by exposing an X-ray beam to the desired area of an object with a photographic plate underneath in order to detect the remnant beam. This meant that the X-ray beam and specific plane in the object stayed in focus on the plate causing X-ray projections elsewhere to be blurred. The acquired images were superimposed upon each other but due to blurring the desired imaged structure had to compete against any structure above or below it. The resulting images were of poor quality and offered no accurate quantitative analysis. Hounsfield in 1973 pointed out conventional radiography was clearly not efficient, as essentially 90% of the information collected was not utilized and created artefacts as 2D images were converted to 3D [40,57,59].

The use of a narrow X-ray beam, as proposed by Hounsfield, fundamentally created slices through sections of the structure and acquired images at several angles, “a series of contiguous cross sections”. Therefore, upon reconstruction the acquired slices where not hindered from any variations in the slices on either side, as the radiation is “confined” to each individual slice [59]. A diagram of the conventional process of capturing the shadow is shown in Figure 1.3 along with Hounsfield’s design.

A

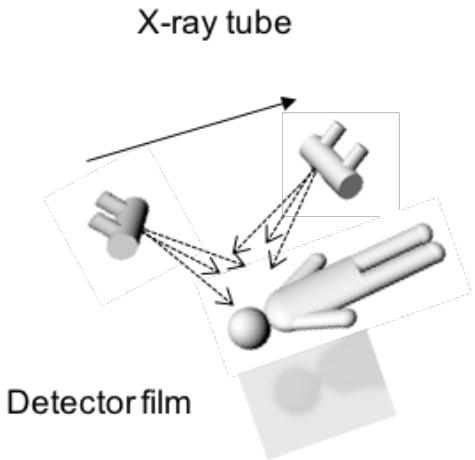

X-ray tube transverses

B

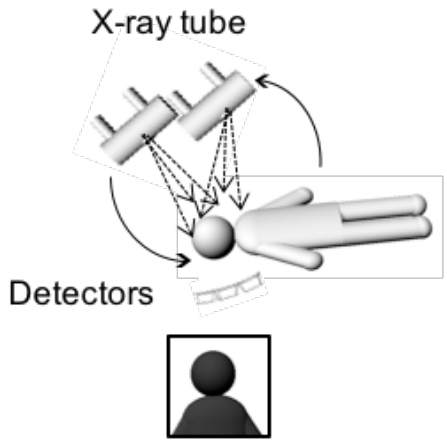

X-ray tube rotates with detectors

C

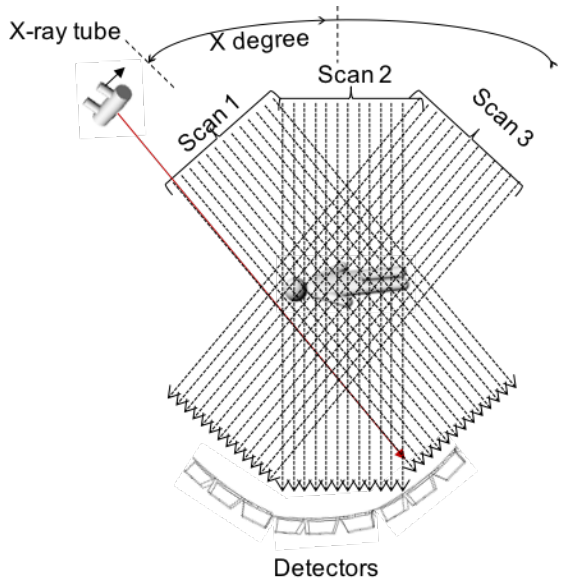

Figure 1.3: Modified Hounsfield's drawings of the method for X-ray acquisition. (A): the conventional method with a photographic plate underneath the patient. (B): Hounsfield's purposed method of X-ray acquisition and collection. (C): Representation of the X-ray acquisition by multiple angles [57,59].

The impact of this new method for acquiring and reading X-ray transmission images was immediate. The sensitivity was substantially improved merely by the number of photons being detected due to the increase of angles acquired. The narrow X-ray beam slice acquisitions allowed for the unencumbered superimposing of the slices/images from 2D to 3D. For the first time, unlike conventional X-ray, CT was able to distinguish the different densities between various soft tissues such as kidneys and liver. CT allowed for quantitative measurement of different tissue densities via X-ray, not just an overall mean X-ray absorption of all soft tissues as previously done.

Fortunately for Hounsfield, the computing power required to handle and process approximately 28,000 transmission projections existed in the 70's, as did the reconstruction method necessary to obtain the CT images, i.e. FBP. Therefore, CT made an easy transition into clinical use, while increasing its usefulness in clinical and preclinical research.

The first commercially available CT (EMI Ltd.), based on Hounsfield's system, detected 3 mm thick X-ray beam projections with NaI:Tl scintillation crystals coupled to PMTs with

acquisitions over 5 minutes. Though acquisition times would eventually be reduced, even by the 70's clinical standards for absorbed radiation doses had been in place for roughly 20 years [60,61]. Generally, todays' CT beam slice thickness can be as small as 0.625 mm, detected by garnet ceramic scintillation crystals coupled to a photodiode array, with gantries having a 0.25 sec rotation speed for shorter scan times [62]. However, absorbed ionized radiation dose remains a concern in the clinical setting. A concern readily ignored in preclinical research, evident by non-existent standards and guidelines. This doctoral project addresses this deficiency by establishing PET/CT standards.

Analogous to the accomplishment and implementation of CT was the development of a scaling factor for quantifying and verifying the accuracy of the distribution and attenuation of X-ray transmission through tissue. In order to assess X-ray attenuation numerical values were ascribed, relating to the attenuation calculations (attenuation coefficients) to tissue densities [28,59,63–65]. Considering X-ray absorption through water is similar to soft tissue, water was set to be 0, with air set at -1000. These values are known as Hounsfield Units (HU), used to differentiate and compare tissue densities. Though HU values are taken as absolute values they are in fact, as stated, a scaling factor. Attenuation coefficients are dependent on the energy of the X-ray beam being emitted and the material the X-rays pass through. Therefore, each CT system will generate slightly varied HU numbers. Due to this variation scanner calibration requirements were established and required for clinical use, ensuring quality assurance. Unfortunately, no such calibration requirements exist in preclinical CT.

Hounsfield's first CT scanner included placing a water tube around the patient's head in order to correct for beam hardening (lower energy X-rays being absorbed, leaving high energy X-rays). This was essentially providing the attenuation coefficient of the water, which was compared and used to determine X-rays attenuation in soft tissue, as seen in Equation 1.1 and 1.2:

$$X_{(CT)} = (X_m - X_w) = (\mu_1 - \mu_w) + (\mu_2 - \mu_w) + (\mu_3 - \mu_w) + \cdots\cdots + (\mu_n - \mu_w) \quad \text{Eq. (1.1)}$$

Therefore, CT numbers (HU):

$$CT = 1000\frac{(\mu_m - \mu_w)}{\mu_w} \qquad \text{Eq. (1.2)}$$

In Equation 1.1 and 1.2, X_m represents the soft tissue and X_w the water. The attenuation coefficients are represented by μ_m and μ_w for the soft tissue and water respectively [57,59,66].

As straightforward as the CT HU Equation 1.2 is, the delineation of the different tissue densities is actually far more convoluted. This is essentially due to tissue inhomogeneity, CT system used for data acquisition, the spectrum of X-ray energies and scatter [67].

Furthermore, the scaling relationship of soft tissue and bone is nonlinear, with a discontinuity around 300 HU. Research in 1994 by LaCroix *et al.* on combined single photon emission computer tomography with CT (SPECT/CT) investigated using the acquired CT data for attenuation corrections [68]. They found a substantial difference in the calculated accuracy of the attenuation coefficients between soft tissue and bone. In conclusion, their results indicated the attenuation coefficients for soft tissues (lung and muscle) were accurately estimated, bone was not. They suggested bone required a different scaling factor from soft tissue. Figure 1.4, a calibration curve, (mass density versus HU) shows the actual bi-linearity [69].

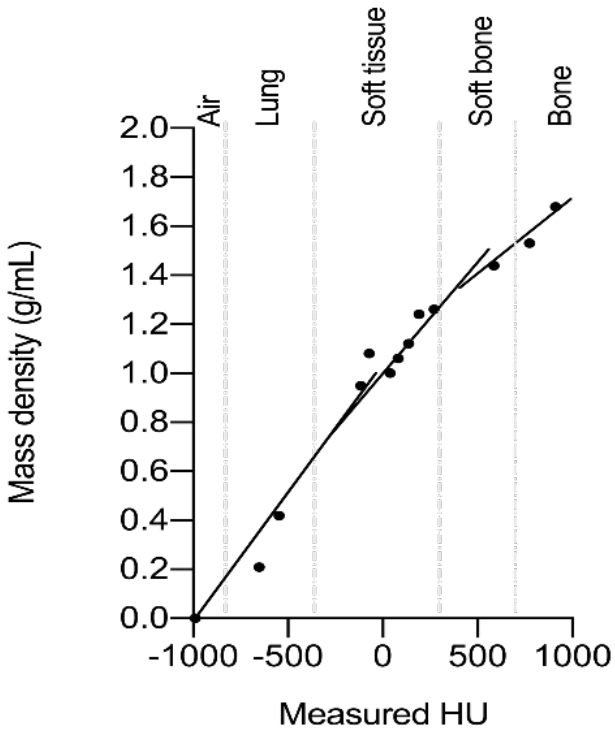

Figure 1.4: Typical (HU, ρ) calibration curve used for the conversation of HU into mass densities and material type [69]. Also shown are the accepted Hounsfield's scale intervals for different materials (-1000 to 1000 HU) based on previously published data [57].

Bilinear scaling algorithms have been developed using 300 HU as threshold (above or below) others simply use >0 HU or < 0 HU. DeMarco *et al.* (1998) in establishing a Monte Carlo simulation tool for dosimetry planning and analysis divided tissue into six categories (lung, air, fat, muscle, water and bone), as well as other subgroups based on a mass density calibration curve [70,71]. Schneider *et al.* (1996 & 2000) developed stoichiometric methods to create groups based on the CT HU scale. The method derived the functional relationship between CT numbers and tissues by defined groupings, (-1000 to -98 HU, -98 to 100 HU and >100 HU) in which the tissue mass density and elemental weights were calculated using either a step function or interpolated [71,72].

The relevance of knowing HU and their limitations is far from trivial. Here, HU values will be used for the development of preclinical anthropomorphic phantoms when assessing 3D printing materials for soft tissue to bone. Converting attenuation coefficients to HU allows for comparable values across different CT scanners. Therefore, direct comparisons between scanners enrolled in the study can be achieved. Questions defining standardized CT protocols will be answered. Questions such as: What are the

HU values each scanner measures for different tissues? How does each scanner's extracted HU measurements compare? How do these preclinical HU values compare to accepted clinically measured HU?

2.3. Fusion of PET and CT

Though not a novel idea, in 2000 integrating PET with CT for co-registration of functional and anatomical information was new and presented problems. Notwithstanding, Dr Thomas Beyer *et al.* (2000), University of Pittsburgh, published the design and results of the first PET/CT manufactured in collaboration with Siemens [73]. Their original concept purposed and designed a clinical oncology scanner, which produced high spatial resolution anatomic CT images to be co-registered with functional PET images. This allowed for the avoidance of patients being scanned on two separate systems then the process of correlating the images from two scanners. Therefore, the primary goal was the precise identification of the distinct anatomical region of the PET radiotracer [74].

As a by-product, generating CT attenuation correction maps for PET was developed. Attenuation corrections for PET had previously been done by acquiring a "blank" (no patient in the bore) transmission scan using a radioactive rod (usually caesium-137 (^{137}Cs) or germanium-68 (^{68}Ge) of a known activity) then applying the calculated corrections to the scanner [75]. Patient PET attenuation correction image data was acquired as a ^{68}Ge transmission scan of the patient then applying the corrections Using the patient's own CT scan anatomical information removed the need for a separate transmission scan being applied to the patient's scan and avoided co-registering separate data sets.[32,73,76,77].

Converting CT quantitative attenuation coefficients are fundamental in generating attenuation correction maps for PET. However, this conversion to PET posed several problems. Such as, accounting for motion corrections. Another crucial concern revolved around the conversion of HU for PET. Different photon energies are a concern as PET is mono-energetic with 511 keV and CT is a polychromatic X-ray range usually from 35 to 160 keV. Furthermore, energy dependent attenuation (absorption/scatter) processes for PET and CT differ: Compton scattering versus photoelectric absorption in denser materials (bone) and Compton scattering in less dense material (soft tissue). In order for the CT information to be used to generate attenuation correction maps for PET, CT

numbers (HU) need to be scaled to match PET [[78–80]]. Under the guidance of the group from the University of Pittsburgh, in conjunction with the development and enhancement of PET/CT, Kinahan *et al.* (1998 & 2000) addressed the application of CT attenuation coefficients for PET. This early work presented the feasibility of CT based corrections via phantom and human studies by using methods of scaling, segmentation, hybrid of the two and dual-energy and later simulation. The results proved the practicality of all the methods but with the segmentation producing the most accurate attenuation coefficients. Notably, in this work a CT effective energy of 70 keV was used on all methods [[67,81]].

Below a basic outline of the steps taken to convert CT numbers to PET is presented based on work done by Burger *et al.* in 2002:

1. CT images interpolated to the resolution of the PET pixels
2. CT values transformed from HU to PET attenuation coefficients

$$\mu^{PET} = \begin{cases} \mu_w^{PET}\left(CT + {}^{1000}/_{1000}\right) & CT \leq 0HU \\ \mu_w^{PET} + CT\,\frac{\mu_w^{CT}\left(\mu_\beta^{PET} - \mu_w^{PET}\right)}{1000\left(\mu_\beta^{CT} - \mu_w^{CT}\right)} & CT > 0HU \end{cases} \qquad \begin{aligned} \mu_w^{PET} &= 0.096cm^{-1} \\ \mu_\beta^{PET} &= 0.172cm^{-1} \\ \mu_w^{CT} &= 0.184cm^{-1} \\ \mu_\beta^{CT} &= 0.428cm^{-1} \end{aligned} \qquad \text{Eq. (1.3)}$$

where in Equation 1.3 w and β represent water and bone respectively. Attenuation coefficients (μ, cm^{-1}) represent the linear attenuation coefficients of PET 511 keV energy and the effective CT energy (80 keV) for water and bone [[82–84]].

3. Attenuation maps calculated from CT data are forward projected to the PET

In their study regarding the transformation of CT into PET attenuation coefficients Burger *et al.* (2002) concluded a bilinear function/algorithm to consign CT values to PET is adequate for human tissue. They, however, determined their empirical PET attenuation coefficient value of 0.093 cm^{-1} produced more accurate results in the soft tissue range. Furthermore, they noted that the accuracy of high atomic number (Z) materials may be in question due to the photoelectric interaction of CT photons, at the lower energies (80 keV in Burger study). Higher density bone material (cortical) poses such a problem, due

to calcium (*Z*=20). Notwithstanding, a simulation study done by Xia *et al.* (2011) for a clinical setting of using "ultra-low dose" (tube voltage of 80 kVp) showed the feasibility of obtaining accurate attenuation maps. As part of their methods they varied tube current, tube voltage, filtration and smoothing techniques [85]. This study is relevant for preclinical even though a tube voltage of 80 kVp is at the high end for some preclinical. A similar simulation study with lower voltages and or greater divide (subsets) in >100 HU should be explored in order to determine accurate CT values of bones for improved attenuation maps. A more accurate high *Z* CT number is also applicable for the advancement and development of preclinical phantoms, enhanced image quality and quantification.

3. Basic principles of positron emission and X-ray

3.1. Basic principles of PET physics

The process of positron emission to detection is outlined and schematically shown below. The basic concept is thus:

For positron decay (β^+): as an unstable atom returns to a stable state via the weak interaction a proton decays to a neutron causing a positron and a neutrino to be emitted. The positron will travel a short distance (range dependent on positron energy, Table 1.2) before annihilating with an electron. This annihilation event results in the emission of two 511 keV gamma (photon) rays travelling in diametrically opposite directions. Though β^+ decay generates a spectrum of energy due to the emission of neutrinos, it is the distinct 511 keV photons in coincidence from the annihilation that are detected by cylindrically arranged photodetectors. As the photons travel they will either be scattered, absorbed before reaching the scintillation crystals or enter the scintillation crystals. In the scintillator the absorption of the annihilation photons lead to the emission of scintillation light, which is then converted to photoelectrons for detection and counted.

Starting with PET radiotracer injection:

1. Positron emitting radiotracers are injected into a subject/patient, common radioisotopes used are shown in Table 1.2.

Table 1.2: Commonly used PET radiotracers [86]. Positron range and energy is dependent on the injected positron emitting radiotracer.

Isotope	Half-life (min)	Maximum positron energy (MeV)	Mean positron range in water (FWHM in mm)	Production method
^{11}C	20.3	0.96	1.1	Cyclotron
^{13}N	9.97	1.19	1.4	Cyclotron
^{15}O	2.03	1.7	1.5	Cyclotron
^{18}F	109.8	0.64	1.0	Cyclotron
^{68}Ga	67.8	1.89	1.7	Generator
^{82}Rb	1.26	3.15	1.7	Generator

Via decay, positrons emitted annihilate with electrons producing two 511 keV gamma rays (photons) at 180 ± 0.6 degrees in opposite directions, Figure 1.5

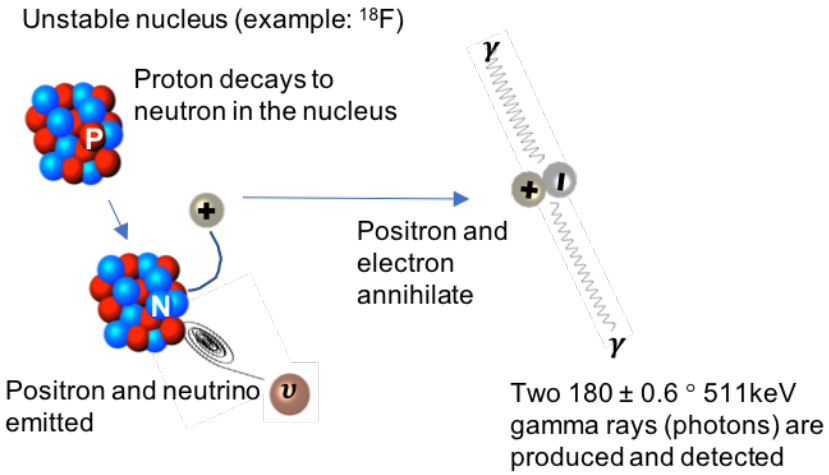

Figure 1.5: Drawing of positron emission and annihilation with an electron producing two gamma rays.

2. Photons are detected in coincidence (2 ns timing, and thresholding window for accepted energies, generally 400 to 700 keV to accommodate detector characteristics, acceptance of sufficient number of photons), Figure 1.6.

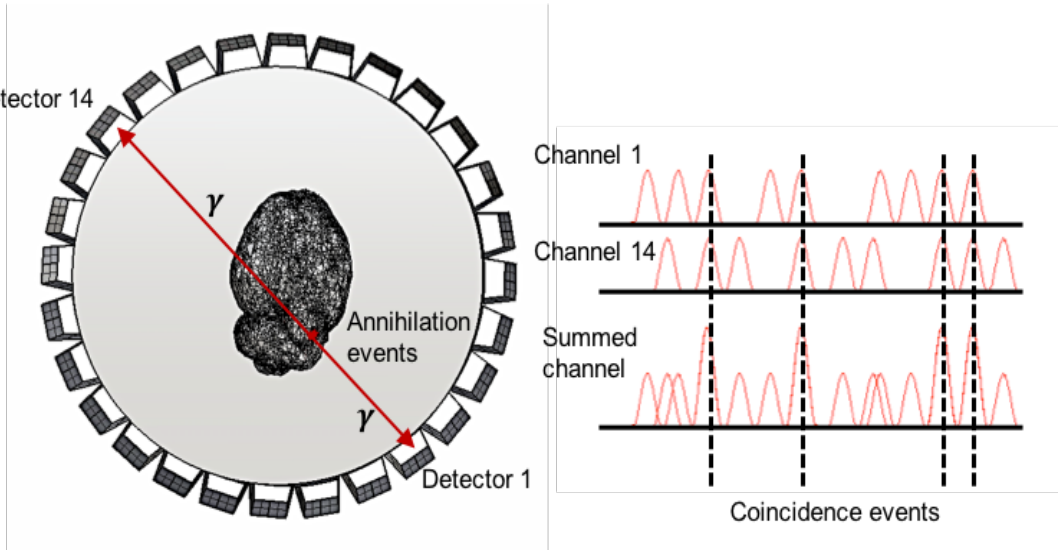

Figure 1.6: Schematic showing the process of coincidence detection of the gamma rays in PET. Modified from University of Washington, *Introduction to PET Physics* by Ramsey Badawi.

The photons detected in coincidence mathematically (line integral) create a line defined as a line of response (LOR), which determine the signal (photons) position and strength to be used in the image reconstruction. Detection of photons are also referred to as counts or events. The measured number of events are proportional to the total radioactivity contained within the LOR. Coincidence detection of the photons can be classified as "true", “scatter” or “random” coincidences Figure 1.7:

A. True coincidence: Both photons detected from the one annihilation and neither one has been scattered.

B. Scatter coincidences: Two photons from the same annihilation event are detected within the timing and energy windowing, but one or both has undergone Compton scattering.

C. Random coincidences: Detection of two photons within the coincidence timing but from different annihilation events.

Scattered and random events will create an incorrect LOR for the reconstruction. They will also increase statistical noise leading to an incorrect measurement of the radioisotope.

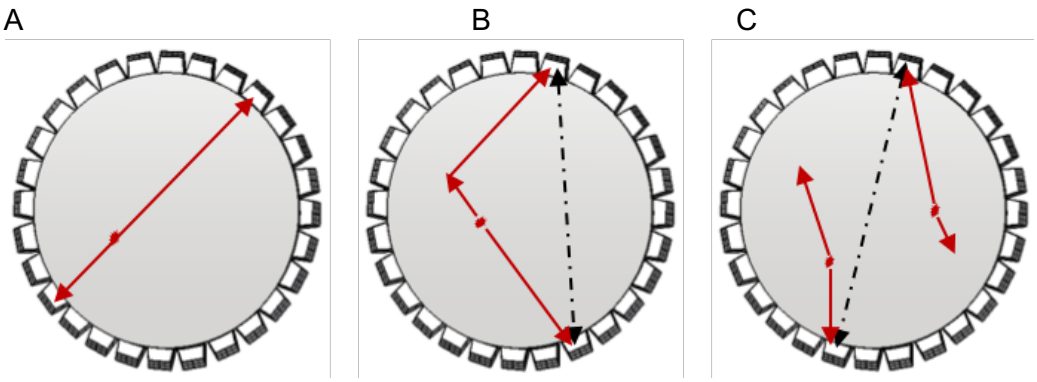

Figure 1.7: Drawings of gamma ray events: (A) true, (B) scattered (C) random.

3.2. Basic principles of X-ray physics

X-rays are ionising electromagnetic radiation generated inside an X-ray tube (cathode and anode), Figure 1.8, in the following manner:

1. Electrons in the electrical circuit consisting of high voltage input to a cathode with a tungsten filament are removed from this circuit by heat. The electrical current passing through the filament heats it causing electrons to be removed.

2. Due to the potential difference between cathode and anode the electrons expelled from the cathode are attracted to the anode. As the electrons move towards the anode their velocity and kinetic energy increase while their potential energy decreases.

3. The electrons are guided by the design of the cathode (cupped shaped) and anode (cut at an angle with a tungsten focal spot) inside a vacuum.

4. The electrons bombarding the surface of the anode will interact with atoms. This interaction results in the generation of Bremsstrahlung or characteristic X-rays - the X-ray beam.

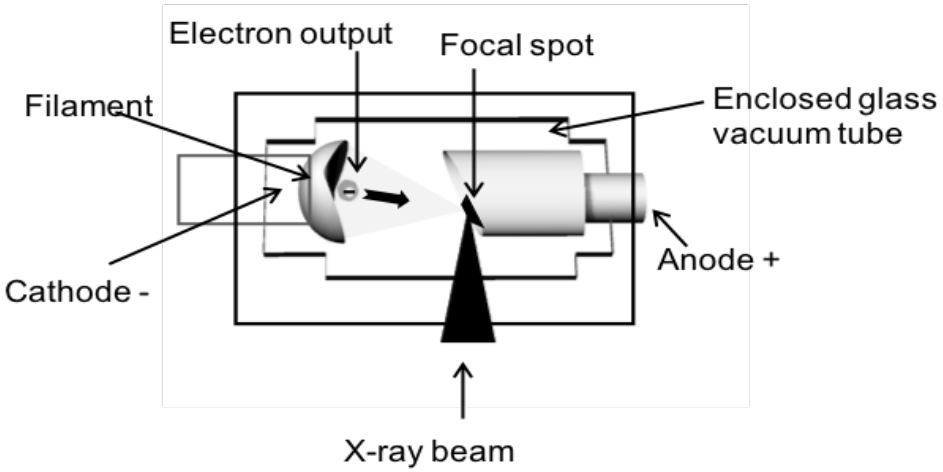

Figure 1.8: Drawing displaying the basic/main components of an X-ray tube; cathode, filament, focal spot and anode. The drawing also indicates the flow of electrons expelled from cathode to anode then out as X-ray beam.

These fast moving high energy electrons will interact with the nucleus or the shells of atoms as they penetrate the surface of the anode. X-rays emitted via interaction in the nucleus are called Bremsstrahlung due to "slowing" down the electrons; a deceleration, directional deflection and loss of energy, Figure 1.9 (A). The X-rays generated from the shells (*K*, *L*, *M*) are the characteristic X-rays, though rarely from the *M* shell. Characteristic X-rays are created when the incident electron's energy is greater than the binding energy of the shell electron. The ejection of the shell electron leaves a "hole" in which an outer electron will fill generating the X-ray, Figure 1.9 (B). The energy of characteristic X-rays are discrete (difference between shells). Whereas the Bremsstrahlung X-rays energies range producing a continuous spectrum, example in Figure 1.10.

A B

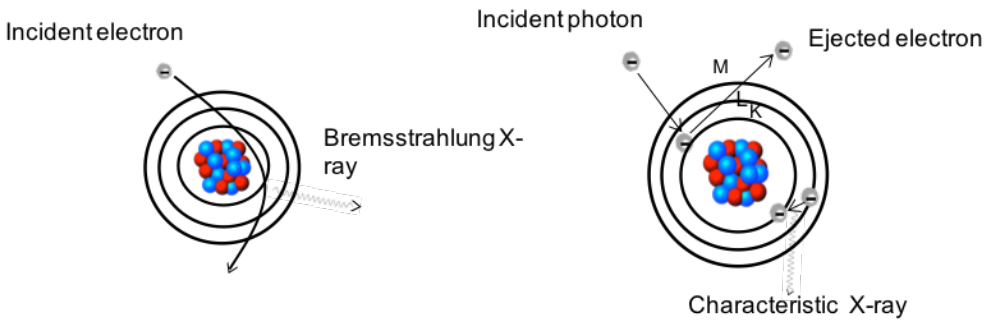

Figure 1.9: (A) schematic representing the principles generating Bremsstrahlung X-rays. (B) schematic representing the principles generating characteristic X-rays.

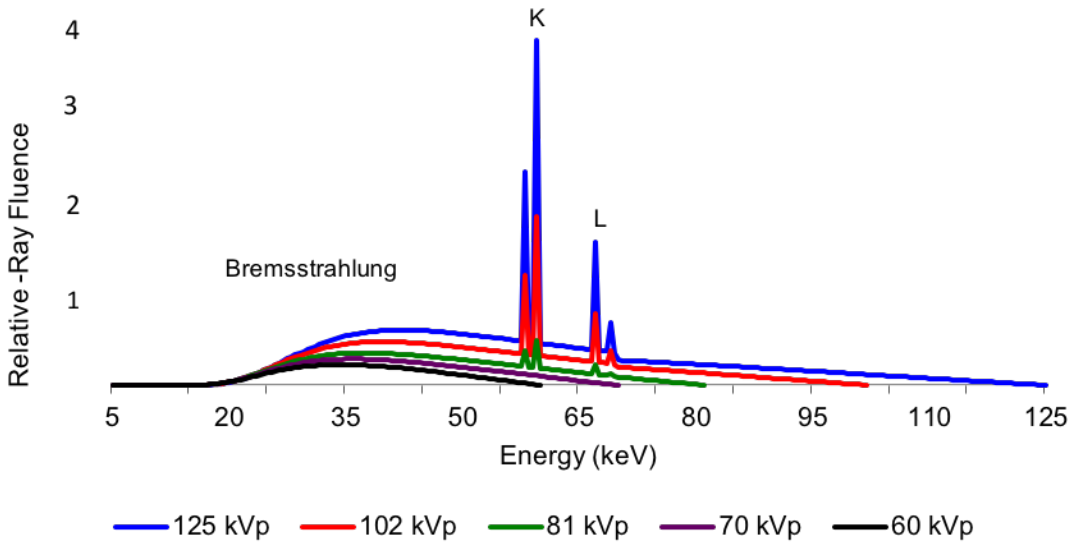

Figure 1.10. Calculated X-ray spectrums (distribution of the number of photons): characteristic X-ray spectrum spike for *L* and *K* shells and Bremsstrahlung at the lower X-ray energies.

This entire process generates a substantial amount of heat. Some anodes are designed to dissipate the heat by rotating, while others will have heat sinks. The tungsten focal spot will absorb and dissipate the heat. The focal spot is also used to influence the CT spatial resolution by changing the size (i.e. smaller size - improved spatial resolution).

3.3. Basic principles of tomographic reconstruction methods

The mathematical details in reconstruction algorithms are beyond the scope of this PhD project. Though, it's important to outline the basic reconstruction methods used by the preclinical sites in this study. As these reconstruction methods play an important role in determining a PET standard protocol. Any imaging modality collecting line integral data, the sinograms, can apply the same mathematical methodologies. There are two types of reconstruction methods; analytical (inverse Radon transform) and iterative (statistical estimation/Poisson likelihood function). The filtered back projection (FBP) is analytical, whereas ordered subsets expectation maximization (OSEM) or maximum likelihood expectation maximization (MLEM) are iterative. The fine tuning of reconstruction algorithms is an active area of research. Currently, FBP and OSEM remain the most commonly used method in PET and FBP in CT.

The FBP method is a 2D Fast Fourier Transformation (FFT), which is the same as applying a Fourier Transformation to the Radon Transformation. The Radon transformation is the quintessential integral projection data (signal) methodology. The Fourier Transform separates the continuous signal into its discrete frequency components. Directly taking a 2D FFT of the projection data (signal) mathematically reduces steps. After the FFT is applied, filtering takes place and an inverse FFT is applied to obtain the wanted image data. Diagrams of projections from a single point representing the back projection and FBP concept shown in Figure 1.11.

In 2D, acquired projection data along the imaging planes perpendicular/mainly perpendicular (direct planes and cross planes) to the scanner axis is binned for reconstruction then stacked for a 3D volumetric image. More scanners are now acquiring projection data in a fully 3D mode (i.e. no septa), collecting the imaging planes perpendicular to the scanner axis and the oblique planes, diagram in Appendix 1. The fully 3D mode data sets are computationally demanding. Therefore, these data sets are rebinned. This allows for a significant reduction in data size while maintaining the ability to reconstruct the projection data using analytical or iterative methods. Rebinning algorithms basically project the oblique sinograms onto the transverse sinograms. In other words, the algorithm rebins the 3D data into a 2D stack for reconstruction. The two most common rebinning methods are single-slice rebinning (SSRB) and Fourier rebinning (FORE) [1,87]

A

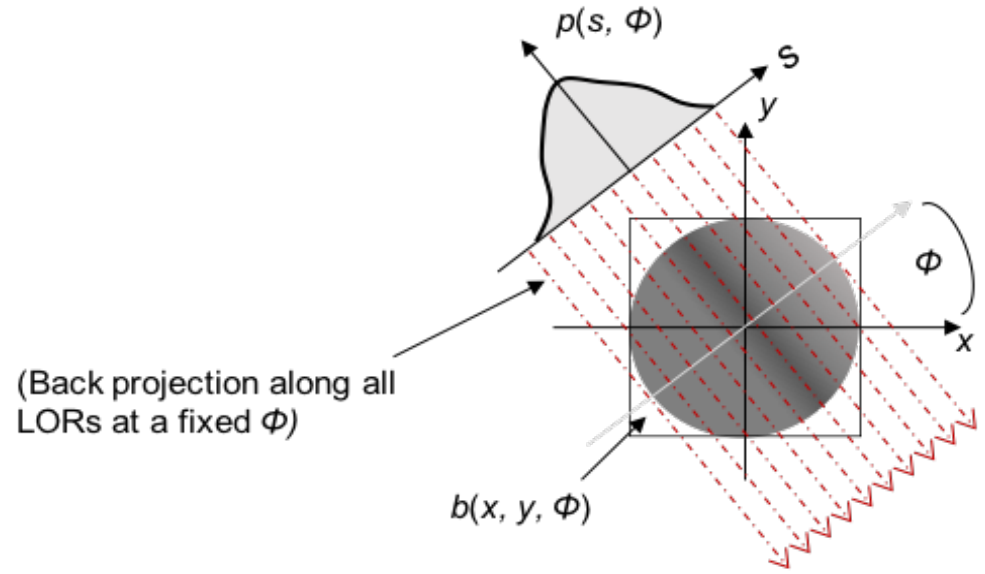

B

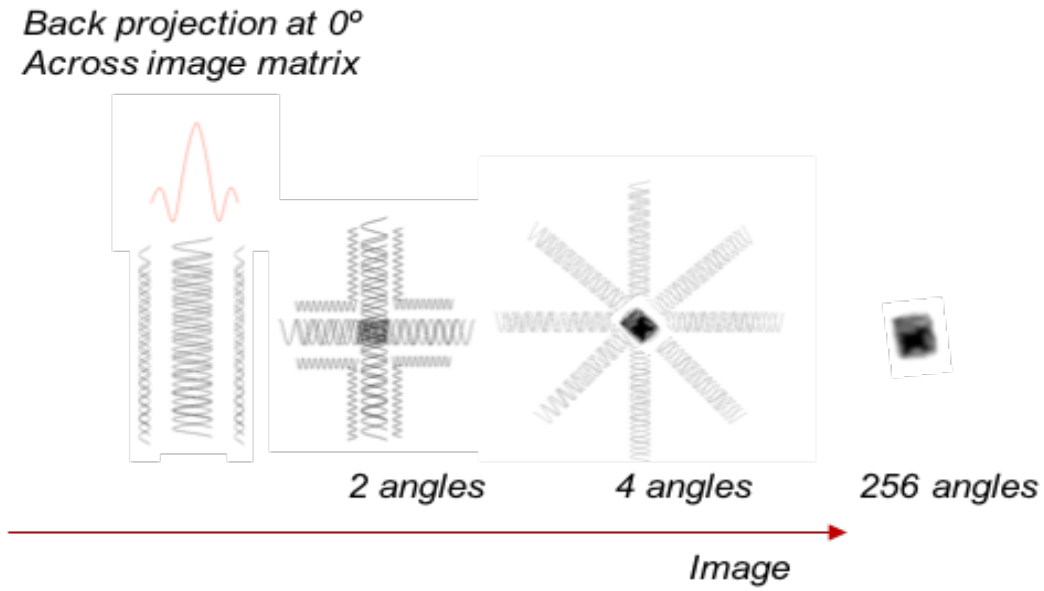

Figure 1.11: (A): Back projection $b(x,y, \Phi)$, into an image reconstruction array of all values of $p(s, \Phi)$ for a fixed value, $p(s, \Phi)$ is the projection formed by integrating along the LORs at angle Φ. (B): visual representation of FBP. Modified from University of Washington, *Introduction to PET Physics* by Ramsey Badawi.

However, blurring is created when using back projection reconstruction methods due to overestimation in the centre and less so at the edges. This can be seen as the "star" like artefact. Frequency filtering is a mathematical approach to remove this image blurring effect of back projection. This approach is implemented in the FBP reconstruction

method. Essentially, FBP reduces the overestimation by applying a “weight” filtering which reduces values in the centre and accentuates values at the edges [1].

Below, Figure 1.12, are diagrams and pictorials representing projections $P(s, \Phi)$ of four sources showing the mathematical sinograms, which are formed by integrating along each LOR at each angle. The sinograms are named as such since they “trace” a sinusoidal path in the projection space.

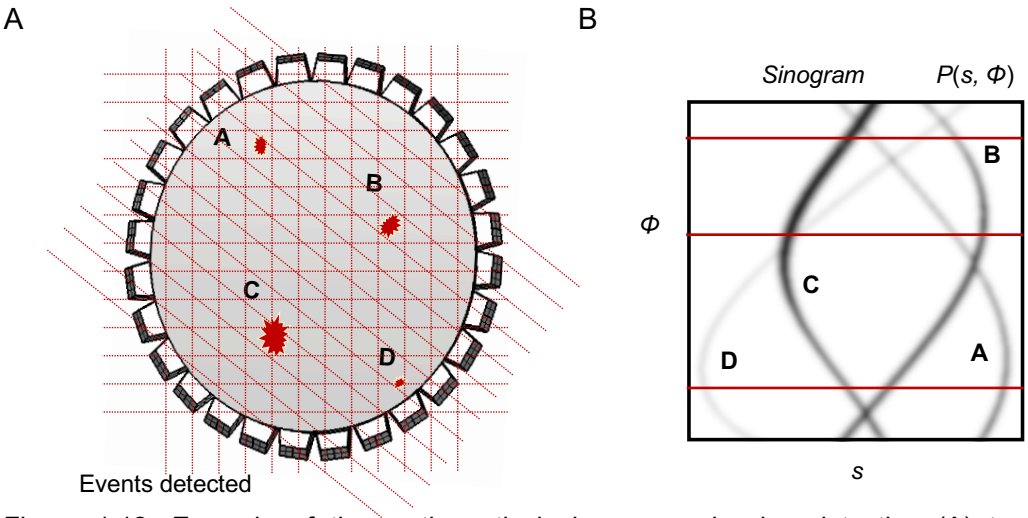

Figure 1.12: Example of the mathematical sinograms showing detection (A) to sinogram representations. (B) Projections from A to D are displayed as their individual sinograms which also shows difference in size and location of each source detected. University of Washington, *Introduction to PET Physics* by Ramsey Badawi.

Iterative methods are more complex than FBP. The concept is to make an initial estimate of the radiotracer distribution and forward project that estimate. Then the estimate projection is compared to the measured and adjusted. Therefore, the process starts with an estimate of the image matrix, calculates a new base, then repopulates the matrix continuing up to the requested number of iterations and/or subsets. Both algorithms (MLEM and OSEM) are based on a method for maximizing the output; Expectation Maximization (EM). MLEM is the method for maximizing the Poisson Likelihood Function. The OSEM method is a variant of MLEM and applies subsets to assist with each estimate. A diagram of the iterative reconstruction process is shown in Figure1.13 using an image matrix of 2x2 for simplicity. The OSEM method will, to a certain degree, also compensate for detector failure.

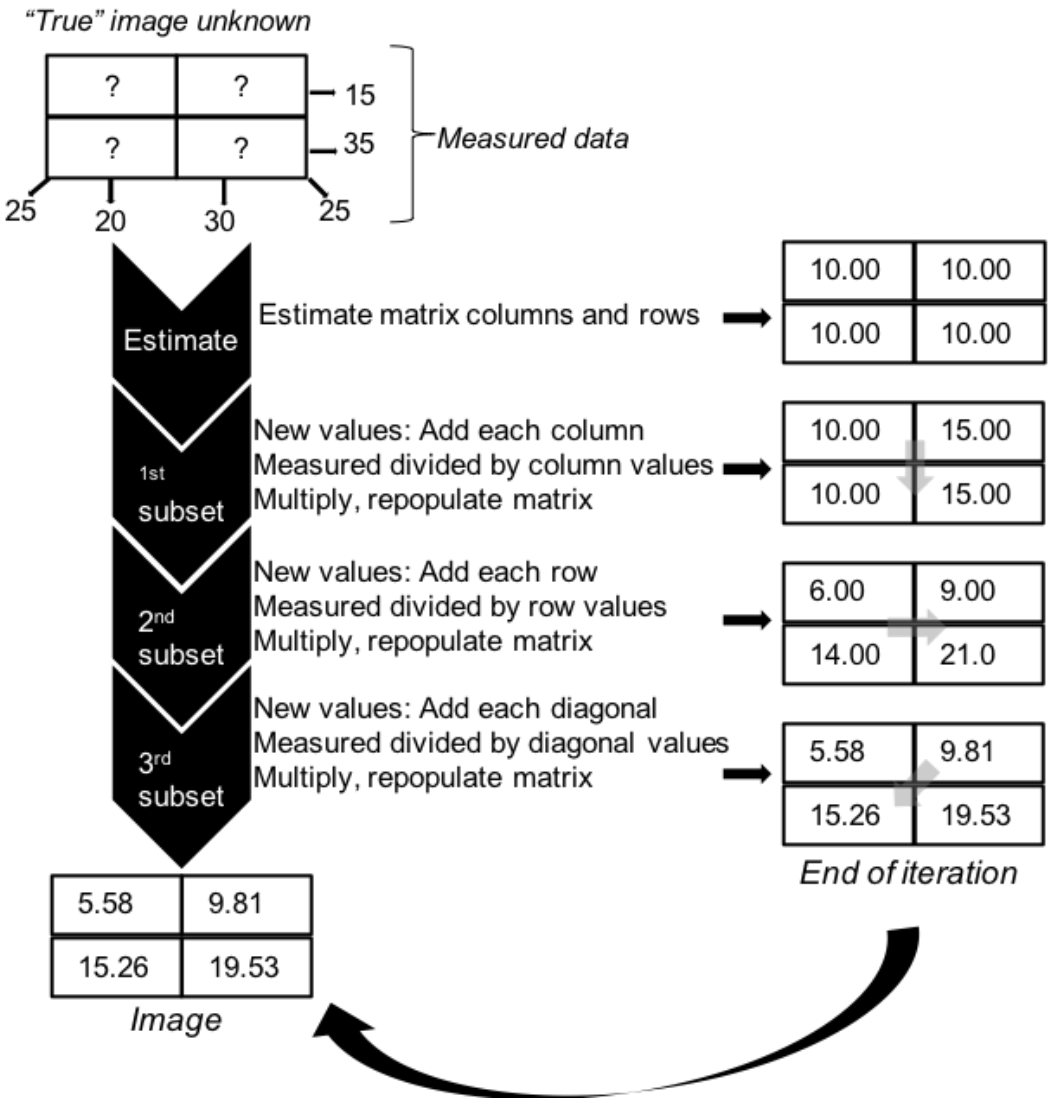

Figure 1.13: Flow diagram represents the mathematical iterative process for OSEM. These steps are repeated until the requested iterations over all projection data is completed.

4. From clinical to today's preclinical PET/CT

In the development and history of PET/CT scanners animals have always played a significant role. Starting back in the 1970's with Brownell's group at the MGH Physics Research Laboratory humans and animals were imaged. Both took part in the development of the PET scanner; the detector designs, the reconstruction techniques as well as in the validation for usage in research and clinical applications. In 1974 Brownell's group using their positron cameras (PC-1 and PC-II) successfully carried out lung, heart, brain, blood flow, metabolism and radiopharmaceutical studies using dogs, rodents and rabbits [38,88]. Not only did animal research studies continue on these early PET scanners

[38]. They led the way to the development of dedicated small animal scanners. It was, though, the desire and push for novel pharmaceuticals that really drove the need for dedicated small animal preclinical PET/CT scanners [89–92]. By the 90's the development of preclinical PET/CT scanners was in full swing. Multiple systems were being designed, such as the PET Methodology, from Bloomfield and Jones at Hammersmith Hospital, London, UK [93]. Their PET system had an axial diameter of 11.5 cm, a 5 cm field of view (FOV) with a spatial resolution of 4.4 mm [93]. However, considered one of the first fully functional small animal preclinical scanner was the Sherbrooke APD-PET, developed at Sherbrooke University, (Québec, Canada). The Sherbrooke scanner didn't become completely operational and available until 1996.

Why did it take so long for a preclinical PET/CT? It seems straightforward - take a clinical PET/CT shrink the bore for a small preclinical PET/CT- no problem. Not so. Indeed, right away it became obvious that you can't just shrink a clinical scanner and expect it to perform with the necessary spatial resolution for small animal imaging. It wasn't only spatial resolution that impeded development. Multiple factors played a role in the delay of commercially available preclinical scanners. Economics reared its head. Feasibility and greater proof of this technology being directly translational to clinical applications was needed along with the assessment of the impact on animals undergoing regular imaging and optimal doses. Input function requirements, gating for motion and count rate/sample size were also issues [89,92,94–96]. However, foremost was detector design [96–98].

Fundamentally, detector design is at the core of obtaining the optimal spatial resolution and sensitivity of a PET scanner. In PET physics the unchangeable limiting spatial resolution constraints are positron range (distance a positron will travel varies with radiotracer) and non-collinearity of the gamma rays emitted from the positron-electron annihilation. Basically, the first preclinical scanners displayed poor spatial resolution due to parallax errors caused mainly by detector ring and design. Hampered by these constraints, detector designs became critical for the success of a dedicated small animal PET scanner. Building such a scanner and obtaining the required spatial resolution for small animal imaging, therefore, took years of design ingenuity, bit of luck and the availability of new detector components. The PET detector research field expanded (and continues to do so) with new faster read out circuit boards, electronics and

programmable micro-processing chips, PMT, silicon photomultipliers (SiPMs) and avalanche photodiodes (APD) improvements and development. New and old scintillation crystal (LYSO:Ce, BGO, GSO:Ce, LSO:Ce, LGSO:Ce, LYSO:Ce) combinations, sizes, discrete or continuous designs, stacking arrangements were tested [96,98,99]. Along with detector design developments the other factors could be tackled. For example, scanner sensitivity, count rate, signal sampling size and scatter correction improvements with detector design allowed for establishing animal doses. Improved spatial resolution via scintillation crystal designs and depth-of-interaction (where gamma rays interact within the crystal) calculations validated feasibility and functionality of preclinical PET for translation to clinical [100,101]. Additionally, during this time, scanner system standardisation was realised. The analysis of the Sherbrooke scanner's characteristics (spatial resolution, sensitivity, count rate, scatter corrections and image quality) set the foundation for the preclinical PET NEMA scanner performance guidelines [90,99]. By the end of the 20th century preclinical PET/CT scanners were a proven reality.

For comparison consider Table 1.3, shows the characteristics of three early preclinical PET/CT scanners and a sneak preview of one of the preclinical scanner characteristics enrolled in this study. Scanner (1) is the Trifoil LabPET/CT enrolled in this study, scanner (2) is the Bloomfield's group, (3) is Sherbrooke and scanner (4) is the microPET designed from the University of California, Los Angeles, CA, USA in 1999.

Table 1.3: Different preclinical PET scanners properties testing results derived from literature [90,91,93,102].

	Scintillator	Bore diameter (cm)	Axial FOV (cm)	Crystal size (mm)	Detector	Peak sensitivity (%)	Resolution
1.	LYSO:Ce* LGSO:Ce	16.2	7.5	2 x 2 x (12+13)	APD	2.36	0.82
2.	BGO	11.5	5.0	30 x 50 x 23	PMT		4.4
3.	BGO	31.0	11.8	3 x 3 x 20	APD	0.51	3.1
4.	LSO:Ce	17.2	11.2	2 x 2 x 10	PMT	0.74	1.8

Great progress continues to be made on all fronts.

5. Project aims (1,2 and 3)

Throughout the chronological history of PET and CT one common thread was the lack of standardisation (including scanner required regular calibrations) in the preclinical PET/CT imaging platform. Furthermore, preclinical literature has shown protocols with increased CT scanning durations, consequently leading to an increase in small animal absorbed doses from X-rays, do not directly translate onto improved image quality [103]. These results are pertinent information when conducting longitudinal preclinical PET/CT studies. Moreover, this supports the need to investigate imaging outcomes from different protocols in order to avoid spurious quantitative comparisons and minimize radiation exposure to small laboratory animals. For quantitative accountability, consistency and reproducibility standardisation in preclinical research is imperative. This project examines several facets to achieve the goal of standardising routine preclinical PET imaging reconstruction protocols and CT acquisition protocols. In order to address the identified gaps in knowledge, develop standardised protocols, suggest CT dose regulations and improve animal welfare in the field of preclinical PET/CT imaging three aims will be achieved:

Aim 1: Improve experimental design in preclinical PET/CT imaging protocols between research groups by investigating and comparing acquisition and reconstruction parameters in different platforms, with the aim to work towards standardisation of imaging protocols across sites.

Aim 2: Assess the impact and significance of different PET/CT parameters on image quality and quantification across different platforms, while delivering the lowest doses to small animals as possible.

Aim 3: Design and manufacture prototypes of rat and mouse anthropomorphic phantoms to be used instead of animals for development of improved PET/CT imaging protocols.

As in the clinical setting, different manufacture scanner characteristics (geometries, hardware, efficiencies and data processing algorithms) will impact acquired images. Nonetheless, it is the empirical quantitative image data results that hold the key for setting a standard protocol across all scanner variabilities regardless of hardware or software. It is how the acquisition or reconstruction parameters can be set and acquired

in the same manner on each different scanner to create the most accurate, precise, consistence and reproducible results that is being sought. In essence, neutralizing the manufactures' difference. This is the scope of this study - replacing scanner variability for scanner similarity to establish global standard imaging protocols. This is not a scanner intrinsic or extrinsic NEMA performance comparison study. Nor does this study address the need for standardisation regarding animal care and handling. It is the quantitative results from the currently used default/daily/general imaging protocols that are compared irrespective of scanner characteristics.

Accomplishing aim 1 and 2 required personally visiting each site multiple times for the acquisition of n=3 imaging data sets for each protocol (sites and developed) per PET and per CT phantom as well as the CT ionising radiation measurements.

6. Research questions

In preclinical research involving small animals, reliable scientific practices and outcomes, colloquially speaking, go hand in hand with animal welfare. Each aim not only seeks improved, refined experimental methods and results but improved animal welfare by reducing CT ionising radiation doses and the number of animals used. Applying the NC3Rs principle of refinement and reduction aims 1 and 2 ask the research questions:

1. Will standardising preclinical PET/CT protocols across multiple scanners reduce quantitative bias in image data, while maintaining image quality?

2. Will refining preclinical PET/CT protocols across multiple scanners reduce the CT absorbed doses to small animals while maintaining image quality and quantification?

The 3rd aim addresses the use of animals for the optimisation of study specific protocols. Thus, applying the NC3Rs principle reduction and replacement aim 3 ask:

3. Can a tissue equivalent material (TEM) anthropomorphic rodent phantom be developed to eventually replace animals used when designing study specific PET/CT imaging protocols?

Therefore, the remaining chapters, as expected go through each aim setting out the method and results. Chapters 2 and 3 cover aim 1 for PET and CT, respectively. Chapter 3 also includes aim 2 as this is directly related to CT only. Aim 3 is presented in Chapter 4. Finally, Chapter 5 is an overall discussion. It needs to be noted that sections of Chapter 1's Introduction as well as Chapter 2 and 3 have been published.

Chapter Two: Standardisation of preclinical PET imaging

1. Introduction

As noted, the preclinical PET/CT community has undertaken efforts towards the development of guidelines regarding animal handling/preparation and scanner quality control testing [18,19,104–106]. Several preclinical studies evaluating PET National Electric Manufactures Association, NEMA NU 4 2008 performance also exist (NEMA performance literature in Table 2.1). However, this project took the novel approach of quantitatively evaluating the empirical data and image quality of the actual PET protocols used across the different sites and scanners. This approach, as shown in the following sections, revealed significant and concerning results. Whilst, setting a foundation for establishing a "least bias" standard imaging protocol base on the empirical imaging data results.

First, routine/default (hereon referred to as default) PET protocols were evaluated for image quality and quantification biases using two commercially available preclinical PET phantoms. Default protocols were set either by the vendor or the site for their routine use of imaging small animals. Secondly, several different PET reconstruction methods were quantitatively analysed for standardisation. Finally, standardised protocols were determined from the least biases between all imaging data sets for uniformity, recovery coefficient (RC), spill-out ratio (SOR) and standard uptake values (SUV).

2. Preclinical PET/CT systems enrolled in this study

PET images were acquired on the five different preclinical PET/CT scanners enrolled in this study; Bruker Albira, Mediso nanoPET/CT, Sedecal Super Argus, Siemens Inveon and Trifoil LabPET/CT. The scanners have been arbitrarily labelled 1 to 5 for the analysis of results. Table 2.1 outlines the basic components and characteristics of the preclinical PET scanners in this study. The information is derived from the reported manufactures' data sheets and published literature regarding preclinical PET scanner NEMA performance results [25,102,107–118]. The evaluation of scanner performance is not a component of this study. Scanner characteristics are noted for general descriptive

information, outlining the variability between scanners enrolled in this study. Further reading on NEMA scanner performances and comparisons are referenced in Table 2.1

Table 2.1: Different preclinical PET scanners properties and NEMA NU4-2008 testing results derived from literature and available manufactures' data sheet [25,102,107–118].

Scanner	Scintillator	Bore diameter (cm)	Axial FOV (cm)	Crystal size (mm)	Number of detector modules	Photo detector	Coincidence timing (ns)	Peak sensitivity (%)	Resolution
Bruker Albira	LYSO:Ce	10.5	14.8	50 x 50 x 10	24	3 ring SiPM	5	5.3	< 2.0
Mediso nano PET/CT	LYSO:Ce	18.1	9.48	1.12 x 1.12 x 13	12	2 ring PMT	5	7.7	< 2.5
Sedecal Super Argus	LYSO:Ce GSO:Ce	11.8	4.8	1.45 x 1.45x (7+8)	36	2 ring PMT	5	4.32	1.14
Siemens Inveon	LSO:Ce	16.1	12.7	1.51 x 1.51 x10	16	4 ring PMT	3.4	6.72	1.08
Trifoil Lab PET/CT	LYSO:Ce LGSO:Ce	16.2	7.5	2 x 2 x (12+13)	768	APD	22	2.36	0.82

3. Commercially available preclinical PET phantoms used in study

In order to avoid animal biological variability and for a protocol baseline comparison two different commercially available preclinical PET phantoms were used. The PET image quality phantom was used for quantification of uniformity, RC and SOR and the PET rod phantom for evaluation of spatial resolution. A brief description of the two preclinical PET phantoms used along with their intended purpose for quality assurance is stated in Table 2.2.

Table 2.2: Summary of PET commercial phantoms used in this study at each site, for the assessment of imaging data sets acquired with the default and standard protocols.

Phantom	Brief description	Measurement
PET Image Quality (IQ), Bartec: PH-60-00-50 8 x 3.5 cm	Three chambers: (1) two 8 mm cylinders, (2) central uniform region (3) five rods with diameters of 1, 2, 3, 4, and 5 mm 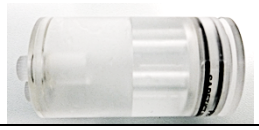	Spill over ratio, uniformity and recovery coefficients

Phantom	Brief description	Measurement
microPET rod, QRM: MicroPET HotRod 7 x 3.5 cm	Set of 6 triangular patterns with rods of diameters: 0.6, 0.8, 1.0, 1.2, 1.5 and 2.0 mm 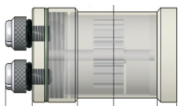	Spatial resolution

4. PET materials and methods

Quantitative biases were evaluated from the acquired phantom imaging data sets on both the default and developed standard protocol. A schematic of this process is shown below in Figure 2.1.

.

Testing PET protocols

Approaches: N=3, Per scanner (5 scanners) Per approach (imaging data sets)

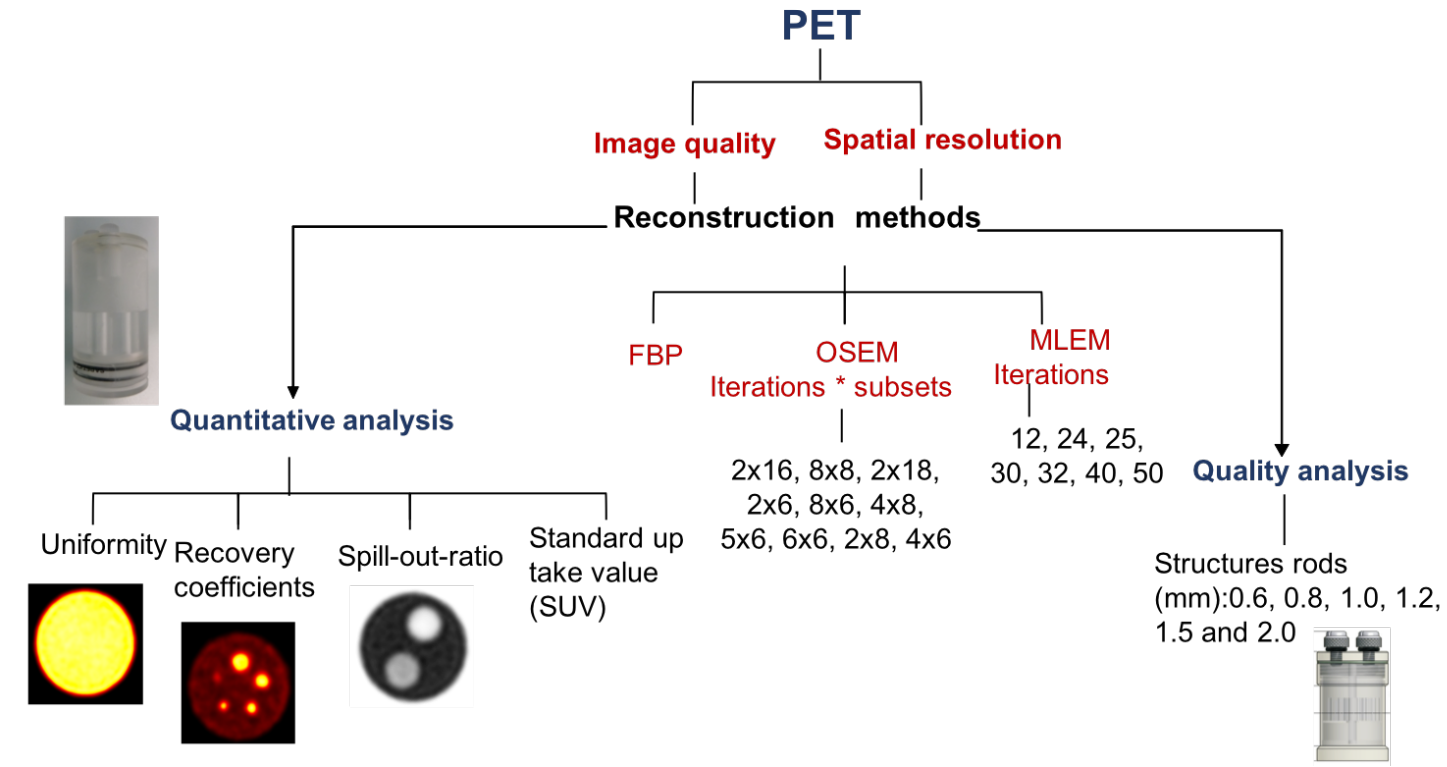

Figure 2.1: Flow chart representing the approach/process of image data analysis: acquisitions with the IQ phantom and the PET rod spatial resolution phantom; multiple reconstruction methods for quantitative analysis; default and standard reconstruction methods for visual analysis.

4.1 PET acquisition method

PET images were acquired as a single bed position for a duration of 20-minutes, energy windowing of 250 - 700 keV with the phantoms placed at the frontend of the scanner bed, positioned inside the bore at the isocenter, aligning sagittal, axial and coronal planes. An activity of 10±6 MBq of ^{18}F-FDG in 23 mL of distilled water was injected into a PET IQ phantom, which includes 5 hots rods 1-5 mm for RC, uniformity section and SOR section composed of 2 cylinders filled with non-radioactive water and air. Whilst, 64±5 MBq of ^{18}F-FDG in 24 mL of distilled water was injected into a PET rod phantom containing 0.6, 0.8, 1.0, 1.2, 1.5 and 2.0 mm rods. PET doses were chosen based on the range of activities consistent with typically reported injected doses into small animals (10-50 MBq on average) as well as the purpose and design of the PET phantoms. All PET imaging IQ phantom data sets per scanner were acquired as n=3 for the analysis.

4.2. Reconstruction methods

Emission data was reconstructed using the sites' default protocols. Protocols are listed by scanner (1-5), method (ordered subset expectation maximization (OSEM) or maximum likelihood expectation maximization (MLEM)), voxel size, filter and matrix size, Table 2.3. Scanners 2 and 3 also correct for partial volume effects by incorporating a point spread function (PSF) into the reconstruction algorithm. All scanners apply scatter, normalization and randoms corrections, whereas scanners 1-4 apply attenuation corrections. Scanners 2, 3 and 4 re-bin 3D projection data using the FORE algorithm.

Table 2.3: Default PET reconstruction methods used at each site.

Scanner	Method	Iterations *subsets or iterations	Filter	Voxel size (mm)	Matrix size
1	2D OSEM	2*16	Ramp	0.4x0.4x0.4	175x175x176
2	3D OSEM	4*6	Ramp	0.4x0.4x0.4	108x110x110
3	3D OSEM	2*18	Hamm	0.3x0.3x0.3	256x25x2566
4	3D MLEM	12	NA	0.7x0.7x0.7	108x108x108
5	2D MLEM	50	NA	0.5x0.5x0.5	200x200x200

4.3. Standardisation methods

Standardising the PET protocol entailed evaluating the impact different reconstruction methods had on the quantification of the PET image data sets. The acquisition protocol was a 20 minute scan, same windowing parameters at each site. Therefore, the biases were assessed based on reconstruction methods. Developed standardised reconstruction protocols were derived from the default protocol analysis results as described above across all imaging data sets/scanners. The results which produced the least biases across all were chosen for the standard protocols. In addition, the actual PET reconstruction parameters available on each manufactures' scanner were taken into consideration. The following reconstruction algorithms were tested: FBP, OSEM with a combination of iterations*subsets of 12, 16, 24, 30, 32, 48 and 64 and MLEM with 12, 24, 25, 30, 32, 40 and 50 iterations. Quantitative analysis of the OSEM updates used in scanners 1, 2 and 3 revealed the optimal reconstruction methods were already being used for these particular scanners, (Section 5, Table 2.5). For that reason, focus was placed on optimising the MLEM method not only for improved accuracy but also for the best equivalent results to the OSEM method. Results were then evaluated in the same manner as the default protocols on each scanner.

Quantitative assessment for standardisation of the PET imaging data noted above included uniformity, RC, SOR, and SUV. Numerical criteria for biases were based on the parameters in Table 2.4.

Table 2.4. Criteria for quantitative analysis of PET results.

PET IQ phantom	
Uniformity	< 15%
Recovery coefficients	1±10%
Spill-out-ratio	< 0.20
Standard uptake value	<10% bias

Establishing a standard PET reconstruction protocol required each imaging data set (n=3 per phantom) acquired on each scanner (n=5) to be quantitatively analysed and compared for the least bias between data sets. This was done between the reconstructed data sets within the same scanner and across/between the different scanners with the different reconstruction methods (OSEM, MLEM, FBP). The variability, percent changes were evaluated using the changes between the default reconstruction protocols and then between the standard reconstruction protocols being tested, listed above. Equation 2.1 represents the percent differences.

$$Difference = \left|(d - s)/d\right) \times 100\right| \qquad \text{Eq. (2.1)}$$

where *d* is the default empirical results being compared and *s* is the standard empirical results with units as per results being evaluated (RC, uniformity, SOR, SUV). Equation 2.1 as noted was used to compare the differences between default protocol results within each scanner, (i.e. default result 1 between 2 and 3... *n*, result 2 between 3... *n*). This type of comparison was carried out between the tested standard as well. Microsoft Excel version 16.16.18 (USA) was used for these comparisons. Additionally, results were compared to the criteria listed above in Table 2.4 for least bias and/or for fitting the criteria requirements.

4.4. PET phantoms

4.4.1. PET IQ phantom

For the PET IQ image analysis, reconstructed data was imported into PMOD version 3.806 (PMOD, Zurich, Switzerland) and a MATLAB software tool implemented by Mediso (Mediso, Hungary). The Mediso MATLAB software program utilizes the NEMA NU 4-2008 standards. The quantitative assessment of the PET data included uniformity, RC, SOR and SUV. In accordance to NEMA, uniformity is reported as the percent standard deviation (%STD) from a 22.5 mm diameter by 10 mm long cylindrical volume of interest (VOI) over the uniform region of the phantom. RC is calculated based on values extracted (measured activity) from regions of interest (ROI) twice the diameter of each hot rod. The MATLAB program draws linear profiles along the hot rods in the axial direction. The mean pixel values of the linear profiles are divided by the mean pixel value of the uniform region, Equation 2.2 below [55,119].

$$RC = \frac{ROI_{rod}}{VOI_{uniformity}} \qquad \text{Eq. (2.2)}$$

ROI_{rod} represents the mean measured activity (kBq/mL) from the hot rods (1, 2, 3, 4 and 5 mm) and $VOI_{uniformity}$ is the mean activity concentration (kBq/mL) from the uniformity region of the IQ phantom.

VOIs were drawn on each air and water chamber with SOR values calculated as ratios between the air or water chamber mean value divided by the uniformity mean measurement, Equation 2.3 [55,119].

$$SOR = \frac{VOI_{chamber}}{VOI_{uniformity}} \qquad \text{Eq. (2.3)}$$

$VOI_{chamber}$ represents the mean pixel value (kBq/mL) from each individual air or water chamber and $VOI_{uniformity}$ is the uniformity measurement stated above in Equation 2.2. Representative images of the Mediso MATLAB software tool for the PET IQ analysis

displaying the regions of the IQ phantom (uniformity, RC and SOR), as well as, the placements of the drawn regions/volumes of interest are shown in Figure 2.2.

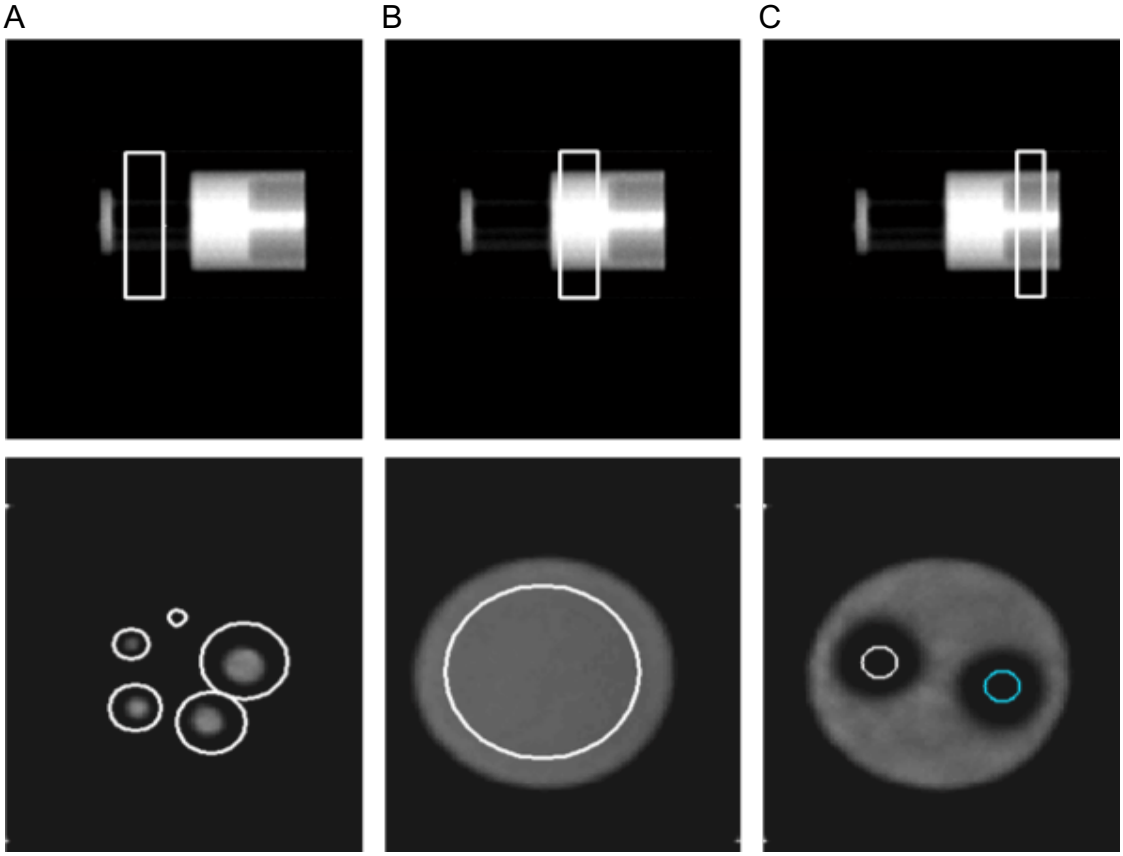

Figure 2.2: Screen shot of the Mediso's MATLAB software tool for the PET IQ analysis displaying the regions of the IQ phantom (uniformity, RC and SOR) as well as the placements of the regions. Panel A top down shows the placement of the ROIs (each hot rod) for RC, panel B top down show the placement of the uniformity ROI and panel C shows the placement of the ROIs for the spill-out ratio, white air chamber, blue water chamber.

The standard uptake value (SUV) is a prevalent quantitative value used to report the radioactivity/volume measured by the scanner. This volumetric metric is based on the amount of radioactivity injected kBq per mL into what is being imaged, in this case the PET IQ phantom. A SUV is normalised to account for administered radioactivity (i.e. radioisotope decay) and weight, (here - weight of the PET IQ phantom), as defined by Equations 2.4 and 2.5.

$$SUV = \frac{R}{d / W} \qquad \text{Eq. (2.4)}$$

$$R = g \times \frac{r}{t}$$ Eq. (2.5)

R (kBq/mL) in Equation 2.4 represents the activity concentration measured by the scanner, where *d* represents the administered radioactivity (kBq) and *W* is the weight of the PET IQ phantom (kg). Equation 2.5 reveals the values used in the calculation of *R* by the scanner. They represent the scanner's global scaling factor (*g*) in kBq/mL, the average pixel value (*r*) in arbitrary units and acquisition time (*t*) in seconds [120].

The SUV results reported as g/mL were obtained first using PMOD's SUV image calculation scaler tool with a phantom measured weight of 0.073 kg. After scaling, a 2.8 mL VOI template was placed on the uniformity section of the PET IQ phantom for the extraction of SUV results. Representative image of VOI placements on the PET IQ phantom is shown in Figure 2.3. The scanner is calibrated using known activity measured in the dose calibrator and decay corrected. Measured SUVs are the mean SUV value extracted from PMOD. The average SUV value per scanner is the average of the mean SUVs per site for n=3 measurements. The SUV data is also presented as normalized to the mean SUV measurement per scanner. For analysis of variance, using Prism 8, (GraphPad, CA, USA) an ordinary one-way (ANOVA) test was applied on the SUV data (default, standard and FBP) with a 95% confidence interval and Welch's ANOVA post-test.

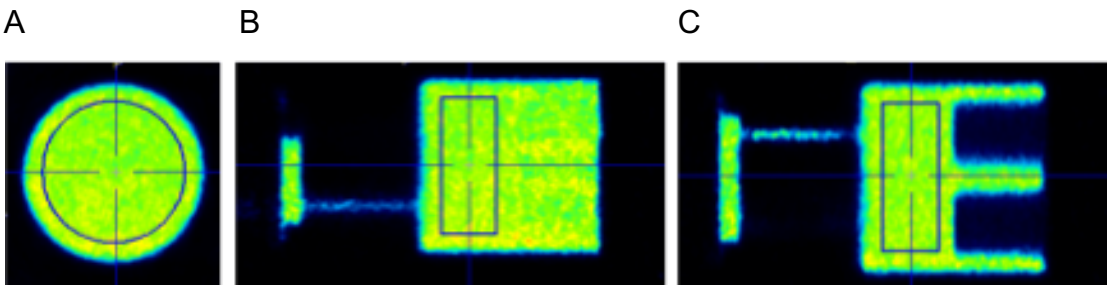

Figure 2.3: PMOD screen shot showing the VOI placement on the PET IQ uniformity region for SUV measurements. Panels (A), (B) and (C) display the VOI placement from axial, sagittal and coronal views respectively.

4.4.2. PET rod phantom

PET spatial resolution assessment was conducted based on a visual assessment of the acquired images using the PET rod phantom. Horizontal profiles (H-profile) were extracted through a centre cross section, which included the largest rods (2 mm) obtained using the PMOD image profile tool.

5. Analysis of PET Acquisitions using Default and Standardised Protocols

5.1. PET IQ phantom

The tested reconstruction methods were limited by the allotted parameters available on each manufactures' scanner. As similar as possible iterative updates were used in the analysis. Table 2.5 shows results from the default reconstruction methods for evaluation, comparison and the establishment of a standard protocol. The data displays the uniformity, RC and SOR for each scanner. Sections are divided by scanners (1-5) in which rows indicate the reconstruction method used and the data analysis results per column heading.

Table 2.5: PET IQ analysis: uniformity, RC, SOR for the default and tested different iterative and FBP methods.

	Reconstruction (updates)	Uniformity (SD%)	RC (1 mm)	RC (2 mm)	RC (3 mm)	RC (4 mm)	RC (5 mm)	Water SOR	Air SOR
Scanner1	2D OSEM								
	24	5.4	0.14	0.67	0.86	0.87	0.87	0.17	0.14
default	**32**	**6.4**	**0.17**	**0.75**	**0.90**	**0.86**	**0.87**	**0.18**	**0.13**
	64	9.2	0.21	0.82	0.85	0.82	0.86	0.17	0.11
	FBP	11.3	0.16	0.41	0.57	0.74	0.76	0.21	0.13
Scanner2	3D OSEM								
	12	4.6	0.05	0.40	0.93	1.04	1.09	0.11	0.10
default	**24**	**4.1**	**0.10**	**0.73**	**1.12**	**1.14**	**1.09**	**0.09**	**0.09**
	30	4.6	0.22	0.79	1.17	1.06	1.20	0.09	0.09
	32	4.7	0.13	0.79	1.13	1.06	1.04	0.08	0.10
	36	4.9	0.19	0.77	1.14	1.15	1.09	0.07	0.06
	48	4.4	0.18	0.76	1.16	1.17	1.10	0.07	0.07
	FBP	10.9	0.12	0.37	0.64	0.75	0.79	0.11	0.08
Scanner3	3D OSEM								
	12	2.7	0.11	0.84	1.24	1.11	1.02	0.03	0.02
	24	3.2	0.18	0.92	1.17	1.03	1.05	0.02	0.02
	32	3.3	0.19	0.91	1.14	0.98	1.05	0.02	0.02
default	**36**	**3.4**	**0.18**	**0.87**	**1.13**	**1.05**	**1.02**	**0.01**	**0.02**
	64	3.7	0.19	0.88	1.14	1.00	1.04	0.03	0.02
	FBP	4.3	0.13	0.41	0.68	0.81	0.87	0.01	0.01
Scanner4	3D MLEM								
default	**12**	**5.2**	**0.03**	**0.35**	**0.64**	**0.75**	**0.82**	**0.28**	**0.22**
	24	4.5	0.09	0.49	0.68	0.79	0.85	0.22	0.13
	25	6.4	0.12	0.64	0.79	0.83	0.87	0.21	0.13
	30	5.1	0.11	0.51	0.68	0.79	0.85	0.21	0.11
	32	6.7	0.12	0.54	0.69	0.78	0.86	0.20	0.12
	40	9.4	0.16	0.68	0.76	0.81	0.88	0.16	0.08
	50	11.70	0.18	0.66	0.74	0.81	0.88	0.18	0.08
Scanner5	2D MLEM								
	12	6.7	0.05	0.45	0.82	0.92	0.96	0.33	0.25
	24	12.4	0.11	0.79	0.92	0.93	0.94	0.25	0.13
	25	10.6	0.10	0.74	0.92	0.94	0.94	0.27	0.17
	30	11.9	0.11	0.78	0.92	0.93	0.94	0.26	0.16
	32	12.1	0.11	0.79	0.92	0.91	0.93	0.24	0.13
	40	14.1	0.13	0.82	0.91	0.91	0.95	0.25	0.14
default	**50**	**16.7**	**0.19**	**0.78**	**0.91**	**0.89**	**0.94**	**0.24**	**0.12**
	FBP	20.8	0.12	0.37	0.58	0.71	0.74	0.24	0.06

The RCs for hot rods of 1, 2, 3, 4 and 5 mm of the PET IQ phantom extracted for each scanner are shown in Figure 2.4. The default reconstruction methods are: scanners 1 (2D OSEM 2 iterations 16 subsets), scanner 2 (3D OSEM 4 iterations 6 subsets, PSF), scanner 3 (3D OSEM 2 iterations 18 subsets, PSF), scanner 4 (3D MLEM 12 iterations), and scanner 5 (2D MLEM 50 iterations). The standardised protocol leaves scanners 1, 2 and 3 with the default reconstruction method. Scanner 4 and 5 MLEM method is changed to 25 iterations instead of 12 and 50, respectively. The RCs for each site using FBP reconstruction is also shown in Figure 2.4.

Seen in Figure 2.4A, scanner 2 and 3 default reconstruction method overestimated the RCs by as much as 13% relative to 1 at the hot rod 3. Whereas, scanners 1, 4 and 5 default reconstruction method underestimated the RCs. The RCs measured for scanners 4 and 5 improved after implementing a standardised number of MLEM iterations at 25, shown in Figure 2.4B. A 43% difference measured between scanner 3 and 4 at the 3 mm hot rod using default protocols was reduced to a 30% relative difference when using the standardised protocol. The FBP method produced the most consistent RCs of all methods, (Figure 2.4C).

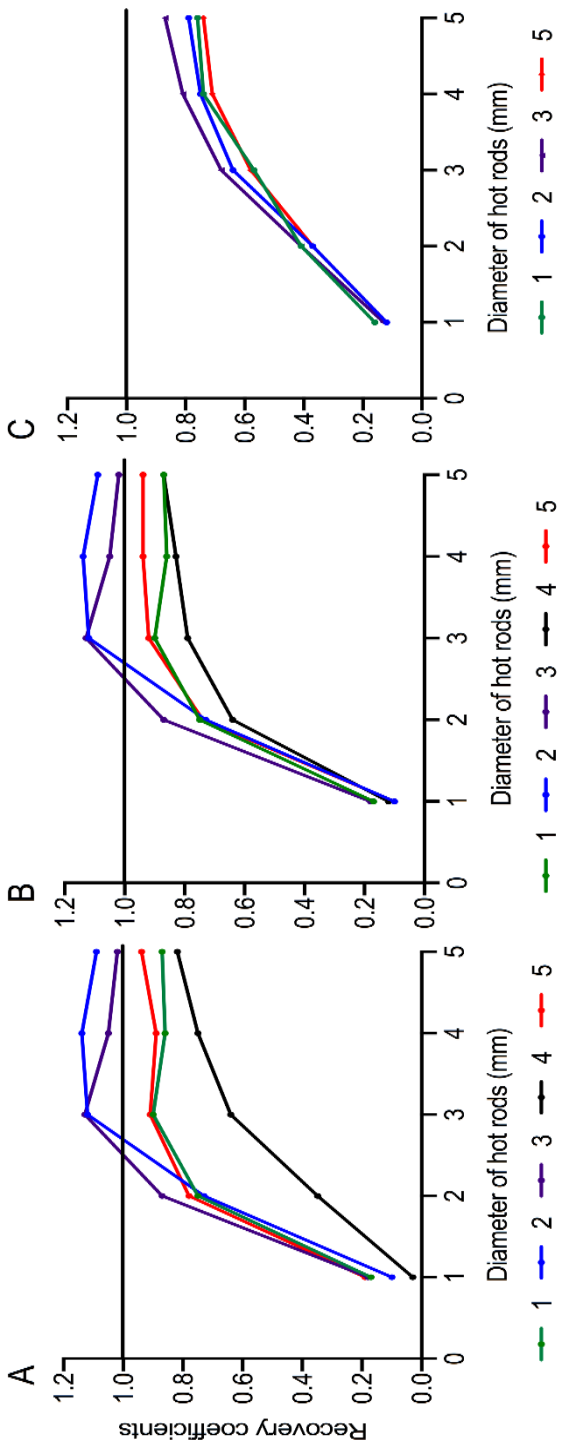

Figure 2.4: Recovery coefficients (RCs) for hot rods of 1, 2, 3, 4 and 5 mm of the PET IQ phantom extracted for each scanner. Panel (A): default reconstruction iterative methods. Panel (B): displays RCs with standardisation of iterative methods of reconstruction. Panel (C): RCs for each site using FBP reconstruction with the exception of scanner 4 (reconstruction option not available yet).

Table 2.6 reveals poor image uniformity in scanner 5 before standardisation. The standardised reconstruction protocol (MLEM 25) improved uniformity in scanner 5 by a relative percentage difference of 36% (i.e. 16.7% to 10.6%). Though protocol standardisation improved scanner 5's uniformity, there was no improvement in water and air SORs. This uniformity improvement was not observed in scanner 4 (MLEM 25), although its uniformity was already similar to OSEM data collected with other scanners. An improvement was seen in scanner 4's SORs for water and air. The mean uniformity value reduced by 12% when standardisation was applied (improved coefficient of variation from 67% to 37%).

Table 2.6: PET IQ measured uniformity and spill-over-ratios (SOR) using the default reconstruction methods and the standardised reconstruction method. Values expressed as mean±standard deviation, n=3.

	Default Protocol			Standardised Protocol		
Scanner	Uniformity (SD%)	SOR water	SOR air	Uniformity (SD%)	SOR water	SOR air
1	6.4±0.01	0.18±0.04	0.13±0.03	6.4±0.01	0.18±0.04	0.13±0.03
2	4.1±1.00	0.09±0.01	0.09±0.01	4.1±1.00	0.09±0.01	0.09±0.01
3	3.4±0.17	0.01±0.01	0.02±0.01	3.4±0.17	0.01±0.01	0.02±0.01
4	5.2±0.60	0.28±0.04	0.22±0.04	6.4±0.00	0.21±0.00	0.13±0.00
5	16.7±0.55	0.24±0.01	0.12±0.02	10.6±0.00	0.27±0.00	0.17±0.00

The measured SUV and the expected values for each scanner using the default, standardised iterative method and FBP are displayed in Table 2.6. Analysis of the SUV variance proved significant for the default protocols and non-significant for the standard and FBP protocols (ANOVA: Default $p<0.001$, Standard $p<0.205$, FBP $p<0.388$ (FBP scanner 4 not included), n=3 per group). The greatest percentage difference (44%) in SUVs obtained using default protocols was between scanner 2 and 4. This was reduced to 14% with standardisation. Using FBP, the greatest percent difference of 6% was measured between scanner 2 and 5. The percentage difference between the average

expected SUV and the average default SUV or to the standardised SUV was 18% and 10%, respectively (Table 2.7 and Figure 2.5). The injected activity is decay corrected. The measured SUV values are also normalised to the average of the measured SUVs for each scanner per reconstruction method (Default, Standard and FBP).

$$Normalised = \frac{SUV_{measured}}{SUV_{average}} \qquad \text{Eq. (2.6)}$$

The values presented in the SUV normalised column are the average values; the average normalised value.

Table 2.7: Measured and injected activity SUVs for each scanner using the default, standardised and FBP reconstruction methods. SUVs are the extracted mean and averaged for n=3 measurements, expressed as mean±standard error of the mean.

Scanner	Injected activity (SUV)	Default (SUV)	SUV normalised (Default)	Standard (SUV)	SUV normalised (Standard)	FBP (SUV)	SUV normalised (FBP)
1	3.61±0.34	3.24±0.19	1.04±0.06	3.24±0.19	0.96±0.05	3.26±0.08	1.03±0.02
2	3.87±0.36	3.77±1.61	1.21±0.19	3.77±1.61	1.12±0.18	3.18±0.23	1.00±0.07
3	4.11±0.07	3.63±0.11	1.17±0.03	3.63±0.11	1.08±0.03	3.29±0.10	1.04±0.03
4	3.64±0.18	2.10±0.04	0.68±0.00	3.24±0.01	0.96±0.00	NA	NA
5	3.52±0.65	2.82±0.09	0.91±0.02	2.93±0.27	0.87±0.07	2.98±0.01	0.94±0.00

Legend: NA=not available, FBP=filtered back projection. ANOVA: Default $p<0.001$, Standard $p<0.205$, FBP $p<0.388$ (n=3 per group).

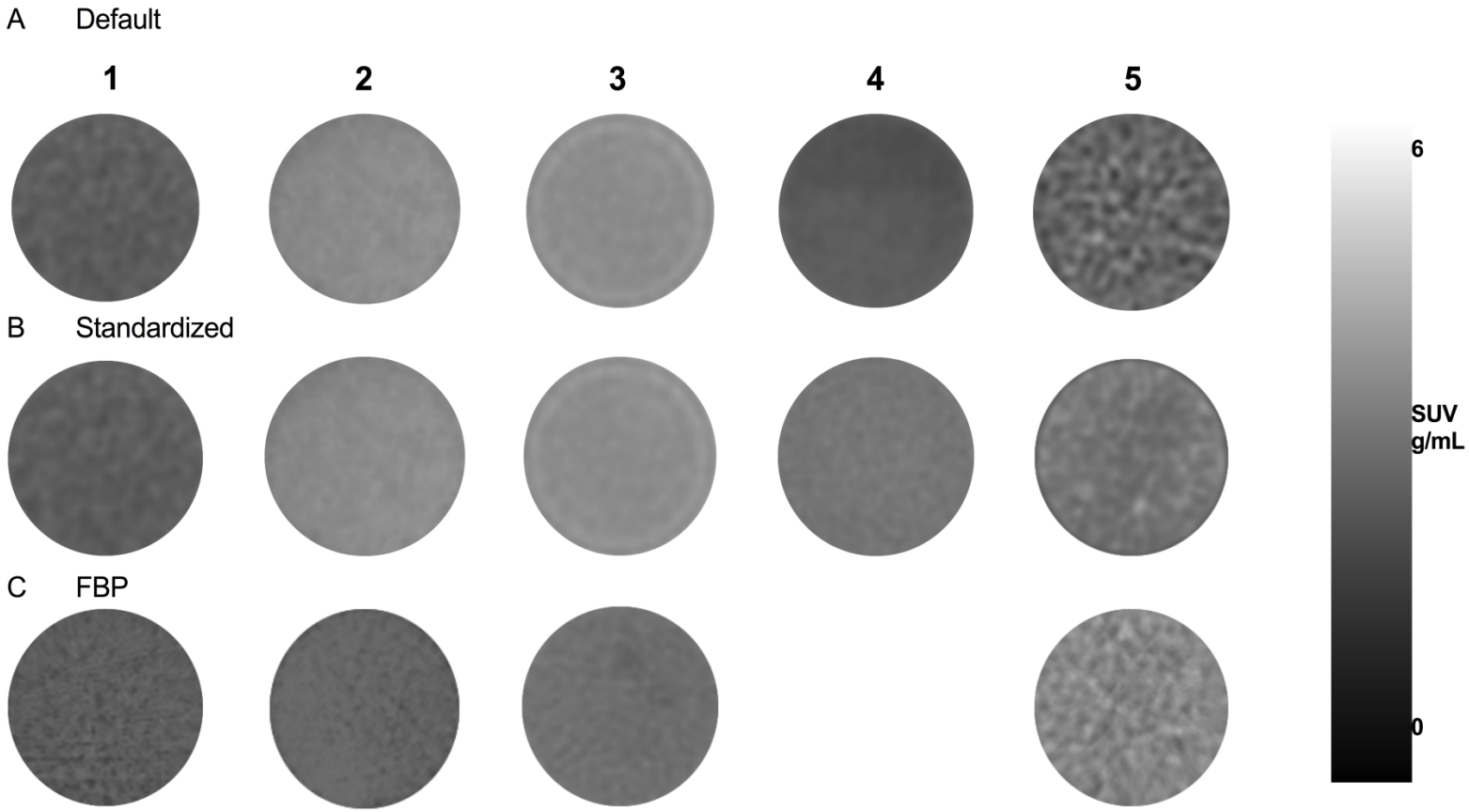

Figure 2.5: Image slice through the uniformity section of the PET IQ phantom for each scanner shows variability in scanner uniformity as well as SUV measurements when using the scanner default and varying reconstruction protocols. Panel (A) shows the default, panel (B) the standard and panel (C) displays the FBP reconstruction method.

5.2. PET rod phantom

Visual and horizontal profile analysis of the collected PET rod phantom data are shown in Figure 2.6. Images reconstructed with the sites' default reconstruction methods showed the highest measured PET image resolution was 1.2 mm, as measured in scanner 3 and 5 (Figure 2.6A). When scanner 4 and 5 PET data were reconstructed using the standardised method 2.0 and 1.5 mm rods became well resolved in scanner 4, whilst scanner 5's spatial resolution remained essentially unchanged (Figure 2.6B).

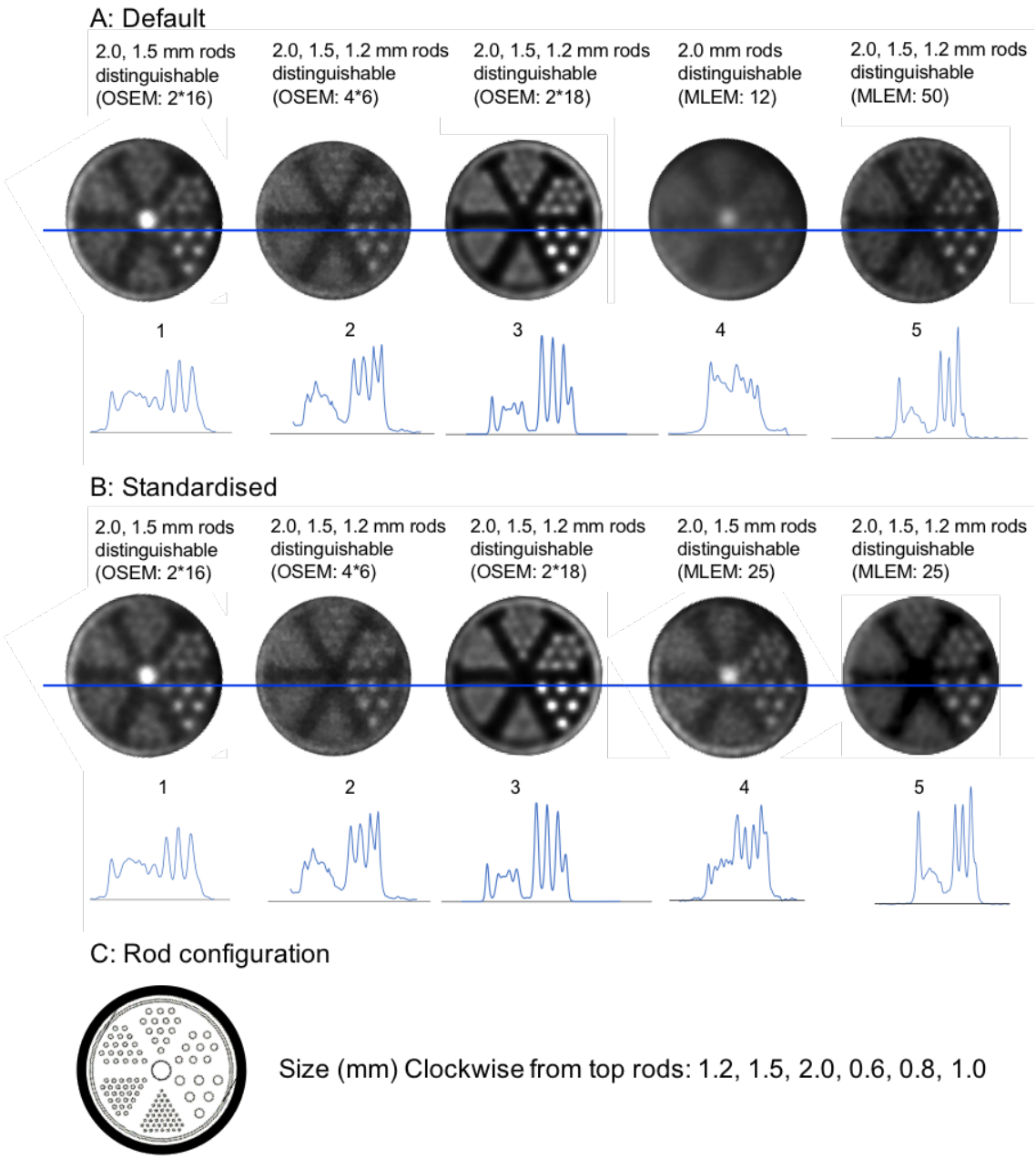

Figure 2.6: Image slice and horizontal profile through the PET rod phantom. Panel (A): Scanners 2, 3 and 5 resolved 2.0, 1.5 and 1.2 mm rods using default reconstruction protocols. Panel (B): Standardised reconstruction methods improved the spatial resolution of scanner 4 (2.0 and 1.5 mm rods are seen) and essentially did not change the spatial resolution of scanner 5. Panel (C) shows the QRM hot rod phantom configuration and size.

6. Discussion

The necessity for standardisation in clinical PET protocols was acknowledged and initiated nearly 20 years ago [121–124]. This recognition mainly stemmed from multi-centre trials focused in quantifying and tracking changes in malignant tumours as well as prognosis and treatment evaluations. Sadly, as stated throughout this thesis, standardisation is still lacking in preclinical PET imaging protocols. Today's preclinical PET/CT is a pivotal quantitative imaging research tool for translations to clinical applications supporting innovative research in areas such as disease diagnosis, prognosis and in the development of novel radiotracers and pharmaceuticals [2,6,8,15,17,125]. The empirical results revealed that the lack of preclinical protocol standardisation impacts quantitative image analysis, reproducibility and consistency across sites. Thus, limiting translational imaging data sets and impacting animal welfare.

The significant quantitative differences measured across routinely used default protocols is concerning. For example, a commonly used analysis tool both in preclinical and clinical is the extractions of SUV measurements. An impacting factor on SUV measurements are the RCs and as shown the RCs greatly vary using different default reconstruction protocols. This is in line with previous reports on different PET reconstruction methods on image data quantification [126–128]. Discordant SUV measurements are not only revealed across sites but internally between scanner's different reconstruction methods. In particular, the measured 54% difference in SUV for scanner 4 when changing from 12 MLEM to 25 MLEM. It was the FBP method that produced the most consistent and reproducible results across all scanners.

The literature spanning reconstruction methods (from FBP to iterative) is vast. Unfortunately, currently there is not a single solution that adequately fits all scanners due to differences in scanner manufacturing. The recently published paper by Mannheim *et al.* (2019) measured PET uniformity, RC and SOR in the Siemens Inveon and Focus using the reconstruction method of 2D OSEM 4*16. This method differs from both the various default reconstruction methods revealed and from the standardised protocol designed. The study protocols in the Siemens platform produced similar uniformity and SOR but different RCs values from the five scanners (reconstruction methods) enrolled [129]. This then begs the question of setting FBP as the standard for quantitative

measurements given the improved precision of RCs and SUVs across sites. Nevertheless, using a combination of reconstructing with FBP and OSEM (as opposed to MLEM) serves the dual purpose of providing more accurate and precise quantitative information. The combined approach will also retain suitable image quality for better delineation of small organs and structures in preclinical animal species [130,131]. Therefore, it is recommended VOIs are drawn on the reconstructed OSEM image for better location/orientation then applied on the FBP image for accurate quantification. It is also recommended that the total number of updates (iterations*subsets or iterations) are no less than 24 and no more than 36 for analysis of image data in conjunction with using FBP. This set of iterations*subsets or iterations covers the range of OSEM and MLEM reconstructed data sets which produced the least biases amongst the different scanners.

In 2017 Mannheim *et al*. (2017) pointed out the difficulties of establishing a standard imaging protocol due to different scanner technical parameters. Their study also discussed the potential impact the variety of technical parameters can have on the inability to reproduce research studies [132]. Here, taking the novel approach of quantitatively assessing imaging data sets default protocols produced as opposed to the scanner offered the opportunity to report actual numerical biases. Thus, overcoming the scanner technical parameter variability problem. Addressing the need for reproducibility, this study allowed for the ability to look at "end results" indicative of research. Acquiring results from each site's default PET reconstructions gave the foundation for direct empirical comparisons and analysis. From these comparisons, options for different and similar reconstruction parameters were identified and tested until a reduction in biases obtained. This task of analysing and comparing was not without limitations. Limitations revolved around reconstruction options available per scanner (OSEM, MLEM). Arguably, a primary concern. However, distinguishing similarities between methods by comparing numerical values as well as analysing the common method of FBP this limitation was vanquished.

Imaging protocols producing unreliable and unreproducible imaging data sets is not the only concern. Mentioned early on, was the concern regarding scanner calibrations. Initially, the scanners at every site visited contained calibration errors and artefacts. With the exception of one site regular calibrations are rarely done or not done at all unless

there is a system failure. Fortunately, the manufactures' engineers responded expeditiously to rectify calibration errors and artefacts identified during site visits. Unfortunately, that may not always be the case. Scanner calibration, whether CT or PET procedures exist [55,56]. Therefore, along with standardising imaging protocols proper scanner calibration needs to be enforced.

Additionally, animal welfare in preclinical PET imaging remains a great concern. Current literature exist discussing preclinical imaging handling and radiotracer injection protocols [104132]. However, the cycle of test re-test using animals essentially due to instrumentational protocol biases is still troubling. Implementing the standard protocols put forth will assist in ending this viscous cycle of repeating acquisitions or increasing group sizes to achieve meaningful PET imaging data.

7. Conclusion

This first standardisation aim set out to determine if improved experimental design, by investigating and comparing PET reconstruction parameters in different platforms, would in fact improve the precision and accuracy of imaging data sets. The question was: Will standardising preclinical PET protocols across multiple scanners reduce quantitative bias in image data, while maintaining image quality? Answer: yes, the imaging data comparisons across sites validated significant biases in PET outcome measures without standardisation. The implementation of preclinical PET/CT standardised protocols developed and tested will provide more robust, reliable and reproducible translational datasets for clinical applications. Moreover, in accordance with the NC3Rs principles, the refinement of PET protocols reduces unnecessary repeated studies and the number of animals used.

Chapter Three: Standardisation of preclinical CT imaging

1. Introduction

Clinically and preclinically CT is already extensively used in PET/CT and on its own, though without guidelines or standard protocols in the preclinical platform. Again, the approach of quantitatively evaluating the empirical data and image quality of the actual CT protocols used across the different sites and scanners was taken. For determining a global CT standard protocol, evaluating image quality and quantification biases was done using five commercially available preclinical CT phantoms. Each CT default protocol was also assessed based on measured absorbed ionising radiation. The standardised CT protocol was determined from the least HU biases between all imaging data sets.

Measuring CT absorbed doses along with assessing HU value biases was always an initial important component of setting protocol parameters. However, it became apparent while visiting each site that the deficiency in understanding the amount of ionising radiation being absorbed per image was great. Along with establishing CT parameters for a standard protocol, this study's CT dose results provides the foundational work for establishing radiation dose guidelines.

In addition to concerns over ionising radiation, site's scanner calibration was initially a concern. Though not a component of this study, it is important to emphasize the need for scanner calibration. Initially more than one scanner was plagued by calibration errors requiring intervention from the scanner manufacturer. Therefore, along with setting a CT protocol, correct calibration (HU values) at the different tube voltages needs to be ensured.

2. Preclinical PET/CT systems enrolled in this study

The five different preclinical PET/CT scanners enrolled and used for PET acquisitions were also used for the CT acquisitions. Scanners were arbitrary labelled the same way they were in Chapter 2. In Table 3.1 the basic characteristic of the CT component are shown; derived from the available manufactures' data sheets and published literature.

Table 3.1: The different CT scanner properties derived from manufactures' data sheets.

Scanner	Tube power (W)	Maximum tube current (mA)	Tube voltage (kVp)	focal spot (µm)	Detector material	Detector area (mm)
Bruker Albira	50	0-1	10 to 50	35	CsI:Tl	120 x 120
Mediso nanoPET/CT	80	0-1	35 to 80	33	CsI:Tl	150 x 120
Sedecal Super Argus	50	0-1	4 to 50	35	CsI:Tl	120 x 120
Siemens Inveon	80	0-500	35 to 80	< 50	Cs:Tl	125 x 125
Trifoil LabPET/CT	80	0-1	40-90	20-120	Cs:Tl	165 x 165

3. Commercially available preclinical CT phantoms used in study

The same rational as in PET applies to CT. In order to avoid animal biological variability and for a protocol baseline comparison five different commercially available preclinical CT phantoms were used. Shown in Table 3.2 are the five different CT phantoms: CT air/water phantom and CT tissue-equivalent phantom (TEM) for measuring and quantifying Hounsfield (HU) bias, CT bar phantom for spatial resolution analysis, CT dose index rat and mouse phantoms to assess the absorbed dose (ionising radiation), measured with an ion chamber.

Table 3.2: Summary of CT commercial phantoms used in this study at each site, for the assessment of imaging data sets acquired with the default and standard protocols.

Phantoms	Brief description	Measurement
Air/water Quality Control (QC), Bartec: PH-60-00-60, 6.5 x 3 cm	Dual chamber air and water 	Accuracy of air and water Hounsfield Units (HU)
CT bar, QRM: MicroCT Bar pattern-NANO, 4 x 2 cm	Chip with bar and circle patterns ranging from 5 to 150µm in thickness and diameter, respectively 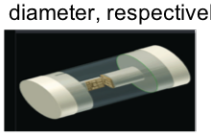	Spatial resolution
Tissue Equivalent Material (TEM), CIRS: MicroCT rods 091, 9.5 x 3 cm	Rods (2 to 5 mm) of polymer materials representing lung, muscle, adipose tissue, and hydroxyapatite (0, 50, 250 & 750 mg/mL) 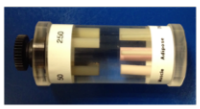	Hounsfield Units (HU) for equivalent/representative tissues
Mouse CT Dose Index (CTDI), Bartec: PH-60-00-05, 15 x 3 cm Rat CT Dose Index (CTDI), Bartec: PH-60-00-06, 15 x 6 cm	Cylinder with central bore - for ion chamber 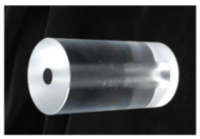	Dose Index (radiation delivered)

4. CT materials and methods

For CT image acquisitions phantoms were placed at the frontend of the scanner bed, positioned inside the bore at the isocenter, aligning sagittal, axial and coronal planes. Images were acquired for the air/water, TEM and bar phantoms. All CT acquisitions were reconstructed using the FBP method. Schematic, Figure 3.1 displays the process of CT acquisition and analysis.

Testing CT protocols

Approaches: N=3, Per scanner (5 scanners) Per approach (imaging data sets)

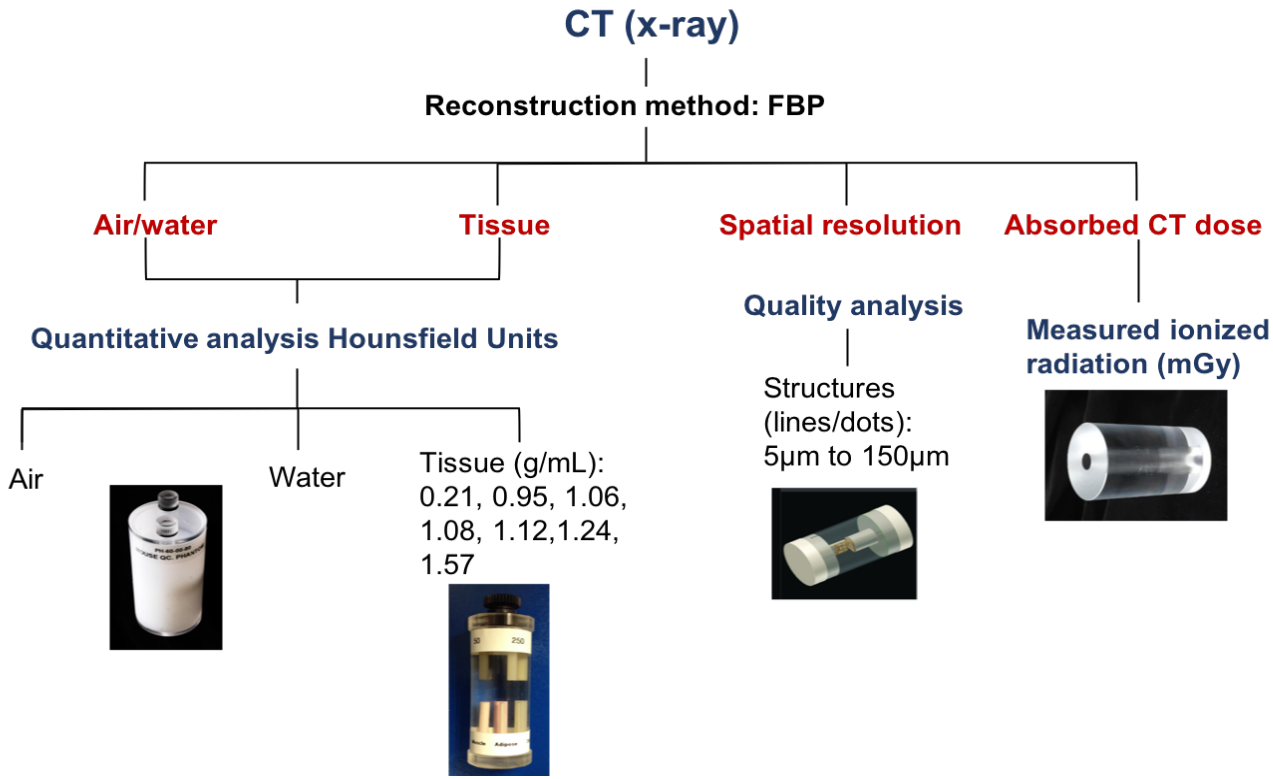

Figure 3.1: Flow chart representing the approach/process of image data analysis: acquisitions with the air/water and TEM phantom for quantitative HU analysis; CT bar phantom default and standard acquisitions for visual analysis. Absorbed dose measurements on all protocols.

4.1. CT acquisition method

For each default protocol, CT basic acquisition parameters varied by tube voltages (kVp), number of projections and exposure time (ms) per scanner. Full CT default protocol parameters per scanner are listed in Table 3.3.

Table 3.3: Summary of each scanner's CT default protocols evaluated.

Scanner	Scan method	Number projections	Tube voltage (kVp)	Exposure time (ms)	Binning	Zoom	Focal spot (µm)	Current (µA)
1	circular	360	40	300	1:1	none	35	140
2	circular	480	50	300	1:4	max FOV	33	520
3	step-in-shoot	220	80	280	1:4	low	< 6	500
4	circular	250	35	300	1:4	none	35	200
5	circular	256	50	555	1:1	low	33	760

4.2. Standardisation methods

From the analysis of the CT data four standardised CT protocols were developed and tested. The tube voltage was set at 50 kVp and exposure time at 300 ms for all scanners with four varying number of projections (170, 360, 480 and 720 projections). Not all the scanners could set the projection parameters at 170 or 480. In those cases, data was only collected for the remaining protocols. CT collected data, including CT absorbed doses, were analysed in the same manner as the default protocols, as outlined above. In the CT result section, CT imaging data derived from default and standard acquisition protocols using 360 projections are presented, given that all scanners allowed for this setting. Presenting only these two data sets in the main results section also avoids the bombardment of copious amounts of data to read through. More importantly and to the fact or heart of the matter it was the 360 projection results that ended up fulfilling the purpose of this PhD's goal of standardisation, thus the most critical to report. With that

said, it is important to show all the data analysis and results which lead up to the decision of the best suited standard protocol. Therefore, results from the other tested CT protocols are displayed in Appendixes 2 through 4 for reading.

Establishing a standard CT imaging parameter protocol required each imaging data set (n=3 per phantom) acquired on each scanner (n=5) to be quantitatively analysed and compared for the least bias and variability between data sets. For the CT, this was accomplished by comparing numerical values acquired between imaging data sets when the imaging acquisition parameters were varied, as each site used the same reconstruction method (FBP). Similar to Chapter 1, the variability, percent changes were evaluated using the changes between the default protocol results and then between the standard protocol results being tested, listed above. From Chapter 1, now Equation 3.1 represents the percent differences.

$$Difference = \left|(d - s)/d\right| \times 100 \qquad \text{Eq. (3.1)}$$

where *d* is the default empirical results being compared and *s* is the standard empirical results with units as per results being evaluated (HUs for air, water, TEM and ionising radiation dose). Equation 3.1 as noted was used to compare the differences between default protocol results within each scanner, (i.e. default result 1 between 2 and 3... *n*, result 2 between 3... *n*). This type of comparison was carried out between the tested standard as well. Microsoft Excel version 16.16.18 (USA) was used for these comparisons. Additionally, results were compared to the criteria listed above in Table 3.4. for least bias, reduced variability and/or for fitting the criteria requirements.

Table 3.4: Criteria for quantitative analysis of CT HU results.

CT Air/water phantom	Air	Water	
	0 ±35	-1000 ±10	
TEM phantom	Lung	Soft tissue (Adipose/muscle)	Bone (Soft/cortical)
	-600 to -700 ±10	-100 to 200 ±50	400 to 800 ±50 2000 to 3000 ±100

Legend: * HU for TEM originally defined based on literature [71]. Preclinical HU ranges are not fully established. For example, water HU > 0 ±7 would be considered as failing in clinical CT calibrations.

4.3. CT phantoms

4.3.1. CT air/water phantom

Reconstructed CT data was imported into PMOD for analysis. A 5 mL VOI was placed on the air and water chamber of the CT air/water phantom to quantify the mean Hounsfield unit (HU) values, (Figure 3.2).

A B

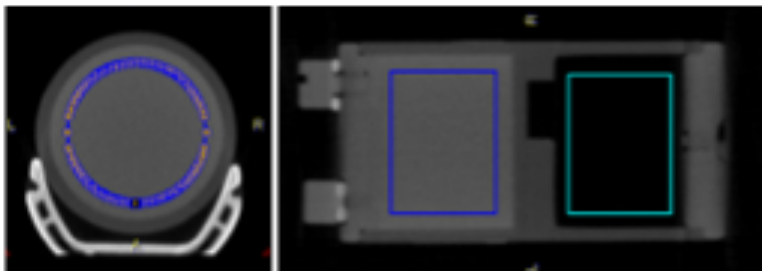

Figure 3.2: PMOD screen shot showing the VOI placement on the CT water and air region for HU measurements. Panel (A) provide an axial view point and panel (B) displays a coronal view showing the water (left) and air (right) chambers.

4.3.2. CT TEM phantom

The TEM phantom data was imported into PMOD and individually co-registered with an in-house developed TEM phantom template in order to ensure correct and consistent placement of VOIs on each rod for each CT image. A VOI template was generated for each rod (0.008 mL for 2 mm and 0.05 mL 4 mm) for extraction of HUs, Figure 3.3. HU quantification accuracy was defined as bias between measured HU relative to established HU value for air, water and tissue. The data is represented as the mean ±standard deviation (SD). Precision is assessed by measuring the SD and coefficient of variation (COV). For analysis of variance, using Prism 8, (GraphPad, CA, USA) an ordinary one-way (ANOVA) test was applied on the TEM data, grouped per tissue density (default, standard) with a 95% confidence interval and Tukey's multiple comparison post-test.

A B

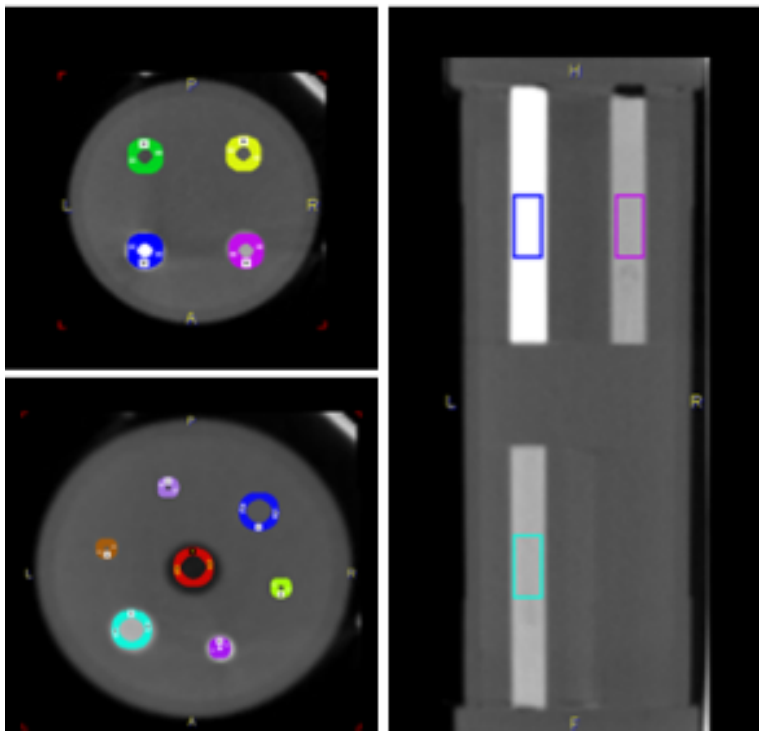

Figure 3.3: PMOD screen shot showing the VOI placement on the CT TEM phantom rods for HU measurements. Panel (A) (axial view) and (B) (coronal) show the different size rods.

In Figure 3.4 the location of the rods (4 mm, 2 mm and lung 5 mm) and their densities are displayed in Figure 3.3, though not to scale. The density values are those reported from the TEM phantom manufacture (CIRS).

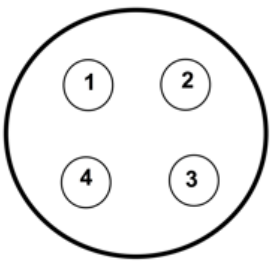

Rods	Material	Density (g/mL)
1	0mg/mL	1.083
2	50mg/mL	1.115
3	250mg/mL	1.24
4	750mg/mL	1.57

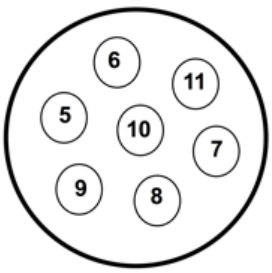

Rods	Material	Density (g/mL)
5	50mg/mL	1.115
6	0mg/mL	1.083
7	adipose	0.95
9	250mg/mL	1.24
8	750mg/mL	1.57
10	lung	0.205
11	muscle	1.063

Figure 3.4: Schematic representation of panel (A) in Figure 3.3 showing the location and identification of the rods, along the manufacture's reported densities . Rods 1- 4 are 4 mm, rods 5-8 are 2 mm, rods 9 and 11 are 4 mm and rod 10 is 5 mm.

The TEM phantom rods related to HU ranges based on the reported densities. TEM: rod density of 0.205 g/mL (lung) HU range of -600 to -700 ±10, rods with densities ranging from 0.95 to 1.115 g/mL (soft tissue) have an acceptable HU range from -100 to 200 ±50, rod density of 1.24 g/mL (bone) acceptable HU range is 400 to 800 ±50, rod density of 1.57 g/mL (cortical bone) acceptable HU range is 2000 to 3000 ±100 [71].

4.3.3. CT bar phantom

CT spatial resolution was evaluated by visual assessment of the image obtained with the spatial resolution bar phantom. The number of structures (lines/dots with widths varying between 5 and 150 µm) on the bar pattern seen were compared to the manufacture's size chart to estimate each protocol spatial resolution.

5. Absorbed dose measurements

An ionisation chamber probe (10x6-0.6 CT Therapy QA Chamber, detection range 1µGy-5kGy with ±4% calibration accuracy, Radcal, California, USA) was used for radiation dose measurements. The ion chamber probe was placed inside the CT dose index (CTDI) phantoms with the chamber in the centre FOV. Default and standardised CT protocol measurements were obtained (n=3) on all scanners with the mouse and rat CTDI phantom.

The Radcal ion chamber software stops collecting/measuring at 300s. Previous work showed the measured CT dose with the RadCal probe is linearly dependent on scan length [103]. Therefore, CT protocols with a scan time longer than 5 minutes were measured to 300s then the dose was calculated based on remaining frames and measured dose, Equation 3.2.

$$\text{Measured CT dose} = \left(\frac{Frames_{protocol}}{Frames_{acquired}} \right) Dose_{measured} \qquad \text{Eq. (3.2)}$$

6. Analysis of CT Acquisitions using Default and Standardised Protocols

Evaluating CT image data sets from all phantom results across site's default protocols revealed significant differences, including absorbed CT dose amounts. Scanner 5 does not output HUs. Therefore, scanner's CT results are a linear grey scale as opposed to HU. Numerical criteria for HU biases were based on the parameters in Table 3.4.

6.1. CT air/water phantom

The HU extracted using CT default acquisition protocols for scanners 2 - 4 were within a global average range from these data sets for air of -989±13 HU (mean ± SD, n=3) and water 38±61 HU (mean ± SD, n=3). The greatest extracted HU for water was 133 HU and for air was -967 HU, measured in scanner 1. When the standardised CT protocols were applied results for scanner 1 improved (water HU improved from 133 HU to -77 HU), while HU water results for scanners 2 - 4 were all within ±30 HU from 0 HU (Table 3.5). The greatest measured HU for air when using CT standardised protocols was -990 HU.

Table 3.5: Hounsfield Units (HU) measured using the CT air/water phantom and default and standardised protocols. Results presented as the mean±standard error of the mean HUs for each scanner (n=3).

	Ave HU Water (0)	Ave HU Air (-1000)
1 Default	133.05±164.18	-967.86±85.59
Standardised	-77.91±91.98	-990.46±50.97
2 Default	-29.62±18.64	-993.84±6.55
Standardised	-27.88±20.55	-993.29±6.97
3 Default	16.97±24.93	-994.98±9.67
Standardised	28.78±26.53	-996.92±4.13
4 Default	24.85±14.11	-1000±0.00
Scanner 5: one data set calibrated to HU (usual output is linear grey scale)		
5 Default	-10.12	-1008.26
Standardised	-3.42	-1024.19

Please note, the standardised protocol was acquired for scanner 4 but could not be quantified. The scanner's vendor/engineer was not able to properly calibrate the scanner for the required tube voltage of 50 kVp. Hence, the data was nonsensical. Scanner 5 is not calibrated to measure HU values; output results are a linear grey scale. In order to report out HU for scanner 5 the data had to be converted manually based on the scanner's water and air calibration data. This conversion was done onsite by the site's in-house physicist, results are displayed on the bottom of Table 3.5. To illustrate the point and importance of correct CT scanner calibration Figure 3.5 displays artefacts observed during site visits.

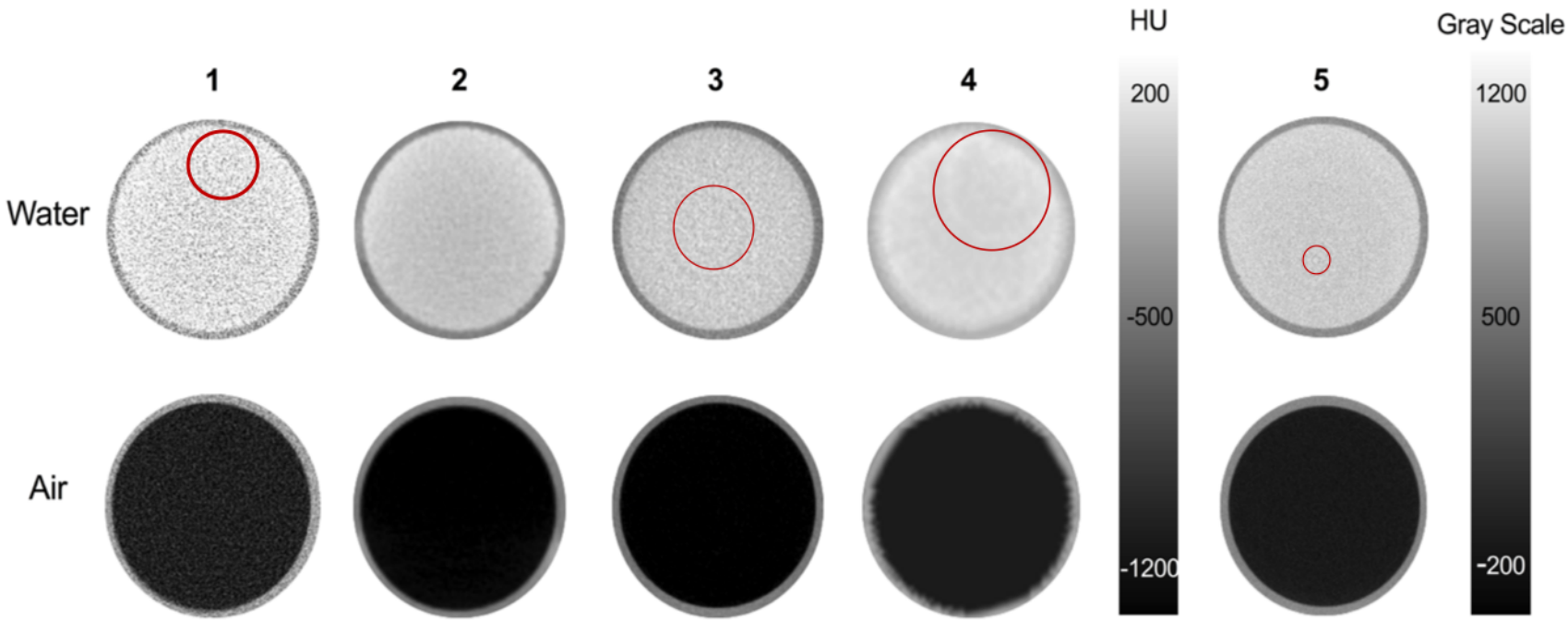

Figure 3.5: Clearly seen in the water section of the CT air/water phantom are ring artefacts. Scanners 1, 3 and 4 all have a centre of rotation error. This error can be corrected for by running the scanner calibrations. Scanner 5, however, has a detector error, which will require replacement. The red circles outline the artefacts.

6.2. CT TEM phantom

A one-way ANOVA revealed significant differences across all tissue groups ($p<0.0001$, $n=3$), with the greatest variability (difference of 1581 HU, i.e. scanner means ranging between 3599 and 2018 HU) measured in the 1.57 g/mL rod when CT default protocol methods were used. The three rods, 1.08, 1.12 and 1.24 g/mL each measured mean percent differences greater than 90%. The greatest mean percentage difference in the adipose rod was 147%, and muscle calculated greatest mean percent difference was 216%. The muscle and adipose rods also had calculated high mean standard deviations and coefficient of variation values, 67% and 104%, 77% and 66%, respectively. Lung measured the least bias, with the greatest mean percent difference of 28%, a mean standard deviation of 75% with a coefficient of variation of 11%.

Two scanners showed a high discrepancy in HU comparison between the 4 mm and 2 mm rods of the same TEM (1.08 g/mL and 1.12 mg/mL hydroxyapatite). Scanner 1 calculated percentage difference between the 4 and 2 mm 1.08 g/mL hydroxyapatite rods was 130% and scanner 3 measured percentage difference between the 4 and 2 mm 1.12 g/mL hydroxyapatite rods was 158%. All HU data points using the default protocols are shown in Figure 3.6A.

The use of a CT standardised protocol improved quantitative precision for all the materials (Figure 3.6B). The greatest improvement was measured in the rods with densities of 0.21, 0.95 and 1.08 g/mL representing lung, adipose and soft tissue, respectively. For example, the quantitative precision for the rod representing adipose tissue (0.95 g/mL) improved from a standard deviation of 77% with a coefficient of variation of 66% to a standard deviation of 22% and a coefficient of variation of 3% relative to the mean. Furthermore, the lung rod measured a reduction of mean differences, in which scanner 3 improved from a mean of -728.4 HU, standard deviation of 35.16%, to a mean of -738.4 HU with a standard deviation of 0.64%. Also, the 1.57 g/mL hydroxyapatite rod's measured mean difference was reduced by 67% between scanners from 1581 to 518 HU. The muscle rod's measured HU values were the least improved with a standard deviation improved to 40%, the coefficient of variation remained greater than 104%.

The large percentage difference seen in scanner 1 between 4 and 2 mm 1.08 g/mL rods when using default protocols reduced by 109% when standardised protocols were applied for CT data collection. However, in scanner 3, the measured percent difference between the 4 and 2 mm 1.12 g/mL hydroxyapatite rod was essentially unchanged.

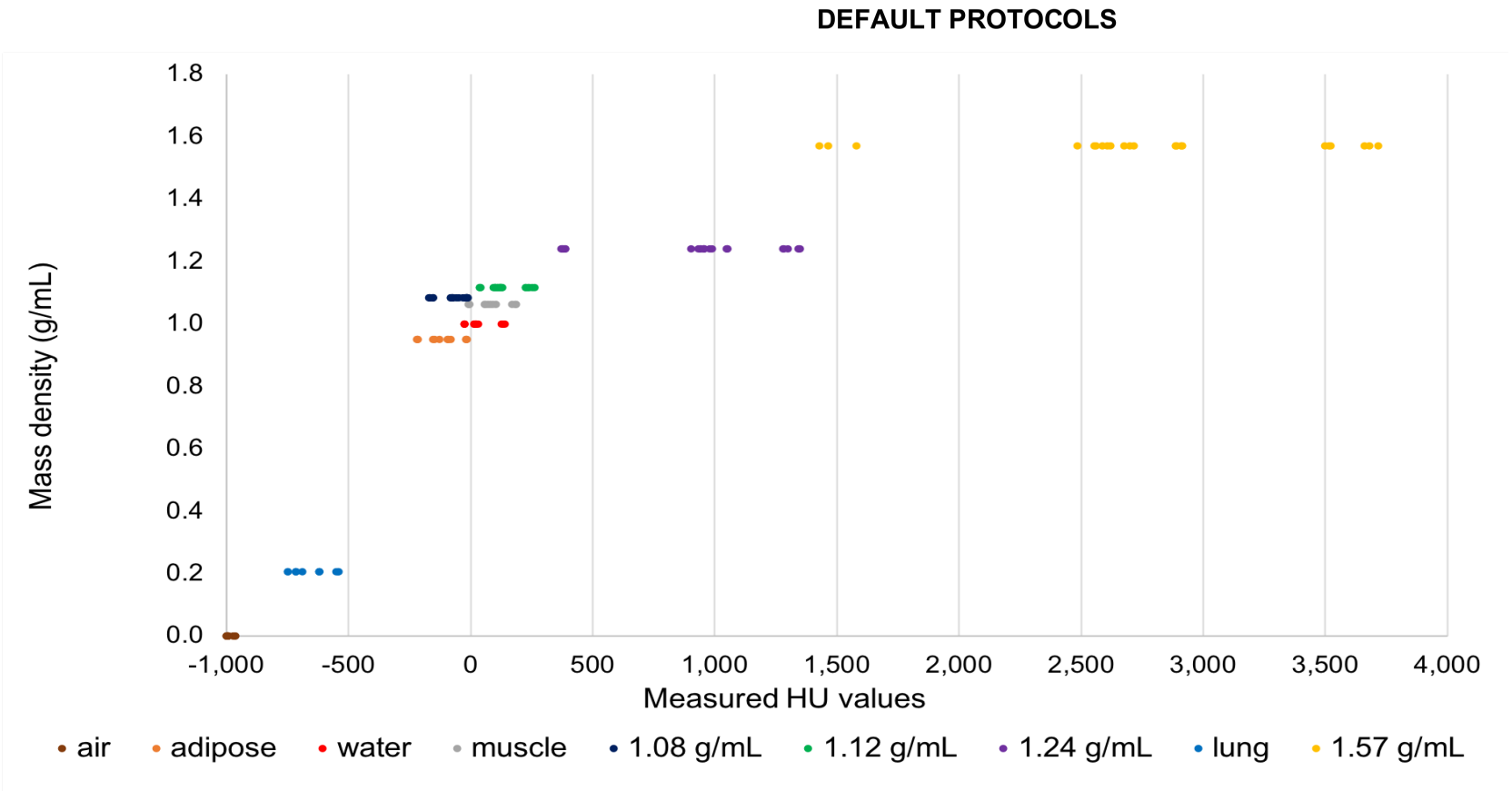

Figure 3.6A: CT TEM, air and water HU results. For each material, each data point represents a measurement from a scanner (n=3) from four different sites. Densities 1.08 to 1.57 g/mL include rod sizes 2 mm and 4 mm as reported by the manufacturer. The x-axis clearly shows the spread of HU values per density (A) and displays the significant variations measured using the default protocols ($p<0.0001$, one-way ANOVA, n=3 per group).

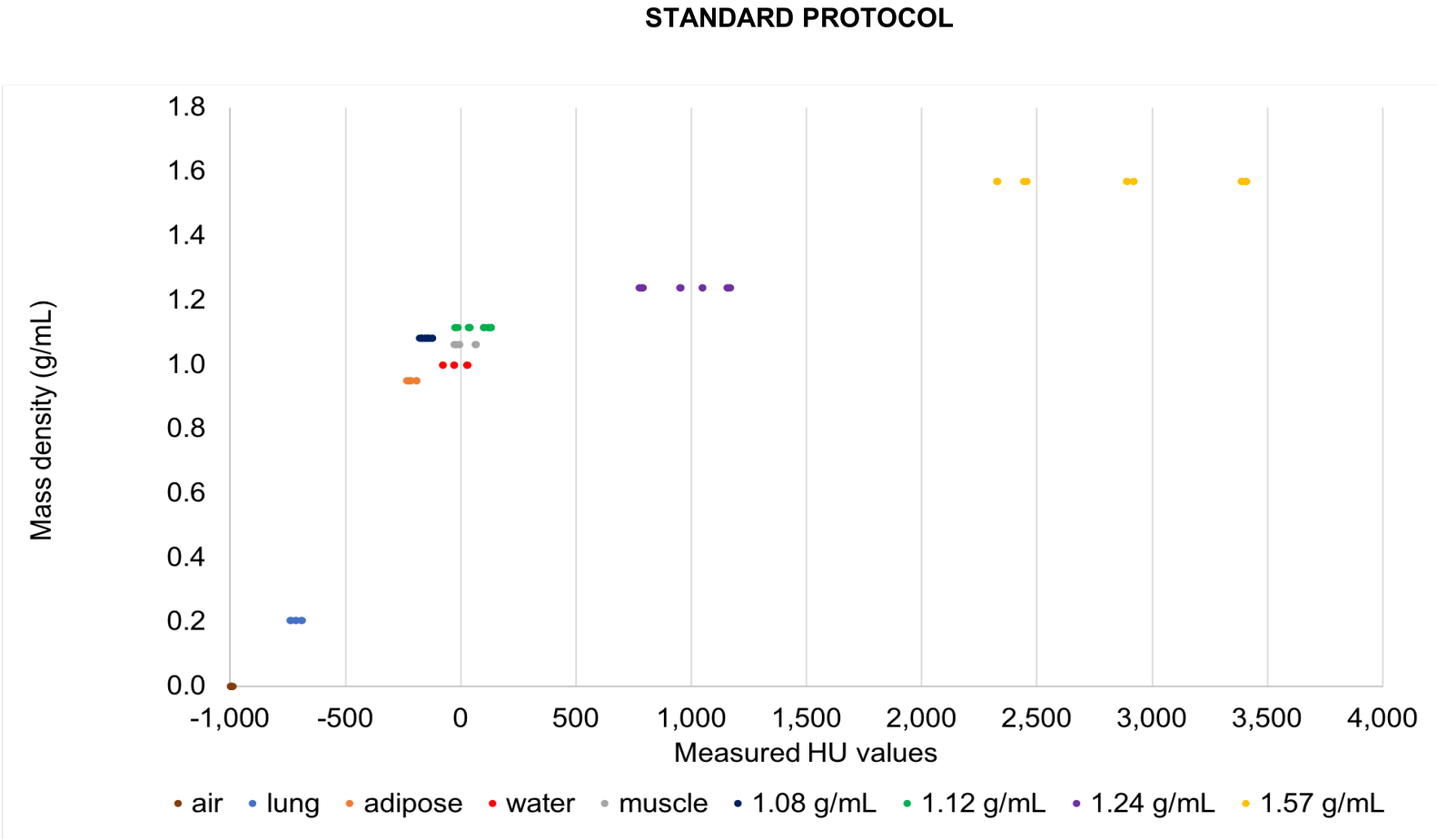

Figure 3.6B: CT TEM, air and water HU results. For each material, each data point represents a measurement from a scanner (n=3) from four different sites. Densities 1.08 to 1.57 g/mL include rod sizes 2 mm and 4 mm as reported by the manufacturer. Panel (B) clearly shows improved precision across scanners and densities when using the standardised protocol.

Previously mentioned, scanner 5 is not calibrated to output HU values. Therefore, a linearity analysis was done on the grey scale output values for the TEM materials, Figure 3.7. The results indicate scanner 5's grey scale does change linearly with increase densities, as hoped.

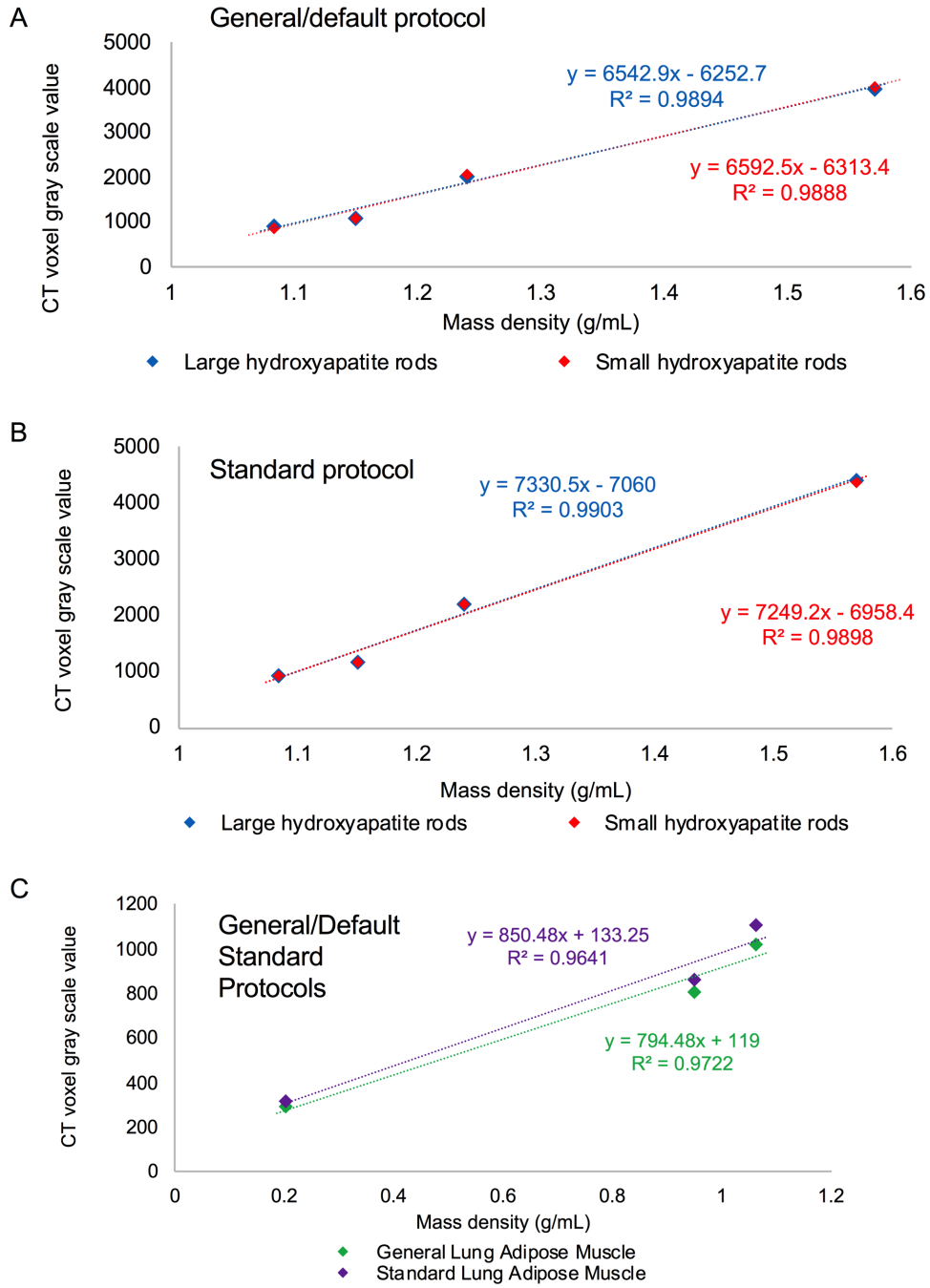

Figure 3.7: Plotted scanner's outputted grey scale values for CT TEM phantom. Grey scale results shows linearity.

6.3. CT bar phantom

Scanners 1, 2 and 4 were unable to resolve 150 µm lines using default protocols or distinguish the sections of lines/dots patterns. Scanner 5 had the highest spatial resolution for a default protocol of 150 µm (Figure 3.8A). A slight improvement (scanners 1-3) or no change in measured spatial resolution was seen when using the CT standardised protocol (Figure 3.8B).

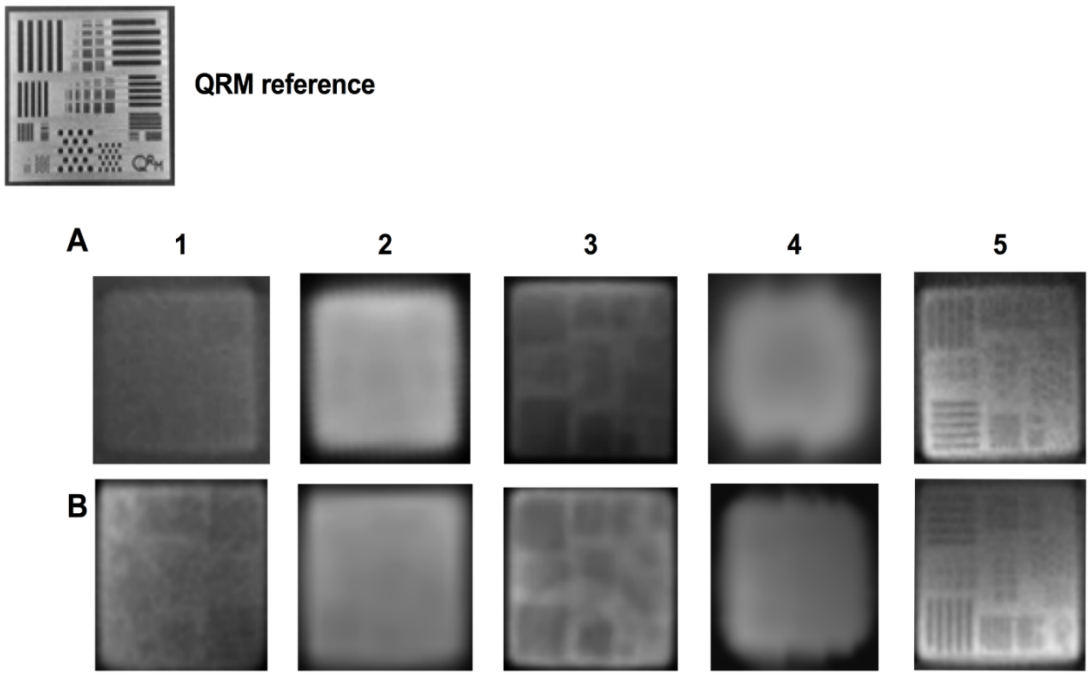

Figure 3.8: CT bar phantom images displaying QRM pattern for spatial resolution using the default (A) and post standardisation (B) of CT protocols.

7. Analysis of measured absorbed CT radiation dose using default and standardised protocols

Measured CT absorbed doses using the default protocols at each site ranged from 11 mGy to 216 mGy (Table 3.6). Ionising radiation absorbed dose measurements in scanner 5 reduced by 81% when using the standard protocol. Overall there was a 48% and 40% reduction in the CT absorbed doses measured with the mouse and rat CTDI phantoms, respectively, when using standardised CT protocols.

Table 3.6: CT absorbed doses determined using default protocols and a standardised protocol for mice and rats. Results expressed as mean±standard deviation, n=3.

	Default (mGy)		Standard (mGy)		Measured dose difference default to standard (%) (Eq. 3.1)	
Scanner	Mouse	Rat	Mouse	Rat	Mouse	Rat
1	11±0.10	7±0.10	20±0.09	13±0.16	+77	+86
2	40±0.11	28±0.02	31±0.23	21±0.08	-23	-23
3	59±0.03	48±0.11	39±0.23	28±0.08	-34	-42
4	32±0.18	15±0.10	56±0.76	25±0.05	+71	+60
5	216±0.02	100±0.17	41±0.02	31±0.03	-81	-69

8. Discussion

Unlike PET, the CT image reconstructions were all done, default and standardised, with the FBP method. Though like PET the quantitative biases revealed with the default protocols were substantial. The significant variations in HU from the various CT default protocols reiterates the necessity of standardisation. In this case the CT acquisition protocols have a more prominent role than reconstruction methods. Applying a standard CT acquisition protocol improved quantification precision of HU values across sites for each TEM measured as well as in air and water. The recommended standard CT protocol sets the tube voltage at 50 kVp for 300 ms with 360 projections. This recommendation is completely feasible given that every

scanner enrolled in this study is capable of those parameters. Initiating the standard CT imaging protocol overcomes the scanner variabilities shown above in section 4.1. Therefore, improving reproducibly of research results across sites. In addition, a set CT standard protocol assist in establishing CT dose guidelines [21,66].

Even though each scanner is capable of setting those CT imaging protocols parameter, each scanner did not successfully produce reasonable results. Already mentioned and shown, Figure 3.5, CT ring artefacts were seen in 4 of the 5 scanners. More importantly, one scanner failed CT calibrations with a tube voltage of 50 kVp and other voltages. Similar to PET, it is imperative CT calibrations are done correctly. To be reiterated in Chapter 5 section 1 and noted in Chapter 2, section 6 literature and general guidelines for scanner calibrations and quality control evaluations exists. For example, *Vanhove et al.* (2015) and *Osborne et al.* (2017) outline the basics of CT quality control and set out time frame for running scanner calibration and quality checks [18,64,104]. The failure of correct CT calibrations impacted this study. Thus, it will most likely impact other research study results wanting to quantify CT data. By the time of writing this thesis, scanner 5's data could only be assessed based on the default values. Multiple attempts were made by the engineer to rectify scanner 5's improper CT numbers. At that point (not part of this study), a new set of data was acquired for the site's manufacturer's engineer as all CT calibrations were failing at multiple tube voltages. Hopefully, this will be resolved prior to any quantification of CT data for research.

In section 7, results from the ionising radiation were reported. It should be noted the ion chamber CTDI measurement were chosen over using the thermoluminescent dosimeters (TLD) due to the ability of the ion chamber to measure the radiation dose over the whole body, x, y and z axis of the phantom. The ion chamber also provides an immediate real time read out of the ionisation occurring inside the chamber. The ionisation inside the chamber creates a current that is directly proportional to an ionising dose a small animal would absorb [133]. That is not to say TLDs are of no use. TLDs are an important and valid research tool for measuring and recording ionising absorbed doses, setting foundational work and continuing to do so regarding preclinical CT dose and radiation therapy [20,21,23,134,135]. The disadvantage of using them in this study was time, (TLDs are sent out to be read, not real time) and the ion chamber is more conducive to the whole body doses.

The ion chamber CTDI CT absorbed dose results indicate standardised protocols produce a reduction of the average absorbed ionised radiation received by small laboratory animals, with no image degradation. Unfortunately, the change in tube voltage to 50 kVp in scanner 1 from 40 kVp and scanner 4 from 35 kVp with increased projections (250 to 360) led to an increase in the absorbed radiation dose. The amounts measured in the mouse and rat were increased by 77% and 86% in scanner 1. Scanner 4 measured an increase of 71% and 60% in the mouse and rat, respectively. However, even with the increase in scanner 1 and 4 all measured absorbed doses are now under limits of damaging ionising radiation absorbed doses reported in the literature (<60 mGy) [19,21,136,137].

The large disparity and measured amounts of CT absorbed ionising radiation amongst sites is alarming. CT ionising radiation is known to have biological adverse effects. Clinically absorbed radiation doses have been regulated since the 1950s [138]. Overexposure of radiation will potentially cause unnecessary animal suffering and confound research outcomes [21,139]. Whether it's to be phase in or immediately implemented CT standardised protocols should be considered as a high priority. These results provide at a minimum the foundation for regulations regarding CT absorbed radiation doses. Following the NC3Rs principles refining and establishing CT protocols will reduce any potential animal suffering while reducing cumulative severity. Additionally, it will reduce the potential impact of biological responses from the radiation effect on research studies, especially in longitudinal imaging studies.

On a side note, one of the most immediate and positive outcomes of measuring CT dose was bringing awareness to each site the amount of exposure a rodent was receiving every time a CT image was acquired. Establishing ionising radiation dose guidelines is a component of CT protocol standardisation that needs greater research and discussed in Chapter 5 section 2.

9. Conclusion

Chapter 3 encompassed aim 1 and 2. Here, the standardisation aim 1 set out to determine if improved experimental design, by investigating and comparing CT acquisition parameters in different platforms, would in fact improve the precision and accuracy of imaging data sets. The second aim addressed assessing the impact and significance of different CT parameters on image quality and

quantification, while delivering the lowest doses to small animals as possible. The two question were: (1) Will standardising preclinical CT protocols across multiple scanners reduce quantitative bias in image data, while maintaining image quality? (2) Will refining preclinical CT protocols across multiple scanners reduce the CT absorbed doses to small animals while maintaining image quality and quantification? The simple and straightforward answer to both those scientific questions is yes. The analysed data from the air/water and TEM phantom both showed standardisation improves precision and accuracy in CT image results across sites. A change in ionising radiation by changing CT default protocols did not degrade the image quality between default and standard. In fact, it was slightly improved in some cases. Overall, the proposed standard CT protocol reduced radiation doses.

Chapter Four: Development of a TEM anthropomorphic rodent phantom for preclinical PET/CT imaging using 3D-printing technology

1. Introduction

Traditionally, preclinical PET/CT phantoms are used for scanner quality control assurance and calibration. This holds true clinically as well. Clinically, phantoms are also used when designing PET/CT imaging protocols. If designing a preclinical experimental imaging protocol generally small laboratory animals are used. The development of anthropomorphic TEM phantoms, by using 3D-printing materials, has the potential to replace the use of animals all together when designing and optimising preclinical imaging protocols [18,72,140–144].

The goal of this aim was and still is for the development of a tissue equivalent material (TEM) anthropomorphic rodent phantom to be used as a replacement for animals when optimising study specific PET/CT imaging protocols. Despite that, a tangent to this goal developed and discussion regarding other purposes such a phantom could be utilised for ensued. Therefore, without going into any great detail, another purpose for an anthropomorphic rodent phantom is in the field of oncology radiotherapy treatment. Preclinical radiotherapy studies are carried out using small animals, Monte Carlo simulations and more recently phantoms [23,145–149]. The development of a TEM anthropomorphic rodent phantom has proven to be feasible. Now research is expanding with greater detail to 3D printing, the material properties and anthropomorphic designs [23,148,150,151]. This subject will be brought back up in Chapter 5.

Knowing the 3D material's properties, such as the density, chemical composition, attenuation coefficients and the range or bias of measured HU using CT parameters, allows for the development of TEM 3D printed phantoms for preclinical PET/CT imaging. Understanding how the measured HU values of the 3D materials, specifically at the lower X-ray energy range of preclinical (30 – 80 kVp), correlate with actual tissue acts as a guide for the development and expansion of anthropomorphic TEM phantoms. 3D printing technologies have the ability to produce complex anatomical shapes and print

multiple materials at one time creating various layered designs. Consequently, these technologies represent a valuable tool for preclinical phantom development.

Gaining the understanding of 3D printing materials' properties using a range of X-ray energies was a necessary element of aim 3. It was the first step in sorting out 3D materials to use for printing. In order to do accomplish this, evaluating the attenuation coefficients of each material was undertaken. This involved; generating linear attenuation coefficients and the comparison between measured and calculated attenuation coefficients as well as comparison between calculated linear attenuation coefficients and tissue. From understanding the 3D material properties in relationship to X-ray energies suitable TEM materials for the development and printing of the phantom were eliminated or chosen. Finally, with the perceived optimal chosen materials a 3D TEM phantom was printed for HU analysis.

Prior to delving into the evaluation of 3D printing materials and the production of a TEM phantom a brief 3D printing background is in order, section 2 below. Section 3 will outline the concept of attenuation. By section 4 details (materials and methods) of the study will be explained. Which leaves sections 5 and 6 to reveal the results.

2. 3D printing technologies

"Absorption, diffusion, dispersion and diffraction all contribute to the difficulties of working deep within the fluid medium on any economical and reliable basis" [152]. Therefore, in 1984 Charles Hull filed and was granted patent number US4575330A, opening up the new industry of 3D printing, which today continues to grow. Hull's design/invention combined computer generated graphics with stereolithography (printing thin layers of a curable material) [152]. Though, stereolithography, is still a common method for 3D printing, many other systems have been developed for a wide range of applications using a variety of materials. For example, just in the medical field 3D printed models of human organs have been incorporated; becoming an integral component in physician teaching aids producing realistic and accurate models, and based off patient images producing surgical planning models or prosthetics [153–166].

Currently, other than stereolighography the main types of 3D printing methods are: (1) Fused Deposition Modelling (FDM), (2) PolyJet/Inkjet, (3) Digital Light Processing (DPL), and (4) Direct Metal Laser Sintering (DMLS) [167–172]. Stereolighography creates an object using a vat of a liquid resin in which a UV laser cures the resin layer by layer based on the desired computer aided design (CAD) of the object [152,172,173]. DPL also uses a vat of liquid photopolymer material, however, the 3D object is built within the vat using an arc lamp and lens/mirror to focus the light underneath the vat to cure the designed object [170–173]. FDM utilizes CAD for the design development, in which the object is built with thin threads of material, forming a support structure as it builds the 3D object bottom up [172,173]. DMLS is another system which the design is created using CAD software. The unique option in DMLS is the use of metals. Here, powder metal alloys are thinly spread on a platform and the design is cured with a laser, building up the object and support material [170–172]. The Polyjet system uses standard tessellation language (STL) or computer aided design (CAD) to develop the model design. In this case, one or more liquid photopolymer materials are simultaneous piped/jetted through a head onto the platform forming the designed object, whilst being cured with a UV laser [170–173].

There are several factors to consider when choosing a printing method; some advantages to one system over the other are the choices of materials available including the option of using multiple materials for one object. Types of materials vary from metallic materials, polymers and polymeric composites (acrylonitrile butadiene styrene, nylon, polycarbonate, polyetherimide, polyphenylsulfone, polypropylene or rubber) [174–176]. Two of the regular Polyjet materials used in medical model designs are the acrylic based photopolymers Vero Clear and Tango Black. Perks *et al.* (2015) used Vero Clear, to create a 3D printed mouse phantom. In their study they investigated the accuracy of ionising radiation dosing from a clinical linear accelerator [23]. This study demonstrated the usefulness and the ability to develop and utilize 3D printed phantoms in research, as it allowed for the refinement of electron irradiation parameters and measurements without the use of live rodents.

3. Attenuation

Expanding upon the "usefulness" of utilizing 3D printing in preclinical research for CT imaging, materials with acceptable measured HUs need to be identified. Specifically, do

the 3D printing materials sufficiently match rodent tissue HUs? Materials, such as acyclic and other polystyrene materials are already commonly used in phantoms. A prime example is the tissue equivalent material (TEM) phantom used in this study, Chapter 2. The main difference in using an anthropomorphic phantom opposed to the TEM phantom used is the multiple overlapping layers and thicknesses of the printing materials required. In the development of an anthropomorphic TEM phantom greater understanding of the attenuation of the X-ray energy through the 3D printing is a key component of its success. Hence, the emphasis on evaluating attenuation coefficients for the 3D materials and comparisons to tissue attenuation coefficients.

To reiterate from Chapter 1; linear attenuation coefficients are dependent on the energy of the X-ray beam being emitted and the material the X-rays pass through. It is the attenuation of the X-ray beam through a material (also known as a medium) that is being measured in CT imaging. The X-rays can travel through, be impacted by photoelectric absorption (photoelectric effect) or scattered mainly by Compton scattering. A diagram showing the process of Compton scattering and photoelectric absorption is shown in Figure 4.1. The diagram of the photoelectric effect (B) is as previously presented in Chapter 1, Figure 1.9. Generally speaking how X-rays (photons/electrons) interact within a medium is determined by size of the particles and energy of X-rays; low energy X-ray might interact with an atom as a whole, whereas higher energy X-ray tend to interact with tightly bound electrons or at the nuclear level. Not shown in Figure 4.1, due to inconsequential impact, is the interaction with an atom as a whole - Coherent scattering. Coherent scattering is simply a deflection off the atom with no loss of energy. Compton scattering plays a role in CT and PET. For CT Compton scattering is prevalent in lower energies, typical in the Bremsstrahlung X-ray range. In Compton scattering the electron energy is transferred from the incident electron to the scattered. The energy transferred is governed by the angle of scatter (θ). The photoelectric effect happens at higher energies, in which the initial (incident) electron energy is absorbed. Energy "absorbed" is actually transferred, causing an electron to be ejected, the incident electron to rebound and typically a Characteristic X-ray emitted.

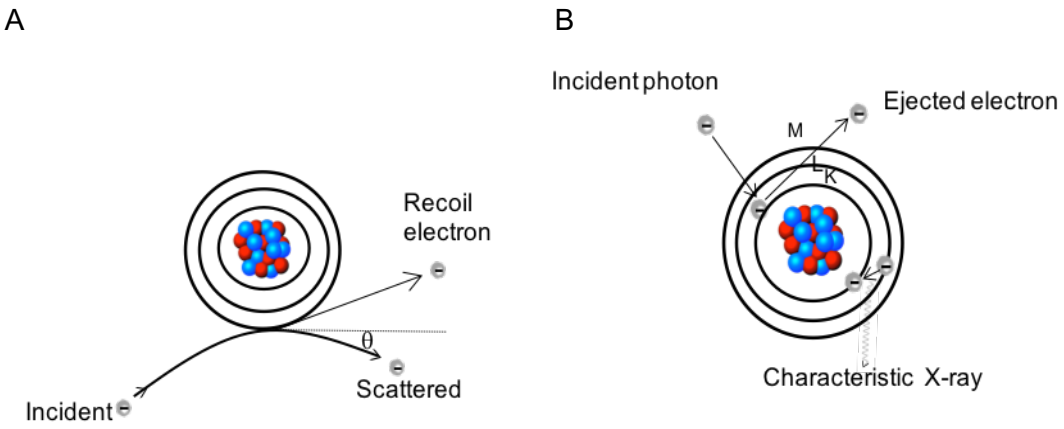

Figure 4.1:(A) schematic representing the principles of generating Compton scattering. (B) schematic representing the principles the Photoelectric effect.

In Chapter 1 the relationship between attenuation and HU was presented. The accepted HU ranges for lung, soft bone, soft tissue and cortical bone are represented in Figure 4.2.

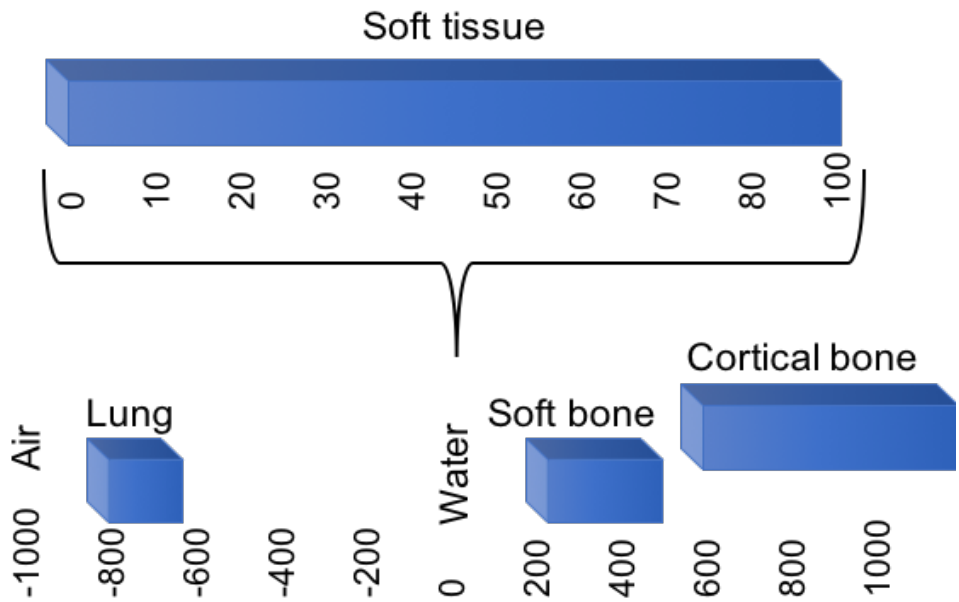

Figure 4.2: Drawing represents the ranges of accepted clinical HU values.

4. Phantom materials and methods

4.1. Background

For the initial evaluation of 3D-printing material X-ray properties a data set from a previous study of measured densities and attenuation coefficients for twenty 3D-printing materials was obtained from Dr Nick Weir from the Department of Medical Physics, National Health Service (NHS) Lothian. The data set acquired by the Medical Physic NHS study was subsequently analysed for use in this study. Sections 4.2 and 4.3 outline the NHS study as well as explain the methods used for analysis and comparisons made between tissues densities and attenuation coefficients. This is followed by introducing the process of developing a 3D anthropomorphic rodent phantom; CT imaging, data analysis, computer phantom designing.

4.2. Generation of calculated attenuation coefficients

The 3D materials from the NHS study were printed using stereolithography, in which single and blended materials of various densities were printed in slabs (150 mm x 150 mm x 5 mm). The slabs of printed materials were provided by the commercial supplier Tri-Tech 3D, UK. The calculation of the densities were done by measuring the material mass on a precision balance with the measurement of volume done using a micrometer and digital ruler. Attenuation coefficient values of varying thickness (0-150 mm) were experimentally measured using the small profile solid state radiation Raysafe Xi Transparent detector (Billdal, Sweden) with the standard clinical Philips Optimus 50 X-ray radiographic equipment (Amsterdam, Netherlands). Each material was X-rayed at 0.5, 0.7, 2.9, 5.8 and 15 cm, as represented in Figure 4.3. The measurements were taken at the X-ray tube voltage energy range of 60 to 125 kVp.

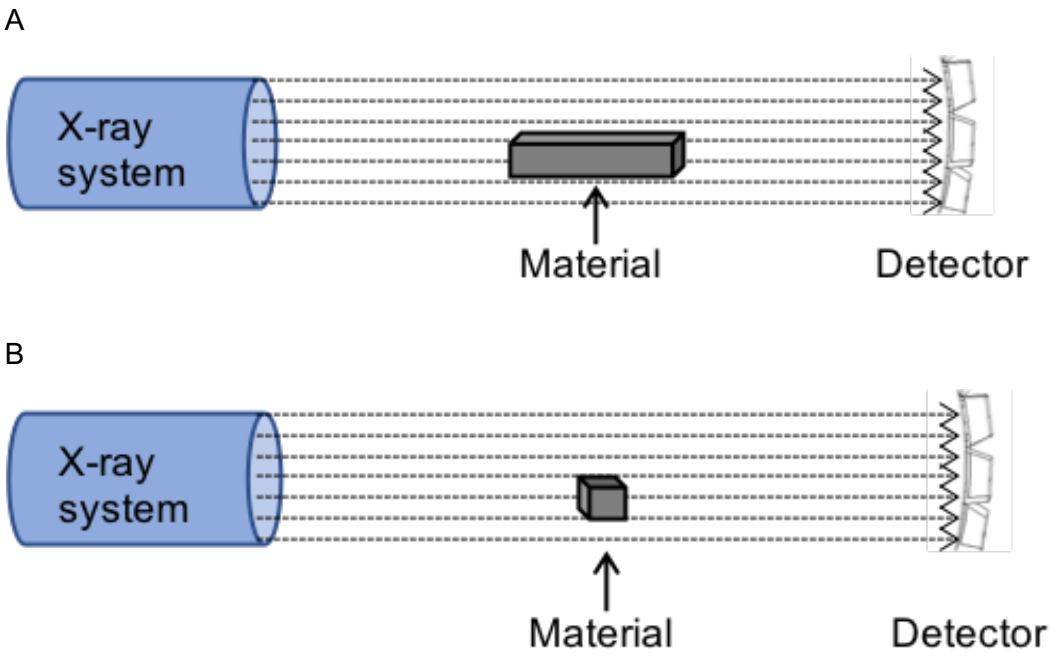

Figure 4.3: Drawing represents the Medical Physics NHS experimental design measuring each material's attenuation coefficient varying tube voltage and material thickness. The thickness of each material was varied by changing the material position, i.e. different thickness are shown in (A) and (B).

For the nine base materials out of the twenty 3D printing materials, element percent composition by mass was derived from manufacture safety sheets, X-ray Phosphorescence Spectroscopy (XPS) and Carbon, Hydrogen, Nitrogen (CHN) analysis, Table 4.1.

Table 4.1: Summary of element percent composition by mass of the nine base 3D-printing materials used in this project.

	3D-printing material chemical composition (%)								
Molecule	Endur	High Temp	MED 610	Tango Black	Tango Black Plus(M)	Vero Clear	Vero White Plus(M)	Vero White Plus(T)	Perspex
[2-[1,1-dimethyl-2-[(1-oxoallyl)oxy]ethyl]-5-ethyl-1,3-dioxan-5-yl]methyl acrylate							15		
2-Propenoic acid, 1,7,7-trimethylbicyclo[2.2.1]hept-2-yl ester, exo-	5			25	25				
2,6-Di-tert-butyl-p-cresol				0.01	0.01				
Acrylate oligomer							15		
Acrylic acid ester		0.3	0.3	0.3	0.3	0.3			
Acrylic monomer	75	55	30			30	15	55	
Acrylic Oligomer	25		15	20	70	15			
Benzyl alcohol				0.5	0.5				
Carbon black				0.1	0.1				
Citral				0.01	0.1				
Dipentene				0.1	0.1				
Epoxy acrylate							6		
Ethylbenzene				0.1	0.1				
Exo-1,7,7-trimethylbicyclo[2.2.1]hept-2-yl acrylate							25		
Geraniol				0.01	0.01				
Isoamyl acetate				0.01	0.1				

Table 4.1 (cont.): Summary of element percent composition by mass of the nine base 3D-printing materials used in this project.

	3D-printing material chemical composition (%)								
Molecule	Endur	High Temp	MED 610	Tango Black	Tango Black Plus(M)	Vero Clear	Vero White Plus(M)	Vero White Plus(T)	Perspex
Isobornyl acrylate		15	25			25		15	
n-Butyl acetate				0.1	0.1				
Phosphoric acid								0.1	
Photo initiator	5	2	2	2	2	2	5	2	
Poly(methyl methacrylate)									100
Propylene glycol monomethyl ether acetate				0.1	0.1			0.1	
Solvent naptha								0.5	
Titanium dioxide	0.8	0.8						0.8	
Urethane acrylate oligomer							30		
Xylenes				0.006	0.006				

For the calculation of X-ray data, the information in Table 4.1 was used in conjunction with the National Institute of Standards and Technology (NIST) tables of X-ray mass attenuation coefficients [177]. This was accomplished by using the X-ray mass attenuation coefficients of each constituent element known in the materials (Carbon, Hydrogen, Oxygen, Titanium, Phosphorus and Nitrogen at energies 5kV through 135kV (increments of 0.5kV) calculated with the percent per element, per element mass at each energy; using Equation 4.1 Computed results were divided by the NHS previously calculated material density, per energy value in order to obtain the calculated attenuation coefficient curves for each of the 9 materials, Equation 4.2.

$$\left[\frac{\mu}{\rho}\right]_x = \frac{[\sum_i w_i \ \mathrm{A}_i \ \left[\frac{\mu}{\rho}\right]_i]}{[\sum_i w_i \ \mathrm{A}_i]} \qquad \text{Eq. (4.1)}$$

where w_i, A_i, and $\left[\frac{\mu}{\rho}\right]_i$ represent the element percent weight in the material, element atomic weight and the mass attenuation coefficient, respectively. Mass attenuation coefficient is expressed as *g/cm*^{2}.

$$\mu = \frac{\left[\frac{\mu}{\rho}\right]_x}{\rho} \qquad \text{Eq. (4.2)}$$

where ρ is the previously calculated material density, density express as *g/cm*^{3}.

The calculated X-ray fluence spectrum was based off the known spectral characteristic of the X-ray tube in the NHS experimental set up and predetermined. The tube details for the calculated X-ray fluence were: tungsten target material, 13 degree anode angle, 0% voltage ripple; aluminium attenuating material of 3.4 mm thickness.

The calculated X-ray fluence spectrums for each material were generated by implementing the Microsoft Excel sumproduct function. This was done for X-ray energies spanning 5 keV to 135 keV, in increments of 0.5. For example, the process is shown below, using the material Endur which has 5 Carbon (C), 8 Hydrogen (H) and 2 Oxygen (O) atoms.

$$Spectrum = \frac{\left[E_1 \frac{\mu}{\rho_1} \times [\alpha_1 \times \omega_1] C\right] + \left[E_2 \frac{\mu}{\rho_2} \times [\alpha_2 \times \omega_2] H\right] + \left[E_3 \frac{\mu}{\rho} \times_3 [\alpha_3 \times \omega_3] O\right]}{[\alpha_1 \times \omega_1] + [\alpha_2 \times \omega_2] + [\alpha_3 \times \omega_3]}$$

Eq. (4.3)

E [μ/ρ] represents the attenuation value of a specific atom at that X-ray energy, α and ω represent the number of atoms and the atomic weight, respectively. Figure 4.4 shows the generated spectrum for Endur.

Using the NHS predetermined X-ray tube fluence (keV), the computed μ (cm^{-1}) values from Equation 4.2 and the material thickness (0.5, 0.7, 2.9, 5.8 and 15 cm) a calculated X-ray spectrum for the materials at each specific thickness was generated. Essentially, each calculated material's spectrum (spanning 5 keV to 135 keV), for the distinct thickness and X-ray tube voltages were computed in the following manner:

$I = I_0 e^{-\mu t}$ Eq. (4.4)

where I_0 is the predetermined X-ray fluence (keV), μ represents the calculated linear attenuation coefficient from Equation 4.2 (cm^1) and t is the distinct material thickness (cm).

In order to compare between calculated and measured attenuation coefficients, using *I* (keV) and the X-ray fluence energies the X-ray beam intensity was determined with Excel's sumproduct function for the values ranging from 5 keV to 125 keV. The beam intensity calculation was repeated for all 9 materials at 60 kVp, 70 kVp, 81 kVp, 102 kVp and 125 kVp for each thickness. Once the beam intensity was determined using the below relationship from Equation 4.4:

$ln(I_0/I)$ Eq. (4.5)

a set of calculated attenuation (μt) values at the distinct thickness for each material was calculated.

4.3. Preclinical CT acquisitions of 3D printing material

All 3D printing material samples were individually imaged using the preclinical CT parameters listed in Table 4.2 on the nanoPET/CT scanner (Mediso, Hungry). Images were acquired with the materials placed at the frontend of a mouse bed, positioned inside the bore at the isocentre, aligning sagittal, axial and coronal planes.

Table 4.2: Summary of each CT protocol used to evaluate the 3D printing material.

Protocol	Scan method	Number projections	Tube voltage (kVp)	Exposure time (ms)	Binning	Zoom	Focal spot (µm)
Low CT dose	semi-circular	360	35	170	1:16	max FOV	33
High CT dose	helical (0.5)	720	35	450	1:1	max zoom	33
Default	circular	480	50	300	1:4	max FOV	33

Newly acquired and the nine 3D printing materials listed below were imaged using the developed CT standard protocol, Table 4.3. Figure 4.4 is an example of 5 different 3D printing materials; hard to rubber consistency. Image shows three varieties of Vero, Perspex and Tango Black.

<u>New materials used:</u>

Tango Plus FLX (930), Vero Black Plus RGD (840), Vero Blue RGD (835), Vero White Plus RGD (835)

<u>Original materials used:</u>

Endur, Heart Print Flex, High Temp, MED 610, Perspex, Tango Black Tango Black Plus (M), Vero Clear and Vero White Plus (M)

Table 4.3: Developed standard CT protocol used for evaluation of HUs.

Protocol	Scan method	Number projections	Tube voltage (kVp)	Exposure time (ms)	Binning	Zoom	Focal spot (μm)
Standard	circular	360	50	300	1:1	max	33

All acquired CT images were reconstructed with FBP and analysed using PMOD image analysis software (PMOD Technologies, Switzerland). A VOI (1.33 mL) was created for systematic placement on each material. This VOI was placed on the centre most area to extract the mean HU values (Figure 4.4F) for each material slab. Quantification accuracy was defined as bias between measured 3D-printing material's HU relative to known HU for tissue, based on Table 3.4, Chapter 3 and accepted tissue HU per literature [71].

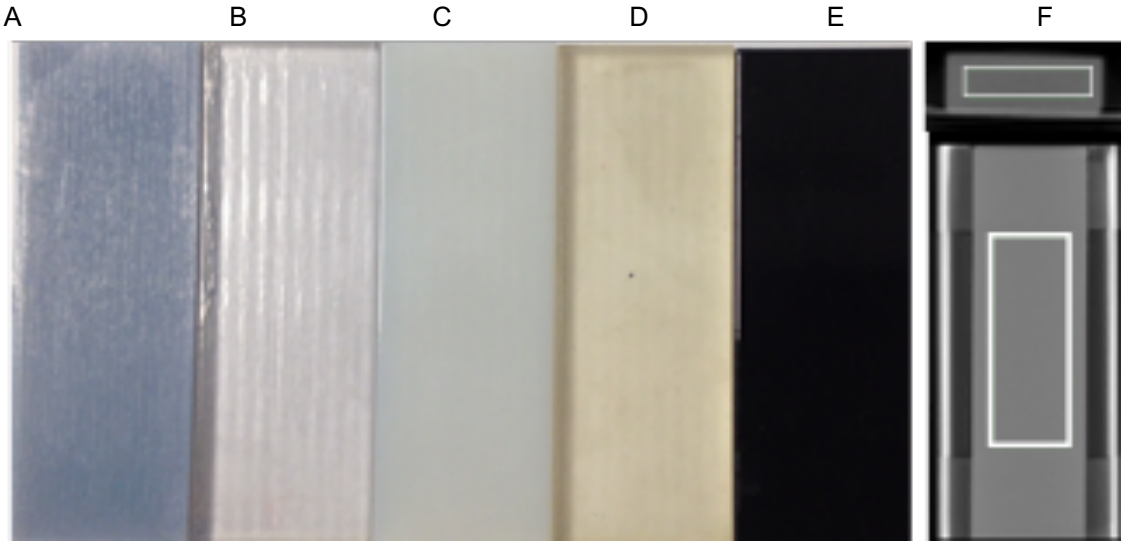

Figure 4.4: Photographs of selected 3D-printing materials used in this study. (A) Vero Blue (B) Perspex, (C) Vero Clear, (D) Vero White and (E) Tango Black. From A to E there is a change in material density. Panel (F) is a representative image (axial and coronal planes in display) showing VOI placement on the CT acquisition for each material for HU measurements (F).

4.4. Process of developing a 3D printed anthropomorphic rodent phantom

A CT acquisition of a scheduled 1 adult male Sprague-Dawley rat was exported into OsiriX v.7.0 (Bernex, Switzerland). OsiriX's 3D volume and surface rendering tools were used for creating several 3D renderings; skeletal and whole body for references. The rodent's brain, heart, liver, kidney and lungs were imaged separately and exported in the same manner. All files were reconstructed with FBP and converted from DICOM to STL

files for exporting into Rhinoceros version 5.3.2 3D CAD software, (Seattle, WA USA). The STL files imported into CAD are mesh (polygons representing the geometric surface) files. This file format is essentially the surface geometry of a 3D object, created by the tessellation process of using overlapping triangles and interlocking triangular surfaces which cannot always be distinguished. This causes the removal and cleaning of unwanted surfaces and artefacts difficult. The CAD software is used to edit the STL mesh files. This process entails: (1) editing and separating out the scanner bed, (2) removing artefacts, (3) rebuilding tessellation surfaces, (4) filling holes, (5) aligning tessellation vertexes and (6) scaling the design. Figure 4.5 outlines the process, whilst Figures 4.6 through 4.11 display images of the process.

The prepared CAD files were used for 3D printing with a Stratasys Objet 260 Connex 3D printer (Los Angeles, CA USA). The Connex printer simultaneously prints two polypropylene polymer materials, thus, allowing for the use of different whole body and organ materials. The phantom was designed with a void for lungs and a calcium hydroxyapatite (CaHA) skeletal insert.

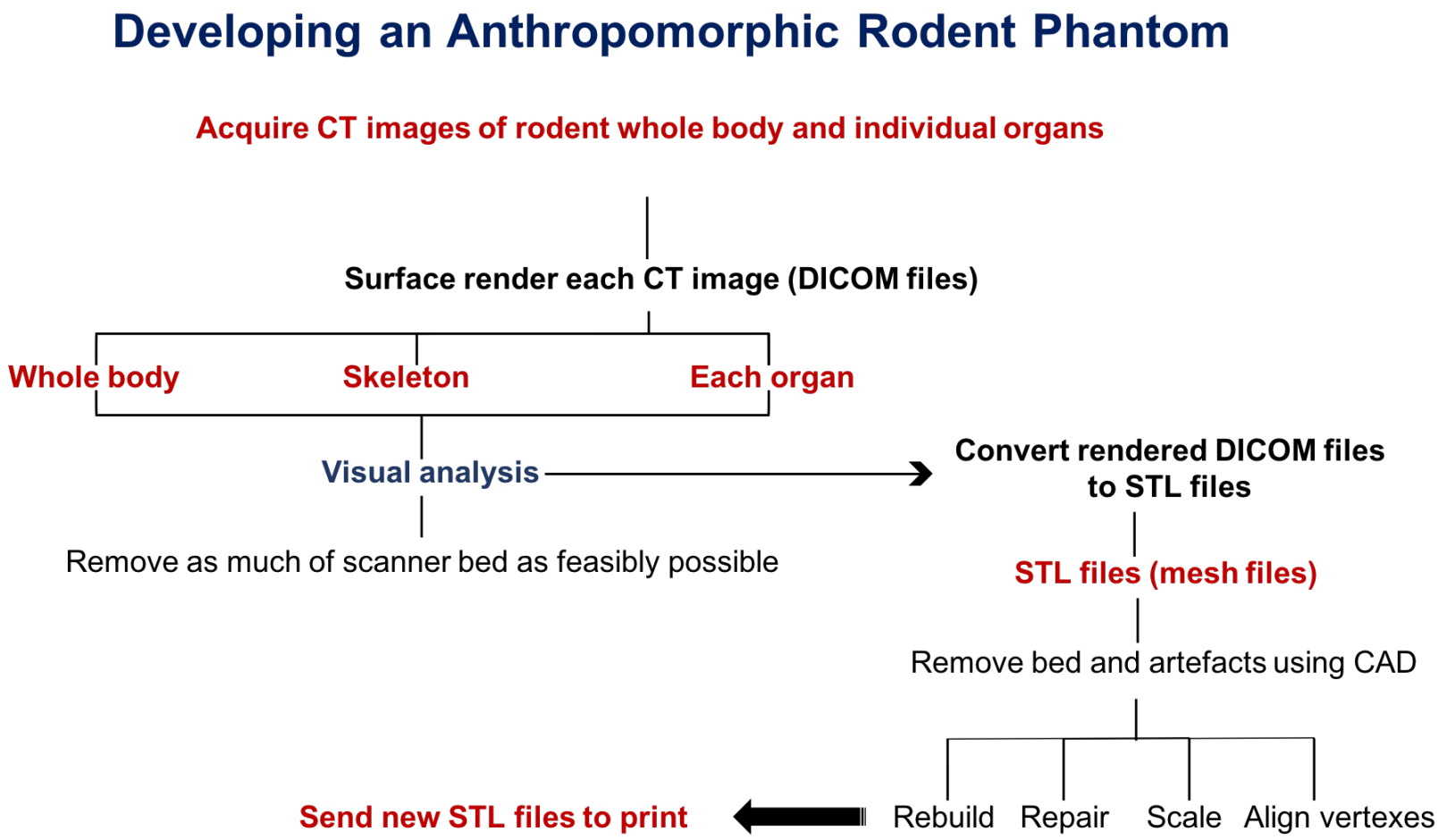

Figure 4.5: Flow chart representing the approach/process of image data analysis: CT acquisitions, surface rendering of DICOM files, conversion to SLT, export to CAD. for 3D printing preparation.

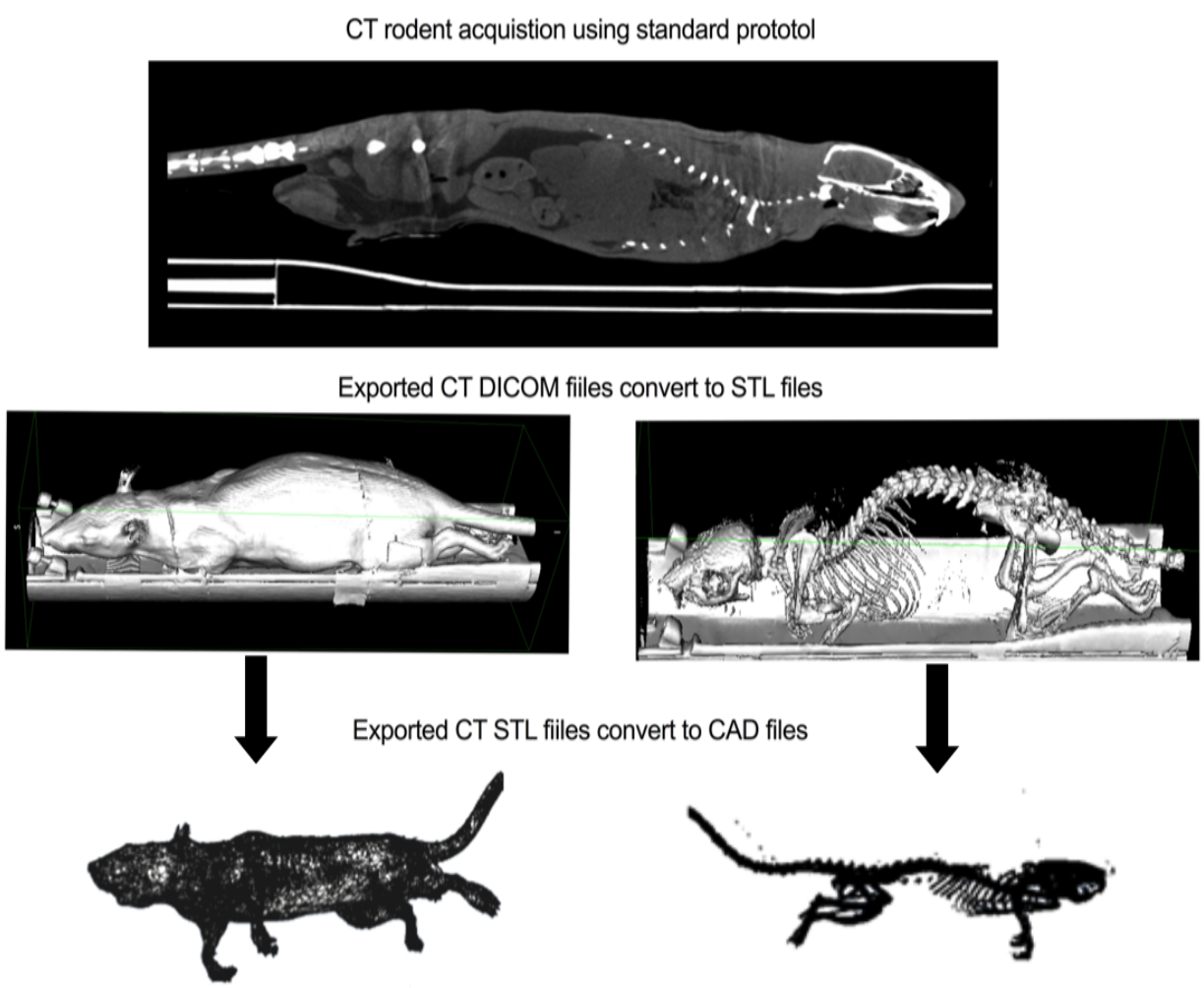

Figure 4.6: Images showing rodent CT acquisition, surface rendered whole body and skeleton to image of whole body and skeleton in CAD software prior to any repairs.

After the bed is removed the process of editing, removing artefacts and rebuilding begins. Figure 4.7 illustrates this process, showing the removal and rebuilding. The skeleton required minimal rebuilding after being removed from the body, shown in Figure 4.8. As an example of the internal organ rebuilding, Figure 4.9 displays the brain and heart before and after editing. For a close up view of the issues faced in preparing the files Figure 4.10 shows the before and after versions of the head and abdomen section of the rat. The final figure in this process shows the completed whole body and a split of the body. The splitting of the CAD file was necessary in order to have the lungs as a void. When the files are printing the whole printed product is supported by a scaffolding material. This includes any internal void. Therefore, the only way to remove the scaffolding material was to split the files. It should be noted that the scaffolding material was X-rayed for HU measurements. These HU measurements were deemed to be unacceptable for lung, thus the scaffolding material was removed.

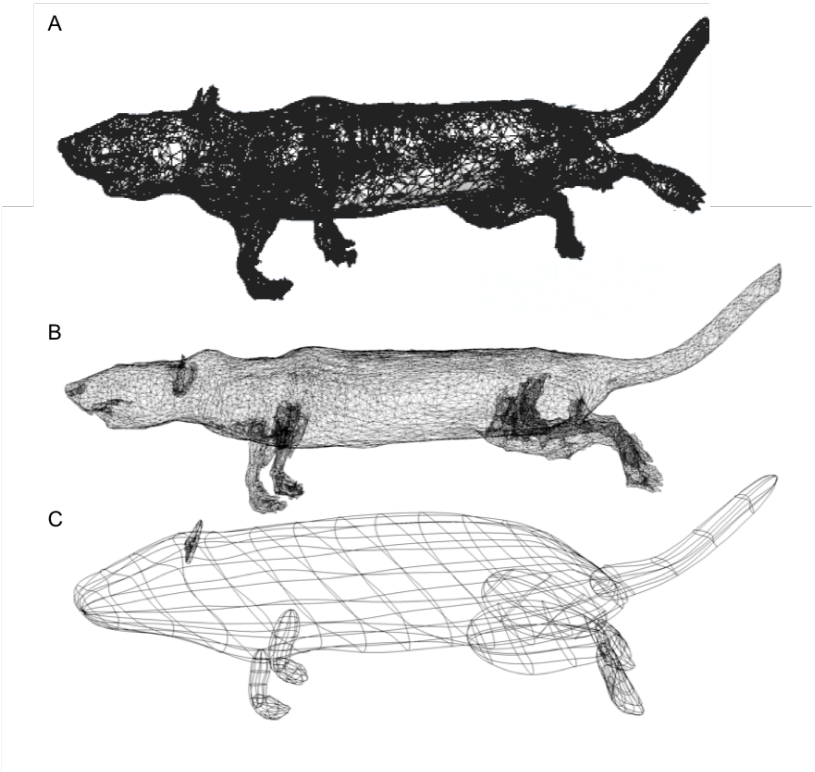

Figure 4.7: Shows the STL files as seen in the CAD software. Panel (A) displays the mesh file voids/holes, overlapping surfaces and artefacts. Panel (B) represents the beginning process of removing artefacts and repairing. Panel (C) shows the outlined version of the cleaned file.

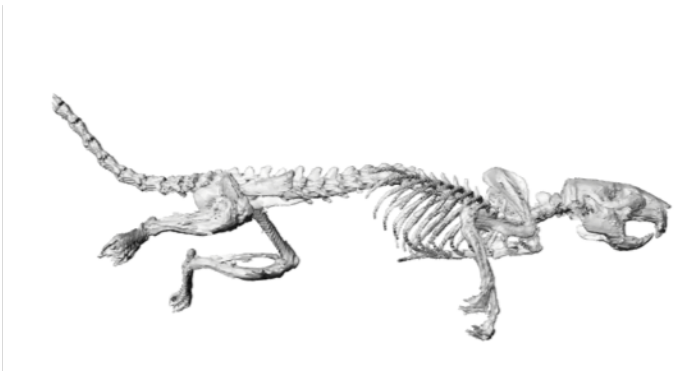

Figure 4.8: The skeleton after being removed from the whole body is shown at its final stage for printing. The 3D printing of the skeleton file is done in the whole body and separately.

A B

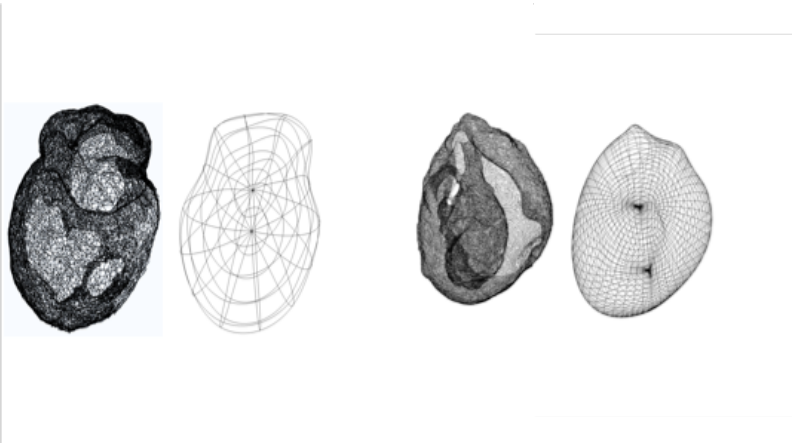

Figure 4.9: Similar to Figure 4.7, Panel (A) represents the beginning process of removing artefacts, repairing and rebuilding for the brain. Panel (B) shows the same for the heart.

A before after B before after

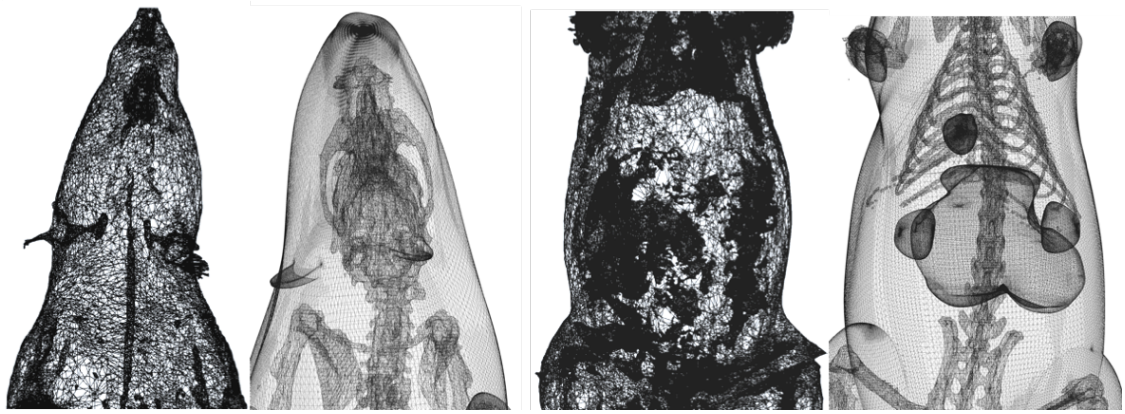

Figure 4.10: Shows the STL files as seen in the CAD software and the fully repaired version. Both panel (A) and (B) are zoomed in views. Panel (A) is the close up of the head showing the striking difference before and after file repairs. The same is true for the abdomen in panel (B).

With all the files rebuilt (whole body, skeleton and all organs) the mesh files were then merged, scaled and split for printing, as shown in Figure 4.11. Each half of the phantom is printed separately.

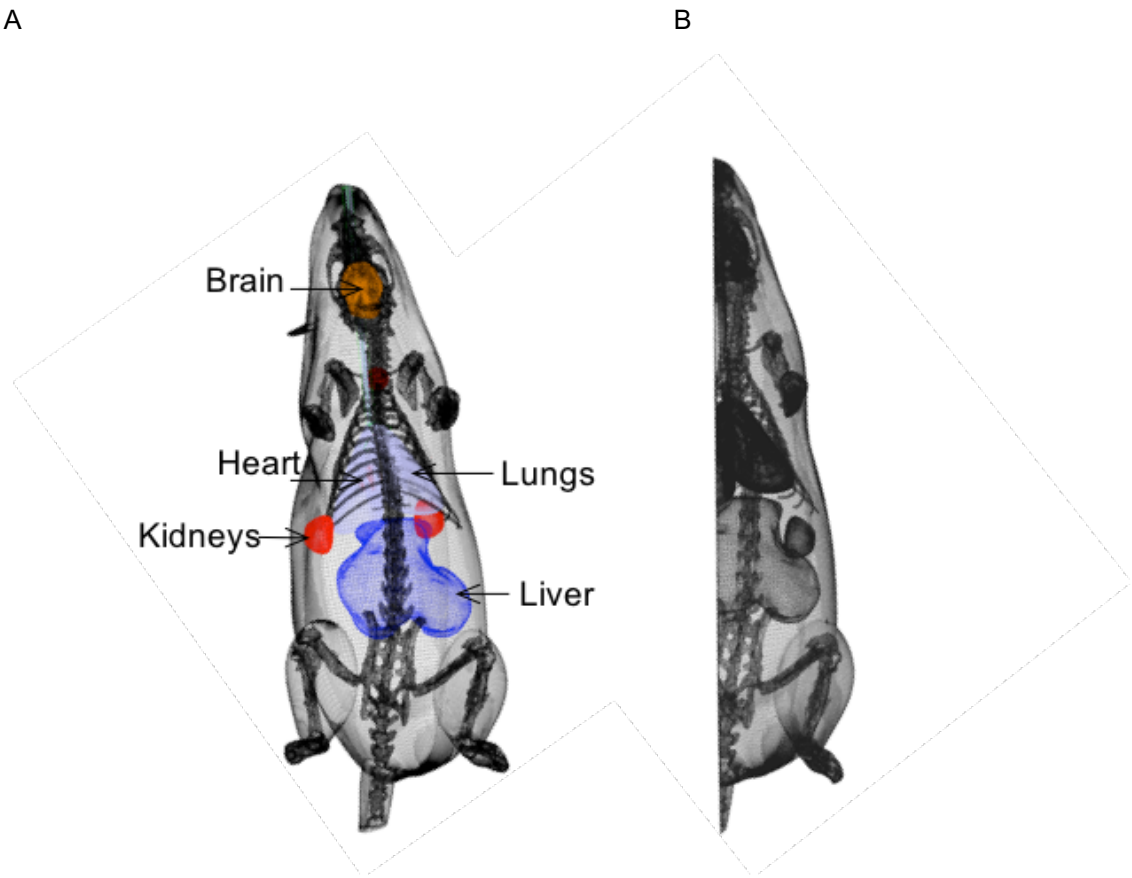

Figure 4.11: Image from the CAD software showing the mesh file repaired, rebuilt, cleaned and all vertexes aligned for printing. The phantom whole body with internal organs and skeleton can clearly be seen in panel (A). Panel (B) shows the split which allows for the removable of scaffolding material in the lungs.

4.5 Printing and CT acquisitions of the TEM anthropomorphic phantom

Two prototype phantoms were initially printed on the Connex 3D printer. The first phantom was printed simply for printing design feasibility using Vero Clear for the body, Vero White Plus (M) for the internal organs and without the skeleton. The second printed phantom was split (each half printed separately) and used for HU analysis. This phantom was a combination of Tango Black Plus (M) for the body, voids for lungs and Vero White Plus (M) for brain, heart, liver, kidneys and skeleton. A CaHA capsule for HU analysis was placed in one of the lungs during imaging. Using Vero Clear, the skeleton was also

printed separately for design testing and assessment of the practicality of using a hydroxyapatite filler material, (CaHA capsule placed next to lung during imaging).

Each phantom was placed at the frontend of the scanner bed as if it were a real rodent, positioned inside the bore at the isocenter, aligning sagittal, axial and coronal planes. All CT acquisitions were reconstructed using the FBP method. Images were acquired using the different CT protocols listed in Table 4.2 as well as the standard CT protocol listed in Table 4.3. These protocols are representative of (1) a CT low ionising dose, (2) a CT high ionising dose, (3) the scanner default and (4) the developed CT standard protocol. Reconstructed images from the second phantom prototype were exported to PMOD for HU analysis. VOIs were placed on the brain, heart, lung, CaHA capsule, both kidneys and liver, Figure 4.12. The same VOIs were placed on an imaged scheduled 1 adult male Sprague-Dawley rat for an additional preliminary HU comparison between the 3D materials and the phantom. As in previous HU analysis, quantification accuracy was defined as bias between measured HU relative to known HU for tissue, based on Table 3.4, Chapter 3 and accepted tissue HU per literature [71].

A B C

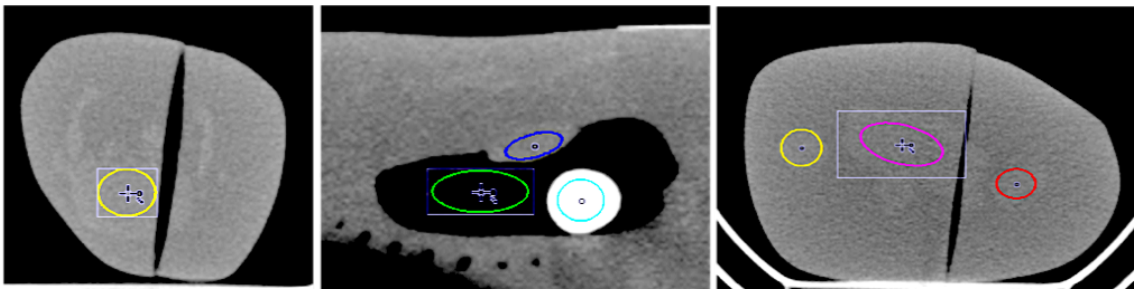

Figure 4.12: PMOD screen shot showing the VOI placement on the CT acquisition on the Tango and Vero Clear 3D printing phantom. Panel (A) is the placement on the brain, panel (B) displays the placement for the lung (green), heart (dark blue) and CaHA capsule (light blue) and panel (C) shows the liver (pink) and both kidneys (orange and red).

5. Analysis of 3D printing materials

5.1. Calculated X-ray attenuation coefficient curves

Presented below in Figure 4.13 are the generated attenuation coefficient curves for all nine 3D-printing materials. As the X-ray tube voltages increased the distinction between the different 3D-printing materials became difficult.

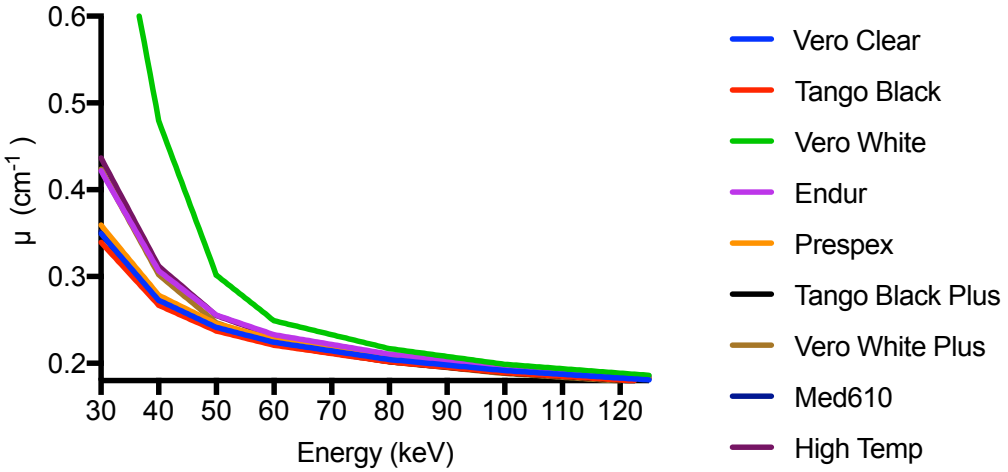

Figure 4.13: Calculated attenuation coefficient curves for all nine 3D-printing materials. Though values were calculated from 5 keV to 135 keV displayed is 30 keV to 120 keV for visual distinction between materials.

5.2. Calculated X-ray fluence spectrums

Figure 4.14 displays the generated X-ray fluence spectrum for the material Endur at each voltage. Clearly seen are the characteristic peaks for the L and K shells as well as the Bremsstrahlung at the lower X-ray energies.

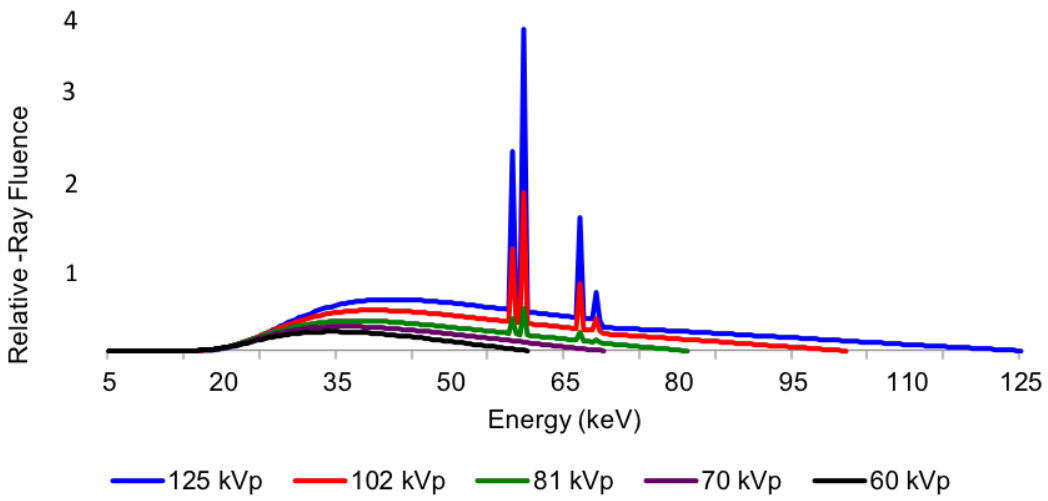

Figure 4.14: Material Endur calculated X-ray fluence spectrum. Data presented as the distribution of the number of photons as a function of their energies.

Evaluating the calculated spectrums by material thickness and energy shows the familiar X-ray spectrum, Figure 4.15 at a tube voltage of 125 kVp. However, as seen in Figure 4.16 the spectrums display more of the Bremsstrahlung X-rays at the lower X-ray tube voltages and with decreased thickness. The spectrums in Figure 4.16 represent each X-ray tube voltage used for all five different thicknesses. The spectrums of the remaining eight 3D printing materials are shown in Appendix 5.

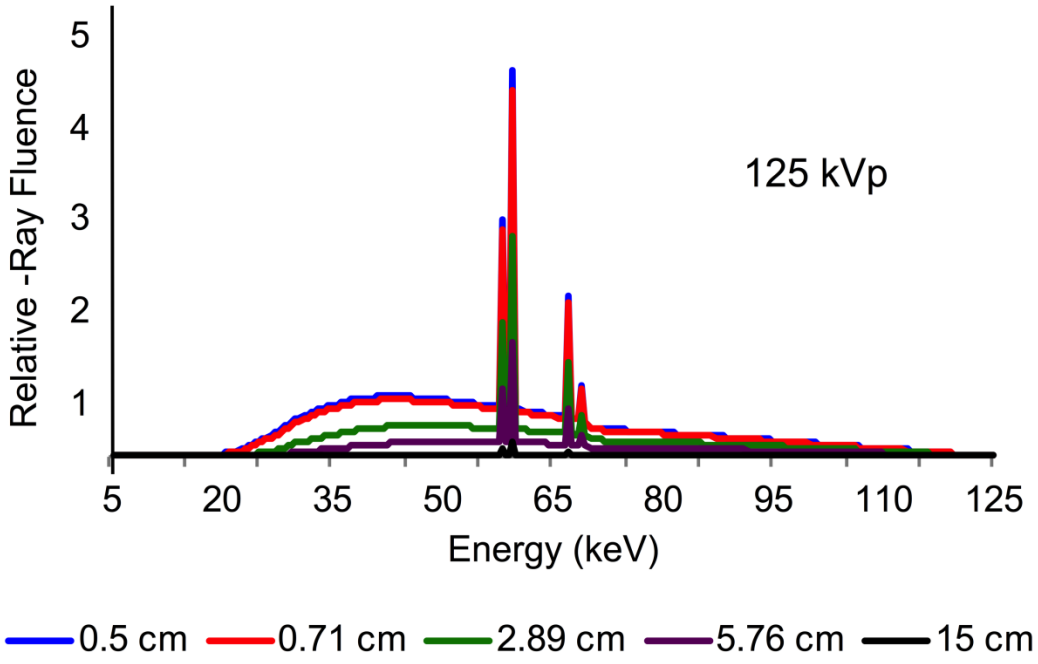

Figure 4.15: Material Endur calculated spectrum at the X-ray tube voltage of 125 kVp, shown per material thickness.

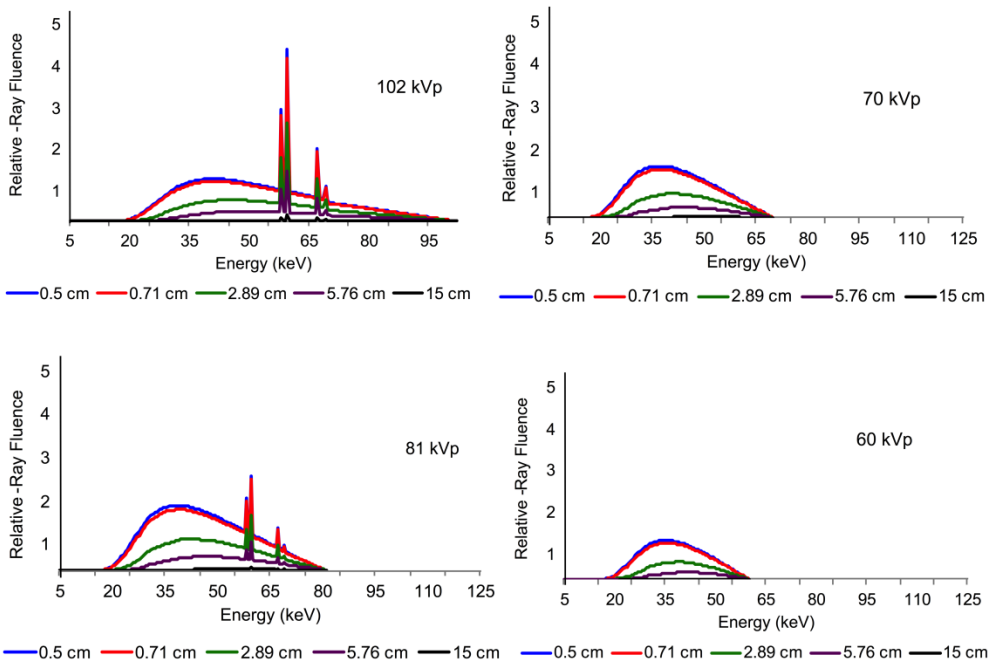

Figure 4.16: Spectrums of the material Endur showing X-ray tube voltage of 102 (A), 81 (B), 70(C) and 60 (D) kVp for the 5 different thicknesses (cm) in which a measurement was obtained, with Bremsstrahlung X-rays clearly dominating at the lower energies.

5.3. Comparison of measured and calculated attenuation coefficients

The calculated attenuation coefficients for nine 3D-printing materials were compared with the previously measured attenuation coefficients from the NHS study. Generating the analysis for comparison between the measured values and the calculated, required using equation 4.4 for each material at each thickness, then again for each tube voltage used (125 kVp, 102 kVp, 81 kVp, 70 kVp, 60 kVp). To reiterate, Equation 4.4.

$$I = I_0 e^{-[\mu]t} \qquad \text{Eq. (4.4)}$$

Therefore, to calculate I (keV) , the predetermined X-ray fluence I_0 (keV) was used with each material's calculated μ (Eq. 4.2) at each thickness used in the NHS study. Thus, giving I and I_0. From Equation 4.5 ($\ln(I_0/I)$) the calculated attenuation values were determined for comparison with the measured. An example calculation process is shown in Table 4.4 using the material Endur. Each material, thickness and tube voltage was analysed and graphed. The measured attenuation coefficients are distinct values, whereas the calculated attenuation values are graphed as a continuous X-ray spectrum to show matching to the measured and linearity (0 to 15 cm).

Table 4.4: Acquired measured (Medical Physics NHS study) and calculated attenuation for Endur at 125 kVp for each thickness. Table displays the process, steps per thickness for obtaining calculated ln(I_0/I) to compare with measured ln(I_0/I).

Material thickness (cm)	NHS measured attenuation ln(I_0/I)	Predetermined X-ray fluence I_0 (keV)	Calculated X-ray fluence per thickness I (keV)	Calculated (Io/I)	Natural log calculation ln(I_0/I)
0.00		409144887	409144887	1	0
0.50	0.14	409144887	360867474.9	1.13	0.13
0.71	0.20	409144887	342702357.8	1.19	0.18
2.89	0.76	409144887	201411198.4	2.03	0.71
5.76	1.32	409144887	102174712.3	4.00	1.39
15.00	2.09	409144887	12518330.18	32.68	3.49

Figure 4.17 displays the relationship between the calculated attenuation coefficients and the measured attenuation coefficients with a tube voltage of 125 kVp at each thickness, for the material Endur.

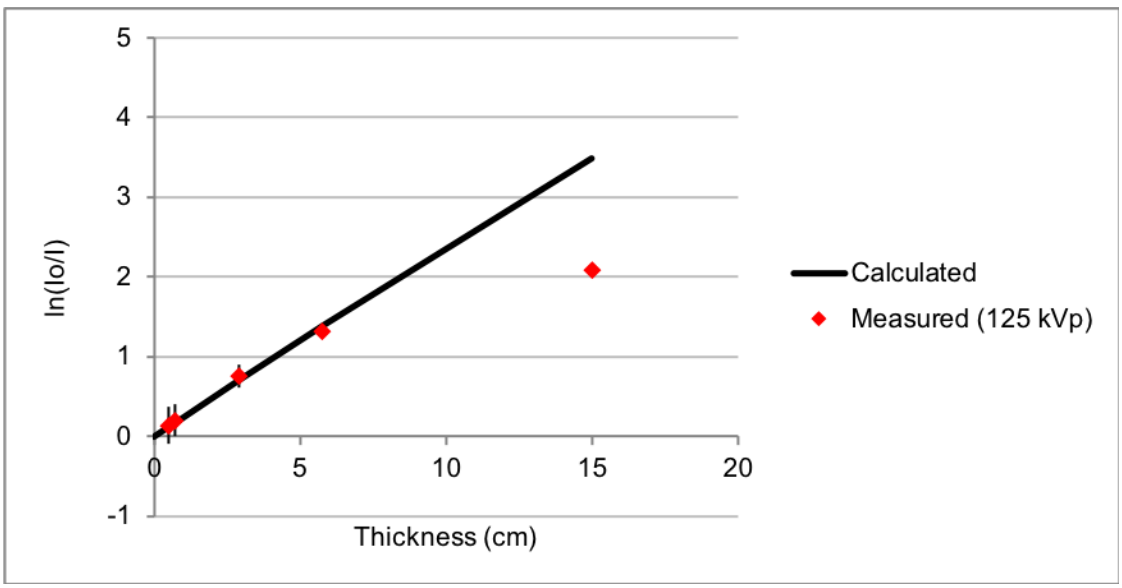

Figure 4.17: Comparison of calculated 3D material Endur at the X-ray tube voltage 125 kVp to each measured output at the defined thicknesses (0.5, 0.7, 2.9, 5.8 and 15 cm).

As noted above, comparison graphs between calculated attenuation and the measured attenuation for all nine 3D printing materials were generated at the designated tube voltages. Shown below in Figure 4.18 are the remaining graphs for the material Endur, displaying the results from the distinct tube voltages of 102 kVp, 81 kVp, 70 kVp and 60 kVp. The results from the remaining materials are presented in Appendix 6.

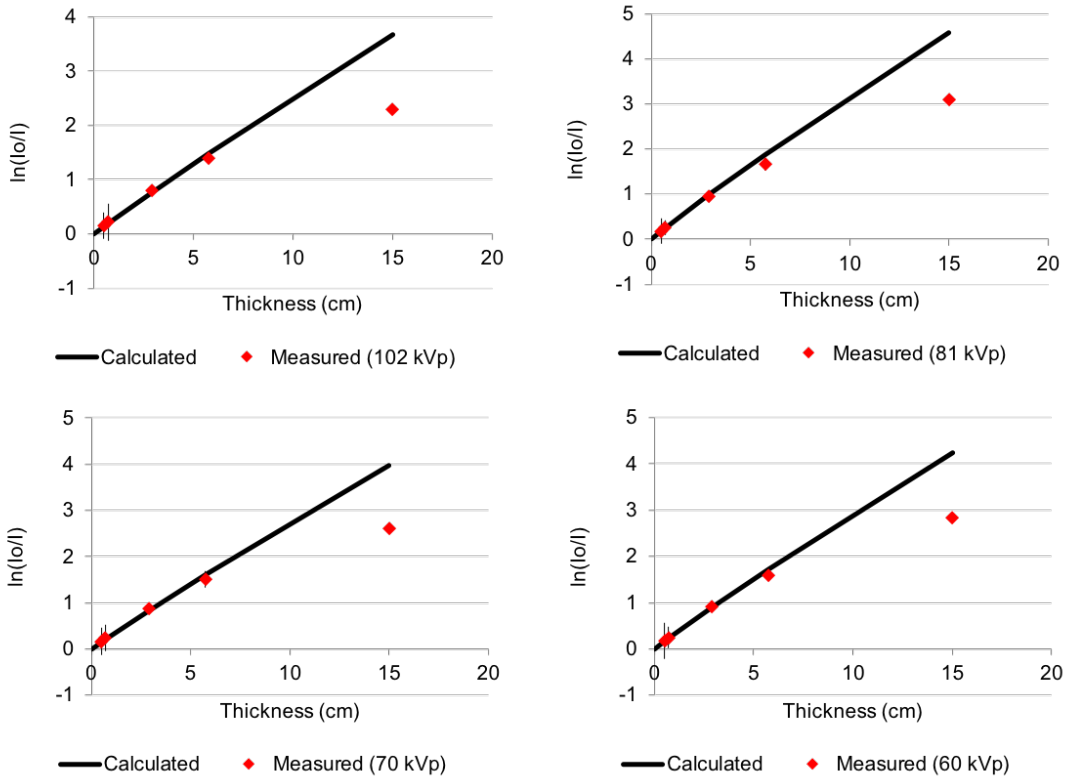

Figure 4.18: Comparison of calculated 3D material Endur at the X-ray tube voltage of 102, 81, 70 and 60 kVp to each measured output at the defined thicknesses (0.5, 0.7, 2.9, 5.8 and 15 cm).

It should be noted that the measurement for all the materials at all the voltages for the thickness of 15 cm is consistently below the calculated values. This is believed to be an experimental set up error when imaging the materials for 15 cm. The slabs were arranged at various angles to achieve the desired thicknesses; it is possible that the 15 cm set up did not allow for the proper detection of the emitted X-rays. The thickness of 15 cm is not practical owing to the typical thickness of rodents used in preclinical research. Therefore, the NHS experimental design was not repeated. The percent difference between the calculated and measured attenuation coefficient values were also tabulated. Table 4.5 displays the percent differences calculated for the material chosen for further use, remaining data tables are in Appendix 7.

Using Equation 2.1 defined in Chapters 2 and 3, the 3D material Vero White displayed the greatest difference between measured and calculated data, with percent differences

above 30% and as high as 71%. However, after discussions with the commercial supplier, Tri-Tech 3D, UK, the large discrepancy was deemed to be due to the poor quality of the actual printing, not the material. Overall the results indicated that the materials performed reasonably well.

Table 4.5: Measured and predicted attenuation coefficients values along with the percent difference from calculated to measured are shown for Endur, Tango Black Plus, Vero Clear and Vero White Plus, per tube voltage per thickness.

Thickness (cm)	Measured ln(Io/I)	Calculated ln(Io/I)	Percent Difference (%)	Measured ln(Io/I)	Calculated ln(Io/I)	Percent Difference (%)	Measured ln(Io/I)	Calculated ln(Io/I)	Percent Difference (%)	Measured ln(Io/I)	Calculated ln(Io/I)	Percent Difference (%)	Measured ln(Io/I)	Calculated ln(Io/I)	Percent Difference (%)
Endur	125 kVp			102 kVp			81 kVp			70 kVp			60 kVp		
0.5	0.14	0.13	-10	0.15	0.13	-12	0.17	0.15	-13	0.17	0.16	-8	0.18	0.18	-1
0.7	0.2	0.18	-14	0.22	0.19	-15	0.24	0.21	-15	0.25	0.23	-9	0.26	0.25	-5
2.9	0.76	0.71	-7	0.81	0.76	-7	0.87	0.83	-5	0.91	0.9	-1	0.96	0.98	2
5.8	1.32	1.39	5	1.4	1.47	5	1.51	1.61	6	1.58	1.73	8	1.67	1.88	11
15	2.09	3.49	40	2.3	3.68	37	2.6	3.97	35	2.83	4.24	33	3.09	4.59	33
Tango Black Plus	125 kVp			102 kVp			81 kVp			70 kVp			60 kVp		
0.5	0.12	0.12	-6	0.13	0.12	-6	0.14	0.13	-8	0.15	0.14	-9	0.16	0.15	-5
0.7	0.18	0.16	-8	0.19	0.17	-11	0.21	0.19	-14	0.22	0.2	-9	0.23	0.22	-8
2.9	0.62	0.66	6	0.66	0.7	5	0.71	0.75	5	0.75	0.8	7	0.78	0.86	9
5.8	1.28	1.3	2	1.38	1.37	-1	1.49	1.48	-1	1.57	1.57	-1	1.66	1.68	1
15	2.58	3.31	22	2.78	3.47	20	3.06	3.71	18	3.26	3.92	17	3.49	4.17	16

Table 4.5 (cont.): Measured and predicted attenuation coefficients values along with the percent difference from calculated to measured are shown for Endur, Tango Black Plus, Vero Clear and Vero White Plus, per tube voltage per

Thickness (cm)	Measured ln(Io/I)	Calculated ln(Io/I)	Percent Difference (%)	Measured ln(Io/I)	Calculated ln(Io/I)	Percent Difference (%)	Measured ln(Io/I)	Calculated ln(Io/I)	Percent Difference (%)	Measured ln(Io/I)	Calculated ln(Io/I)	Percent Difference (%)	Measured ln(Io/I)	Calculated ln(Io/I)	Percent Difference (%)
Vero Clear	125 kVp			102 kVp			81 kVp			70 kVp			60 kVp		
0.5	0.13	0.12	-12	0.14	0.12	-14	0.16	0.13	-16	0.16	0.14	-13	0.17	0.15	-12
0.7	0.19	0.17	-15	0.21	0.18	-19	0.23	0.19	-19	0.23	0.2	-16	0.24	0.22	-13
2.9	0.69	0.67	-4	0.73	0.7	-4	0.79	0.76	-4	0.83	0.81	-3	0.87	0.86	-1
5.8	1.39	1.32	-5	1.48	1.38	-7	1.6	1.49	-7	1.68	1.58	-7	1.9	1.68	-13
15	2.48	3.35	26	2.68	3.51	24	2.95	3.74	21	3.17	3.95	20	3.41	4.19	19
Vero White Plus	125 kVp			102 kVp			81 kVp			70 kVp			60 kVp		
0.5	0.13	0.12	-11	0.15	0.13	-12	0.16	0.15	-10	0.17	0.16	-5	0.18	0.18	-3
0.7	0.2	0.17	-15	0.21	0.18	-16	0.23	0.21	-13	0.24	0.22	-9	0.26	0.25	-4
2.9	0.71	0.69	-3	0.75	0.73	-3	0.81	0.81	0	0.85	0.88	4	0.9	0.97	7
5.8	1.46	1.34	-9	1.56	1.43	-9	1.69	1.57	-8	1.78	1.69	-5	1.85	1.85	0
15	2.59	3.36	23	2.82	3.55	21	3.16	3.85	18	3.4	4.12	18	3.69	4.49	18

5.4. Comparison between calculated linear attenuation coefficients and known tissue attenuation coefficients

Graphs were generated in order to assess the correlation between derived calculated linear attenuation coefficients and accepted human tissue linear attenuation coefficients, (Figures 4.19 through 4.21). The tissue attenuation coefficients were taken from NIST data tables [178].

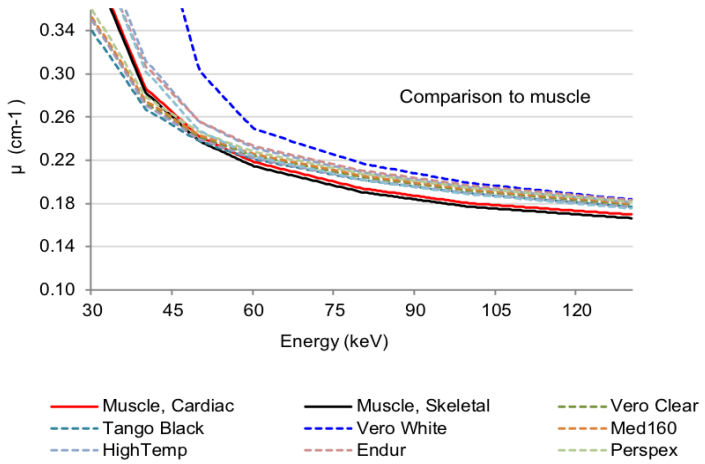

Figure 4.19: Comparison of calculated material linear attenuation coefficients to accepted muscle tissue attenuation coefficients. Strong correlation between calculated and accepted is seen at energies above 75 keV and less so as the energy decreases.

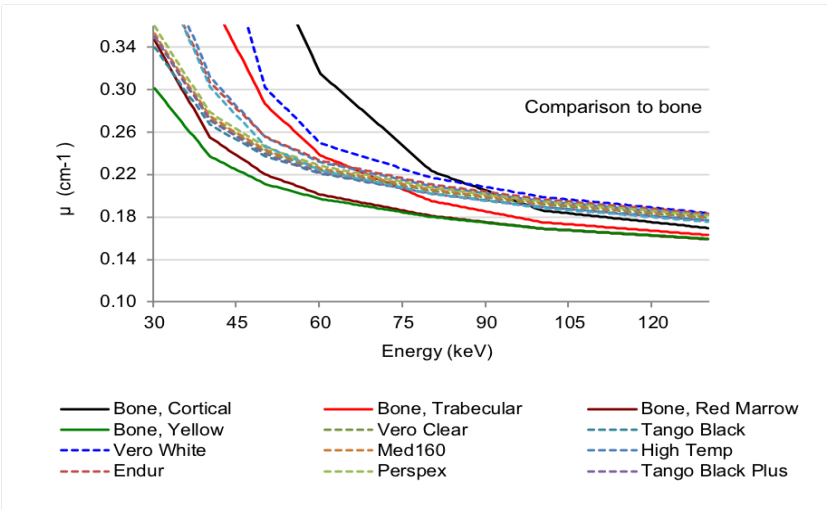

Figure 4.20: Comparison of calculated material linear attenuation coefficients to accepted bone attenuation coefficients. A decent correlation between calculated and accepted is seen at energies above 90 keV but substantial differences are seen less than 90 keV.

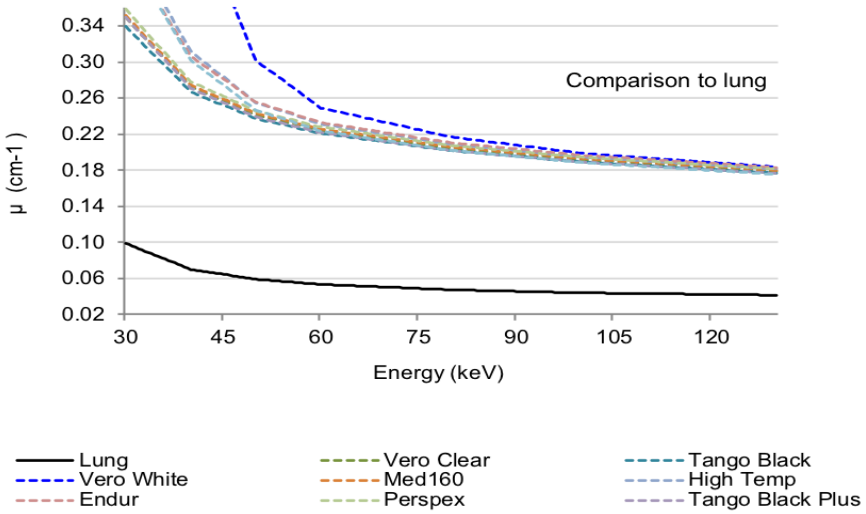

Figure 4.21: Comparison of calculated material linear attenuation coefficients to accepted lung tissue attenuation coefficients. Clearly evident, no material displayed a close similarity to lung.

The calculated curves for all materials aligned well with muscle. Though the calculated curves correlate with cortical or trabecular bone at energies above 90 keV, notably there are substantial differences under 90 keV. However, result shown in Figure 4.19 and Figure 4.20 demonstrate that energy ranges below 80 keV still correlate well with soft tissue and soft bone. As seen above in Figure 4.21, none of the 3D materials were remotely similar or equivalent to lung.

6. Analysis of 3D printing materials imaged using preclinical X-ray tube voltages and the printed phantom

6.1. Measured HU evaluation of 3D printing materials

Table 4.6 displays the results for nine materials at the four CT acquisition protocols. HU values for the 3D printed materials at these lower X-ray energy measurements were similar to the diagnostic clinical energy range, with the majority measuring well within the soft tissue range.

3D-printing materials Endur yielded the highest (62 HU to 230 HU) and Tango Black Plus(T) the lowest (-53 HU to -60 HU) HU values. Using the high dose

protocol, all measured HU values were in line with the expected HU values for soft tissue, while 16 out of 20 and 19 out of 20 measured HU values were in line with the HU soft tissue values for low dose and the default CT protocol, respectively. Evaluations of other materials are shown in Appendix 8.

Table 4.6: Measured HU values for nine 3D printing materials, acquired using four different preclinical CT protocols.

CT Protocol	Measurement	Endur	Heart Print Flex	High Temp	MED610	Perspex	Tango Black	Tango Black Plus(M)	Vero Clear	Vero White Plus(M)
Low Dose	Average	229.93	104.6	169.13	67.3	-44.1	69.44	-14.88	119.41	169.79
	Standard Deviation (%)	78.05	235.55	285.78	58.73	34.67	63.5	85.71	56.29	56.73
High Dose	Average	87.64	-29.16	75.45	-20.01	-11.03	-5.72	-45.01	8.33	55.98
	Standard Deviation (%)	78.84	82.36	78.14	73.64	81.22	76.24	77.48	79.67	80.47
Default	Average	62.19	-65.38	44.17	-19.35	-48.2	-29.05	-158.04	-20.24	17.03
	Standard Deviation (%)	20.11	55.07	49.13	20.19	21.88	19.91	78.49	23.36	24.70
Standard	Average	39.27	-41.94	-18.28	-16.70	-31.80	-24.41	-38.60	-17.23	22.12
	Standard Deviation (%)	23.91	22.53	67.15	22.76	22.05	22.82	22.32	23.25	24.15

6.2. Measured HU evaluation of 3D printed TEM anthropomorphic phantom

Based on the comparison analysis between tissue and material HU as well as the availability of the 3D printing materials Tango Black Plus (M), Vero Clear and Vero White Plus (M) where chosen for the prototype printings. All were within a similar soft tissue range, shown in Table 4.7 and available. Vero White Plus (M) and Tango Black Plus (M) also served as "different" soft tissues values.

Table 4.7: 3D printing material and HU used for printing TEM anthropomorphic phantom. CT acquisition was done using the standard preclinical CT protocol.

Material	Material density (g/mL)	Average HU	Standard deviation
Tango Black Plus (M)	1.164	-38.60	22.32
Vero Clear	1.175	-17.23	23.25
Vero White Plus (M)	1.149	22.12	24.15

Excluding the printed prototype, the decision to begin with Tango Black Plus (M) and Vero White Plus (M) was based on the idea of using two materials with a substantial difference in HU values. Under the same conditions, Tango Black Plus (M) has a measured HU of -38.60 whilst Vero White Plus (M) has a measured HU of 22.12. Therefore, even though both would be considered soft tissue, the concept was to measure how the materials measured as the X-ray beam attenuated through one then the other. How this would impact the HU values.

In Figure 4.22 each 3D printing is shown, imaged with the standard CT protocol. As stated in section 4.5. The first phantom (Figure 4.2A) was printed using Vero Clear for the body, Vero White Plus (M) for the internal organs and without the skeleton. The second printed phantom (Figure 4.2B) was Tango Black Plus (M) to serve as the "skin" of the rodent phantom, encapsulating the other 3D printed components. With a measured HU value of -38.60HU this indicated X-rays would be less attenuated, pass through to the other components. The lungs were printed as voids. Vero White Plus (M)

was used to 3D print the brain, heart, liver, kidneys and skeleton components. The skeleton was printed with Vero White Plus (M) (Figure 4.2C). Seen in the images, the CaHA capsule is placed in the lung for the CT acquisition (Figure 4.2B & C). Images of the CT acquisitions using the four protocols with the second phantom are shown in Figure 4.23.

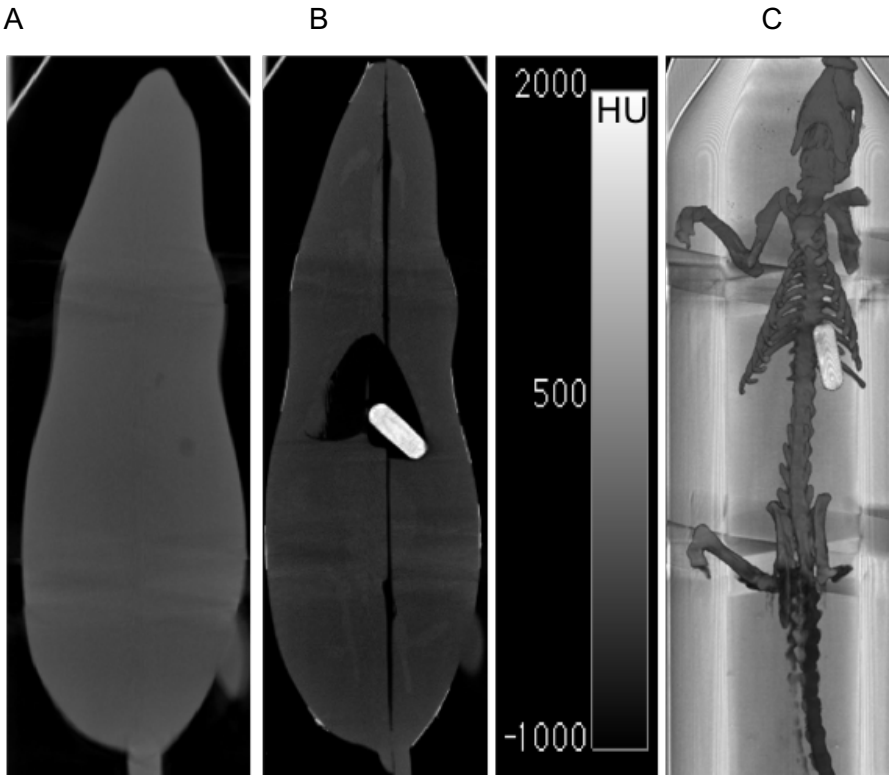

Figure 4.22: CT images shown are with the standard protocol acquisition. Panel (A) is the printed prototype, (B) is the split phantom for testing HU. Panel (C) is a separate CT image of the skeleton, maximum intensity projection (MIP) image. A calcium hydroxyapatite (CaHA) capsule was imaged inside the lung for HU analysis in the phantom (B) and the skeleton (C).

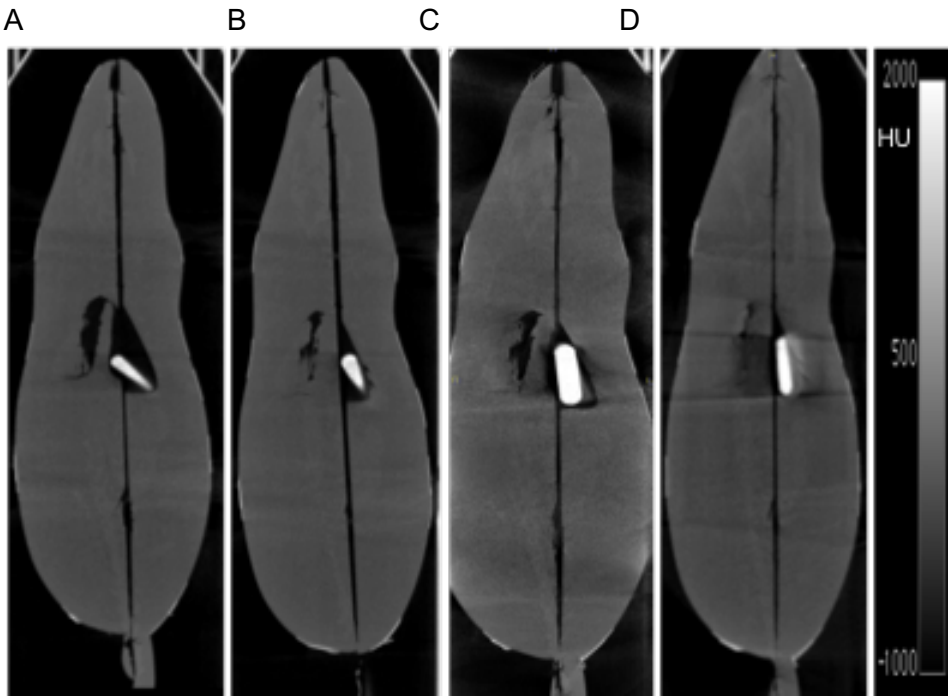

Figure 4.23: CT images of the split phantom for each CT acquisition protocol; (A) standard; (B) default; (C) low dose; (D) high dose.

The image quality is essentially indistinguishable between standard and default protocol, Figure 4.23 panels (A) and (B), respectively. Increased artefacts are seen in the high and low dose CT protocols, Figure 4.23 panels (C) and (D), respectively. The extraction of HU from the heart, lung, liver, kidneys and brain produced similar values for the standard and default protocols. The results are comparable across the standard, default and high protocols. Using Equation 2.1 to compare HU values between the CT protocols revealed substantial difference.

$$Difference = \left|(s - x)/s\right| \times 100 \qquad \text{Eq. (2.1)}$$

in this incidence *s* represents the standard protocol and *x* is the other protocols or as noted in the text

Deviating from the standard protocol produced the greatest percent difference in measured HU for the kidneys between the standard and low dose of 429%. The high dose HU deviation from the standard was greatest in the liver, 230%, Figure 4.24 and Table 4.8. The VOI placements for measuring the HU on each segment are shown in Figure 4.12.

The HU percent differences comparing the phantom to the measured rat using Equation 2.1, (s = measured rat HU, x = measured phantom HU) revealed the low CT dose produced the greatest differences. Shown in Table 4.9, the phantom HU using the low dose CT protocol was a 268% difference in the liver from the rat HU. The phantom CT low dose kidneys measured a 246% and 298%, left and right kidney respectively, difference from the rat HU.

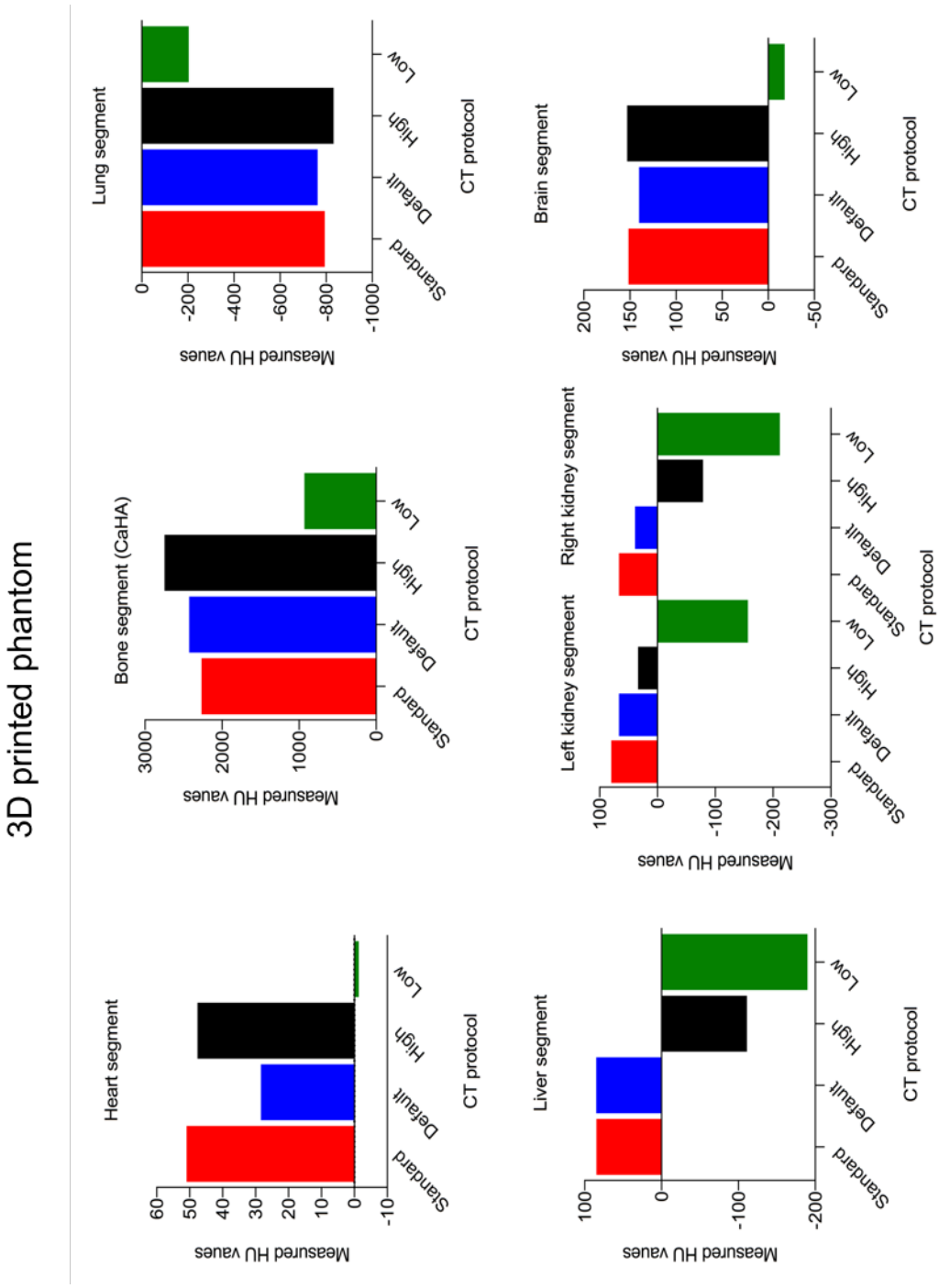

Figure 4.24: HU values measured from the 3D printed phantom using the four CT protocols according to Table 4.8.

Table 4.8: HU comparison between 3D printed anthropomorphic phantom standard protocol and the different protocols (default, high, low) HUs.

Percent difference from the standard protocol (%)							
CT protocol	Heart	CaHA	Lung	Liver	Kidney left	Kidney right	Brain
Default	44.31	-7.10	3.91	-0.24	16.71	39.25	7.51
High	6.57	-21.22	-4.82	230.79	57.75	222.36	-0.97
Low	102.50	58.80	74.43	323.72	294.76	429.21	111.57

Table 4.9: HU comparison between 3D printed anthropomorphic phantom different protocols (standard, default, high, low) and measured rat HUs (default protocol).

Percent difference from the measured rat HU (%)						
CT protocol	Heart	Lung	Liver	Kidney left	Kidney right	Brain
Standard	60.03	-56.98	24.98	24.77	39.77	36.63
Default	77.74	-50.84	24.8	37.34	63.41	41.39
High	62.65	-64.54	198.13	68.21	173.69	36.02
Low	101	59.87	267.85	246.53	298.27	107.33
Rat	127.58	-505.29	113.03	106.6	105.9	239.59

7. Discussion

Data analysis studies supports the feasibility and development of an anthropomorphic TEM rodent phantom using 3D printing materials for potentially replacing the usage of animals all together when optimising CT imaging study specific protocols. Previous studies using 3D printing materials for generic rodent phantom development have also proven successful [23,173,179]. Unfortunately, results revealed no material displaying a close similarity to the cortical bone. Nonetheless, the data does support using a CaHA material as a filler for the skeleton. Future work should include investigating further the use of ceramic calcium salts mixed with a polymer for simulation of denser bone tissue. Another option to consider and pursue is the possibility of using specialized 3D microstructure fabricated biomaterials. These materials are currently developed for tissue engineering and scaffolding for cells [162,180–183]. The 3D fabricated biomaterials are potentially the best printing

option, given that the materials are developed as printing materials. In addition to the 3D cortical bone material being a concern, the attenuation coefficient data indicated a 3D material for lung would also be an issue. To circumvent this, the first-generation rodent phantom for analysis was printed with a void for lung. The measured HUs showed that a void, fortunately, produced compatible lung HUs for all the CT protocols. While this solution proved simple and practical the design needs to be questioned. Splitting the phantom produced air gaps along the phantom as can be seen in Figure 4.23. Thus, simple, practical but possibly not ideal. Creating a CAD design for printing the lungs as a "mesh" also remains an option. Overall, using the commercial 3D printer on site posed two main issues. The first being the limitations of materials available; availability of the material itself and the types of material usable on the printer. The second main issue, as discussed was the inability to print the design without splitting it, plus the inability of the printer to print three materials at the same time.

The discrepancy of HU values measured from the rat compared to the phantom, especially seen in the CT low dose protocol (liver, kidney, brain) raises some concern. However, the rat measurements are only of n=1. Whereas, the results between rat and phantom for the other CT protocols and 3D printed organ segments are reasonable. Closer scrutiny is clearly called for not only in the use of different CT protocols, but in the HU values at the lower preclinical X-ray energies. As mentioned earlier, Hounsfield established the HU values using a tube voltage of 80 kVp. A typical preclinical low dose CT would reduce the tube voltage to 35 kVp or less.

Even with the current HU variability, design and printer concerns the developed anthropomorphic TEM phantom shows great potential as a tool to aid in the design and refinement of preclinical imaging experimental study specific protocols. It will allow for the tailoring of and testing of study specific protocols replacing any animals used in this process. Additionally, a phantom for this purpose reduces the likelihood of biological bias or variability introduced when using animals.

8. Conclusion

This third aim set out to design and manufacture a prototype rodent anthropomorphic phantom to be used instead of animals for development of improved PET/CT imaging study specific protocols. From attenuation coefficients

to printed phantom to HU measurements, each step proved success of this aim. The question was: Can a tissue equivalent material (TEM) anthropomorphic rodent phantom be developed to eventually replace animals used when designing study specific PET/CT imaging protocols? The answer is yes.

Chapter Five: Final conclusions and future work

This doctoral research set out to accomplish three main goals

1. Improve experimental PET/CT imaging protocols through standardisation across sites.
2. Assess the impact and significance of different CT parameters with the aim to reduce absorbed ionising radiation.
3. Develop a prototype TEM anthropomorphic rodent phantom to be used instead of animals for designing study specific imaging protocols.

Each of these goals were met with success. Nonetheless, each presented not only problems along the way, but a set of new research questions. The next and final three sections of this thesis will discuss the fruition of PET/CT standardisation, ionising radiation dose concerns, anthropomorphic phantom development issues and future work.

1. Standardisation of preclinical PET/CT protocols

Not until this study has establishing preclinical imaging standard protocols been directly addressed and set forth. The PET and CT empirical data collected from default protocols conclusively showed significant variability across every measurement taken, even within sites not just across sites, (Chapters 2 and 3). Looking at quantitative data for accuracy and precision, irrespective of scanner differences provided the opportunity to establish a standard imaging protocol, recapitulated in Table 5.1 below. Both PET and CT standards protocols are relatively straightforward, feasible on all tested scanner platforms and were shown to reduce biases (improve accuracy and precision) over all measurements within site and across site's datasets.

Table 5.1A: Proposed preclinical PET standard reconstruction protocol for daily routine use regardless of scanner/site.

PET reconstruction:
Iterative algorithms OSEM or MLEM total updates (iterations*subsets or iterations) to be in the range of 24 to 36 - used to draw VOI and as a visual tool.
FBP is recommended for quantitative analysis in conjunction with iterative methods. VOIs from the iterative method are to be placed on the FBP image.

Table 5.1B: Proposed preclinical CT standard acquisition protocol for daily routine use regardless of scanner/site.

CT parameters:
Tube voltage set at 50 kVp with 360 projections and exposure time of 300 ms.

Without a doubt everyone agrees that preclinical PET/CT scanner characteristics and capabilities vary from manufacture to manufacture. Therefore, the attainment of a standard protocol focused on the similarities in order to generate reproducible results irrespective of scanner. This approach has worked. During the course of data collection and at the time of writing this dissertation the implementation of the standard protocol has already begun. After data analysis was shared with sites, bringing awareness of the significance more than one site switched to the standard for all new research studies. These results generated discussions, launched other standardisation studies in PET/CT and were used in conference educational sessions. To date, fortunately, discussions regarding standardisation in PET/CT and other preclinical modalities continue amongst the imaging community globally. For example, the European Society for Molecular Imaging (ESMI) has established a coalition of preclinical imaging researchers, Standardisation of Small Animal Imaging (STANDARD) whose priority is to standardise preclinical imaging. In the United States of America, the Society of Nuclear Medicine and Molecular Imaging (SNMMI) preclinical research website now suggest nine topics for establishing imaging guidelines for the preclinical community. Two of those topics are the "development of standardise image format and data analysis". Both the ESMI and SNMMI recent initiatives hold promise for global preclinical imaging standardisation. The important factor is to get the word out, have the discussions, do due diligence - improve reliability.

Generating continued said discussions, awareness and standardisation studies opens the avenue for further improvements. This also allows the opportunity to address additional preclinical imaging instrumentation concerns. A main concern noted at each site but one and throughout this study was the lackadaisical irregular calibration of scanners. The same sort of scanner quality assurance seen in the clinical setting should apply to preclinical - improving the robustness and translation of imaging data results. While it is important to test and verify scanner characteristics per accepted NEMA and ACRIN standards, it is as equally important to maintain scanner stability and reliability. Concluding, standardisation and proper

scanner quality control/assurance avoids confounding factors generating spurious quantitative imaging results.

Turning concerns directly to CT, furthermore, not until this study has the range of HUs values been measured at preclinical CT voltages across different scanners for evaluation. The traditional HU scale was established using clinical protocols with a higher tube voltage than 50 kVp [71]. As known and further shown, (Chapter 4), lower CT energies are dominated by Bremsstrahlung X-rays. To reiterate, attenuation coefficients are impacted by the initial ionising radiation and the medium they go through. Therefore, research, validation or clarification for a greater understanding of preclinical X-ray ranges and the relationship with HU is in order. The average HU values reported in Chapter 3 per TEM across multiple scanners can be used to establish or set a foundation for preclinical HU ranges, Table 5.2. Hence, these concerns lead to future work in this regard. For example, a possible extension of this work and validation of rodent HUs is to vary X-ray energies at preclinical tube voltage settings with rodent tissue density parameters in Monte Carlo simulation studies. Monte Carlo simulations can provide more detailed information on rodent tissue attenuation coefficients and then calculated HU values for comparison to measured values.

Table 5.2: Proposed preclinical Hounsfield Unit (HU) range generated using the standard CT protocol (tube voltage at 50 kVp, 300 ms and 360 projections) and the tissue equivalent material phantom. Soft tissue and bone HUs are averaged using the 2mm and 4mm rods.

	Range of Hounsfield Units		
Lung range	-778	to	-686
Adipose range	-233	to	-177
Muscle range	-8	to	64
Soft tissue range (0.95 to 1.115 g/mL)	-204	to	74
Bone range (1.24 to 1.57 g/mL)	987	to	2900

Furthermore, and as stated this work did not cover many other aspects of preclinical standardisation. The focus here was purely on preclinical PET/CT imaging

protocols. Some of the more recent literature on preclinical standardisation point out the critical issue of how animal welfare, handling and husbandry potential impact research and animals alike [104,184]. Literature from Osborne *et al*. (2017), Vanhove *et al.* (2015) and Kuntner *et al*. (2014) expand preclinical standardisation needs and considerations to include facility requirements, animal handling and husbandry as well as preclinical experimental designs [18,104,106]. These papers also point out the need for system quality control in preclinical imaging modalities. Recently, Mannheim *et al.* (2019) reiterated the concerns regarding animal handling [129]. Therefore, preclinical PET/CT imaging protocols is only a piece of the ongoing research and cry for standardisation in the preclinical imaging community.

Currently, there are also ongoing discussions within the preclinical imaging community about requiring more transparent and explicit reporting of all procedures/protocols in published papers, which include the concept of using "open resources" for data files. A DICOM open source software, first for each site and ultimately available to be shared for researchers was discussed for data sets in this study. Therefore, all the imaging data sets were saved as DICOM files. This allowed for the same file format regardless of scanner or site. The difficultly of using an open source became apparent after the initial visits. The DICOM data sets pulled and moved off the different scanners sometimes ended up with missing information (DICOM headers), incorrect information (dates, bed positions). In order to avoid incorrect files and adding biases to the quantitative data analysis results it was decided all DICOM files were kept on a secure data base and loaded directly to PMOD. In the future the intention is to make the files available for researchers.

2. Characterisation and reduction of absorbed ionising radiation

The amount of ionising radiation being absorbed by small laboratory animals during even one default X-ray CT acquisition was unknown at every site enrolled in this project. The success of determining a standard protocol (detailed above) had an immediate impact on CT doses. Mentioned in Chapter 3 was scanner 5's high measured CT dose (>200 mGy). Due to animal welfare and the potential impact on research results, that site expeditiously decided to stop using their default protocol and adopt the standard protocol.

It is known that ionising radiation has biological effects on cells and DNA; causing damage or death [185,186]. Additionally, the use of ionising radiation as cancer

therapy is an active area of research preclinically and with Monte Carlos simulation studies [187,188]. However, to date the CT doses regularly received by laboratory animals through imaging remains widely unknown. Therefore, the potential biological responses from excessive CT radiation is a concern for animals and research results. The simple approach of switching a default protocol to a low CT dose is not sufficient. Future work in this area should expand to include in depth research into the effects of ionising radiation at preclinical energies on cell and/or DNA damage as well as the repair process from that damage.

On a positive note, the results from this doctoral research did show standardised protocols produce a reduction of the average absorbed ionised radiation received by small laboratory animals, (40% reduction, Chapter 3) with no image degradation.

3. Anthropomorphic TEM rodent phantom

The advantage of designing an anatomical phantom allows for the evaluations of X-ray attenuation through the different heterogeneous overlapping layers, organs and scatter. Therefore, a lot of focus, work and analysis was placed on the calculated and measured attenuation coefficients early on in the phantom development, the weeding out of materials. This weeding out is a vital component of the overall design decisions. If the TEM phantom is to be fully incorporated into use it is important the material's properties respond characteristically similar to tissue and organs when exposed to various X-ray beam energies. The attenuation coefficient results presented (Chapter 4) clearly indicated that several materials could be used for soft tissue. The measured HU also correlated well with the HU soft tissue range. Measured HU for lungs revealed that the void produced reasonable, acceptable values. A suitable and a feasible 3D printing bone material has yet to be identified. At this point, a fabricated bone biomaterial is most likely the solution. Currently, there are several research groups conducting successful tissue engineering (TE) fabrication studies for 3D printing [162,181,189] Biomaterials; degradable, non-degradable, synthetic polymers, natural polymers for a variety of uses are now available in academia as are modified 3D printers for handling biomaterials. The structural, mechanical and biological properties of cartilage is extensively studied in the TE field, providing a range of cartilage biomaterials; calcium composites, metals, ceramic oxides, hydroxyapatite [180,190]. In other words, future development of the anthropomorphic TEM rodent phantom should be moved to, expanded to biomaterials. Transferring the 3D printing to an academic setting

with modified 3D printers to accommodate biomaterials will also possibly resolve the problem of splitting the phantom. Commercial 3D printers requires support material, whereas a modified printer can be stopped allowing for changing layers of materials. In 2018 Zhang *et al*. published similar findings to this work [151]. Their work however did not move forward to biomaterials and bone material requirements.

Once fully developed the TEM anthropomorphic phantom's purpose has the potential to expand beyond imaging experimental protocol design. A future possibility is in dosimetry and radiation therapy studies. There is a growing interest in using small animals and/or phantoms as well as Monte Carol simulations in this regard [145,150,187,191]. Dancewicz *et al.*(2017) conducted a set of experiments using 3D printed rods representing the various tissues (lung, soft tissue, brain, bone) and water as inserts into a phantom (Gammex phantom, Gammex Inc., Middleton , USA). For radiation therapy the CT tube voltages are substantially greater than the routine preclinical CT tube voltages [192]. Even so, they also concluded 3D printed materials can be used to model various tissues.

Appendix

Appendix 1. Diagram of projection data collection for 2D and fully 3D mode

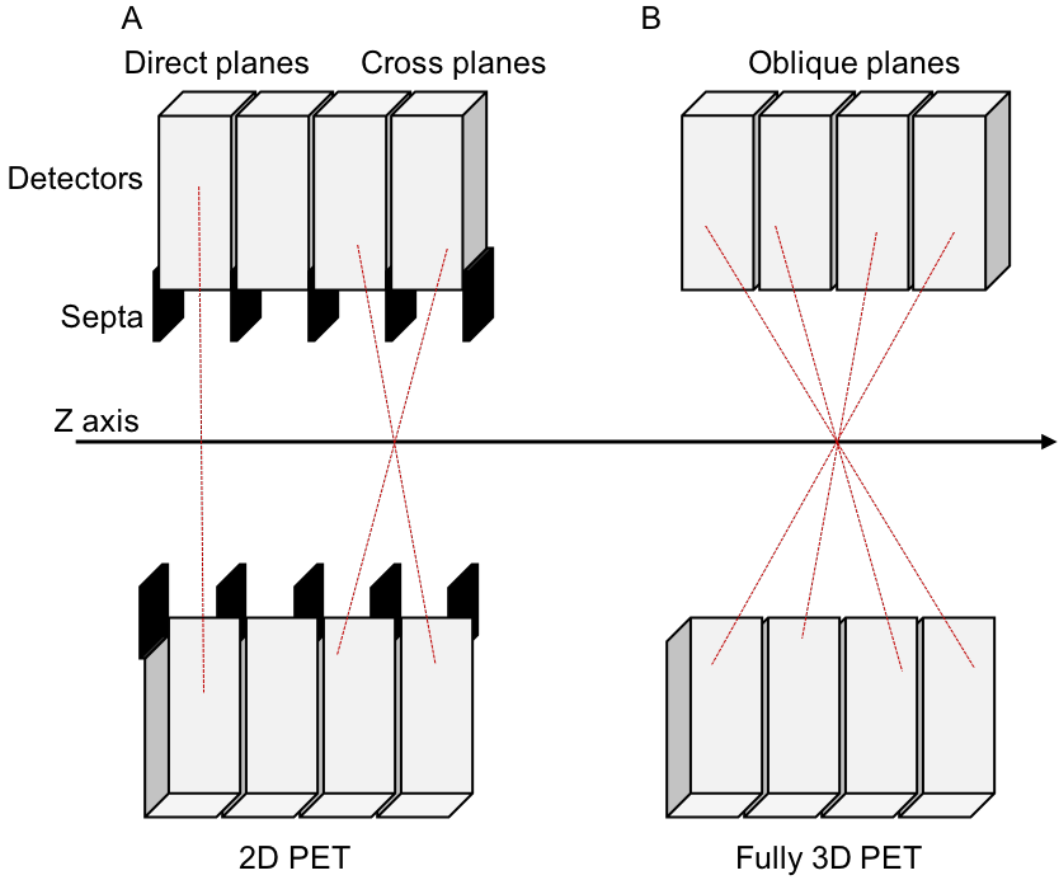

Figure A1.1: Modified drawing from Dr Adam Alessio showing the difference between 2D and fully 3D measurements [1]. (A): Displays detectors with septa, in which 2D modes collects projection data in the direct and cross planes. (B): Represents the collection of fully 3D projection data, no septa allowing collection from the oblique planes (data is re-binned to 2D for reconstruction). Note not to any scale.

Appendix 2. CT air and water phantom measurements for non-standard tested protocols

All CT protocols tested for a potential standard have a tube voltage of 50 keV and exposure time of 300 ms (as detailed in Chapter 2). The number of projections varied (170, 360, 480, 720) during the development of a standard CT protocol. Not all scanners were capable of the different number of projections, noted in the Tables below by NA (not available). As stated and reported in the main text of Chapter 2 standard protocol is with 360 projections.

Table A2.1: Hounsfield Units (HU) measured using the CT air/water phantom and default or 170 projections acquisition protocol. Results presented as the mean±standard error of the mean HUs for each scanner (n=3).

	Ave HU Water (0)	Ave HU Air (-1000)
1 Default	133.05±164.18	-967.86±85.59
170 projections	NA	NA
2 Default	-29.62±18.64	-993.84±6.55
170 projections	-21.62±28.24	-998.56±13.05
3 Default	16.97±24.93	-994.98±9.67
170 projections	32.23±37.18	-994.30±6.57
Scanner 4 experienced failures; engineer work required; data reported as measured		
4 Default	24.85±14.11	-1000±0.00
170 projections	-147.73±13.42	-1000±0.00
Scanner 5 not converted to HU		

Table A2.2: Hounsfield Units (HU) measured using the CT air/water phantom and default or 480 projections acquisition protocol. Results presented as the mean±standard error of the mean HUs for each scanner (n=3).

	Ave HU Water (0)	Ave HU Air (-1000)
1 Default	133.05±164.18	-967.86±85.59
480 projections	NA	NA
2 Default	-29.62±18.64	-993.84±6.55
480 projections	-29.62±18.64	-993.84±6.55
3 Default	16.97±24.93	-994.98±9.67
480 projections	26.69±23.33	-997.58±3.46
Scanner 4 experienced failures; engineer work required; data reported as measured		
4 Default	24.85±14.11	-1000±0.00
480 projections	-151.55±9.85	-1000±0.00
Scanner 5 not converted to HU		

Table A2.3: Hounsfield Units (HU) measured using the CT air/water phantom and default or 720 projections acquisition protocol. Results presented as the mean±standard error of the mean HUs for each scanner (n=3).

	Ave HU Water (0)	Ave HU Air (-1000)
1 Default	133.05±164.18	-967.86±85.59
720 projections	-82.30±72.74	-992.59±59.80
2 Default	-29.62±18.64	-993.84±6.55
720 projections	-29.59±17.44	-993.71±6.53
3 Default	16.97±24.93	-994.98±9.67
720 projections	29.56±19.00	-998.80±2.55
Scanner 4 experienced failures; engineer work required; data reported as measured		
4 Default	24.85±14.11	-1000±0.00
720 projections	-153.39±9.14	-1000±0.00
Scanner 5 not converted to HU		

Appendix 3. CT TEM phantom measurements for non-standard tested protocols

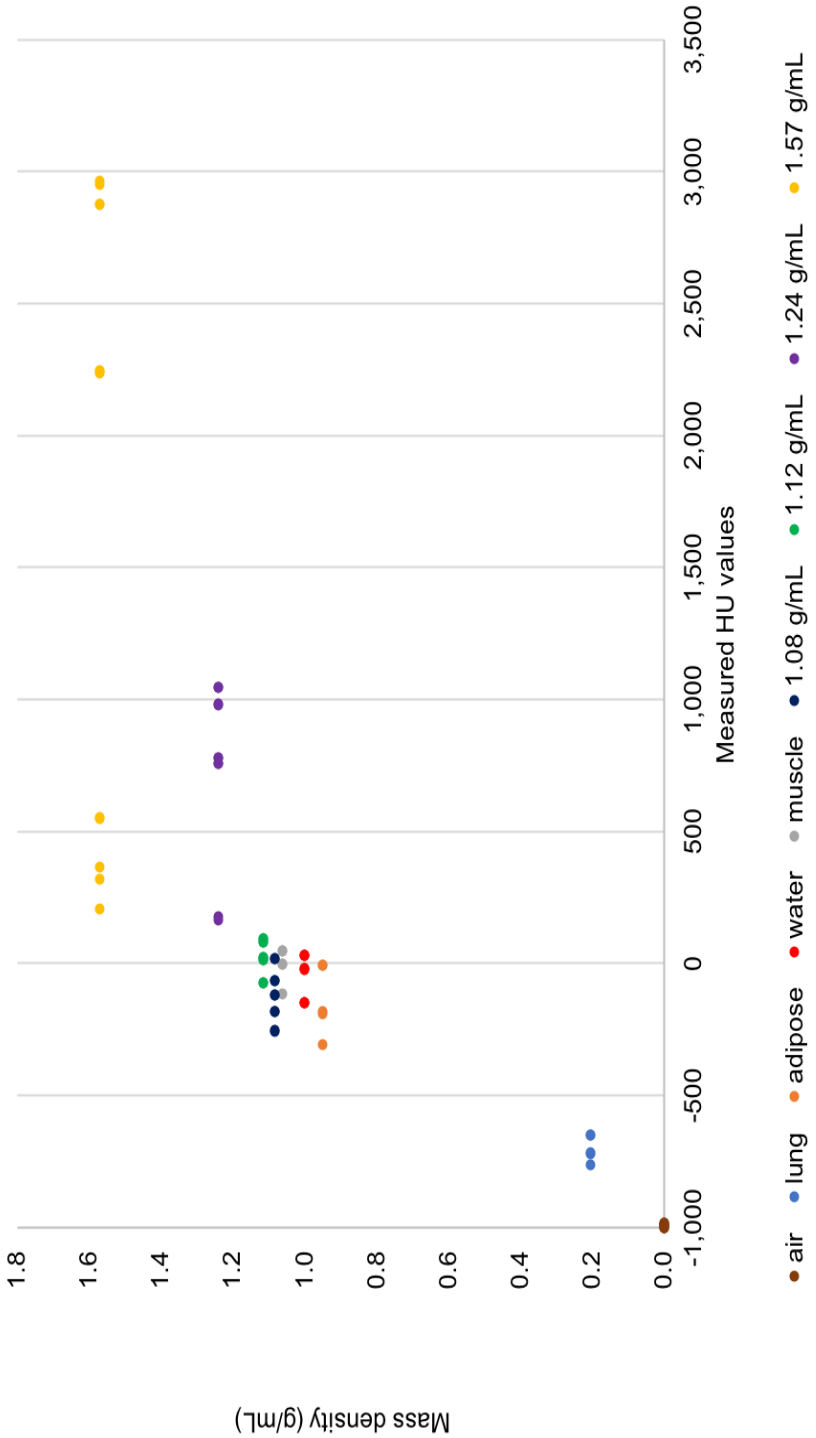

Figure A3.1: CT TEM, air and water HU results for tested protocol with 170 projections. For each material, each data point represents a measurement from a scanner (n=3) from four different sites. Densities 1.08 to 1.57 g/mL include rod sizes 2 mm and 4 mm as reported by the manufacturer. The x-axis clearly shows the spread of HU values per density.

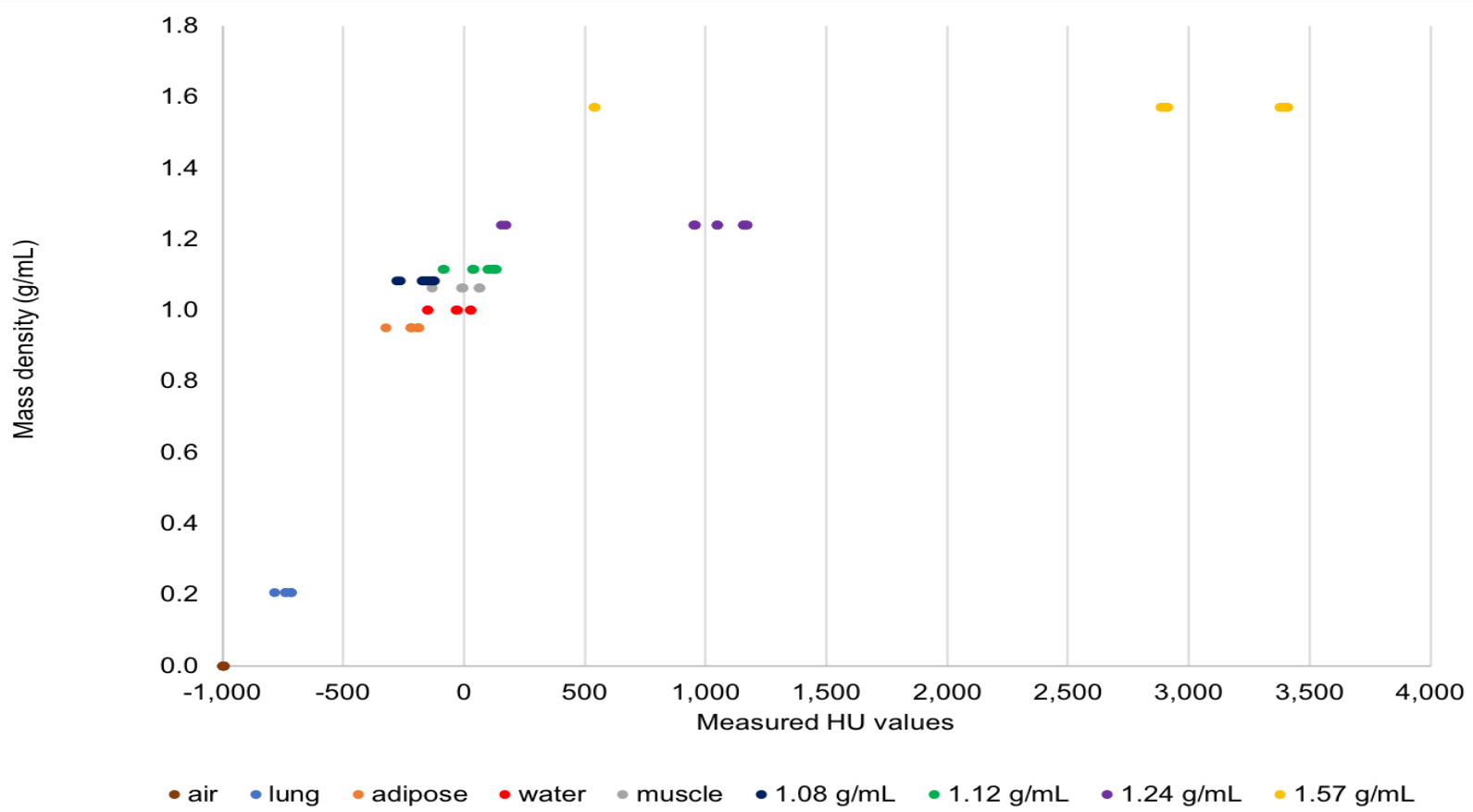

Figure A3.2: CT TEM, air and water HU results for tested protocol with 480 projections. For each material, each data point represents a measurement from a scanner (n=3) from four different sites. Densities 1.08 to 1.57 g/mL include rod sizes 2 mm and 4 mm as reported by the manufacturer. The x-axis clearly shows the spread of HU values per density - though not as bad as the 170 data.

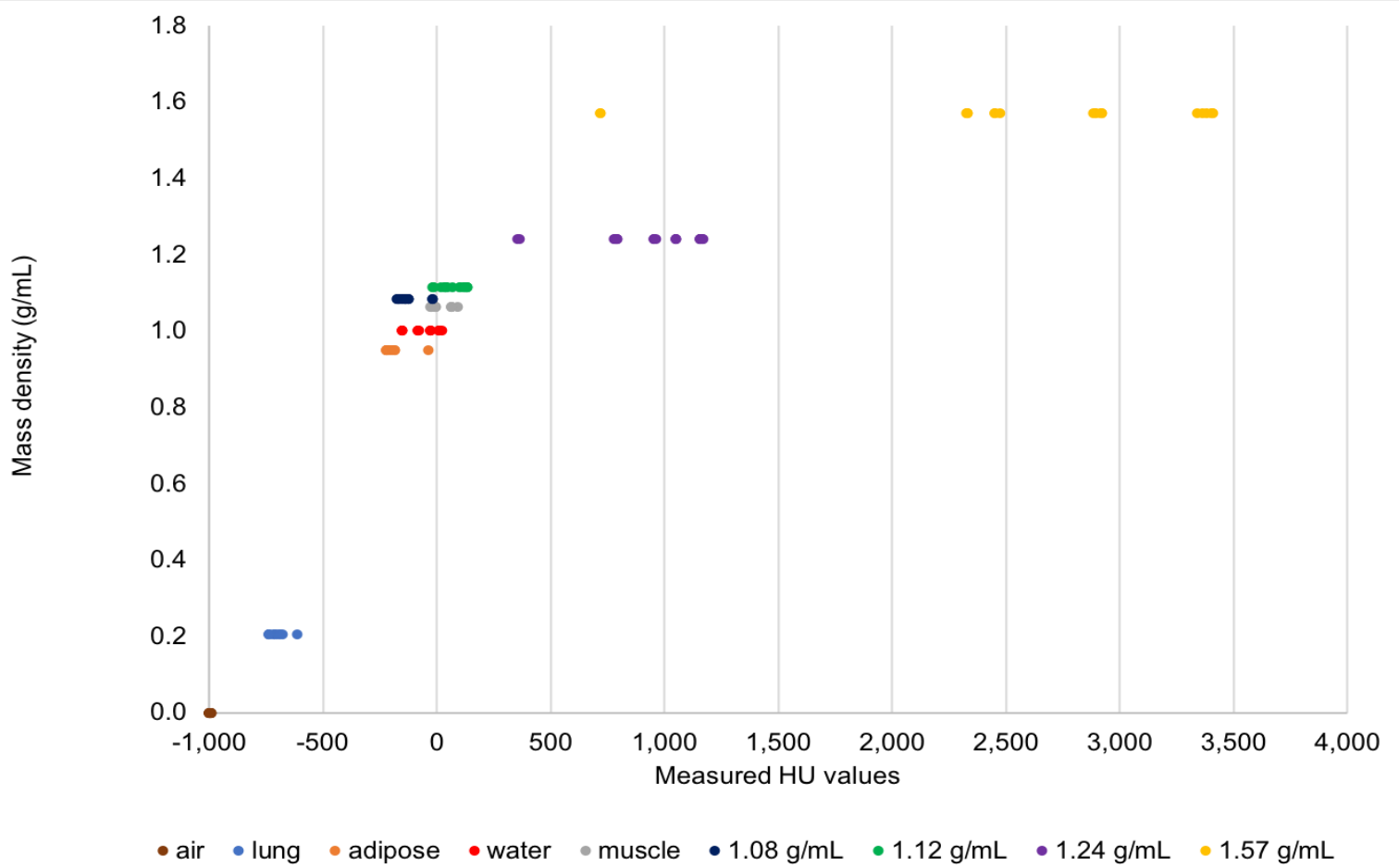

Figure A3.3: CT TEM, air and water HU results for tested protocol with 720 projections. For each material, each data point represents a measurement from a scanner (n=3) from four different sites. Densities 1.08 to 1.57 g/mL include rod sizes 2 mm and 4 mm as reported by the manufacturer. The x-axis clearly shows the spread of HU values per density, similar to the 480 projections.

Appendix 4. CT dose readings for non-standard tested protocols

Table A4.1 CT absorbed doses measured using default protocols and CT protocol 170 projections for mice and rats. Results expressed as mean±standard deviation, n=3.

	Default (mGy)		170 projections (mGy)		Measured dose difference default to 170 (%)	
Scanner	Mouse	Rat	Mouse	Rat	Mouse	Rat
1	11±0.10	7±0.10	NA	NA	NA	NA
2	40±0.11	28±0.02	18±0.01	13±0.03	-54	-54
3	59±0.03	48±0.11	19±0.02	13±0.12	-69	-72
4	32±0.18	15±0.10	36±0.02	16±0.11	+12	+7
5	216±0.02	100±0.17	NA	NA	NA	NA

Table A4.2: CT absorbed doses measured using default protocols and CT protocol 480 projections for mice and rats. Results expressed as mean±standard deviation, n=3.

	Default (mGy)		480 projections (mGy)		Measured dose difference default to 480 (%)	
Scanner	Mouse	Rat	Mouse	Rat	Mouse	Rat
1	11±0.10	7±0.10	NA	NA	NA	NA
2	40±0.11	28±0.02	40±0.11	28±0.02	0	0
3	59±0.03	48±0.11	53±0.17	38±0.11	-11	-21
4	32±0.18	15±0.10	151±0.25	115±0.48	+371	+667
5	216±0.02	100±0.17	55±0.11	36±0.48	-75	-64

Table A4.3: CT absorbed doses measured using default protocols and CT protocol 720 projections for mice and rats. Results expressed as mean±standard deviation, n=3.

	Default (mGy)		720 projections (mGy)		Measured dose difference default to 720 (%)	
Scanner	Mouse	Rat	Mouse	Rat	Mouse	Rat
1	11±0.10	7±0.10	40±0.13	27±0.14	+245	+270
2	40±0.11	28±0.02	59±0.06	41±0.04	+47	+47
3	59±0.03	48±0.11	81±0.00	57±0.14	+37	+20
4	32±0.18	15±0.10	381±0.07	297±0.17	+1090	+1880
5	216±0.02	100±0.17	81±0.01	59±0.08	-63	-42

Appendix 5. 3D-printing material calculated x-ray spectrums

Perspex:

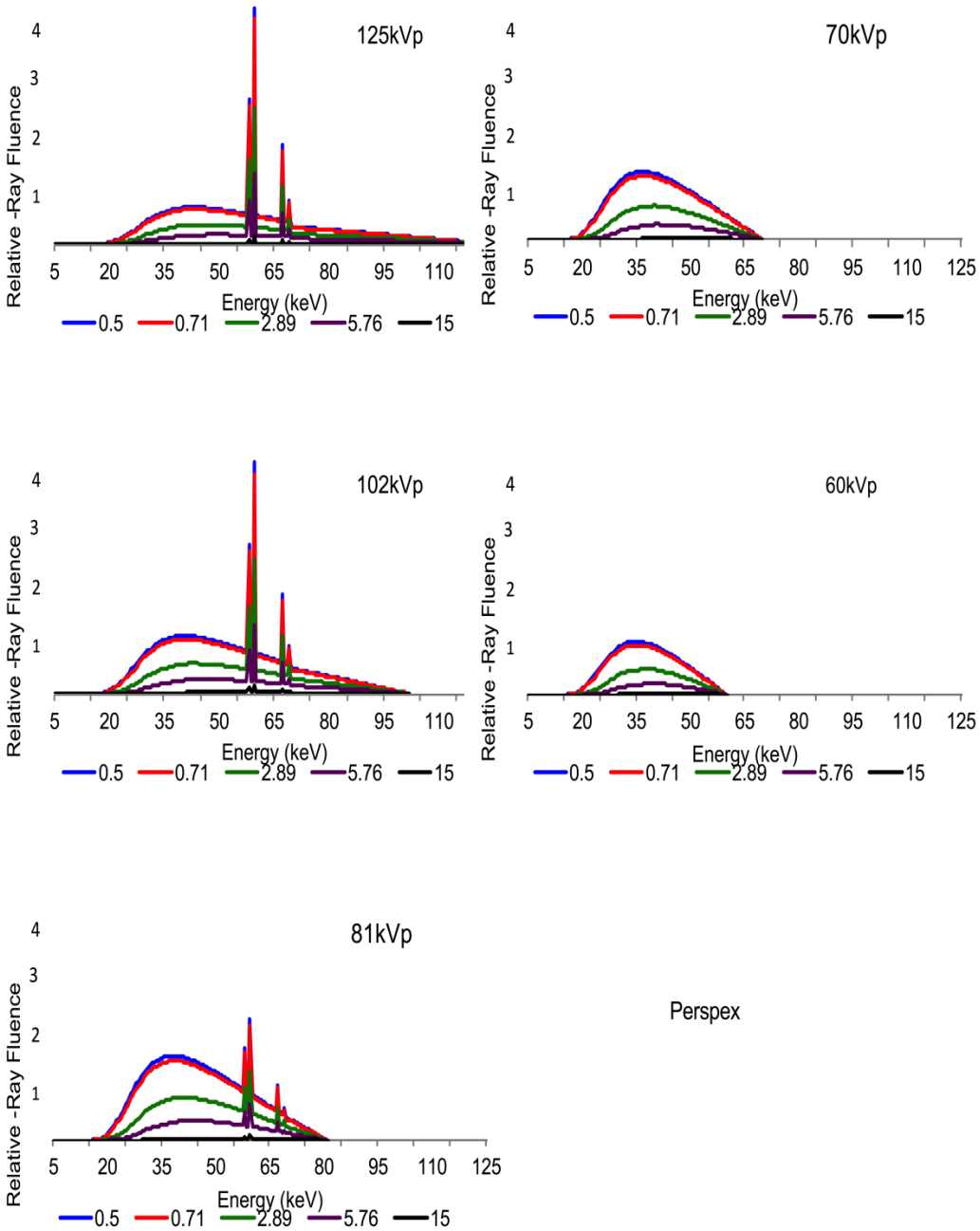

Figure A5.1: Spectrums of the material Perspex showing X-ray tube voltages of 102, 81, 70 and 60 kVp for the 5 different thicknesses in which a measurement was obtained.

Med 160:

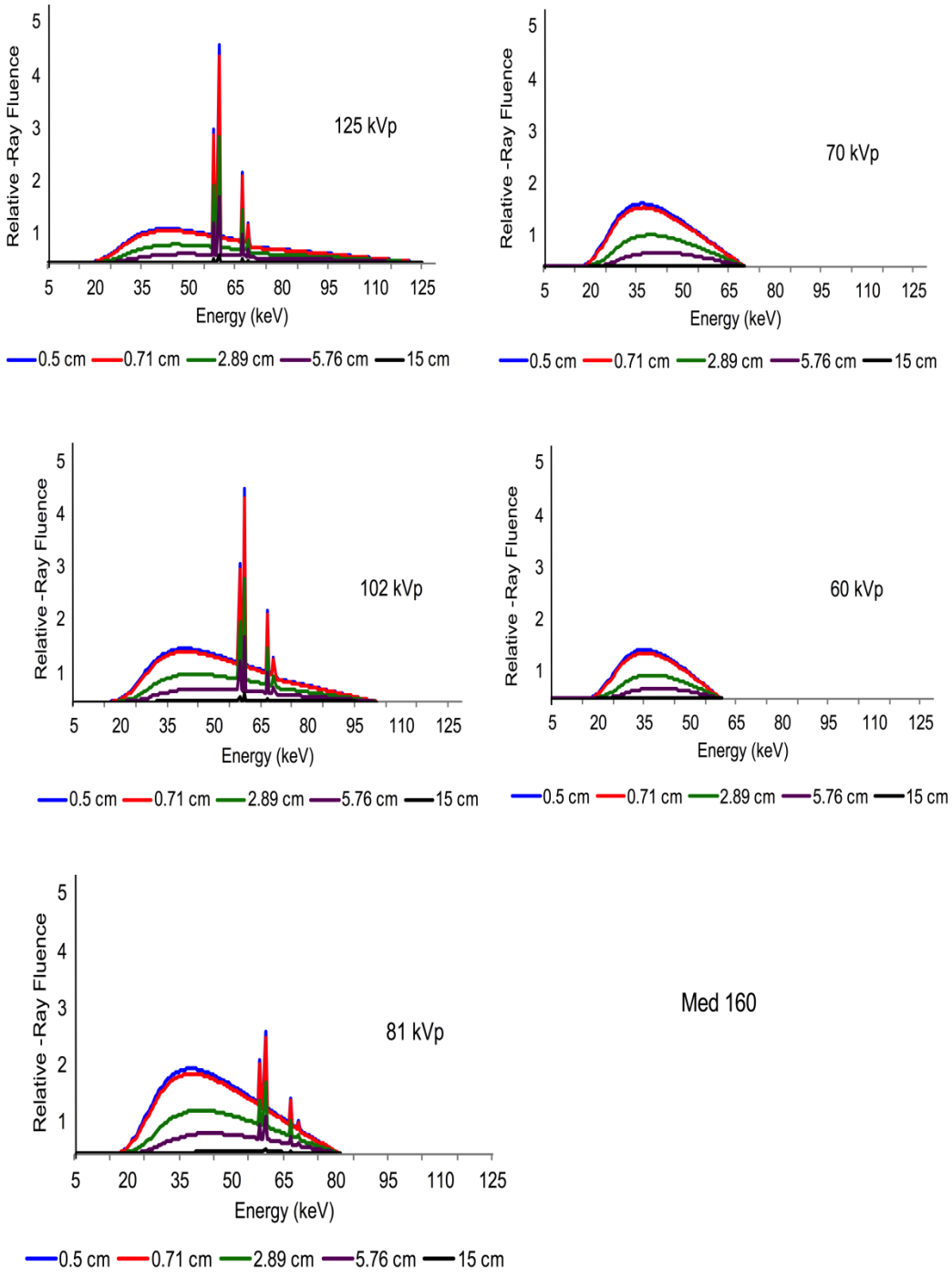

Figure A5.2: Spectrums of the materials Med 160 showing X-ray tube voltages of 102, 81, 70 and 60 kVp for the 5 different thicknesses in which a measurement was obtained.

High Temp:

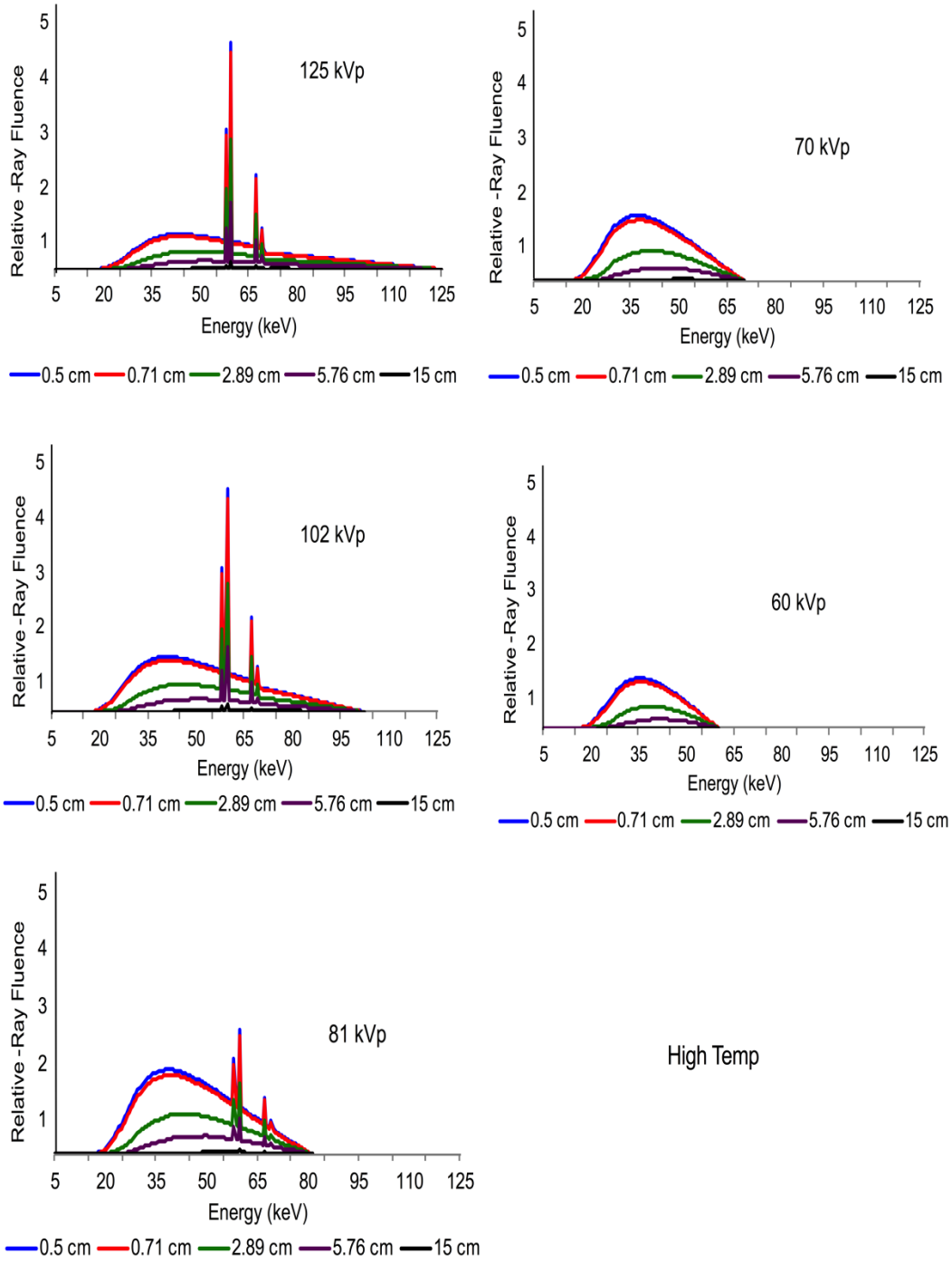

Figure A5.3: Spectrums of the materials High Temp showing X-ray tube voltages of 102, 81, 70 and 60 kVp for the 5 different thicknesses in which a measurement was obtained.

Vero Clear:

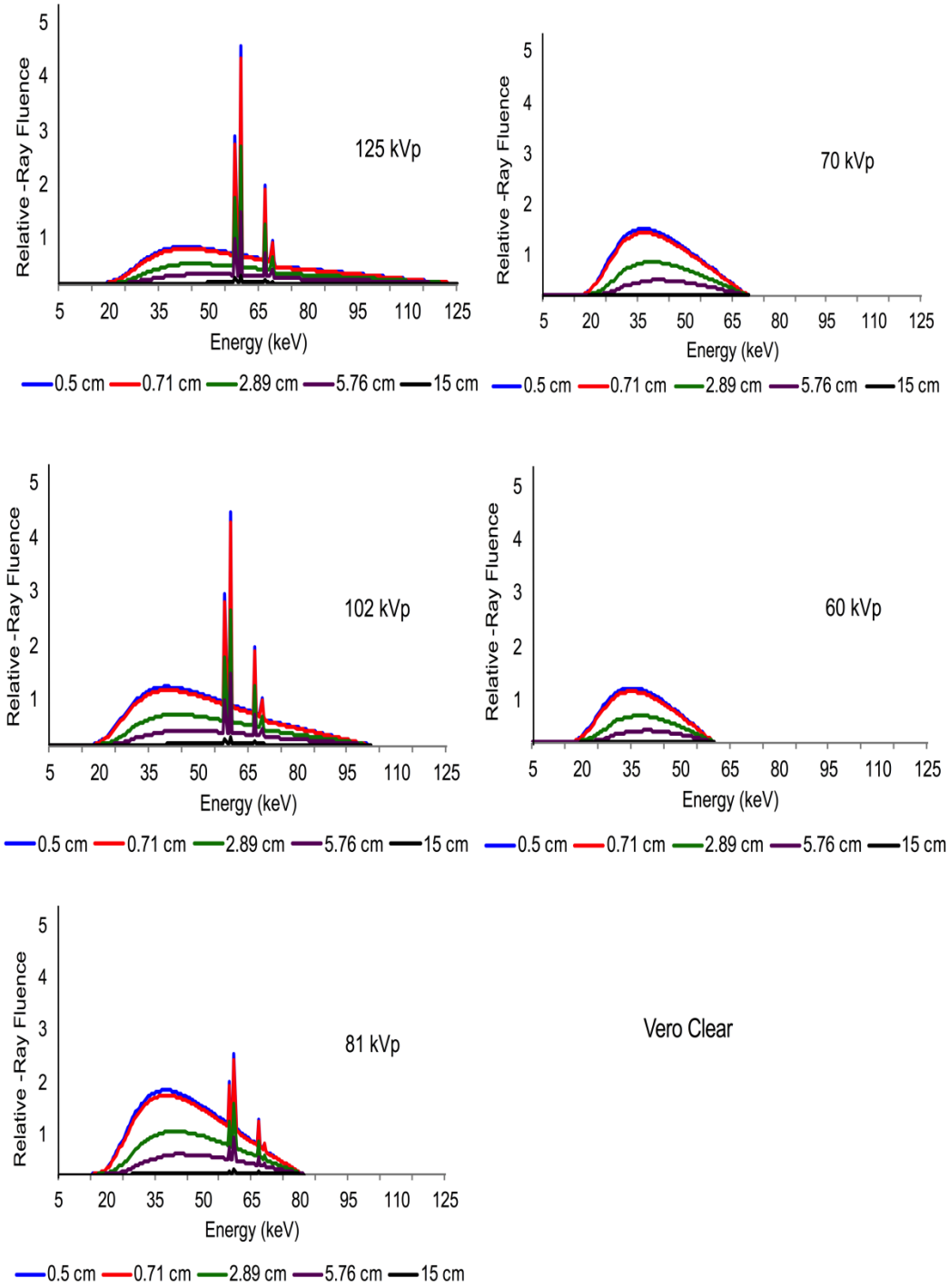

Figure A5.4: Spectrums of the materials Vero Clear showing X-ray tube voltages of 102, 81, 70 and 60 kVp for the 5 different thicknesses in which a measurement was obtained.

Vero White:

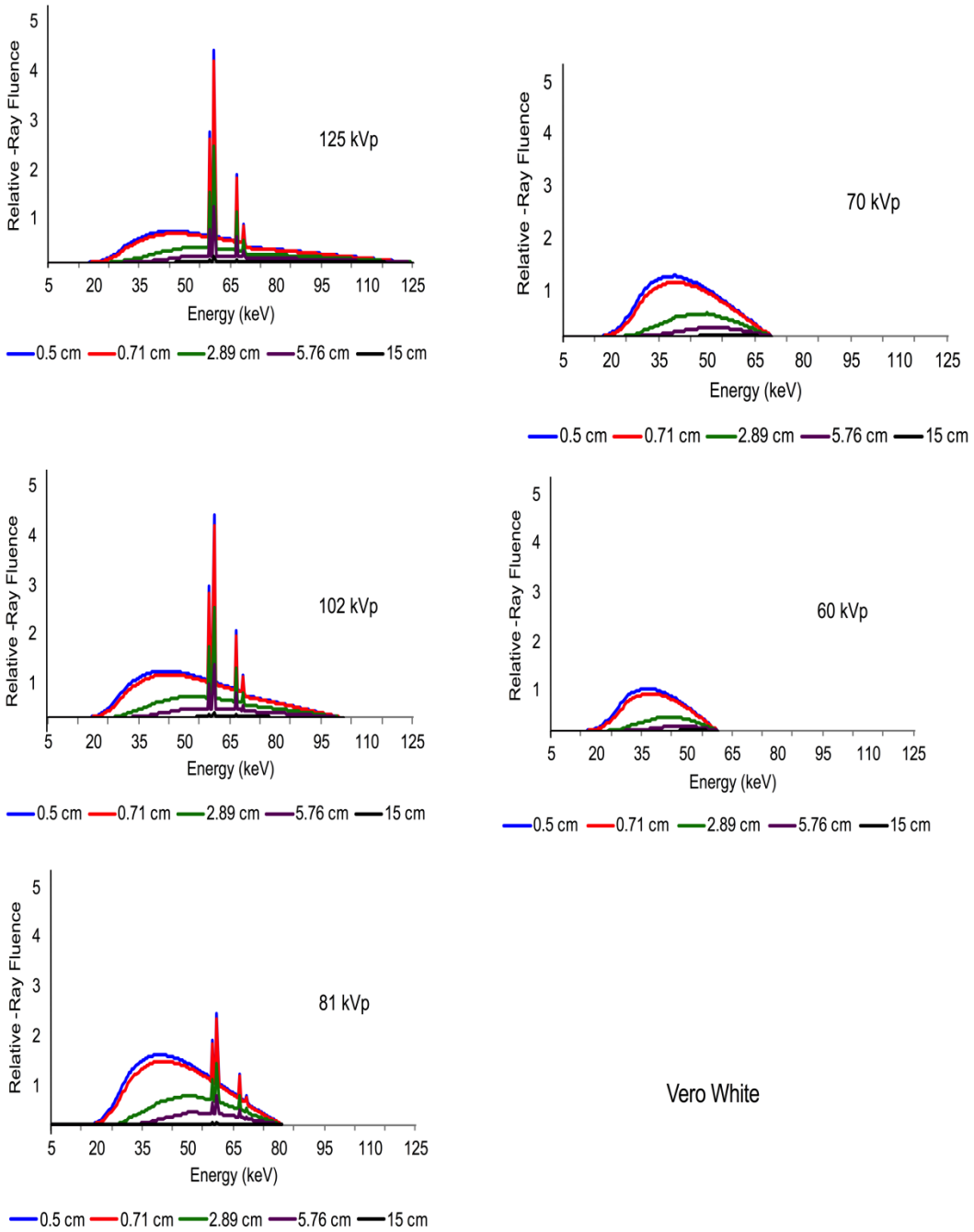

Figure A5.5: Spectrums of the materials Vero White showing X-ray tube voltages of 102, 81, 70 and 60 kVp for the 5 different thicknesses in which a measurement was obtained.

Vero White Plus:

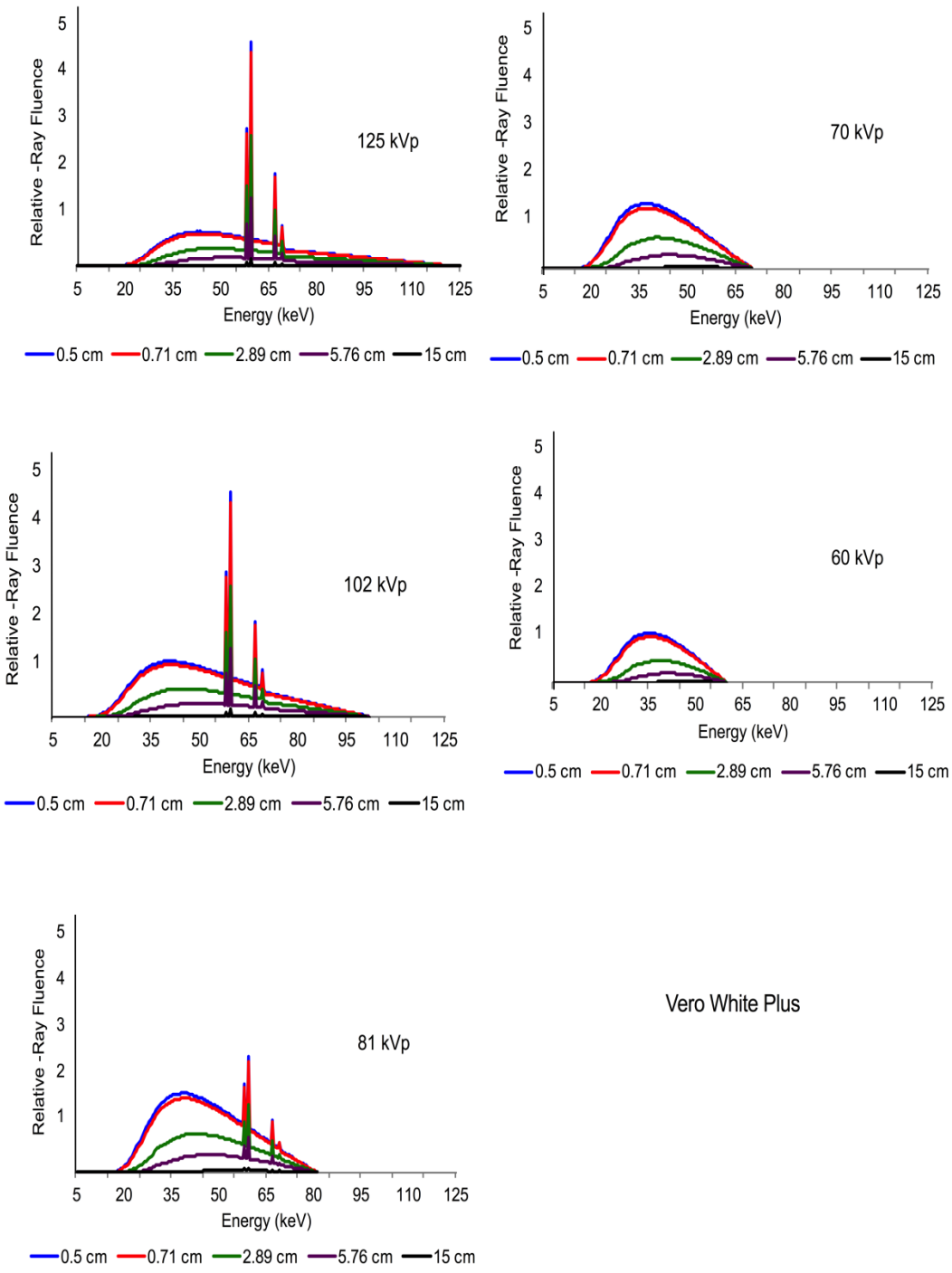

Figure A5.6: Spectrums of the materials Vero White Plus showing X-ray tube voltages of 102, 81, 70 and 60 kVp for the 5 different thicknesses in which a measurement was obtained.

Tango Black:

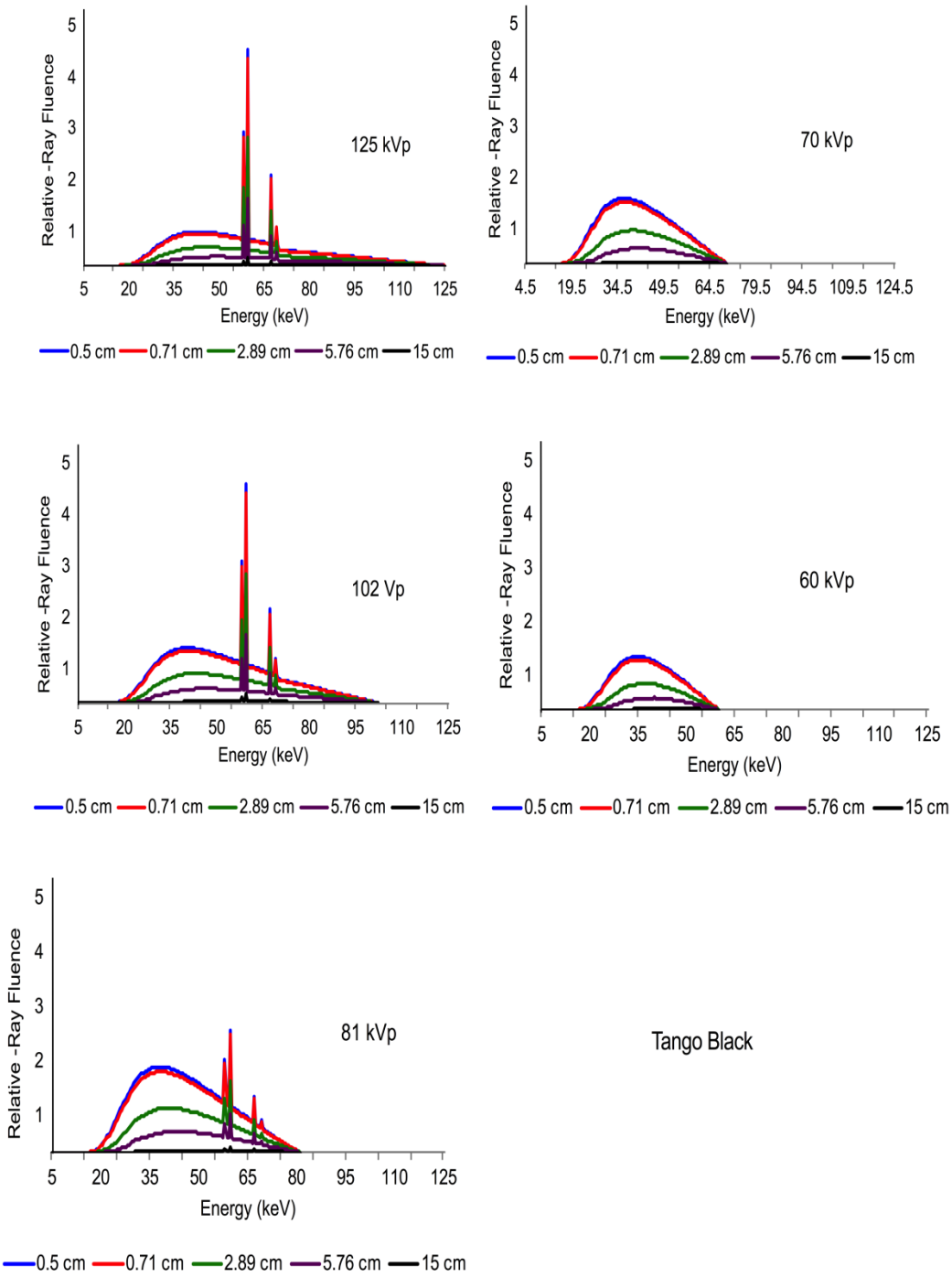

Figure A5.7: Spectrums of the materials Tango Black showing X-ray tube voltages of 102, 81, 70 and 60 kVp for the 5 different thicknesses in which a measurement was obtained.

Tango Black Plus:

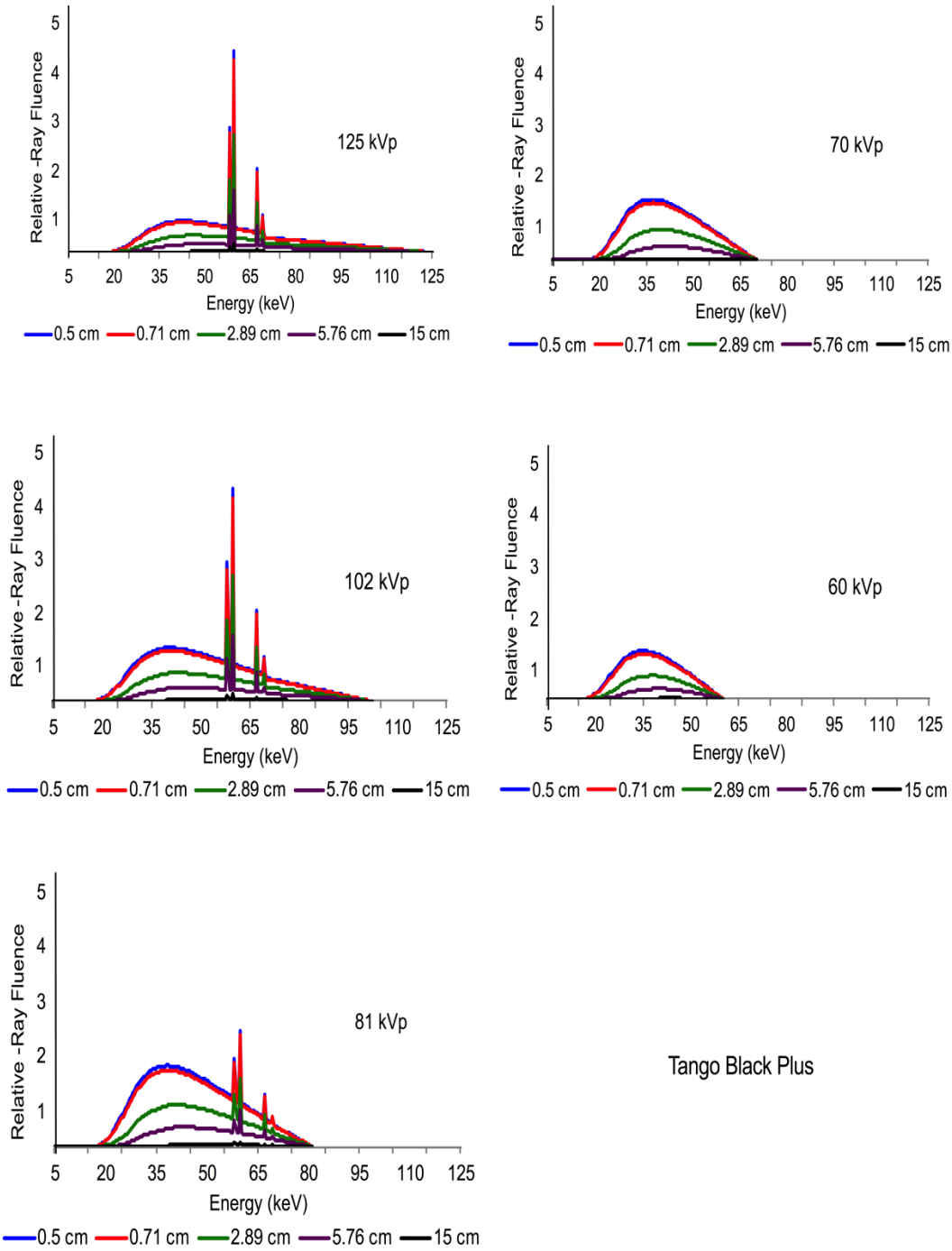

Figure A5.8: Spectrums of the materials Tango Black Plus showing X-ray tube voltages of 102, 81, 70 and 60 kVp for the 5 different thicknesses in which a measurement was obtained.

Appendix 6. 3D-printing material calculated versus measured graphs

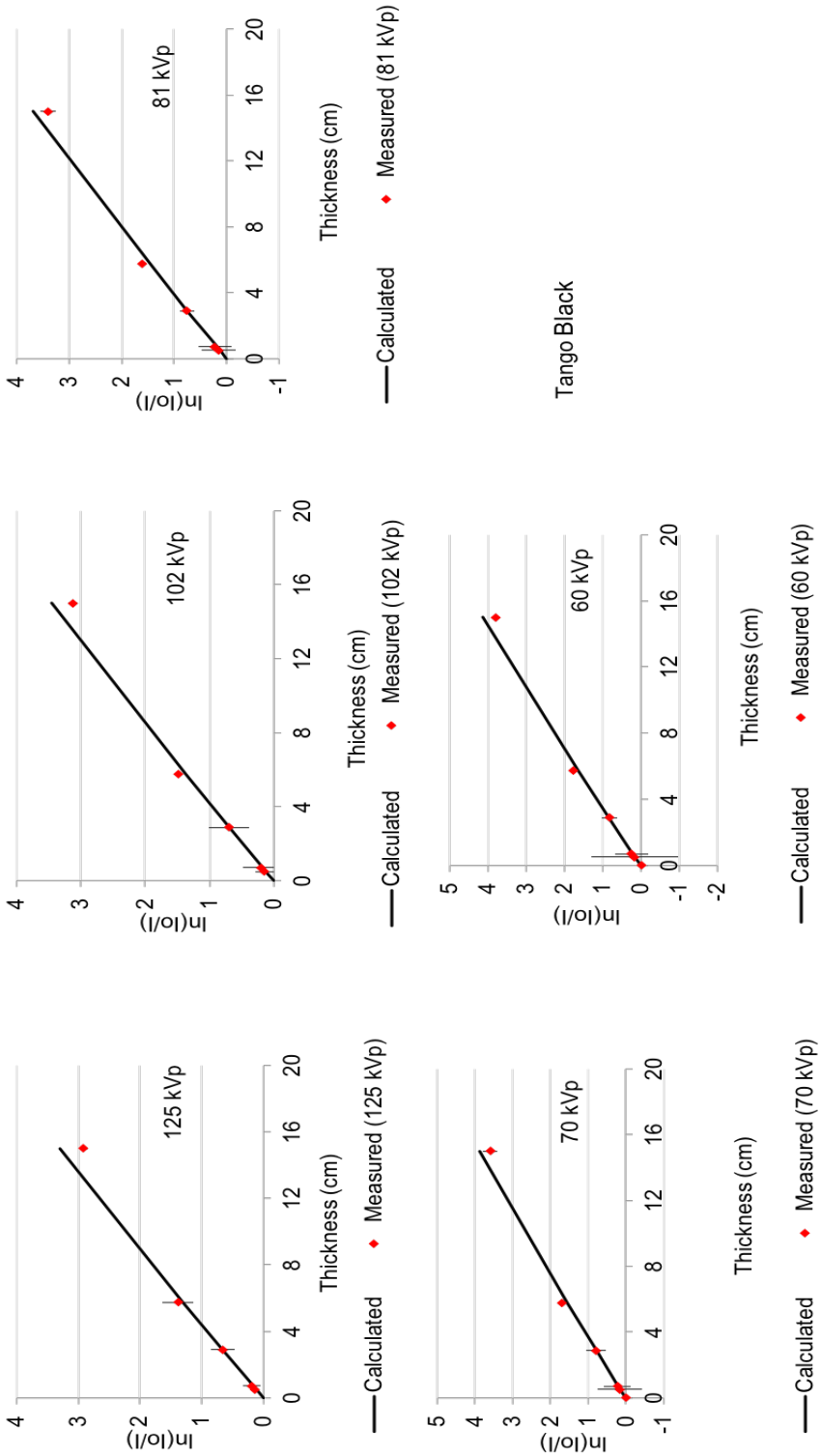

Figure A6.1: Comparison of predicted 3D material Tango Black at the X-ray tube voltage of 125,102, 81, 70 and 60 kVp to each measured output at the defined thicknesses (0.5, 0.7, 2.9, 5.8 and 15 cm).

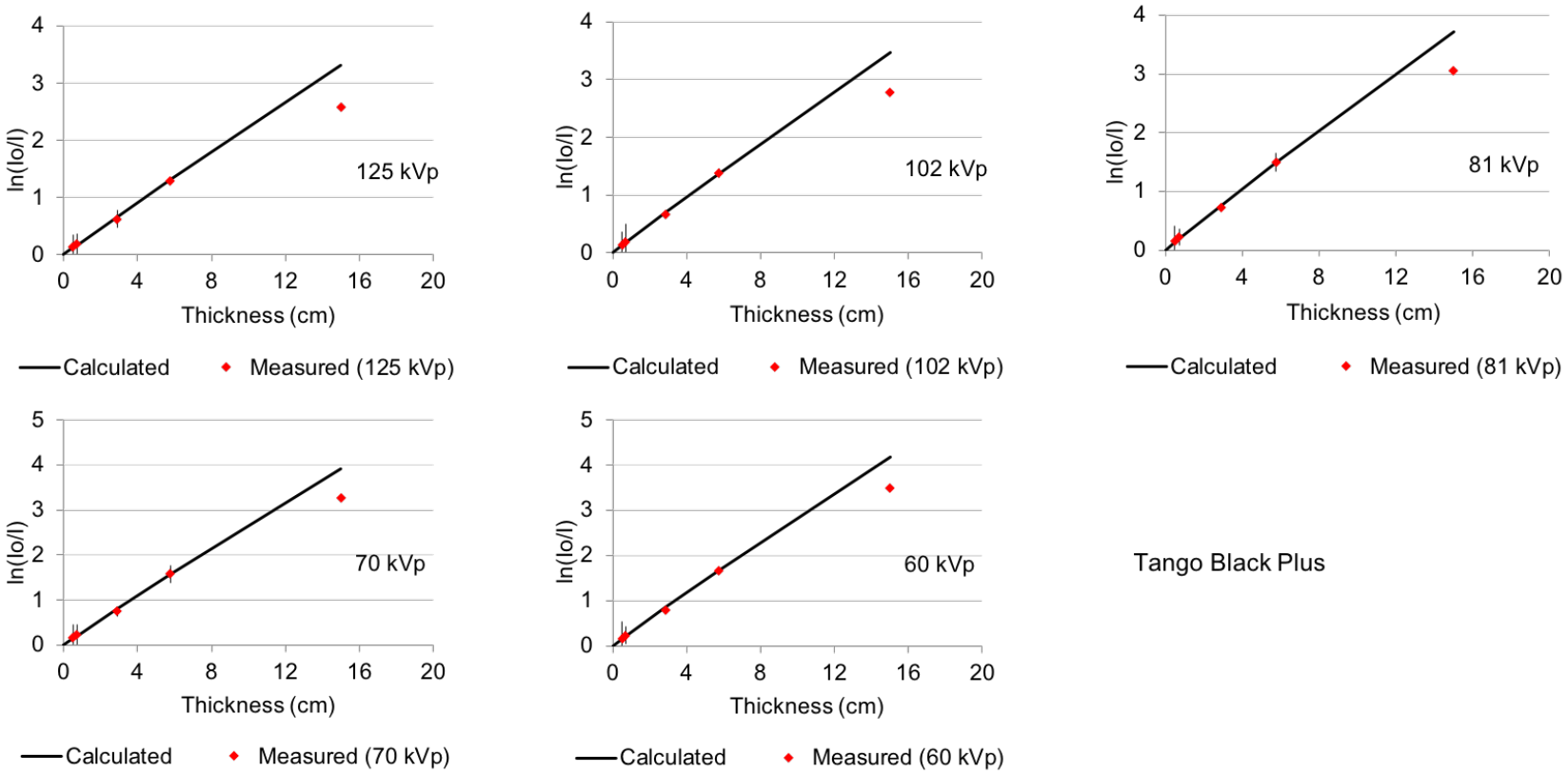

Figure A6.2: Comparison of predicted 3D material Tango Black Plus at the X-ray tube voltage of 125,102, 81, 70 and 60 kVp to each measured output at the defined thicknesses (0.5, 0.7, 2.9, 5.8 and 15 cm).

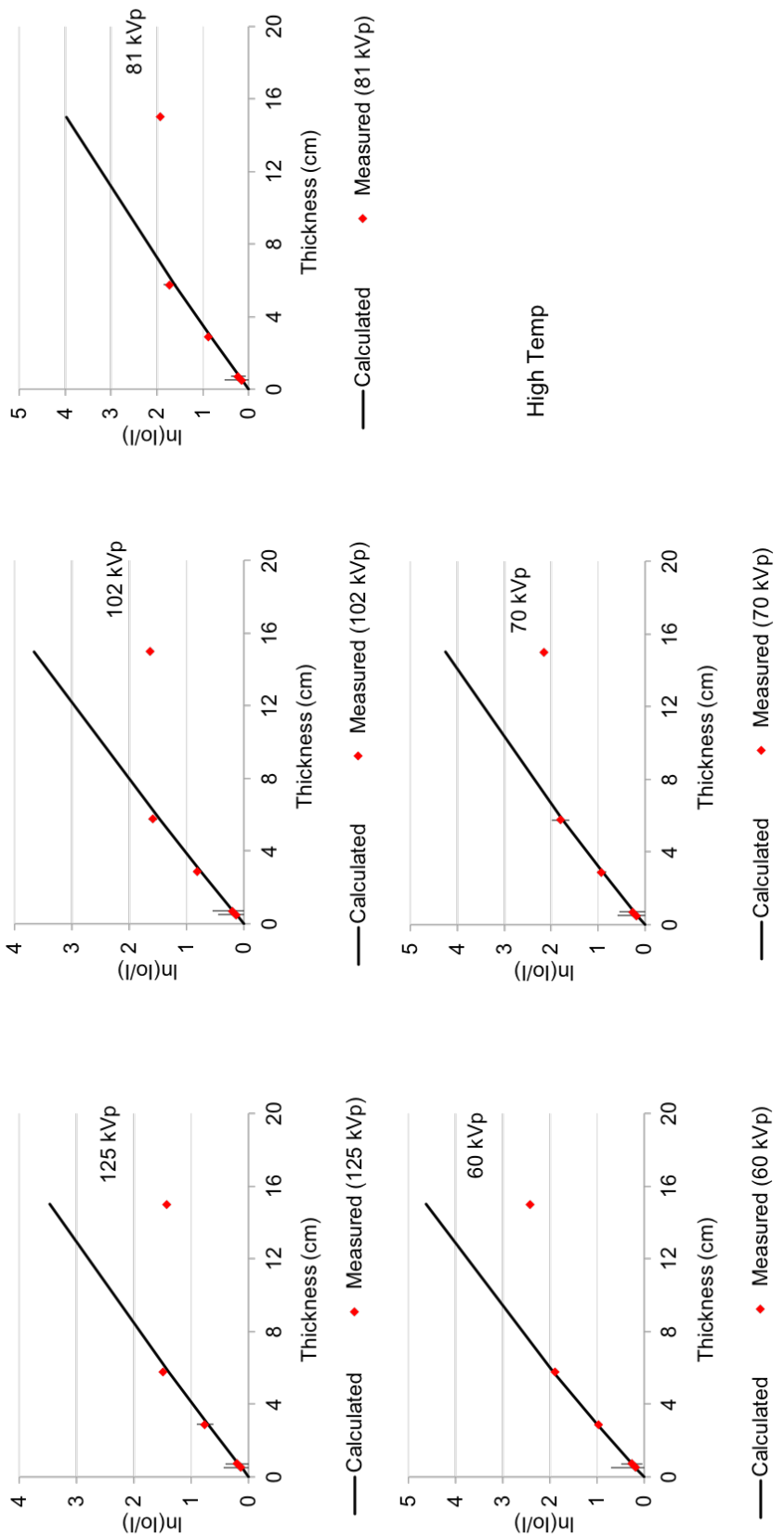

Figure A6.3: Comparison of predicted 3D material High Temp at the X-ray tube voltage of 125, 102, 81, 70 and 60 kVp to each measured output at the defined thicknesses (0.5, 0.7, 2.9, 5.8 and 15 cm).

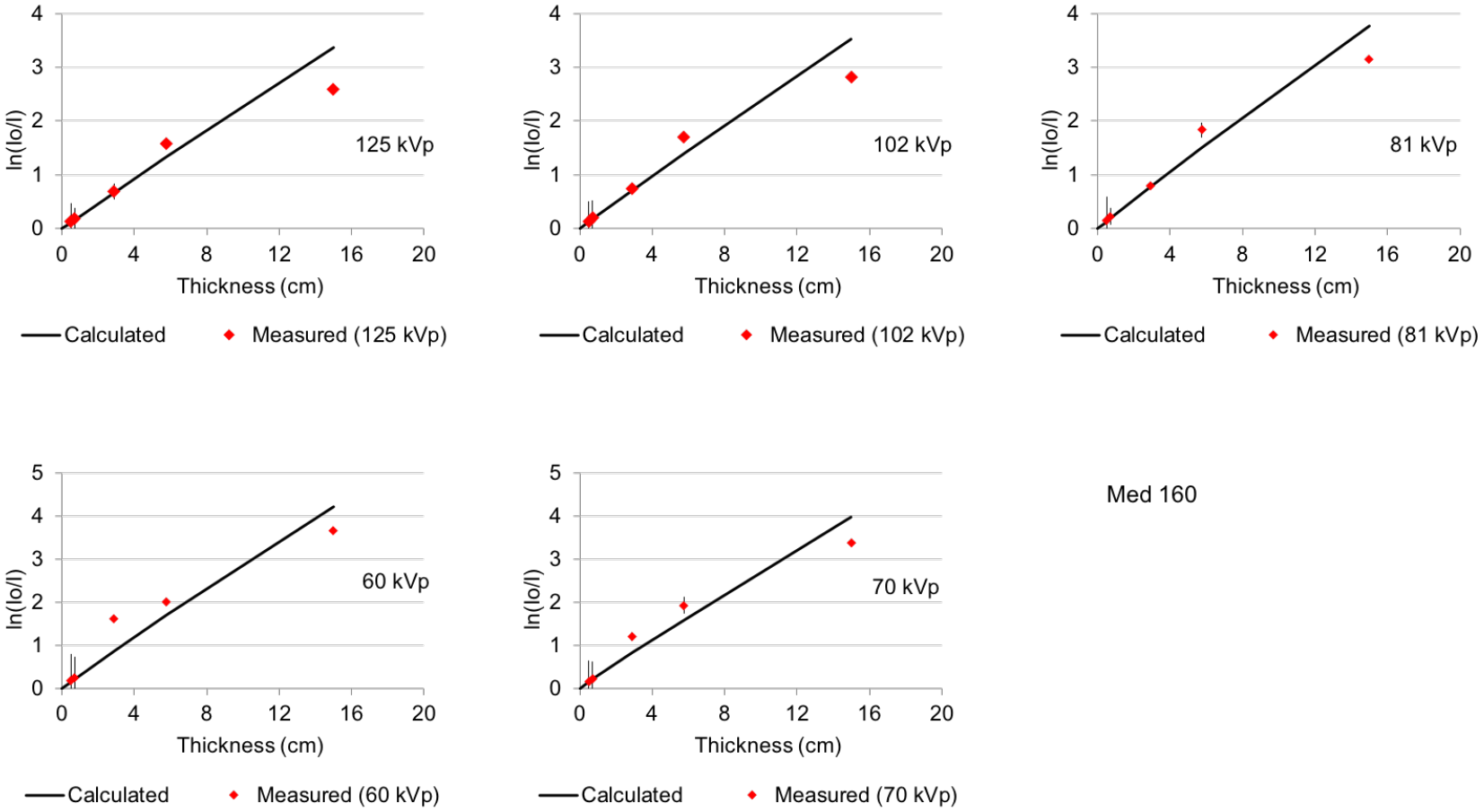

Figure A6.4: Comparison of predicted 3D material Med 160 at the X-ray tube voltage of 125,102, 81, 70 and 60 kVp to each measured output at the defined thicknesses (0.5, 0.7, 2.9, 5.8 and 15 cm).

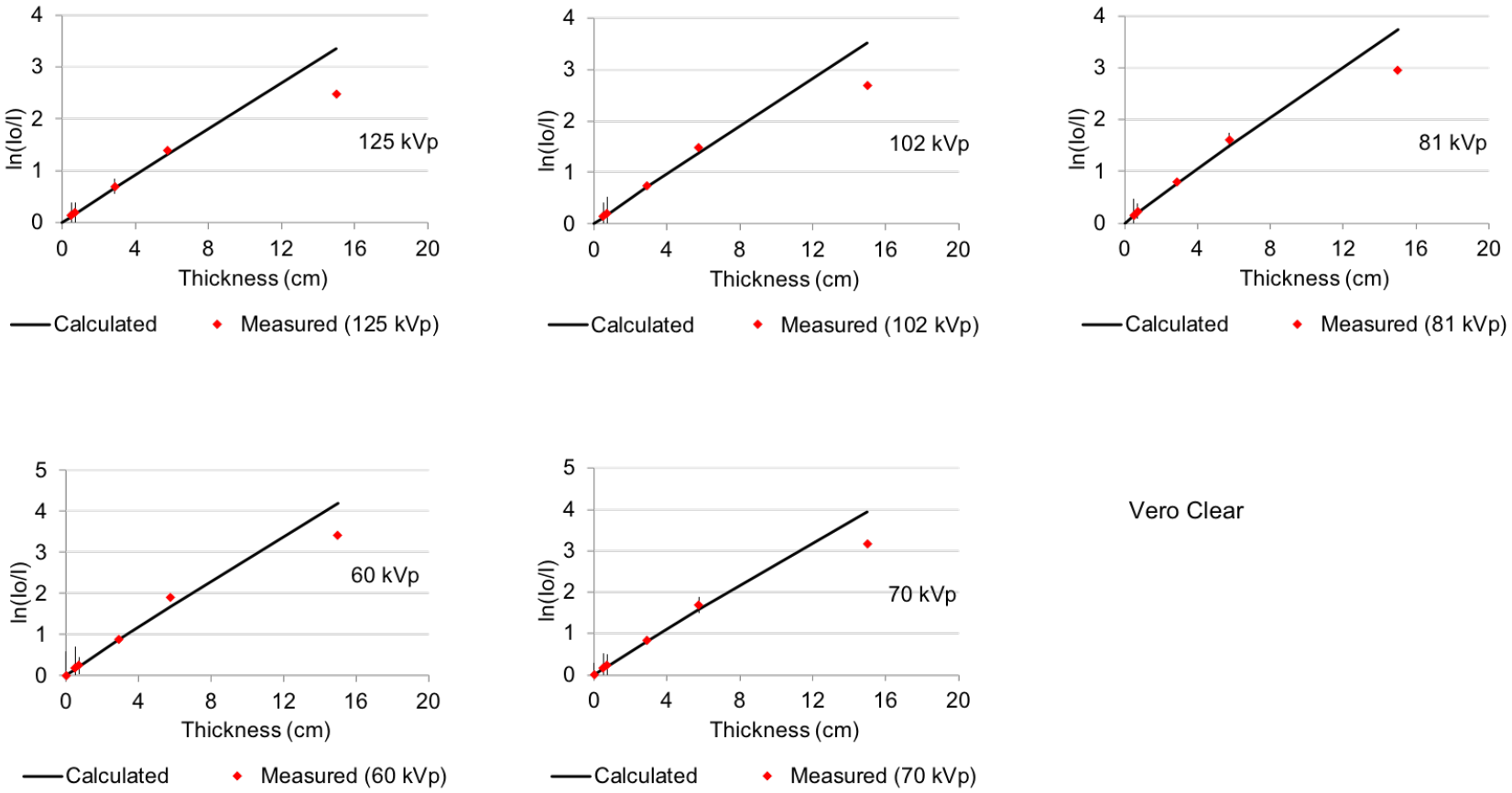

Figure A6.5: Comparison of predicted 3D material Vero Clear at the X-ray tube voltage of 125,102, 81, 70 and 60 kVp to each measured output at the defined thicknesses (0.5, 0.7, 2.9, 5.8 and 15 cm).

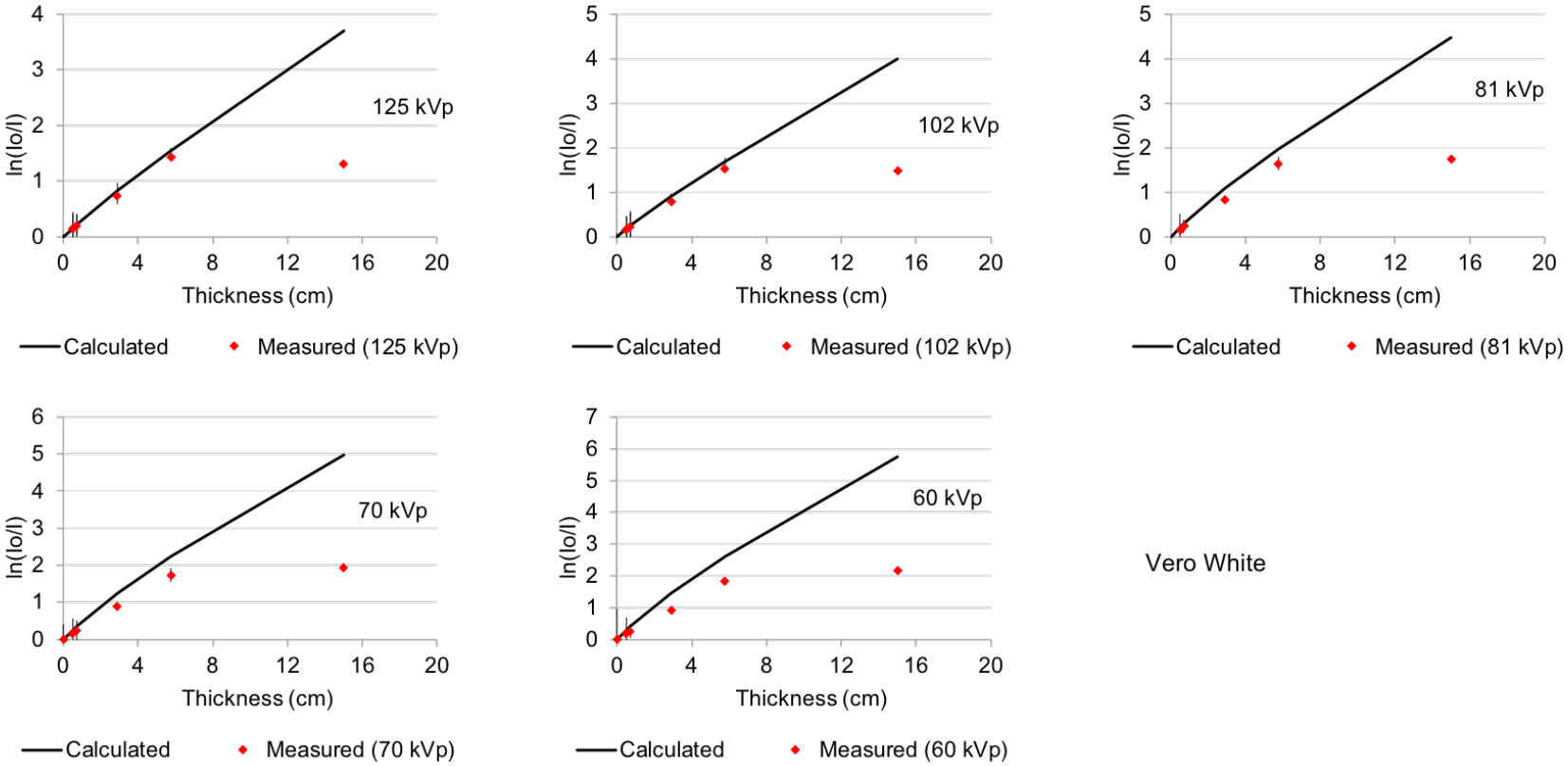

Figure A6.6: Comparison of predicted 3D material Vero White at the X-ray tube voltage of 125,102, 81, 70 and 60 kVp to each measured output at the defined thicknesses (0.5, 0.7, 2.9, 5.8 and 15 cm).

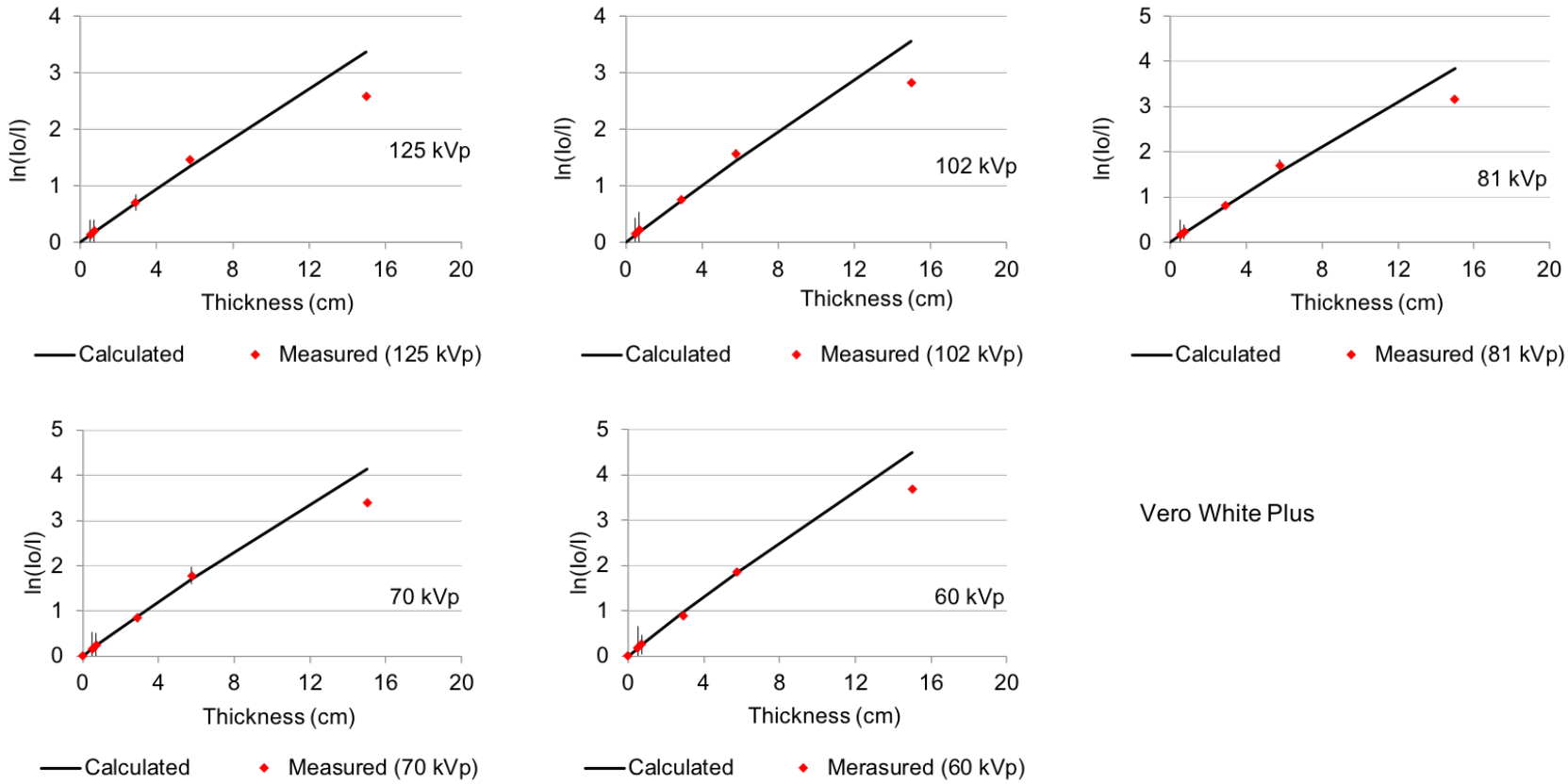

Figure A6.7: Comparison of predicted 3D material Vero White Plus at the X-ray tube voltage of 125,102, 81, 70 and 60 kVp to each measured output at the defined thicknesses (0.5, 0.7, 2.9, 5.8 and 15 cm).

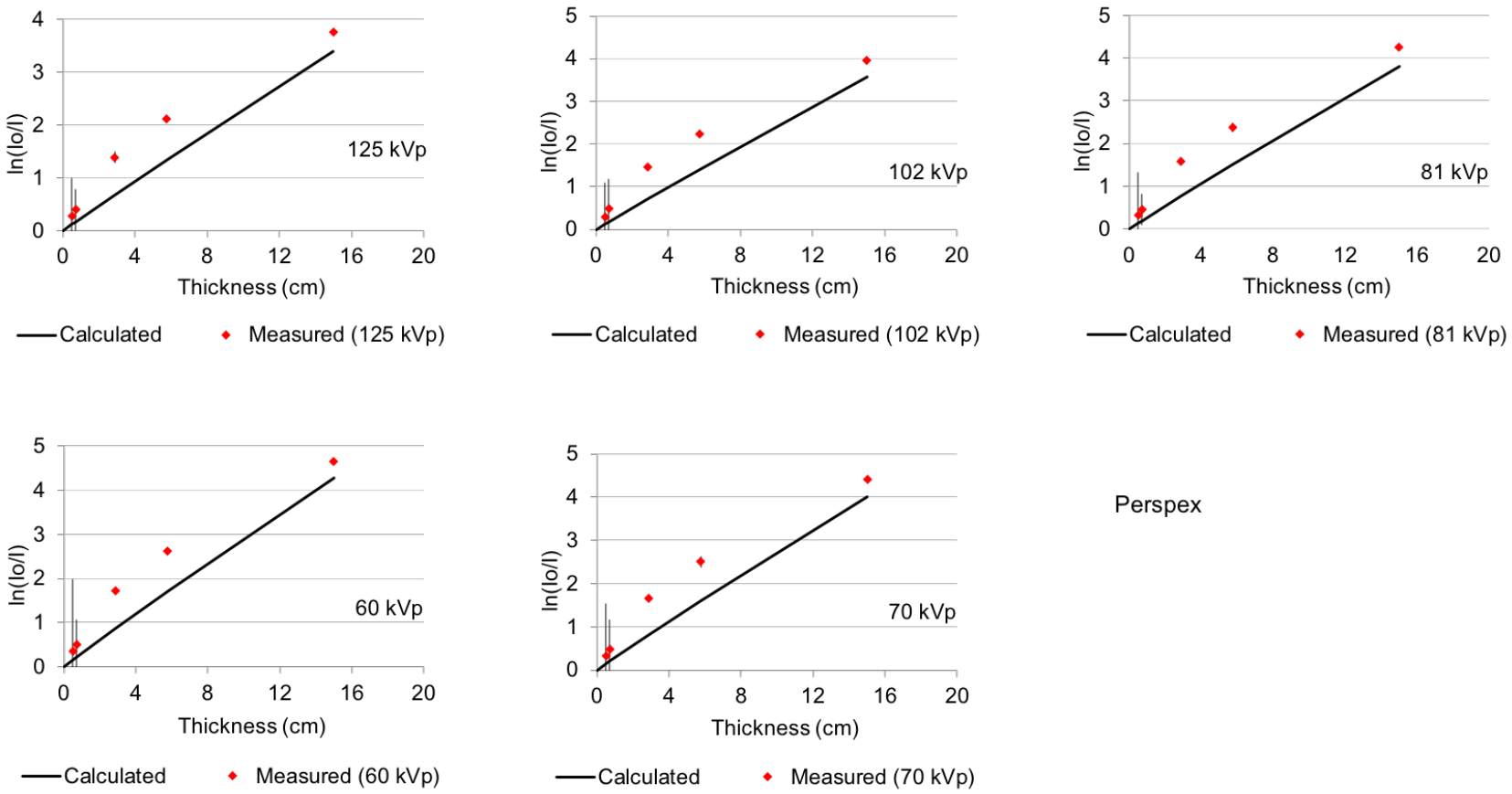

Figure A6.8: Comparison of predicted 3D material Perspex at the X-ray tube voltage of 125,102, 81, 70 and 60 kVp to each measured output at the defined thicknesses (0.5, 0.7, 2.9, 5.8 and 15 cm).

Appendix 7. 3D-printing material measured versus calculated percent differences

Thickness (cm)	Measured ln(Io/I)	Calculated ln(Io/I)	Percent Difference (%)	Measured ln(Io/I)	Calculated ln(Io/I)	Percent Difference (%)	Measured ln(Io/I)	Calculated ln(Io/I)	Percent Difference (%)	Measured ln(Io/I)	Calculated ln(Io/I)	Percent Difference (%)	Measured ln(Io/I)	Calculated ln(Io/I)	Percent Difference (%)
High Temp	125 kVp			102 kVp			81 kVp			70 kVp			60 kVp		
0.5	0.14	0.13	-10	0.15	0.14	-10	0.17	0.15	-10	0.17	0.16	-2	0.18	0.18	1
0.7	0.2	0.18	-12	0.21	0.19	-12	0.24	0.21	-12	0.25	0.23	-8	0.26	0.26	-2
2.9	0.76	0.71	-8	0.81	0.76	-7	0.87	0.84	-5	0.92	0.91	-1	0.97	1	3
5.8	1.49	1.38	-8	1.59	1.47	-8	1.72	1.62	-7	1.8	1.75	-3	1.89	1.91	1
15	1.44	3.47	59	1.64	3.66	55	1.93	3.97	51	2.15	4.25	49	2.41	4.62	48
Med 160	125 kVp			102 kVp			81 kVp			70 kVp			60 kVp		
0.5	0.13	0.12	-12	0.14	0.12	-15	0.16	0.14	-18	0.16	0.14	-11	0.17	0.15	-11
0.7	0.19	0.17	-15	0.21	0.18	-18	0.23	0.19	-21	0.23	0.2	-14	0.25	0.22	-14
2.9	0.7	0.67	-4	0.74	0.71	-5	0.8	0.76	-5	1.21	0.81	-49	1.61	0.87	-85
5.8	1.59	1.33	-20	1.69	1.39	-22	1.83	1.5	-23	1.93	1.59	-22	2.01	1.69	-18
15	2.59	3.37	23	2.83	3.53	20	3.15	3.77	16	3.39	3.97	15	3.66	4.22	13

Table A7.1: Measured and predicted attenuation coefficients values along with the calculated percent difference from predicted to measured are shown for High Temp and Med 160.

Thickness (cm)	Measured ln(Io/I)	Calculated ln(Io/I)	Percent Difference (%)	Measured ln(Io/I)	Calculated ln(Io/I)	Percent Difference (%)	Measured ln(Io/I)	Calculated ln(Io/I)	Percent Difference (%)	Measured ln(Io/I)	Calculated ln(Io/I)	Percent Difference (%)	Measured ln(Io/I)	Calculated ln(Io/I)	Percent Difference (%)
Tango Black	125 kVp			102 kVp			81 kVp			70 kVp			60 kVp		
0.5	0.13	0.12	-12	0.14	0.12	-17	0.16	0.13	-20	0.16	0.14	-15	0.17	0.15	-11
0.7	0.19	0.16	-16	0.2	0.17	-19	0.23	0.19	-22	0.23	0.2	-16	0.25	0.21	-17
2.9	0.65	0.66	1	0.7	0.69	-1	0.75	0.74	-1	0.79	0.79	0	0.82	0.84	3
5.8	1.38	1.3	-7	1.48	1.36	-9	1.6	1.46	-10	1.69	1.54	-10	1.76	1.65	-7
15	2.92	3.3	12	3.12	3.45	10	3.4	3.68	8	3.6	3.88	7	3.79	4.11	8
Vero White	125 kVp			102 kVp			81 kVp			70 kVp			60 kVp		
0.5	0.14	0.16	13	0.15	0.18	16	0.16	0.22	24	0.17	0.25	33	0.18	0.3	40
0.7	0.2	0.22	9	0.22	0.25	13	0.24	0.3	21	0.24	0.35	31	0.26	0.42	37
2.9	0.73	0.82	11	0.78	0.92	15	0.84	1.08	22	0.88	1.24	29	0.93	1.46	37
5.8	1.42	1.55	8	1.52	1.7	11	1.64	1.96	16	1.74	2.23	22	1.82	2.62	30
15	1.3	4.51	71	1.49	3.99	63	1.75	4.47	61	1.94	4.97	61	2.15	5.74	62

Table A7.1 (cont.): Measured and predicted attenuation coefficients values along with the calculated percent difference from predicted to measured are shown for Tango Black and Vero White.

Appendix 8. Measured HU values for 3D-printing materials using three CT protocols

Table A8.1: Evaluation of HU values for the 3D printing materials, acquired using 3 different CT protocols..

CT Protocol	Measured	Digital ABS	Tango Black Plus(T)	Vero White Plus(T)	DM9840	DM9850	DM9860 (M)	DM9860 (T)	DM9870	DM9885 (B)	DM9885 (W)	DM9895
Low Dose	Average	49.59	-60.30	169.41	50.54	36.65	68.60	56.45	79.18	92.66	59.32	113.16
	Standard Deviation (%)	54.99	63.27	185.65	59.00	51.46	54.73	42.05	178.84	67.56	65.39	58.49
High Dose	Average	-9.63	-53.03	65.39	-1.87	-30.24	-34.36	-30.47	-6.79	-2.38	-11.09	6.07
	Standard Deviation (%)	75.83	73.58	94.06	83.70	74.01	73.24	73.71	81.69	78.20	75.00	78.02
Default	Average	-13.12	-54.87	23.91	-34.49	-36.47	-30.96	-41.77	-40.80	-35.20	-26.87	-23.55
	Standard Deviation (%)	28.48	51.05	41.40	19.80	19.78	19.10	19.60	30.08	20.97	21.25	22.26

Table A8.2: Evaluation of HU values for the 4 newly acquired 3D printing materials, acquired using the standard CT protocol.

CT Protocol	Measured	Tango Plus FLX (930)	Vero Black Plus RGD (840)	Vero Blue RGD (835)	Vero White Plus RGD (835)
Standard	Average	-32.00	-11.094	21.04	29.51
	Standard Deviation (%)	26.33	24.25	25.16	26.08

Publication abstracts

1. Standardisation of preclinical PET/CT imaging to improve quantitative accuracy, precision and reproducibility: a multi-center study. *Journal of Nuclear Medicine*, 2019, 27/09. doi:10.2967/jnumed.119.231308

Preclinical Positron Emission Tomography/Computed Tomography (PET/CT) is a well-established non-invasive imaging tool for studying disease development/progression and the development of novel radiotracers and pharmaceuticals for clinical applications. Despite this pivotal role, standardization of preclinical PET/CT protocols, including CT absorbed dose guidelines, is essentially non-existent. This study: (1) quantitatively assesses the variability of current preclinical PET/CT acquisition and reconstruction protocols routinely used across multiple centers and scanners; and (2) proposes acquisition and reconstruction PET/CT protocols for standardization of multi-center data, optimized for routine scanning in preclinical PET/CT laboratory. **Methods:** Five different commercial preclinical PET/CT scanners in Europe and USA were enrolled. Seven different PET/CT phantoms were used for evaluating biases on default/general scanner protocols; followed by developing standardized protocols. PET, CT and absorbed dose biases were assessed. **Results:** Site default CT protocols: Greatest extracted Hounsfield Units (HU) for water was 133HU and -967HU for air, significant differences in all tissue equivalent material (TEM) groups were measured. Average CT absorbed dose for mouse and rat was 72 mGy and 40 mGy, respectively. Standardized CT protocol: Greatest extracted HU for water was -77HU and -990HU for air, TEM precision improved with a reduction in variability for each tissue group. Average CT absorbed dose for mouse and rat was reduced to 37 mGy and 24 mGy, respectively. Site default PET protocols: Uniformity was substandard in one scanner, Recovery Coefficients (RCs) were either over or under estimated (maximum of 43%), standard uptake values (SUVs) were biased by a maximum of 44%. Standardized PET protocol: Scanner with substandard uniformity improved by 36%, RC variability was reduced by 13% points and SUV accuracy improved to 10%. **Conclusion:** Data

revealed important quantitative bias in preclinical PET/CT and absorbed doses with default protocols. Standardized protocols showed improvements in measured PET/CT accuracy and precision with reduced CT absorbed dose across sites. Adhering to standardized protocols generates reproducible and consistent preclinical imaging datasets, thus augmenting translation of research findings to the clinic.

2. Multi-centre standardisation of preclinical PET/CT imaging: a necessary step towards achieving translational imaging datasets. *Mol Imaging Biol*. 2018;20(1):84. doi:10.1007/s11307-018-01305-2.

Preclinical Positron Emission Tomography/Computed Tomography (PET/CT) is a key non-invasive imaging tool for studying disease development/progression and the development of novel radiotracers and pharmaceuticals for translation to clinical trials. Despite this pivotal role, standardization in preclinical PET/CT protocols is essentially non-existent. This project addresses such lack of global standardized preclinical PET/CT imaging protocols by evaluating biases across centers using default scanner protocols; followed by developing standardized protocols for optimisation of PET/CT imaging at multiple centers.

Five different commercial preclinical PET/CT scanners in Europe and USA were enrolled in the study. Seven different phantoms were used: CT air/water phantom, CT tissue-equivalent phantom (TEM) for measuring and quantifying Hounsfield (HU) bias, CT spatial resolution phantom, CT dose index rat and mouse phantoms to assess the absorbed dose, PET image quality phantom for quantification of PET uniformity, recovery coefficients (RC) and spill-out-ratios (SOR), PET rod phantom for evaluation of spatial resolution.

Site default CT protocols: greatest difference in extracted HU was 127% for water and 12% for air, measured TEM HU analysis indicated significant differences in all tissue groups ($p < 0.0001$, one-way ANOVA, $n=3$ per group), ionized radiation absorbed doses ranged from 11.5 mGy to 216.1 mGy. Standardized CT protocol: overall reduction of average water HU bias by

179%, TEM analysis showed improved precision, CT absorbed dose was reduced by 81% in one scanner and an overall global reduction of 40%. Default PET: only two PET scanners resolved 1.2 mm rods; none resolved <1.0mm rods, one scanner's measured PET uniformity was substandard, RCs were either overestimated or underestimated (maximum of 43%) relative to expected activity, SUV values varied from 2.1 to 3.6 g/mL. Standardized PET protocol: improved uniformity by 36% in scanner with substandard uniformity, reduced RC variability by 13% points.

Data revealed important quantification bias in PET and CT, as well as substantial variability in radiation absorbed doses across sites when using default protocols. This highlights the importance of preclinical PET/CT protocol standardization. use of standardized protocols showed improvements on PET uniformity, RC and improved precision in measured HU as well as CT absorbed dose reductions. Adhering to standardized protocols has the potential to improve reproducible and consistent imaging datasets, thus augmenting translational value of preclinical findings to the clinic.

3. Multi-centre standardisation of preclinical PET/CT imaging: a necessary step towards achieving translational imaging datasets. *Mol Imaging Biol*. 2018;20(1):84. doi:10.1007/s11307-018-01305-2.

Introduction: Preclinical Positron Emission Tomography/Computed Tomography (PET/CT) is a key non-invasive imaging tool for studying disease development and progression as well as for the development of novel radiotracers and pharmaceuticals. Despite this pivotal role, standardization of acquisition and reconstruction in PET/CT protocols is essentially non-existent. This project addresses such lack of global standardized preclinical PET/CT imaging protocols by evaluating biases across centres using default scanner protocols; followed by developing standardized protocols for optimisation of PET/CT imaging at multiple centres.

Methods: Six different commercial preclinical PET/CT scanners in Europe and USA were enrolled in this study. Eight different phantoms were used: CT air/water phantom to quantify Hounsfield (HU) bias in water/air, tissue-equivalent phantom to measure HU bias in different tissue-equivalent materials (TEM), CT spatial resolution phantom, CT dose index rat and mouse phantoms to assess the absorbed dose, PET image quality phantom (PET uniformity, recovery coefficients (RC) and spill-out-ratios (SOR)), PET rod phantom (measurement PET resolution) and linearity phantom (noise equivalent counts (NEC).

Results: Four scanners' extracted HU values within expected range for air (-999±40HU), and water (34±95HU). One scanner had HU values in water of 133±284HU. Another scanner outputted CT results as a linear grey scale instead of HU (Fig. 1A). In general, measured TEM HU values were within expected range, apart from one scanner, which output was severely dependent on rod size (difference between 4 mm and 2 mm rod material up to 315%). Measured CT spatial resolution was on average 150 µm, though two scanners were unable to resolve 150µm lines using default protocols. Spatial resolution improved to 100 µm when using high-dose CT protocols. CT absorbed doses using default protocols at each site ranged from 11.5 mGy to 268.2 mGy. Using the PET rod phantom, all but one scanner resolved 2.0, 1.5 and 1.2 mm rods; none resolved 0.6, 0.8 and 1.0 mm rods. Spatial resolution varied due to default scanner reconstruction algorithms used (maximum-likelihood expectation–maximization (MLEM) or ordered-subset-expectation-maximization (OSEM)), each implementing different iterations and subsets (Fig. 1B). One scanner failed PET uniformity limit of 15% and the SOR values were above 0.15. RCs were either overestimated or underestimated by a maximum of 16% at 3, 4, and 5 mm cylinders relative to expected activity.

Conclusion: Data collected revealed important quantification bias in PET and CT preclinical protocols, and variability in CT absorbed doses across sites when using variable default protocols. This highlights the importance of preclinical PET/CT protocol standardization. Standardized protocols that are currently being piloted at

the enrolled sites in this seminal project could be expanded to other preclinical PET/CT sites globally. Adhering to standardized protocols has the potential to improve reproducible and consistent imaging datasets, thus augmenting translational value of preclinical findings to the clinic.

4. High Dose MicroCT Does Not Contribute Toward Improved MicroPET/CT Image Quantitative Accuracy and Can Limit Longitudinal Scanning of Small Animals. *Front Phys*. 2017;5 (October):1-11. doi:10.3389/fphy.2017.00050.

Obtaining accurate quantitative measurements in preclinical Positron Emission Tomography/Computed Tomography (PET/CT) imaging is of paramount importance in biomedical research and helps supporting efficient translation of preclinical results to the clinic. The purpose of this study was two-fold: (1) to investigate the effects of different CT acquisition protocols on PET/CT image quality and data quantification; and (2) to evaluate the absorbed dose associated with varying CT parameters.

Methods: An air/water quality control CT phantom, tissue equivalent material phantom, an in-house 3D printed phantom and an image quality PET/CT phantom were imaged using a Mediso nanoPET/CT scanner. Collected data was analysed using PMOD software, VivoQuant software and National Electric Manufactures Association (NEMA) software implemented by Mediso. Measured Hounsfield Unit (HU) in collected CT images were compared to the known HU values and image noise was quantified. PET recovery coefficients (RC), uniformity and quantitative bias were also measured. **Results:** Only less than 2% and 1% of CT acquisition protocols yielded water HU values < -80 and air HU values < -840, respectively. Four out of eleven CT protocols resulted in more than 100 mGy absorbed dose. Different CT protocols did not impact PET uniformity and RC and resulted in <4% overall bias relative to expected radioactive concentration. **Conclusion:** Preclinical CT protocols with increased exposure times can result in high absorbed doses to the small animals. These should be avoided, as they do not contribute towards improved microPET/CT image quantitative accuracy and could limit longitudinal scanning of small animals.

References

1. Alessio A, Kinahan P. PET image reconstruction. *Nucl Med*. 2006;1(figure 1):1-22. doi:10.1088/0031-9155/54/12/007.Iterative
2. Massoud TF, Gambhir SS. Molecular imaging in living subjects: Seeing fundamental biological processes in a new light. *Genes Dev*. 2003;17(5):545-580. doi:10.1101/gad.1047403
3. Sundaram GSM, Dhavale DD, Prior JL, et al. Fluselenamyl: A Novel Benzoselenazole Derivative for PET Detection of Amyloid Plaques (Aβ) in Alzheimer's Disease. *Sci Rep*. 2016;6(November):35636. doi:10.1038/srep35636
4. Boschi S, Lee JT, Beykan S, et al. Synthesis and preclinical evaluation of an Al18F radiofluorinated GLU-UREA-LYS(AHX)-HBED-CC PSMA ligand. *Eur J Nucl Med Mol Imaging*. 2016;43(12):2122-2130. doi:10.1007/s00259-016-3437-y
5. Koba W, Jelicks L a, Fine EJ. MicroPET/SPECT/CT imaging of small animal models of disease. *Am J Pathol*. 2013;182(2):319-324. doi:10.1016/j.ajpath.2012.09.025
6. Haylock AK, Spiegelberg D, Mortensen AC, et al. Evaluation of a novel type of imaging probe based on a recombinant bivalent mini-antibody construct for detection of CD44v6-expressing squamous cell carcinoma. *Int J Oncol*. 2016;48(2):461-470. doi:10.3892/ijo.2015.3290
7. Fodero-Tavoletti MT, Okamura N, Furumoto S, et al. 18F-THK523: A novel in vivo tau imaging ligand for Alzheimer's disease. *Brain*. 2011;134(4):1089-1100. doi:10.1093/brain/awr038
8. Zhang C, Pan J, Lin K-S, et al. Improved 68Ga-labelled truncated peptides targeting the neuropeptide Y1 receptor for cancer imaging by positron emission tomography. *J Nucl Med*. 2016;57(supplement 2):1160-1160. doi:10.1021/acs.molpharmaceut.6b00464
9. Chapman SE, Diener JM, Sasser TA, et al. Dual tracer imaging of SPECT and PET probes in living mice using a sequential protocol. *Am J Nucl Med Mol Imaging*. 2012;2(4):405-414. www.ajnmmi.us.
10. Manook A, Yousefi BH, Willuweit A, et al. Small-animal PET imaging of amyloid-beta plaques with [11c]PiB and its multi-modal validation in an APP/PS1 mouse model of Alzheimer's disease. *PLoS One*. 2012;7(3). doi:10.1371/journal.pone.0031310

11. Nie X, Laforest R, Elvington A, et al. PET/MRI of Hypoxic Atherosclerosis Using 64Cu-ATSM in a Rabbit Model. *J Nucl Med*. 2016;57(12):2006-2011. doi:10.2967/jnumed.116.172544
12. Hartwig H, Silvestre-Roig C, Hendrikse J, et al. Atherosclerotic plaque destabilization in Mice: A comparative study. *PLoS One*. 2015;10(10):1-14. doi:10.1371/journal.pone.0141019
13. Saraste A, Laitinen I, Weidl E, et al. Diet intervention reduces uptake of avB3 integrin-targeted PET tracer 18F-galacto-RGD in mouse atherosclerotic plaques. *J Nucl Cardiol*. 2012;19(4):775-784. doi:10.1007/s12350-012-9554-5
14. Tremoleda JL, Kerton A, Gsell W. Anaesthesia and physiological monitoring during in vivo imaging of laboratory rodents: considerations on experimental outcomes and animal welfare. *EJNMMI Res*. 2012;2(1):44. doi:10.1186/2191-219X-2-44
15. McGirr R, Hu S, Yee SP, Kovacs MS, Lee TY, Dhanvantari S. Towards PET imaging of intact pancreatic beta cell mass: A transgenic strategy. *Mol Imaging Biol*. 2011;13(5):962-972. doi:10.1007/s11307-010-0435-5
16. Fushiki H, Miyoshi S NA. Pre-clinical Validation of Orthotopically-implanted Pulmonary Tumor by Imaging with 18F-Fluorothymidine-Positron Emission Tomography/Computed Tomography. *Anticancer Res*. 2013;33(11):4741-4749. http://ar.iiarjournals.org.ezp-prod1.hul.harvard.edu/content/33/11/4741.full.
17. Palner M, Shen B, Jeon J, Lin J, Chin FT, Rao J. Preclinical kinetic analysis of the Caspase-3/7 PET tracer 18F-C-SNAT: quantifying the changes in blood flow and tumor retention after chemotherapy. *J Nucl Med*. 2015;56(9):1415-1421. doi:10.2967/jnumed.115.155259
18. Osborne DR, Kuntner C, Berr S, Stout D. Guidance for efficient small animal imaging quality control. *Mol Imaging Biol*. 2017;19(4):485-498. doi:10.1007/s11307-016-1012-3
19. Kersemans V, Thompson J, Cornelissen B, et al. Micro-CT for anatomic referencing in PET and SPECT: Radiation dose, biologic damage, and image quality. *J Nucl Med*. 2011;52(11):1827-1833. doi:10.2967/jnumed.111.089151
20. Figueroa SD, Winkelmann CT, Miller HW, Volkert W a, Hoffman TJ. TLD assessment of mouse dosimetry during microCT imaging. *Med Phys*. 2008;35(9):3866-3874. doi:10.1118/1.2959847
21. Willekens I, Buls N, Lahoutte T, et al. Evaluation of the radiation dose in micro-CT with

optimization of the scan protocol. *Contrast Media Mol Imaging*. 2010;5(4):201-207. doi:10.1002/cmmi.394

22. Wagner LK, Eifel PJ, Geise RA. Potential biological effects following high X-ray dose interventional procedures. *J Vasc Interv Radiol*. 1994;5(1):71-84. doi:10.1016/S1051-0443(94)71456-1
23. Perks JR, Lucero S, Monjazeb AM, Li JJ. Anthropomorphic Phantoms for Confirmation of Linear Accelerator-Based Small Animal Irradiation. *Cureus*. 2015;7(3):e254. doi:10.7759/cureus.254
24. Black QC, Grills IS, Kestin LL, et al. Defining a radiotherapy target with positron emission tomography. *Int J Radiat Oncol Biol Phys*. 2004;60(4):1272-1282. doi:10.1016/j.ijrobp.2004.06.254
25. Goertzen a. L, Bao Q, Bergeron M, et al. NEMA NU 4-2008 Comparison of Preclinical PET Imaging Systems. *J Nucl Med*. 2012;53(8):1300-1309. doi:10.2967/jnumed.111.099382
26. Wagner HN. A brief history of positron emission tomography (PET). *Semin Nucl Med*. 1998;28(3):213-220. doi:10.1016/S0001-2998(98)80027-5
27. Nutt R. The history of positron emission tomography. *Mol Imaging Biol*. 2002;4(1):11-26. doi:10.1016/S1095-0397(00)00051-0
28. Dirac P. The Quantum Theory of the Electron. *R Soc London*. 1928;Series A.
29. Anderson CD. The Production and Properties of Positrons. *Nobelprize.org*. 1936:6-19. doi:10.1080/00405167.1978.10750134
30. Feynman RP. The theory of positrons. *Phys Rev*. 1949;76(6):749-759. doi:10.1103/PhysRev.76.749
31. Valk PE, Delbeke D, Bailey DL, Townsend DW, Maisey MN. *Positron Emisson Tomography*.; 2006.
32. Townsend DW. Physical principles and technology of clinical PET imaging. *Ann Acad Med Singapore*. 2004;33(2):133-145.
33. Livingston L. Production of High Speed Light Ions without the use of High Voltages. *Phys Rev*. 1932;40.
34. Lawrence E. The Evolution of the Cyclotron. *Nobelprize.org*. 1939:430-443. http://www.nobelprize.org/nobel_prizes/physics/laureates/1939/lawrence-lecture.pdf.

35. Joliot F, Curie I. Artificial Production of a New Kind of Radio-Element. *Nature*. 1934;133(3354):201-202. doi:10.1038/133201a0
36. Hutton BF. The contribution of Medical Physics to Nuclear Medicine: looking back - a physicist's perspective. *EJNMMI Phys*. 2014;1(1):2. doi:10.1186/2197-7364-1-2
37. Wrenn FR, Good ML. of Positron-emitting Radioisotopes. 1951:525-528.
38. Brownell GL. A History of Positron Imaging. *Phys Res Lab Massachusetts Gen Hosp*. 1999:1-11. http://www.petdiagnostik.ch/PET_History/alb.html.
39. Sweet WH. The uses of nuclear disintegration in the diagnosis and treatment of brain tumor. *N Engl J Med*. 1951;245(23):875-878. doi:10.1056/NEJM195112062452301
40. Ter-pogossian MM. Basic Principles of Computed Axial Tomography.
41. Kay DB, Keyes JW, Simon W. Radionuclide tomographic image reconstruction using Fourier transform techniques. *J Nuc Med*. 1974;15(11):981-986. jnm 15 11 981.
42. Phelps ME, Hoffman EJ, Huang SC, Kuhl DE. ECAT: A new computerized tomographic imaging system for positron- emitting radiopharmaceuticals. *J Nucl Med*. 1978;19(6):635-647.
43. Stearns CW, Chesler DA, Brownell GL. Three-dimensional image reconstruction in the Fourier domain. *IEEE Trans Nuc Sci*. 1987;34(1):374-378.
44. Ludgate SM, Merrick M V. The pathogenesis of post-irradiation chronic diarrhoea: Measurement of SeHCAT and B12 absorption for differential diagnosis determines treatment. *Clin Radiol*. 1985;36(3):275-278. doi:10.1016/S0009-9260(85)80059-3
45. Phelps M, Hoffman EJ, Nizar M, Higgins C, Ter-pogossian MM. Design considerations for a positron emission transaxial tomograph (PET III). *IEEE Trans Nucl Sci*. 1976;NS-23(1):515-522.
46. Phelps ME, Huang SC, Hoffman EJ, Selin C. Tomographic Measurement of Local Cerebral Glucose Metabolic Rate in Humans with Validation of Method. 1978:371-388.
47. Phelps ME, Hoffman EJ, Mullani NA, Ter-Pogossian MM. Application of annihilation coincidence detection to transaxial reconstruction tomography. *J Nucl Med*. 1975;16(3):210-224.
48. Wilkinson F. Scintillators. In: *The Fundamentals of PET and SPECT*. ; 2004. https://books.google.co.uk/books?isbn=0080521878.
49. Van Eijk CWE. Inorganic scintillators in medical imaging detectors. *Nucl Instruments*

Methods Phys Res Sect A Accel Spectrometers, Detect Assoc Equip. 2003;509(1-3):17-25. doi:10.1016/S0168-9002(03)01542-0

50. Wilkinson III F. Methodology for packaging reliable scintillation detectors. 2007;6707:670702. doi:10.1117/12.740809
51. Melcher CL. Scintillation crystals for PET. *J Nucl Med*. 2000;41(6):1051-1055.
52. Sokoloff L, Reivich M, Kennedy C, et al. The [14 C]Deoxyglucose Method for the Measurement of Local Cerebral Glucose Utilization: Theory, Procedure, and Normal Values in the Conscious and Anesthetized Albino Rat. *J Neurochem*. 1977;28(5):897-916. doi:10.1111/j.1471-4159.1977.tb10649.x
53. Fowler JS, Ido T. Initial and subsequent approach for the synthesis of18FDG. *Semin Nucl Med*. 2002;32(1):6-12. doi:10.1053/snuc.2002.29270
54. Gallagher B, Ansari A, Atkins H. deoxy-2-fluoro-D-glucose as a radiopharmaceutical for measuring regional myocardial glucose metabolism in vivo: tissue distribution and imaging studies. *J Nucl Med*. 1977:4-9.
55. Electrical N, Assocation M. NEMA Standards Publication NU 4 – 2008 Performance measurements of small animal positron emission tomographs. 2008.
56. Levering A, Reddin J, Siegel B. Qualification Procedures for PET or PET / CT Imaging. *Am Coll Radiol*. 2009:1-2.
57. Hounsfield GN. Computed medical imaging. *Med Phys*. 1980;7(4):283-290. doi:10.1118/1.594709
58. Block MS, Zide F, Kent JN. Reconstruction and. 1966:244-246.
59. G.N H. Computerized transverse axial scanning(tomography):Part I description of system. *Br J Radiol*. 1973;46(552):1016-1022. doi:10.1259/0007-1285-46-552-1016
60. Muller HJ. The Productions of Mutations by X-Rays. *Proc th Natl Acad Sci United States Am*. 1928;14(9):714-726. https://www.ncbi.nlm.nih.gov/pubmed/16587397.
61. Consultants AB. Historical Development of Radiation Practices in Radiology. *RadioGraphics*. 1989:267-275. doi:10.1148/radiographics.9.6.2685944
62. Simplified VS, Crotty D, Ph D. Technology White Paper GSI Xtream on Revolution TM CT.
63. Schneider W, Bortfeld T, Schlegel W. Correlation between CT numbers and tissue parameters needed for Monte Carlo simulations of clinical dose distributions. *Phys Med*

Biol. 2000;45(2):459-478. doi:10.1088/0031-9155/45/2/314

64. Eloot L, Buls N, Covens P, Willekens I, Lahoutte T, de Mey J. Quality control of micro-computed tomography systems. *Radiat Prot Dosimetry*. 2010;139(1-3):463-467. doi:10.1093/rpd/ncq088
65. Mah P, Reeves TE, McDavid WD. Deriving Hounsfield units using grey levels in cone beam computed tomography. *Dentomaxillofacial Radiol*. 2010;39(6):323-335. doi:10.1259/dmfr/19603304
66. Goldman LW. Principles of CT and CT Technology. *J Nucl Med Technol*. 2007;35(3):115-128. doi:10.2967/jnmt.107.042978
67. Kinahan PE, Hasegawa BH, Beyer T. X-ray-based attenuation correction for positron emission tomography/computed tomography scanners. *Semin Nucl Med*. 2003;33(3):166-179. doi:10.1053/snuc.2003.127307
68. Lacroix KJ, Hasegawa BH, Phantom ATM. Investigation of the Use of X-ray CT Images For Attenuation Compensation in SPECTt. 1994;41(6).
69. Bazalova M, Carrier J-F, Beaulieu L, Verhaegen F. Dual-energy CT-based material extraction for tissue segmentation in Monte Carlo dose calculations. *Phys Med Biol*. 2008;53(9):2439-2456. doi:10.1088/0031-9155/53/9/015
70. DeMarco JJ, Solberg TD, Smathers JB. A CT-based Monte Carlo simulation tool for dosimetry planning and analysis. *Med Phys*. 1998;25(1):1-11. doi:10.1118/1.598167
71. Schneider U, Pedroni E, Lomax A. The calibration of CT Hounsfield units for radiotherapy treatment planning. *Phys Med Biol*. 1996;41(1):111-124. doi:10.1088/0031-9155/41/1/009
72. ACR, Adiseshaiah PP, Patel NL, et al. NIH Public Access. *J Nucl Med*. 2015;5(3):ajplung.00098.2015. doi:10.1111/j.1741-2358.2011.00571.x
73. Beyer T, Townsend DW, Brun T, et al. A combined PET/CT scanner for clinical oncology. *J Nucl Med*. 2000;41(8):1369-1379. doi:10.3390/su71013920
74. Townsend DW. A Combined PET / CT Scanner : The Choices. 2001;42(3).
75. Beyer T, Kinahan PE, Townsend DW, Sashin D. The use of X-ray. 1995:1573-1577.
76. Townsend DW, Beyer T, Blodgett TM. PET/CT scanners: A hardware approach to image fusion. *Semin Nucl Med*. 2003;33(3):193-204. doi:10.1053/snuc.2003.127314
77. Townsend DW. Combined PET / CT : the historical perspective. *Semin Ultrasound, CT, MRI*. 2009;29(4):232-235. doi:10.1053/j.sult.2008.05.006.Combined

78. Alvarez R, Macovski A. Energy selective reconstructions in X-ray Computerized Tomography. *Phys Med Biol*. 1976;21(5):733-744.
79. Rutherford RA, Pullan BR, Isherwood I. Measurement of Effective Atomic Number and Electron Density Using an EMI Scanner. *Neuroradiology*. 1976;11:15-21. http://dx.doi.org/10.1007/BF00327253.
80. Carney JPJ, Townsend DW, Rappoport V, Bendriem B. Method for transforming CT images for attenuation correction in PET/CT imaging. *Med Phys*. 2006;33(4):976-983. doi:10.1118/1.2174132
81. Kinahan PE, Townsend DW, Beyer T, Sashin D. Attenuation correction for a combined 3D PET/CT scanner. *Med Phys*. 1998;25(10):2046-2053. doi:10.1118/1.598392
82. Burger C, Goerres G, Schoenes S, Buck A, Lonn A, Von Schulthess G. PET attenuation coefficients from CT images: Experimental evaluation of the transformation of CT into PET 511-keV attenuation coefficients. *Eur J Nucl Med*. 2002;29(7):922-927. doi:10.1007/s00259-002-0796-3
83. Desh V, Grove B. (12) United States Patent / CT DATA ; 2005;2(12).
84. Hubbell JH. Photon mass attenuation and energy-absorption coefficients. *Int J Appl Radiat Isot*. 1982;33(11):1269-1290. doi:10.1016/0020-708X(82)90248-4
85. Xia T, Alessio AM, Man B De, Manjeshwar R, Asma E, Kinahan PE. Ultra-low dose CT attenuation correction for PET / CT. 2012;309. doi:10.1088/0031-9155/57/2/309
86. Lewellen TK. The challenge of detector designs for PET. *Am J Roentgenol*. 2010;195(2):301-309. doi:10.2214/AJR.10.4741
87. Defrise M, Kinahan PE, Townsend DW, Michel C, Sibomana M, Newport DF. Exact and approximate rebinning algorithms for 3-d pet data. *IEEE Trans Med Imaging*. 1997;16(2):145-158. doi:10.1109/42.563660
88. Brownell GL. *New Imaging System in Nuclear Medicine*.; 1977.
89. Cherry SR, Gambhir SS. Use of positron emission tomography in animal research. *ILAR J*. 2001;42(3):219-232. doi:10.1093/ilar.42.3.219
90. Lecomte R, Cadorette J, Richard P, Rodrigue S, Rouleau D. Design and Engineering Aspects of a High Resolution Positron Tomograph for Small Animal Imaging. *IEEE Trans Nucl Sci*. 1994;41(4):1446-1452. doi:10.1109/23.322930
91. Chatziioannou AF, Cherry SR, Shao Y, et al. Performance evaluation of microPET: A high-

resolution lutetium oxyorthosilicate PET scanner for animal imaging. *J Nucl Med*. 1999;40(7):1164-1175.

92. Mi W. Are AnimalScannersReallyNecessary for PET? *Inorg Chem*. 1993;35(8):1396-1397.
93. Bloomfield PM, Rajeswaran S, Spinks TJ, et al. The design and physical characteristics of a small animal positron emission tomograph. *Phys Med Biol*. 1995;40(6):1105-1126. doi:10.1088/0031-9155/40/6/010
94. Budinger TF. PET instrumentation: What are the limits? *Semin Nucl Med*. 1998;28(3):247-267. doi:10.1016/S0001-2998(98)80030-5
95. Tornai MP, Jaszczak RJ, Turkington TG, Coleman RE. Small-animal PET: Advent of a new era of PET research. *J Nucl Med*. 1999;40(7):1176-1179.
96. Lewellen TK, Janes M, Miyaoka RS, et al. System integration of the MiCES small animal PET scanner. *IEEE Nucl Sci Symp Conf Rec*. 2004;5(November):3316-3320. doi:10.1109/NSSMIC.2004.1466400
97. Miyaoka RS, Janes ML, Lee K, Park B, Kinahan PE, Lewellen TK. Development of a single detector ring micro crystal element scanner: QuickPET II. *Mol Imaging*. 2005;4(2):117-127. doi:10.1162/15353500200504154
98. Shih YC, Sun FW, MacDonald LR, et al. An 8x8 row-column summing readout electronics for preclinical positron emission tomography scanners. *IEEE Nucl Sci Symp Conf Rec*. 2009;2:2376-2380. doi:10.1109/NSSMIC.2009.5402200
99. Cherry SR, Silverman RW, Meadors K, et al. MicroPET : A High Resolution PET Scanner for Imaging Small Animals. *IEEE Trans Nucl Sci*. 1997;44(3):1161-1166.
100. Lewellen TK, Ieee F, Macdonald LR, et al. New Directions for dMiCE – a Depth-of-Interaction Detector Design for PET Scanners . *IEEE Nucl Sci Symp Conf Rec*. 2007;5:3798-3802.
101. Burr KC, Ivan A, Castleberry DE, et al. Depth-of-interaction-encoding high-resolution PET detector with sub-nanosecond timing. *IEEE Nucl Sci Symp Conf Rec*. 2004;6(C):3880-3884.
102. Bergeron M, Member S, Cadorette J, et al. Performance Evaluation of the LabPET APD-Based Digital PET Scanner. *IEEE Trans Nuc Sci*. 2009;56(1):10-16.
103. McDougald WA, Collins R, Green M, Tavares AAS. High dose MicroCT does not contribute toward improved MicroPET/CT image quantitative accuracy and can limit longitudinal scanning of small animals. *Front Phys*. 2017;5(October):1-11.

doi:10.3389/fphy.2017.00050

104. Vanhove C, Bankstahl JP, Krämer SD, Visser E, Belcari N, Vandenberghe S. Accurate molecular imaging of small animals taking into account animal models, handling, anaesthesia, quality control and imaging system performance. *EJNMMI Phys*. 2015;2(1):1-25. doi:10.1186/s40658-015-0135-y
105. Cavanaugh D, Johnson E, Price RE, Kurie J, Travis EL, Cody DD. In vivo respiratory-gated micro-CT imaging in small-animal oncology models. *Mol Imaging*. 2004;3(1):55-62. doi:10.1162/153535004773861723
106. Kuntner C, Stout D. Quantitative preclinical PET imaging: opportunities and challenges. *Front Phys*. 2014;2(February):1-12. doi:10.3389/fphy.2014.00012
107. Kis SA, Valastyán I, Hegyesi G, et al. Performance Characteristics of a miniPET Scanner Dedicated to Small Animal Imaging. In: *IEEE Nuclear Science Symposium Conference Record*. Vol 3. ; 2005:1645-1648. doi:10.1109/NSSMIC.2005.1596635
108. Yang Y, Tai Y-C, Siegel S, et al. Optimization and performance evaluation of the microPET II scanner for in vivo small-animal imaging. *Phys Med Biol*. 2004;49(12):2527-2545. doi:10.1088/0031-9155/49/12/005
109. Vaezi M, Seitz H, Yang S. A review on 3D micro-additive manufacturing technologies. *Int J Adv Manuf Technol*. 2013;67(5-8):1721-1754. doi:10.1007/s00170-012-4605-2
110. Herrmann K, Dahlbom M, Nathanson D, et al. Evaluation of the Genisys4, a Bench-Top Preclinical PET Scanner. *Nucl Med*. 2013;54(7):1162-1167. doi:10.2967/jnumed.112.114926.Evaluation
111. Nagy K, Toth M, Major P, et al. Performance Evaluation of the Small-Animal nanoScan PET/MRI System. *J Nucl Med*. 2013;54(10):1825-1832. doi:10.2967/jnumed.112.119065
112. Constantinescu C, Mukherjee J. NIH Public Access. 2010;54(9):2885-2899. doi:10.1088/0031-9155/54/9/020
113. Canadas M, Sanz E, Vives M, et al. Performance Evaluation for 68Ga and 18F of the ARGUS Small-Animal PET Scanner Based on the NEMA NU-4 Standard. *IEEE Nucl Sci Symp Conf Rec*. 2010.
114. Disselhorst J a, Brom M, Laverman P, et al. Image-quality assessment for several positron emitters using the NEMA NU 4-2008 standards in the Siemens Inveon small-animal PET scanner. *J Nucl Med*. 2010;51(4):610-617. doi:10.2967/jnumed.109.068858

115. Szanda I, Mackewn J, Patay G, et al. National Electrical Manufacturers Association NU-4 Performance Evaluation of the PET Component of the NanoPET/CT Preclinical PET/CT Scanner. *J Nucl Med*. 2011;52(11):1741-1747. doi:10.2967/jnumed.111.088260

116. Bao Q, Newport D, Chen M, Stout DB, Chatziioannou AF. Performance evaluation of the inveon dedicated PET preclinical tomograph based on the NEMA NU-4 standards. *J Nucl Med*. 2009;50(3):401-408. doi:10.2967/jnumed.108.056374

117. Pajak MZ, Volgyes D, Pimlott SL, et al. NEMA NU4-2008 Performance Evaluation of Albira : A Two-Ring Small-Animal PET System Using Continuous LYSO Crystals. 2016. doi:10.2174/1874220301603010012

118. Tai Y, Ruangma A, Rowland D, et al. Performance evaluation of the microPET focus: a third-generation microPET scanner dedicated to animal imaging. *J Nucl Med*. 2005;46(3):455-463. doi:46/3/455 [pii]

119. Szanda I, Mackewn J, Patay G, et al. National Electrical Manufacturers Association NU-4 performance evaluation of the PET component of the NanoPET/CT preclinical PET/CT scanner. *J Nucl Med*. 2011;52(11):1741-1747. doi:10.2967/jnumed.111.088260

120. Lockhart CM, MacDonald LR, Alessio AM, McDougald WA, Doot RK, Kinahan PE. Quantifying and Reducing the Effect of Calibration Error on Variability of PET/CT Standardized Uptake Value Measurements. *J Nucl Med*. 2011;52(2):218-224. doi:10.2967/jnumed.110.083865

121. Smith WJM, Policy C, Schelbert HR, et al. Procedure guideline for tumor imaging using fluorine-18-FDG. *J Nucl Med*. 1998;39(7):1302-1305.

122. Young H, Baum R, Cremerius U, et al. Measurement of clinical and subclinical tumour response using [18F]- fluorodeoxyglucose and positron emission tomography: Review and 1999 EORTC recommendations. *Eur J Cancer*. 1999;35(13):1773-1782. doi:10.1016/S0959-8049(99)00229-4

123. Boellaard R, Oyen WJG, Verzijlbergen FJ, et al. The Netherlands protocol for standardisation and quantification of FDG whole body PET studies in multi-centre trials. 2008:2320-2333. doi:10.1007/s00259-008-0874-2

124. Boellaard R, Doherty MJO, Weber WA, et al. FDG PET and PET / CT : EANM procedure guidelines for tumour PET imaging : version 1 . 0. 2010:181-200. doi:10.1007/s00259-009-1297-4

125. Appelbe OK, Zhang Q, Pelizzari CA, Weichselbaum RR, Kron SJ. Image-guided radiotherapy targets macromolecules through altering the tumor microenvironment. *Mol Pharm*. 2016;13(10):3457-3467. doi:10.1021/acs.molpharmaceut.6b00465

126. Ko H, Park S, Kim J, et al. A study on comparative analysis of SUVs before and after correction with use of recovery coefficient (RC) in partial volume effect (PVE). *Imaging Sci J*. 2014;62(1):11-15.

127. Srinivas SM, Dhurairaj T, Basu S, Bural G, Surti S, Alavi A. A recovery coefficient method for partial volume correction of PET images. *Ann Nucl Med*. 2009;23(4):341-348. doi:10.1007/s12149-009-0241-9

128. Soret M, Bacharach SL, Buvat I. Partial-volume effect in PET tumor imaging. *J Nucl Med*. 2007;48(6):932-945. doi:10.2967/jnumed.106.035774

129. Mannheim JG, Mamach M, Reder S, et al. Reproducibility and comparability of preclinical PET imaging data: A multi-center small animal PET study. *Jounal Nucl Med*. 2019. doi:10.2967/jnumed.118.221994

130. Qi J, Leahy RM, Cherry SR, Chatziioannou A, Farquhar TH. High-resolution 3D Bayesian image reconstruction using the microPET small-animal scanner. *Phys Med Biol*. 1998;43(4):1001-1013. doi:10.1088/0031-9155/43/4/027

131. Qi J, Leahy RM. Iterative reconstruction techniques in emission computed tomography Iterative reconstruction techniques in emission. *Phys Med Biol*. 2006;51. doi:10.1088/0031-9155/51/15/R01

132. Mannheim JG, Kara F, Doorduin J, et al. Standardization of small animal imaging — current status and future prospects. *Mol Imaging Biol*. 2017;20(October):716-731. doi:10.1007/s11307-017-1126-2

133. Morin RL, Gerber TC, McCollough CH. Radiation dose in computed tomography of the heart. *Circulation*. 2003;107(6):917-922. doi:10.1161/01.CIR.0000048965.56529.C2

134. Mcdougald W, Collins R, Green M, Tavares AAS. Evaluation of the effects of different microCT parameters on microPET/CT imaging. *Eur J Nucl Med Mol Imaging*. 2016;43:S523-S524.

135. Osborne DR, Yan S, Stuckey A, Pryer L, Richey T, Wall JS. Characterization of X-ray Dose in Murine Animals Using microCT, a New Low-Dose Detector and nanoDot Dosimeters. *PLoS One*. 2012;7(11):1-9. doi:10.1371/journal.pone.0049936

136. Carlson SK, Classic KL, Bender CE, Russell SJ. Small animal absorbed radiation dose from serial micro-computed tomography imaging. *Mol Imaging Biol*. 2007;9(2):78-82. doi:10.1007/s11307-007-0080-9

137. Foster WK, Ford NL. Investigating the effect of longitudinal micro-CT imaging on tumour growth in mice. *Phys Med Biol*. 2011;56(2):315-326. doi:10.1088/0031-9155/56/2/002

138. Linet M, Kim K, Kleinerman R, Simon S, Berrington de Gonzalez A. Historical Review of Cancer Risks in Medical Radiation Workers. *Radiat Res*. 2010;174(6):793-808. doi:10.1667/RR2014.1.Historical

139. Boone JM, Velazquez O, Cherry SR. Small-animal X-ray dose from micro-CT. *Mol Imaging*. 2004;3(3):149-158. doi:10.1162/1535350042380326

140. Kiarashi N, Sturgeon GM, Nolte LW, et al. Development of matched virtual and physical breast phantoms based on patient data. *SPIE Med Imaging Phys Med Imaging*. 2013;8668:866805. doi:10.1117/12.2008406

141. About P, Service A, Events N, et al. Spatial resolution testing of microCT. 2017.

142. Gallas RR, Hünemohr N, Runz A, Niebuhr NI, Jäkel O, Greilich S. An anthropomorphic multimodality (CT/MRI) head phantom prototype for end-to-end tests in ion radiotherapy. *Z Med Phys*. 2015;25(4):391-399. doi:10.1016/j.zemedi.2015.05.003

143. Jakab G, Rácz A, Nagy K. High Quality Cone-beam CT Reconstruction on the GPU. *Quality*.

144. Putzer D, Gabriel M, Henninger B, et al. Bone metastases in patients with neuroendocrine tumor: {68Ga-DOTA-Tyr3-octreotide} {PET} in comparison to {CT} and bone scintigraphy. *J Nucl Med*. 2009;50(8):1214-1221. doi:10.2967/jnumed.108.060236

145. Winslow JF, Hyer DE, Fisher RF, Tien CJ, Hintenlang DE. Construction of anthropomorphic phantoms for use in dosimetry studies. *J Appl Clin Med Phys*. 2009;10(3):195-204. doi:10.1120/jacmp.v10i3.2986

146. Jaffee EM, Dang C Van, Agus DB, et al. Future cancer research priorities in the USA: a Lancet Oncology Commission. *Lancet Oncol*. 2017;18(11):e653-e706. doi:10.1016/S1470-2045(17)30698-8

147. Biglin ER, Price GJ, Chadwick AL, Aitkenhead AH, Williams KJ, Kirkby KJ. Preclinical dosimetry: exploring the use of small animal phantoms. *Radiat Oncol*. 2019;14(1):1-10. doi:10.1186/s13014-019-1343-8

148. Welch D, Turner L, Speiser M, Randers-Pehrson G, Brenner DJ. Scattered Dose Calculations and Measurements in a Life-Like Mouse Phantom. *Radiat Res*. 2017;187(4):433-442. doi:10.1667/rr004cc.1

149. McGurk R, Hadley C, Jackson I, Vujaskovic Z. Development and dosimetry of a small animal lung irradiation platform. *Heal Phys*. 2012;103(4):454-462. doi:10.1097/hp.0b013e3182632526

150. Xie T, Zaidi H. Development of computational small animal models and their applications in preclinical imaging and therapy research. *Med Phys*. 2016;43(1):111-131. doi:10.1118/1.4937598

151. Zhang H, Hou K, Chen J, et al. Fabrication of an anthropomorphic heterogeneous mouse phantom for multimodality medical imaging. *Phys Med Biol*. 2018;63(19). doi:10.1088/1361-6560/aadf2b

152. Fujii N. 'United States Patent [19]. 1981:4-9.

153. Bagaria V, Rasalkar D, Bagaria SJ, Ilyas J. Medical Application Of Rapid Prototyping - A New Horizon. *Adv Appl Rapid Prototyp Technol Mod Eng*. 2011:1-21.

154. Abdel-Sayed P, Segesser L Von. Rapid Prototyping for Training Purposes in Cardiovascular Surgery. *Adv Appl Rapid Prototyp Technol Mod Eng*. 2011. doi:10.5772/20498

155. Petzold R, Zeilhofer HF, Kalender W a. Rapid protyping technology in medicine--basics and applications. *Comput Med Imaging Graph*. 1999;23(5):277-284. doi:10.1016/S0895-6111(99)00025-7

156. Schönberger M, Hoffstetter M. *3 - Design of Plastic Medical Devices*.; 2016. doi:http://dx.doi.org/10.1016/B978-0-323-37023-3.00003-8

157. Branch C. 3D Printing In Healthcare 3D Printing In Healthcare. 2015;16:1-4. http://fisherpub.sjfc.edu/cgi/viewcontent.cgi?article=1142&context=ur.

158. Martelli N, Serrano C, Van Den Brink H, et al. Advantages and disadvantages of 3-dimensional printing in surgery: A systematic review. *Surg (United States)*. 2016;159(6):1485-1500. doi:10.1016/j.surg.2015.12.017

159. Anchieta MVM, Quaresma MM, De Salles FA. Rapid Prototyping Applied to Maxillofacial Surgery. *Adv Appl Rapid Prototyp Technol Mod Eng*. 2011:153-172. doi:10.5772/1437

160. Raphael O, Hervé R. Clinical Applications of Rapid Prototyping Models in Cranio-

Maxillofacial Surgery. 2011;(C):173-207.

161. Seitz H, Tille C, Irsen S, Bermes G, Sader R, Zeilhofer H-F. Rapid Prototyping models for surgical planning with hard and soft tissue representation. *Int Congr Ser*. 2004;1268:567-572. doi:10.1016/j.ics.2004.03.139
162. Murphy S V, Atala A. 3D bioprinting of tissues and organs. *Nat Biotechnol*. 2014;32(8):773-785. doi:10.1038/nbt.2958
163. Esses SJ, Berman P, Bloom AI, Sosna J. Clinical applications of physical 3D models derived from MDCT data and created by rapid prototyping. *Am J Roentgenol*. 2011;196(6):683-688. doi:10.2214/AJR.10.5681
164. Zemnick C, Woodhouse SA, Gewanter RM, Raphael M, Piro JD. Rapid prototyping technique for creating a radiation shield. *J Prosthet Dent*. 2007;97(4):236-241. doi:10.1016/j.prosdent.2007.02.005
165. Mitsouras D, Lee TC, Liacouras P, et al. Three-dimensional printing of MRI-visible phantoms and MR image-guided therapy simulation. *Magn Reson Med*. 2016;00(October 2015):1-10. doi:10.1002/mrm.26136
166. Melchels FPW, Feijen J, Grijpma DW. A review on stereolithography and its applications in biomedical engineering. *Biomaterials*. 2010;31(24):6121-6130. doi:10.1016/j.biomaterials.2010.04.050
167. Marro A, Bandukwala T, Mak W. Three-Dimensional Printing and Medical Imaging: A Review of the Methods and Applications. *Curr Probl Diagn Radiol*. 2016;45(1):2-9. doi:10.1067/j.cpradiol.2015.07.009
168. Negi S, Dhiman S, Sharma RK. Basics and applications of rapid prototyping medical models. *Rapid Prototyp J*. 2014;20(3):256-267. doi:10.1108/RPJ-07-2012-0065
169. Raman R, Bashir R. *Stereolithographic 3D Bioprinting for Biomedical Applications*. Elsevier Inc.; 2015. doi:10.1016/B978-0-12-800972-7/00006-2
170. Gurr M, Mülhaupt R. Rapid prototyping. *Polym Sci A Compr Ref*. 2012;8(March 2015):77-99. doi:10.1016/B978-0-444-53349-4.00202-8
171. Ma D, Lin F, Chua CK. Rapid prototyping applications in medicine. Part 1: NURBS-based volume modelling. *Int J Adv Manuf Technol*. 2001;18(2):103-117. doi:10.1007/s001700170081
172. ASTM International. *F2792-12a - Standard Terminology for Additive Manufacturing*

Technologies.; 2013. doi:10.1520/F2792-12A.2

173. Dimitrov D, Schreve K, Beer N De. Advances in three dimensional printing - state of the art and future perspectives. *Rapid Prototyp J*. 2006;12(3):136-147. doi:10.1108/13552540610670717
174. Sst SD. Index. *Med Model*. 2015:487-500. doi:10.1016/B978-1-78242-300-3.18001-1
175. Maher PS, Keatch RP, Donnelly K, Vorstius JB. Bio-Mechanical Evaluation of a 3D Printed Composite Material. *World Congr Med Phys Biomed Eng Vol 25, Pt 10 Biomater Cell Tissue Eng Artif Organs*. 2009;25(10):130-133.
176. Stansbury JW, Idacavage MJ. 3D printing with polymers: Challenges among expanding options and opportunities. *Dent Mater*. 2016;32(1):54-64. doi:10.1016/j.dental.2015.09.018
177. Hubbell JH, Seltzer SM. X-Ray Mass Attenuation Coefficients. *NIST Stand Ref Database 126*. 2004.
178. National Institute of Standards and Technology. X-Ray Mass Attenuation Coefficients. 2014. http://physics.nist.gov/PhysRefData/XrayMassCoef/chap2.html.
179. Welch D, Harken AD, Randers-Pehrson G, Brenner DJ. Construction of mouse phantoms from segmented CT scan data for radiation dosimetry studies. *Phys Med Biol*. 2015;60(9):3589-3598. doi:10.1088/0031-9155/60/9/3589
180. Hutmacher DW. *Scaffolds in Tissue Engineering Bone and Cartilage*. Vol 21. Woodhead Publishing Limited; 2000. doi:10.1016/B978-008045154-1.50021-6
181. Cui H, Nowicki M, Fisher JP, Zhang LG. 3D Bioprinting for Organ Regeneration. *Adv Healthc Mater*. 2017;6(1):1-54. doi:10.1002/adhm.201601118
182. Cui X, Breitenkamp K, Finn MG, Lotz M, D'Lima DD. Direct human cartilage repair using three-dimensional bioprinting technology. *Tissue Eng - Part A*. 2012;18(11-12):1304-1312. doi:10.1089/ten.tea.2011.0543
183. Markstedt K, Mantas A, Tournier I, Martínez Ávila H, Hägg D, Gatenholm P. 3D bioprinting human chondrocytes with nanocellulose-alginate bioink for cartilage tissue engineering applications. *Biomacromolecules*. 2015;16(5):1489-1496. doi:10.1021/acs.biomac.5b00188
184. Stout DB, Chatziioannou AF, Lawson TP, Silverman RW, Gambhir SS, Phelps ME. Small Animal Imaging Center Design: The Facility at the UCLA Crump Institute for Molecular Imaging. *Mol Imaging Biol*. 2005;7(6):393-402. doi:10.1007/s11307-005-0015-2

185. Rosen DB, Leung LY, Louie B, et al. Quantitative measurement of alterations in DNA damage repair (DDR) pathways using single cell network profiling (SCNP). *J Transl Med*. 2014;12(1):1-14. doi:10.1186/1479-5876-12-184

186. Georgakilas AAG, Neill PO, Stewart RD, Georgakilas AG, Neill PO, Stewart RD. Induction and Repair of Clustered DNA Lesions : What Do We Know So Far ? Induction and Repair of Clustered DNA Lesions : What Do We Know So Far ? *Radiat Res Soc*. 180(1):100-109. doi:10.1667/RR3041.1

187. Lee MS, Hwang D, Kim JH, Lee JS. Deep-dose: a voxel dose estimation method using deep convolutional neural network for personalized internal dosimetry. *Sci Rep*. 2019;9(1):1-9. doi:10.1038/s41598-019-46620-y

188. Verhaegen F, Dubois L, Gianolini S, et al. ESTRO ACROP Guideline ESTRO ACROP : Technology for precision small animal radiotherapy research : Optimal use and challenges. 2018;126:471-478.

189. Jammalamadaka U, Tappa K. Recent advances in biomaterials for 3D printing and tissue engineering. *J Funct Biomater*. 2018;9(1). doi:10.3390/jfb9010022

190. Cohen J, Reyes SA. Creation of a 3D printed temporal bone model from clinical CT data. *Am J Otolaryngol - Head Neck Med Surg*. 2015;36(5):619-624. doi:10.1016/j.amjoto.2015.02.012

191. Biglino G, Schievano S, Taylor AM. The Use of Rapid Prototyping in Clinical Applications. 2008.

192. Dancewicz OL, Sylvander SR, Markwell TS, Crowe SB, Trapp J V. Radiological properties of 3D printed materials in kilovoltage and megavoltage photon beams. *Phys Medica*. 2017;38:111-118. doi:10.1016/j.ejmp.2017.05.051